

Copyright is owned by the Author of the thesis. Permission is given for a copy to be downloaded by an individual for the purpose of research and private study only. The thesis may not be reproduced elsewhere without the permission of the Author.

OPTICAL PROPERTIES OF
ORGANIC NLO CHROMOPHORES
FOR TERAHERTZ APPLICATIONS

A Thesis Presented in Partial Fulfilment of the Requirements
for the Degree of

Doctor of Philosophy
in Physics

at

Massey University, Palmerston North,
New Zealand.

YASAR KUTUVANTAVIDA

2012

Abstract

This thesis was motivated by the potential of organic nonlinear optical (NLO) zwitterionic chromophores to be used as active components in THz emitters and detectors. This study presents the results from measurements of the electro-optic (EO) coefficient, photostability and the THz properties of organic NLO chromophores.

An EO coefficient of over 700 pm/V was measured for some EO polymers using the Teng-Man modulation ellipsometry technique at low frequencies. A roll off in the value of the EO coefficient was observed for frequencies over 10 kHz and converging to the theoretically estimated value of ~ 2 pm/V. The large over estimate of the EO coefficient at low frequencies using the Teng-Man method is attributed to contributions from the cavity resonance and interference effects.

The EO coefficient was also measured using a new method based on the electric field induced modulation of diffraction gratings. The measured EO coefficient using this technique is an order of magnitude lower than that measured using the Teng-Man method but it is an order of magnitude higher than the theoretically expected value. By investigating DC and AC measurements it was possible to deduce that the large apparent EO coefficient is due to the inverse piezoelectric effect and thin film interference. The large EO coefficient at low frequencies may also have a contribution from dipole clusters. The small EO coefficient at high frequency shows that the chromophores may not be particularly useful for THz applications. However, they have potential in low frequency applications such as modulators, and dense wavelength division multiplexing.

The current photodegradation models are shown to be inadequate and the photodegradation can be modeled by considering a distribution in the photodegradation quantum efficiencies. The addition of a singlet oxygen quencher has been found to enhance the photostability of some chromophores by up to 6 times. Structural modifications also affect the photostability. A correlation between the photostability

and bond length alternation (BLA) was found where there is a trade-off between the chromophores molecular NLO effect and photostability.

Calculations based on the THz dielectric properties showed that the EO polymers have a reasonable coherence length for THz generation using optical rectification. Low wavenumber Raman spectroscopy measurements made on recrystallised compounds exposed some theoretically predicted modes that were not been reported found experimentally. Low temperature and low energy Raman spectroscopy measurements made on some selected organic compounds showed a strong temperature dependence of the low energy vibrational modes. The temperature dependent red-shift and line broadening have been primarily attributed to thermal expansion and a distribution in the distance between monomers.

Acknowledgements

I would like to express my sincere gratitude to my day-to-day supervisor Dr Grant Williams at the School of Chemical and Physical Sciences, Victoria University of Wellington. His enthusiastic supervision, constant encouragement and useful discussions made this thesis possible. My sincere thanks to my Massey University supervisor Associate Professor Mark Waterland for his support and help ensuring my thesis was on track.

I gratefully acknowledge the support of Dr Sebastiampillai Raymond at Industrial Research Limited during this study. My sincere thanks to Dr Delower Bhuiyan and Dr Andrew Kay at Industrial Research Limited for their invaluable help, including the supply of organic compounds used in this study.

My sincere thanks to Professor Roger Lewis at University of Wollongong for the THz laboratory facility, Jessianta Anthony at University of Auckland for providing THz-TDS data of electro-optic polymers, Professor Pablo Etchegoin at Victoria University of Wellington for the Raman facility, and Dr Graeme Gainsford at Industrial Research Limited for the crystallography data.

I am indebted to those who helped me proof read this thesis, especially, Damian Carder, Adam Swanson, Robert Breukers, James Quilty and Jibu Stephen at Industrial Research Limited. My sincere thanks to the rest of the current and former Photonics team at Industrial Research Limited - Ayla Middleton, David Clarke, Mohamed Ashraf, Victoria Peddie, Christin Gaedtke, Stefaan Janssens and Tra My Do for their support during this thesis.

I would like to gratefully acknowledge the PhD scholarship by the Industrial Research Limited from the project “Photonic Imaging and Sensing Program” funded by the New Zealand Ministry of Research and Innovation. My sincere thanks to the MacDiarmid Institute for Advanced Materials and Nanotechnology for the funding to attend international conferences. My sincere thanks go as well to the staff of

the Institute of Fundamental Sciences, Massey University for the administrative support.

Finally, I wish to thank my family and friends for their support and encouragement throughout my stay in New Zealand.

Contents

1	Introduction	1
2	Basic Concepts	5
2.1	Nonlinear optics	5
2.2	Electro-optic effect	6
2.2.1	Linear electro-optic coefficient	8
2.2.2	Optical rectification and frequency mixing	9
2.3	Electro-optic materials	10
2.3.1	Electro-optic polymers	11
2.3.2	Electro-optic polymer systems	11
2.3.3	Glass transition temperature	14
2.4	Organic nonlinear optical chromophores	14
2.4.1	Microscopic NLO effect	15
2.4.2	Bond length alternation	17
2.5	Absorption	19
2.5.1	Linear absorption	19
2.5.2	Two-photon absorption	19
2.5.3	Kramers-Kronig relation	20
2.6	Aggregation	21
2.7	Solvatochromism	22
2.8	THz radiation	23
2.8.1	EO effect in THz technology	24
2.9	Interaction of photons with phonons	25
2.9.1	Infrared absorption	25
2.9.2	Raman scattering	27

3	Instruments and Techniques	29
3.1	Spin coater	29
3.2	UV-Vis-NIR spectroscopy	29
3.2.1	Lambda 1050 UV/Vis/NIR spectrophotometer	30
3.2.2	Varian Cary 50	31
3.2.3	Fibre optic spectrometer	31
3.3	Measurement of thickness and refractive index	31
3.3.1	Prism coupler	31
3.3.2	DekTak profilometer	33
3.3.3	Interferometry technique	33
3.4	Poling apparatus	35
3.5	Teng-Man apparatus	35
3.6	DSC-TGA	37
3.7	Infrared spectroscopy	38
3.7.1	Nicolet TM FTIR spectrometer	39
3.8	THz time domain spectroscopy	39
3.9	Raman spectroscopy	40
3.10	Lasers	41
4	Fabrication and Processing of EO Polymers	43
4.1	Preparation of ultra-clean substrates	43
4.2	Polymer thin film fabrication	45
4.2.1	Host polymer	45
4.2.2	Preparation of solution	46
4.2.3	Solution casting for thick films	48
4.2.4	Spin coating for thin films	49
4.3	Measurement of thickness and refractive index	51
4.3.1	Refractive index dispersion	52
4.4	Chromophore concentration in films	53
4.5	Poling to induce electro-optic effect	54
4.5.1	Poling techniques	56
4.5.2	Contact electrode poling	58
4.5.3	Optimising poling conditions	58
4.5.4	Dielectric breakdown	60

5	Measurement of r_{33} Using Modulation Ellipsometry	63
5.1	Teng-Man apparatus for the measurement of r_{33}	63
5.1.1	Teng-Man apparatus optimisation	67
5.2	Temporal stability of induced EO effect	69
5.2.1	Relaxation of the induced r_{33} of a PYR-3 system	70
5.2.2	Analysis of the relaxation process	72
5.3	Structural alterations for improved molecular nonlinearity	74
5.3.1	Effects of donor strength	75
5.3.2	Effects of conjugation length	76
5.3.3	Effects of ring-locking	77
5.3.4	Effects of bulky group substitution	78
5.4	Effects of structural alternations at the macroscopic level	79
5.4.1	Bulky substitution in PYR-3	80
5.4.2	Bulky substitution in IND-5	81
5.4.2.1	Hydrogenated bulky group	82
5.4.2.2	Fluorinated bulky group	83
5.4.2.3	Mixed bulky groups	83
5.4.3	Ring-locking of QUN-7 and IND-7	84
5.5	Theoretical calculation of r_{33}	84
5.5.1	Translating microscopic quantities to r_{33}	86
5.5.2	Calculation of r_{33} for a PYR-3/APC system	87
5.5.3	Mismatch between experiment and calculation	88
5.6	Analysis of the mismatch between experimental and calculated r_{33}	89
5.6.1	Frequency response of r_{33}	89
5.6.2	Contribution from acoustic and optical phonons	91
5.6.3	Contribution from piezoelectric effect	93
5.6.4	Effects of acoustic velocity in the host polymer	95
5.6.5	Contribution from the formation of chromophore clusters	95
5.7	Conclusions	96
6	Measurement of r_{33} Using Diffraction Method	99
6.1	Diffraction gratings	100
6.2	Diffraction efficiency	101
6.2.1	Small Q: “thin” grating	102
6.2.2	Large Q: “thick” grating	104

6.2.3	Sinusoidal grating with small modulation	105
6.3	Periodic gratings on poled polymers	106
6.3.1	Grating inscription using interferometry	106
6.3.2	Modulation of refractive index	108
6.3.3	Skin depth	111
6.3.4	Estimation of diffraction efficiency	112
6.4	Estimation of r_{33} from diffraction efficiency	114
6.4.1	Condition of validity	115
6.5	Experiment using DC modulating field	116
6.5.1	Estimation of EO coefficient using DC field	117
6.6	Experiment using AC modulating field	119
6.6.1	Estimation of EO coefficient using AC field	120
6.7	Analysis of diffraction technique	121
6.7.1	Effects of modulating frequency	121
6.7.2	Change in diffraction efficiency with lock-in phase settings . .	122
6.7.2.1	Inverse piezoelectric effect	123
6.7.2.2	Interference effect	124
6.8	Conclusions	126
7	Photostability of NLO Chromophores	129
7.1	Light induced degradation of NLO chromophores	130
7.1.1	Photodegradation mechanism	132
7.1.2	Photochemistry of photo-oxidation	134
7.1.3	Basic photodegradation model	135
7.2	Experimental setup	136
7.3	Effects of light intensity and oxygen partial pressure	138
7.4	Modified model of photodegradation	141
7.4.1	Model based on multiple photodegradation pathways	143
7.5	Effects of film thickness	148
7.6	Effects of chromophore concentration	149
7.7	Strategies to achieve high photostability	151
7.7.1	Bulky substitution on PYR-3	152
7.7.2	Partial ring-locking on IND-7 and QUN-7	153
7.7.3	Addition of singlet oxygen quencher	155
7.8	Influence of bond length alternation on photostability	157

7.8.1	Effects of ring-locking on the BLA of IND-7	158
7.8.2	Effects of ring-locking on the BLA of QUN-7	159
7.8.3	Trade-off between hyperpolarisability and photostability . . .	161
7.9	Conclusions	162
8	Material Characterisation at THz Frequencies	165
8.1	THz generation and detection using EO polymers	166
8.1.1	Phase matching	167
8.1.2	Phase matching for THz generation	167
8.1.3	Phase matching for THz detection	169
8.2	Properties of polymers in THz region	169
8.2.1	THz time domain spectroscopy	170
8.2.2	Absorption in the THz region	172
8.2.3	THz refractive index	172
8.2.4	Coherence length for THz generation using PYR-3/APC . . .	173
8.2.5	Raman and IR on APC film	174
8.3	Low energy vibrational spectra of organic crystals	175
8.3.1	Experimental details	175
8.3.2	Spectrum of benzoic acid derivatives	176
8.3.3	Spectrum of aspirin	177
8.3.4	Spectrum of nitro derivatives of toluene	179
8.4	Temperature dependence of low energy vibrational modes	180
8.4.1	Temperature dependence in salicylic acid	181
8.4.2	Temperature dependent Raman in 2,4-DNT	182
8.5	Conclusions	182
9	Summary	185
	Bibliography	189
	List of Publications	205

List of Figures

2.1	Polarisation as a function of electric field in a linear and a nonlinear medium.	6
2.2	Refractive index as a function of applied electric field in (a) a linear EO medium and (b) a quadratic EO medium.	8
2.3	An example scheme of a Pockels cell showing the change in polarisation of a wave through an EO material in the presence of an external electric field. Arrows indicate the polarisation direction.	8
2.4	Electro-optic polymer systems: (a) Host-guest, (b) Side-chain, (c) Main-chain and (d) Cross-linked polymer systems.	12
2.5	(left) Schematic of a push-pull molecule (chromophore) with an electron donor (D) and an electron acceptor (A) connected by a conjugated π -bridge. (right) An example structure of an NLO chromophore.	15
2.6	Definition of regions of BLA correspond to the degree of mixing the neutral (N) and charge-separated (CS) resonance structures to the ground state. The nature of the conjugated π -bridge changes from neutral polyene-like (1) to polar cyanine-like (3) to very polar charge separated polyene-like (5).	18
2.7	Energy level diagram showing excitation of chromophores; ISC represents inter system crossing.	20
2.8	Schematics of H- and J- aggregated chromophores.	22
2.9	Energy level diagram showing the transitions involved in IR absorption and Raman scattering.	26
3.1	A WS-400E-6NPP-LITE spin processor by Laurell Technologies Corporation. (a) Front view and (b) Rear-view of the instrument.	30

3.2	Schematic of the measurement of film thickness using prism coupler. Left side is the schematic of geometry of the apparatus and shown right is the example for the coupling modes.	32
3.3	Schematic of the transmission through a thin film on a glass substrate.	34
3.4	Photograph of the poling apparatus being used in our laboratory; shown inset is the film with electric field applied across the block electrode and ITO layer over the glass.	35
3.5	Schematic of the Teng-Man modulation ellipsometry apparatus. . .	36
3.6	Teng-Man experimental set-up used in our laboratory at IRL. . . .	37
3.7	Schematic of a THz-TDS system using optical rectification technique for THz generation and electro-optic sampling method for THz detection.	40
4.1	Structures of the organic NLO chromophores used in the experiments in this thesis.	47
4.2	Effects of spin speed and viscosity of the solution on determining the thickness of spin-processed films of APC in 1,1,2-TCE.	50
4.3	Interferometry method to estimate film thickness.	52
4.4	(a) Absorption coefficient of a $2\mu\text{m}$ polymer film containing 5 wt% PYR-3 in APC. (b) Dispersion of change in refractive index Δn with wavelength calculated using the Kramers-Kronig transform from the absorption coefficient. (c) Refractive index dispersion of the host polymer APC estimated using first order Sellmeier equation on the measured values at 633, 1300 and 1550 nm, and the total effective refractive index of the polymer film.	53
4.5	Schematic of chromophore orientation in the polymer films before, during and after poling.	56
4.6	Schematic of an <i>in situ</i> contact electrode poling system.	59
4.7	Current flow across the film and temperature as a function of time during poling.	61
5.1	Output laser intensity (I_O) and modulated intensity (I_M) as a function of SBC retardation.	65
5.2	Modulated intensity as a function of modulating voltage on a poled film containing 5 wt.% PYR-3B in APC.	69

5.3	Optical bias curve and modulated intensity obtained as a function of compensator position correspond to the phase retardation induced by the compensator.	70
5.4	Analysis of the Teng-Man ellipsometry data from a poled polymer. . .	71
5.5	Relaxation of r_{33} of a poled 5 wt.% PYR-3/APC film.	71
5.6	Structures of the PYR-3, QUN-3 and IND-3 chromophores.	76
5.7	Structure of PYR-3 chromophore and its bulky group derivative PYR-3B.	80
5.8	(a) Plot of the molar extinction coefficient of PYR-3B in solutions. (b) Plot of the optical absorption coefficient of PYR-3B in films. . .	81
5.9	Plot of the measured r_{33} of a poled 8 wt.% PYR-3B/APC film against time and a bi-exponential fit to the data.	82
5.10	Structures of the IND-5 chromophore and its bulky group derivatives.	82
5.11	Structures of the QUN-7 and IND-7 chromophores and their ring-locked structures QUN-7R and IND-7R.	84
5.12	Dependence of the EO coefficient on the modulation frequency measured at $\lambda = 1314$ nm for a $4 \mu\text{m}$ film made of 5 wt% PYR-3/APC.	90
5.13	Small angle XRD data of a 5 wt.% PYR-3/APC film on (a) glass and (b) ITO coated glass substrate.	93
6.1	The geometry of a thick periodic grating; I_{inc} is the incident wave, \mathbf{K} is the grating vector, Λ is the grating period, I_0 is the zeroth order beam, I_1 is the first order diffracted beam, d is the thickness of grating and θ is the angle corresponding to each beams.	100
6.2	Experimental set up used to inscribe Bragg grating on polymer thin films using two coherent interfering beams.	107
6.3	(a) Absorption coefficient of a $\sim 6 \mu\text{m}$ PYR-3/APC film at 488 nm during the grating inscription. (b) The first order diffraction efficiency measured during the the grating inscription.	108
6.4	(a) $\Delta\alpha$ as a function of wavelength and (b) the refractive index dispersion estimated for a 5 wt.% PYR-3/APC film using Kramers-Kronig approximation on $\Delta\alpha$	109
6.5	Change in $\Delta\alpha$ with incident energy when the grating inscribed on a 5 wt.% PYR-3/APC film using two-beam interference.	110

6.6	Skin depth, δ_p , estimated for a 5 wt.% PYR-3/APC film in the visible spectrum.	112
6.7	(a) Q factor of a 5 wt.% PYR-3/APC thin film with thickness $6.08 \mu\text{m}$ and grating period $2.85 \mu\text{m}$. (b) Diffraction efficiency estimated for for small modulation.	113
6.8	Schematic of the experimental set up to estimate EO coefficient using diffraction technique with DC modulating field.	116
6.9	(a) Diffraction efficiency for the first order diffracted beam, η as a function of applied DC field for a $6.06 \mu\text{m}$ film of 5 wt% PYR-3/APC. (b) $\Delta\eta(E)/\eta_0$ vs. E for the same data.	117
6.10	(a) Diffraction efficiency as a function of applied DC field for a $6.1 \mu\text{m}$ film of 5 wt.% PYR-3/APC with 170 pm/V when measured using Teng-Man modulation ellipsometry. (b) $\Delta\eta(E)/\eta_0$ vs. electric field for the same data.	118
6.11	Schematic of the experimental set up to estimate r_{33} using diffraction technique with an AC modulating field with a modulating frequency of 1 kHz.	119
6.12	(a) Diffraction efficiency as a function of applied field for a poled $\sim 6 \mu\text{m}$ thick 5 wt.% PYR-3/APC film. (b) $\Delta\eta/\eta$ as a function of applied AC modulating field.	120
6.13	Plot of the effect of AC modulation on the zeroth order beam. This kind of strong modulation on zeroth order was not observed during the measurements using DC field.	121
6.14	(a) Diffraction efficiency as a function of modulating frequency for a $6.1 \mu\text{m}$ PYR-3/APC film for a 760 nm beam. The modulating field was $0.82 \text{ V}/\mu\text{m}$. (b) A similar effect observed in the r_{33} measurement using Teng-Man modulation ellipsometry.	122
6.15	(a) Change in the effective transmittance simulated for a $6.0 \mu\text{m}$ and a $6.1 \mu\text{m}$ PYR-3/APC film due to the thin film interference effect; vertical dashed line shows the wavelength of interest, 760 nm . (b) Change in effective transmittance at 760 nm for a PYR-3/APC film for a small variation in thickness from $6.1 \mu\text{m}$. (c) The same as in (b) for $6.0 \mu\text{m}$	124

7.1	Absorption spectra during progressive bleaching of of IND-7 solution in CHCl_3 by exposure to UV radiation at 365 nm.	131
7.2	Absorption spectrum of IND-7 solution in CHCl_3 at different concentrations.	131
7.3	(a) Absorbance of a 3% IND-7/APC film while progressive bleaching using a 655 nm beam, arrow indicates increasing bleaching time (b) Normalised absorbance.	131
7.4	Energy level diagram for a chromophore molecule, where S_0 is the ground state (with lifetime τ_g), S_1 the singlet excited state (with lifetime τ_1), T_1 the triplet excited state (with lifetime τ_T) of the chromophore molecule, ISC is the inter system crossing.	133
7.5	(a) The trans and (b) the cis form of a PYR-3 chromophore (c), (d) and (e) the expected products formed after photo-oxidation process. .	134
7.6	Photodegradation experimental set up.	136
7.7	Picture of a photodegradation experimental set using a 532 nm Nd:YVO ₄ laser beam.	137
7.8	Transmittance as a function of time while photodegrading a 2.4 μm , 5 wt% PYR-3/APC film with a 1 mW/mm ² 532 nm laser beam. . . .	137
7.9	$F(\beta)$ against β plot for the photodegradation data obtained by optically degrading a 5 wt.% IND-7/APC film at different light intensities.	139
7.10	Plot of photodegradation quantum efficiency as a function of light intensity.	140
7.11	Plot of the transmittance $T(t)$ against time during illumination at 532 nm for (a) a 2.4 μm 5% PYR-3/APC film with an incident intensity 1 mW/mm ² , and (b) a 2.05 μm 15% PYR-3/APC film with an incident intensity 0.47 mW/mm ²	143
7.12	Plot of the transmittance against $\beta/2.67 \times 10^{19}$ (solid curves) for (a) a 2.4 μm thick 5% PYR-3/APC films and (b) a 2.05 μm thick 15% PYR-3/APC film.	145
7.13	Plot of the photostability enhancement factor, η , against light intensity at 532 nm.	148
7.14	Transmittance data when photodegrading 5 wt% PYR-3/APC films of 2.4 μm , 3.84 μm and 7.5 μm using 532 nm and intensity 50 mW/mm ² .	

7.15	Plot of $F(\beta)$ against β plot for three concentrations of IND-7 chromophores in APC with $2.1\mu\text{m}$ thickness when photodegradating with 655 nm laser and intensity $15.7\text{ mW}/\text{mm}^2$. Inset is the plot of $\beta_{1/e}$ against chromophore loading by wt% in APC.	150
7.16	Absorption spectra of 1%, 3%, 5% and 8% IND-7 film in APC.	150
7.17	Structures and absorption spectra of PYR-3 and PYR-3B in the films made of similar chromophore concentration and thicknesses in APC. Dashed line indicates the wavelength used to degrade the chromophores.	152
7.18	Plot of the transmittance at 532 nm against incident photon flux for a 8 wt.% PYR-3B/APC film with incident laser intensities of $1\text{ mW}/\text{mm}^2$ and $5\text{ mW}/\text{mm}^2$	153
7.19	Structures and absorption spectra of IND-7 and IND-7R in the films made of mixing similar chromophore concentrations, 5 %, and thicknesses, $2.2\mu\text{m}$, in APC.	154
7.20	(a) Plot of the transmittance at 655 nm against time for a $2.2\mu\text{m}$ thick 5 wt.% IND-7/APC film (green solid curve) and a $2.1\mu\text{m}$ thick 5 wt.% IND-7R/APC film (red dashed curve) for incident laser intensity of $35\text{ mW}/\text{mm}^2$ (b) Plot of $F(\beta)$ against β	154
7.21	Structures and absorption spectra of QUN-7 and QUN-7R in the films made of mixing similar chromophore concentrations in APC.	155
7.22	(a) Plot of the Plot of $F(\beta)$ against β at 760 nm for a $5.1\mu\text{m}$ thick 5 wt.% QUN-7/APC film (black solid curve) and a $5.06\mu\text{m}$ thick 5 wt.% QUN-7R/APC film (red solid curve) for incident laser intensity of $10\text{ mW}/\text{mm}^2$ (b) Plot of transmittance against time.	155
7.23	Structure of trans- and cis- isomers of β -carotene.	156
7.24	Energy level diagram showing excitation of the PYR-3 chromophore (left) to the S_1 state, inter-system crossing (ISC) to the T_1 state, energy transfer to β -carotene (middle) that leaves PYR-3 in the ground S_0 state and β -carotene in the triplet excited state, and finally multiphonon decay from the β -carotene excited triplet state to the singlet ground state.	157
7.25	Absorption coefficient and photodegradation experimental data for films containing 5% PYR-3/APC and 0%, 1%, 5% and 10% β -carotene.	158

7.26	Absorption spectra of (a) IND-7 and (b) IND-7R in solutions of different $E_T(30)$ values.	159
7.27	Normalised absorption spectra of (a) QUN-7 and (b) QUN-7R in solutions of different $E_T(30)$ values.	160
7.28	Schematic of the relation between first hyperpolarisability, β_0 and photostability, B	161
8.1	Scheme of THz-TDS in transmission mode.	170
8.2	Time domain THz data collected for a $320\ \mu\text{m}$ 5 wt.% PYR-3/APC film with air as reference. Time delays are relative to each another.	171
8.3	Absorption spectrum of a 5 wt% PYR-3/APC film between 0.2 and 1.1 THz estimated from THz-TDS data.	172
8.4	Refractive index of a 5 wt% PYR-3/APC for the range 0.2 to 1.1 THz.	173
8.5	Low wavenumber Raman spectra of APC.	174
8.6	Structures of the compounds considered for this study; Benzoic acid (a) monomer and (b) dimer, (c) 2-hydroxy benzoic acid, and (d) 3-hydroxy benzoic acid.	176
8.7	Raman spectra of benzoic acid, 2-hydroxy benzoic acid, and 3-hydroxy benzoic acid for energies corresponding to the THz region.	177
8.8	Infrared absorption spectra of benzoic acid, 2-hydroxy benzoic acid, and 3-hydroxy benzoic acid for the THz region. Also shown is the spectra of PB100XF (dash-dotted curve).	179
8.9	Low wavenumber Raman spectrum of Aspirin and Salicylic acid. Structure the monomer units of both compounds are shown inset.	180
8.10	Low wavenumber Raman on 4-nitro toluene (4-NT) and 2,4-dinitro toluene (2,4-DNT) in the THz frequency range.	180
8.11	Temperature dependent low wavenumber Raman spectrum of Salicylic Acid.	181
8.12	Temperature dependent low wavenumber Raman spectrum of 2,4-DNT.	182

List of Tables

4.1	Physical properties of Bayer APEC 9389 Amorphous Polycarbonate (APC).	46
5.1	Effect of varying donor groups on the molecular NLO response of chromophores. β_{zzz} was measured at 1314 nm.	76
5.2	Effect of conjugation length on the molecular NLO response of chromophores. β_{zzz} was measured at 1314 nm.	77
5.3	Effect of partial ring-locking at the conjugated π -bridge on the molecular NLO response IND-7 chromophore, β_{zzz} was measured at 1314 nm.	77
5.4	Effect of bulky substitution on the molecular NLO response of PYR-3 chromophore, β_{zzz} was measured at 1314 nm.	78
5.5	Effect of bulky substitution on the macroscopic EO response of IND-5 chromophore.	83
5.6	Effects of ring-locking on the EO coefficient of IND-7 and QUN-7 chromophores.	84
5.7	Physical quantities used in the calculation of r_{33} in electrostatic and SI units.	87
5.8	Physical properties of the PYR-3 chromophore used in the calculation of r_{33}	87
6.1	Diffraction efficiency for the first order beam of a 6.1 μm , 5 wt % PYR-3/APC film with grating period, $\Lambda = 2.85 \mu\text{m}$. n_{av} is the average refractive index of the film.	113
6.2	Measured and estimated values of diffraction efficiencies at 16 V/ μm for a 5 wt.% PYR-3/APC film.	118

7.1	Chromophore number densities correspond to the chromophore loading in APC.	138
7.2	Table of parameters used to model the transmittance data in Fig. 7.11 and Fig. 7.12 for 2.4 μm thick 5% PYR-3/APC films at 532 nm. . . .	146
7.3	Table of parameters used to model the transmittance data in Fig. 7.11 and Fig. 7.12 for 2.05 μm thick 15% PYR-3/APC films at 532 nm. . .	147
7.4	Structural and electronic properties of IND-7 and IND-7R. Absorption maxima, λ_{max} , in films and in selected solvents having different $E_T(30)$ values are summarized.	159
7.5	Structural and electronic properties of QUN-7 and QUN7R. Absorption maxima, λ_{max} , in films and in selected solvents having different $E_T(30)$ values.	160
7.6	Relationship between the magnitude of BLA values and corresponding photostability (B) of IND-7 & IND-7R ($\sim 2 \mu\text{m}$ thick, light intensity 35 mW/mm ²), and QUN-7 & QUN-7R ($\sim 5 \mu\text{m}$ thick, light intensity 10 mW/mm ²) for similar chromophore loading.	161
8.1	Summary of the experimental and calculated vibrational modes of benzoic acid, 2-hydroxy benzoic acid and 3-hydroxy benzoic acid. . .	178

Chapter 1

Introduction

There has been a rapid development in the research of organic electro-optic polymer materials because of their potential applications in a range of areas such as broad band THz generation and detection, and ultrafast electro-optic modulators. Reported electro-optic coefficients for a number of nonlinear optical chromophores in polymer matrices greatly exceed those found in conventional single crystals (e.g. LiNbO₃). Organic electro-optic polymers are expected to lead to significant improvements in the performance of photonic devices for optical communications, computer interconnects, and THz generation and detection. Despite the promise of high electro-optic response of organic electro-optic polymer materials, there are some issues that need to be addressed before devices containing organic chromophores can become widely available. These include ensuring the long term stability of the aligned dipole moments in electro-optic polymers, along with the long term photochemical and thermal stability. It is also important to accurately determine if the reported large electro-optic coefficients are purely of electronic origin, so that they can be used in high frequency applications. Materials synthesized in our group are believed to have potential for THz generation and detection and hence it is important to determine their electro-optic, photostability, and THz properties. THz spectroscopy is useful because it can distinguish polymorphic compounds, which is not easy using other methods. Some materials also have low absorption in the THz region and this can have useful applications, for example, imaging through packaging in addition to other potential security and pharmaceutical applications. The contents of this thesis is arranged as follows.

Chapter 2: In this chapter a theoretical background to the electro-optic effect and

methods and materials related to this phenomenon are explained. An introduction to the electro-optic effect and electro-optic materials followed by a brief description of the polymer electro-optic materials, and nonlinear optical chromophores is given. An overview of the theory required to investigate the properties of electro-optic materials is given in this chapter. An overview of the interaction of light with materials that have applications in material characterisation is also discussed.

Chapter 3: This chapter gives an overview of some of the general instruments and techniques used to perform experiments to investigate properties of organic nonlinear optical chromophores and to characterise some useful organic compounds that have potential in pharmaceutical and industrial applications.

Chapter 4: This chapter discusses preparatory works and general quantitative analysis to prepare samples for the research. These include cleaning substrates for film deposition, preparation of the solution, spin processing and casting for film fabrication, drying to evaporate residual solvents, measurement of the film thickness and refractive indices and an estimation of the chromophore concentration in films. Details of electric field poling of thin films to induce the electro-optic effect and methods employed to optimize poling conditions are discussed.

Chapter 5: The chapter reports the investigation of the magnitude and temporal stability of the poling induced electro-optic effect in a variety of chromophores measured using the Teng-Man modulation ellipsometry method. Ways to enhance the efficiency of the host-guest electro-optic materials are also discussed. Experimental results from the measurement of the electro-optic coefficient are analyzed and compared to the theoretically calculated values. A mismatch observed between the experimental results and the theoretical estimation and the roll off-of the electro-optic coefficient with modulation frequency are discussed.

Chapter 6: This chapter introduces a new technique to estimate the electro-optic coefficient of organic NLO polymer films using the electric field dependent diffraction efficiency of diffraction gratings made on thin films. This technique does not require a modulating AC field and thus provides an estimate of the static electro-optic coefficient. This is a particularly useful method to filter out the possible overestimation of the electro-optic coefficient due to non-electronic contributions such as the cavity resonance and multiple reflection effects. The theory is derived and tested using AC and DC modulating fields and the limitations of this technique are discussed. The contribution of inverse piezoelectric effect and multiple interference effect to the diffraction efficiency are also discussed.

Chapter 7: Investigations towards better understanding of the photodegradation mechanism of organic NLO chromophores in polymer matrices and methods to enhance optical stability are discussed in this chapter. A photodegradation model based on a distribution in the photodegradation quantum efficiencies is presented. Effects of environmental parameters such as light intensity, oxygen concentration etc on the photostability of the chromophores are investigated. A systematic approach is followed to investigate how the chromophore structure, chromophore concentration in the films, aggregation, and the quantum chemical mixing of the ground state and the charge separated state as defined by bond length alternation are related to photostability.

Chapter 8: This chapter is divided mainly into two major sections. The first section deals with the evaluation of polymer electro-optic materials used in this research in the THz frequency range. The theoretical efficiency of the electro-optic polymers synthesized by the IRL photonics team for THz generation is reported. Infrared and Raman spectroscopy were performed in the THz frequency range on organic compounds to investigate the material properties in the THz region. Low temperature, low energy Raman experiments were performed on some organic crystals and are discussed in this chapter.

The findings are summarised and the future prospects of this research work are discussed in chapter 9.

Chapter 2

Basic Concepts

The branch of optics exploring nonlinear behaviour of light and the materials causing this effect is classified as nonlinear optics. Electro-optics is a sub class of nonlinear optics in which light can interact with an external electric field in certain materials. This chapter forms a theoretical background to the electro-optic (EO) effect, and materials and methods related to this phenomenon. An introduction to the EO effect and EO materials followed by a brief description of the polymeric EO materials, and nonlinear optical (NLO) chromophores is given. An overview of the theoretical aspects of methods required to investigate the properties of EO materials is given in this chapter. An overview of the importance of EO polymers in terahertz (THz) technology is given. Finally, an introduction to the interaction of photons with materials is discussed to form a background to infrared (in particular, THz) and Raman spectroscopy.

2.1 Nonlinear optics

Light propagation through a dielectric medium can be characterised by the polarisation that the light induces on the medium. The polarisation equation as a power series expansion of macroscopic polarisation \vec{P} in presence of an applied field \vec{E} is given by,

$$P_i = \epsilon_0 \left(\sum_j \chi_{ij}^{(1)} E_j + \sum_{jk} \chi_{ijk}^{(2)} E_j E_k + \sum_{jkl} \chi_{ijkl}^{(3)} E_j E_k E_l + \dots \right) \quad (2.1)$$

where $\chi^{(n)}$ is the n^{th} order electric susceptibility tensor, E_i is the i^{th} component of the applied electric field and ϵ_0 is the dielectric constant of air. In a linear medium,

the relation between electric field and polarisation can be represented as $\vec{P} = \epsilon_0\chi\vec{E}$ where polarisation (\vec{P}) shows a linear relationship with the applied electric field (\vec{E}) in a medium having an electric susceptibility χ . However, this linear relationship is an approximation to the generalized polarisation equation for low electric field and/or negligibly small higher order electric susceptibilities.

Eq. 2.1 shows that if a material has a non zero $\chi^{(2)}$ the polarisation shows a quadratic relationship if the applied field is sufficiently large. A schematic of the linear and nonlinear polarisation is shown in Fig. 2.1. A material in which the polarisation has a nonlinear relationship with the electric field is known as nonlinear medium and the branch of optics related to this property is known as nonlinear optics. The usual linear susceptibility $\chi^{(1)}$ is much greater than the coefficients of the nonlinear terms $\chi^{(2)}$, $\chi^{(3)}$ and so on and hence the latter contribute noticeably only at higher amplitudes of the incident radiation.

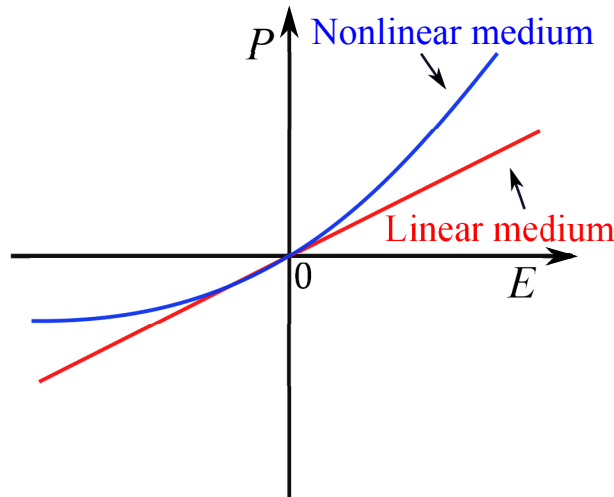


Figure 2.1 – Polarisation as a function of electric field in a linear and a nonlinear medium.

2.2 Electro-optic effect

The EO effect is a nonlinear wave mixing process where the optical field mixes with a DC electric field. Optical nonlinearities occur when an internal or external electric field is applied to a dielectric medium to alter the phase, amplitude or frequency of an electromagnetic wave in the medium. The induced nonlinear polarisation obtained by this wave mixing process can be represented using the quadratic and

cubic terms of Eq. 2.1 by [1],

$$P_i^{\text{LEO}} = \epsilon_0 \chi_{ijk}^{(2)}(\omega : 0, \omega) E_j(0) E_k(\omega) \quad (2.2)$$

$$P_i^{\text{QEO}} = \epsilon_0 \chi_{ijkl}^{(3)}(\omega : 0, 0, \omega) E_j(0) E_k(0) E_l(\omega) \quad (2.3)$$

where Eq. 2.2 represents the linear EO effect and Eq. 2.3 represents the quadratic EO effect. EO effects can be treated as a second order NLO property that perturb the refractive index of a material under the influence of an applied electric field. One can write the power series expansion of the refractive index of a material, subject to a light field passing through it, under the influence of an external field E as [2],

$$n(E) = n - \frac{1}{2} r n^3 E - \frac{1}{2} s n^3 E^2 + \dots \quad (2.4)$$

The coefficient corresponds to the linear relationship with E in the Eq. 2.4 is known as the linear EO coefficient (r) or Pockels coefficient and the quadratic term is known as the quadratic EO coefficient or Kerr coefficient (s). Since the higher order terms are several magnitude lower than n , the first two terms in E of the power series have been predominantly investigated as the linear EO effect and quadratic EO effect. In the linear EO effect the field induced change in refractive index of the medium has a linear relationship with the applied field. In the second type, the induced change in refractive index has a quadratic relationship with the applied field, which is known as quadratic EO effect or Kerr effect [3]. The change in the refractive index of a material due to an applied electric field in a linear EO and a quadratic EO media are shown in Fig. 2.2. A schematic of the change in polarisation of a wave due to an applied electric field in linear EO medium (Pockels cell) is shown in Fig. 2.3. This thesis focus on materials with linear EO properties. The quadratic EO effect is beyond the scope of this thesis.

The EO effect of a material allows *control* of the speed of light passing through certain materials. To exhibit nonlinearity, the material should not have an inversion symmetry [2]. Also, the field applied across the medium must be of sufficient strength to overcome any internal electrostatic interactions. In contrast to pure electronics or optics where the information carriers are electrons and photons respectively, in electro-optics the information is carried by both electrons and photons. Electrons and photons interact with each other in an EO material [2] as discussed in the

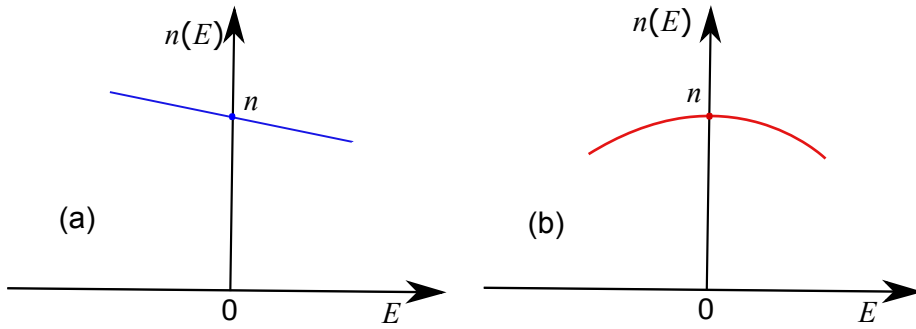


Figure 2.2 – Refractive index as a function of applied electric field in (a) a linear EO medium and (b) a quadratic EO medium.

following sections.

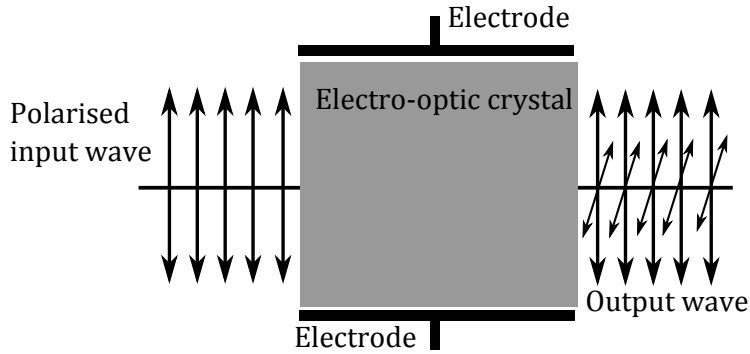


Figure 2.3 – An example scheme of a Pockels cell showing the change in polarisation of a wave through an EO material in the presence of an external electric field. Arrows indicate the polarisation direction.

2.2.1 Linear electro-optic coefficient

The EO coefficient (Pockels coefficient) is a measure of the efficiency of a material to change its refractive index under an external electric field. The linear EO coefficient is closely related to the second order nonlinear susceptibility. The linear EO coefficient r_{ij} can be derived from the second order NLO susceptibility as follows:

The induced change in refractive index of an EO material in the presence of an electric field can be explained using the Pockels equation,

$$\delta n_i = p_{ij} E_j \quad (2.5)$$

Where the Pockels tensor components p_{ij} are related to the NLO coefficient through the relation

$$p_{ij} = \frac{\chi_{ijk}^{(2)}}{n_i} \quad (2.6)$$

The equation relating the EO coefficient, r_{ij} with the second order susceptibility $\chi_{ijk}^{(2)}$ can be written as,

$$r_{ij} = \frac{2\chi_{ijk}^{(2)}}{n_i^4} \quad (2.7)$$

Since poled polymers of amorphous materials possess an ∞mm symmetry, the non zero components of r_{ij} in poled polymers are, r_{13} , r_{31} , and r_{33} . From the symmetry conditions of a poled polymer, $r_{13} = r_{31}$. Considering the symmetry of a poled polymer system a reasonable approximation for r_{13} and r_{33} is given as [4],

$$r_{33} \approx 3r_{13} \quad (2.8)$$

The unit of the linear EO coefficients is the reciprocal of that of electric field (m/V) since the refractive index is dimensionless. As the value of EO coefficient is very low when compared to the applied field, for convenience, the unit of EO coefficient is quoted in 10^{-12} m/V or simply pm/V. As an example, the EO coefficient of a widely used EO crystal, lithium niobate (LiNbO₃), is 30.8 pm/V [5, 6, 7].

2.2.2 Optical rectification and frequency mixing

Frequency mixing is an NLO process where two different waves interact with each other resulting in new waves. Considering two optical fields having oscillating electric field components of $E_1 = E_0 \cos(\omega_1 t)$ and $E_2 = E_0 \cos(\omega_2 t)$ then the polarisation equation given in Eq. 2.2 can be expressed as,

$$\begin{aligned} P^{\text{DFG/SFG}} &= \epsilon_0 \chi_{ijk}^{(2)} E_0 \cos(\omega_1 t) \cdot E_0 \cos(\omega_2 t) \\ &= \frac{\epsilon_0 \chi_{ijk}^{(2)} E_0^2}{2} (\cos[(\omega_1 - \omega_2)t] + \cos[(\omega_1 + \omega_2)t]) \end{aligned} \quad (2.9)$$

The polarisation equation above consists of two terms corresponding to the difference of two frequencies and a term proportional to the sum of two frequencies.

Optical rectification is the development of DC or low-frequency polarisation when laser beams of sufficient intensity propagates through a nonlinear optical material.

Optical rectification is a special case of Eq. 2.9 where $E_1 = E_2 = E = E_0 \cos(\omega t)$. In this case, the polarisation consists of a DC polarisation as well and a frequency dependent polarisation as,

$$P^{\text{OR}} = \epsilon_0 \chi_{ijk}^{(2)} (E_0 \cos \omega t)^2 = \frac{\epsilon_0 \chi_{ijk}^{(2)} E_0^2}{2} (1 + \cos 2\omega t) \quad (2.10)$$

where the DC polarisation, $\epsilon_0 \chi_{ijk}^{(2)} E_0^2 / 2$ results from the rectification of the incident optical electric field by the second order nonlinear optical susceptibility of the material. The second term of the Eq. 2.10 describes the second harmonic generation or frequency doubling.

2.3 Electro-optic materials

As already discussed, EO materials are capable of changing their refractive index under the influence of an electric field. EO crystals has been widely used for EO modulators and EO deflectors. Naturally occurring EO effects are observed in non-centrosymmetric crystals (crystals lacking an inversion symmetry) such as gallium arsenide (GaAs, $r=1.6$ pm/V [4]), lithium niobate (LiNbO₃, $r=30.8$ pm/V [7, 6]), and zinc telluride (ZnTe, $r=3.9$ pm/V [8]) are some of the EO materials being used as active materials in existing devices based EO effect [9].

Despite the promise of EO effect in applications such as wideband THz emitters and detectors, ultra-fast EO switches and modulators, wavelength shifters, optical interrogators, spectroscopy and sensors the full potential of this effect has not been exploited with the existing inorganic EO crystals. This is primarily because of the problems associated with inorganic EO materials such as relatively low EO coefficients, slower response time, poor phase-matching for wave mixing and higher harmonic generation, and presence of low energy phonon modes. Other challenges in the development of devices based on EO effect using EO crystals are the difficulty to grow optical quality crystals on preferred substrates [1].

There has always been a need for new materials having higher efficiency to contribute to the growing requirement in communication, imaging and sensing applications. Development of polymer based EO materials has overcome most of the issues related to the inorganic materials. An overview of EO polymers is given in following section. There is a substantial interest in developing EO polymers based

on organic nonlinear optical chromophores for EO switching devices and THz applications. The following sections and chapters are mostly focused on the developing new EO polymers having very large EO coefficients and optical stability.

2.3.1 Electro-optic polymers

EO polymers have attracted intense research interest in the past two decades because of their merits over their inorganic counterparts that include large EO coefficient, ease of fabrication, lower refractive indices, broad-band phase matching and absence of crystalline phonons [1, 10]. EO polymers have high potential in photonic devices with a wide range of applications that include EO modulators, optical storage, optical image amplification, real-time interferometry, optical phase conjugation, holography and THz generation and detection [1, 11].

EO polymers owe their large macroscopic EO effect to the molecular nonlinear optical effect of the constituent molecules containing highly delocalised π -electrons connected to electron donor and electron acceptor groups on either end of the molecule [1]. These molecules that are generally called NLO chromophores are highly active and can easily be polarised in presence of an external electric field. The combination of a low refractive index amorphous polymer and an organic NLO chromophore having large molecular NLO activity and sub-picosecond response time together form materials having large EO response [4].

For an organic nonlinear optical material, the criteria to achieve a high macroscopic nonlinearity is that the system possesses a non-zero total dipole moment. This means that the chromophores in the polymer system have to be at least partially aligned in a polar order, otherwise the system would not show an EO effect. Polar ordering of the chromophores in the polymer is generally achieved by electric field poling of the sample.

2.3.2 Electro-optic polymer systems

The following is an overview of methods being widely used to incorporate nonlinear optical chromophores with the polymers. The EO effect in polymers is due to the constituent chromophores that are incorporated in a transparent and inert polymeric host material. Chromophores can be incorporated in the polymer matrix in a number of different ways, for example, as shown in Fig. 2.4. An overview of some of the major EO polymer systems those are widely being investigated to develop organic

EO polymer systems is given below.

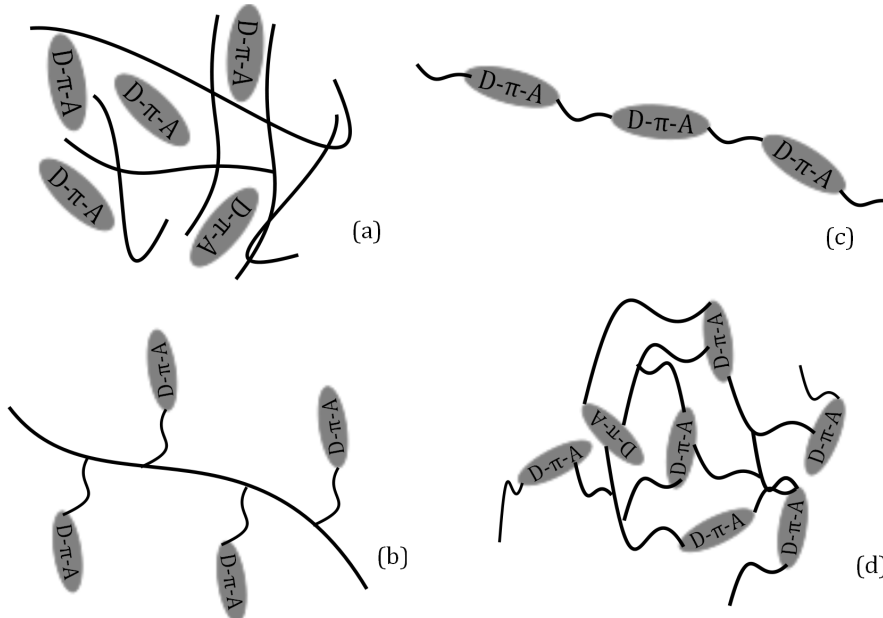


Figure 2.4 – Electro-optic polymer systems: (a) Host-guest, (b) Side-chain, (c) Main-chain and (d) Cross-linked polymer systems.

Host-guest system

In host-guest systems the chromophores are dispersed in the host polymer without any chemical attachment between the chromophore and the polymer. Host guest systems were the earliest poled polymer systems to be investigated. This is a relatively simple and efficient method to investigate the properties of chromophores in host polymers as well as to estimate the efficiency of chromophores in contributing to the macroscopic EO effect. Despite the simplicity of the system the usefulness of the system at application level is limited unless the system has sufficiently large thermal stability of polar order [1, 12]. Mobility of the chromophores within the host polymer host causes fast relaxation of the system. This is related to the free volume inside the polymer, the size of the chromophores and the glass transition temperature (T_g) of the host polymer. Crystallization and phase separation due to inhomogeneous distribution of chromophores at higher concentrations limits the system from reaching dense concentrations and thereby large EO coefficients. This has motivated investigations into more advanced systems such as side-chain, main chain and cross-linked polymer systems [4, 2].

Side-chain system

In a side-chain polymer system the chromophores are chemically attached to the polymer backbone as a side-chain pendant group. One of the advantages of this system is it permits higher chromophore loading without crystallization, phase separation or the formation of concentration gradients [4]. Furthermore, the relaxation of chromophores from the poled order is expected to be relatively slow because the mobility of the chromophores is hindered due to the chromophores being attached to the polymer backbone. This leads to an enhancement in the magnitude and stability of the macroscopic EO activity of the system [2, 4]. Generally the glass transition temperature of the side-chain polymers is substantially higher than that of host-guest polymers. This is because the guest chromophores tend to plasticize the system, while in the side chain system the chromophores are attached to the polymer backbone [2].

Main-chain system

A main-chain system is similar to the side-chain system but the chromophores are not just linked but are a part of the polymer backbone itself. The movement of chromophores in main-chain system is further reduced which is expected to substantially reduce the relaxation of the polar order. Poling is more difficult in main-chain system compared to side-chain because of the reduced mobility of the chromophores [4]. Improved thermal stability of polar order and improved tensile strength are the key improvements in main-chain system over side-chain system [4, 2].

Cross-linked system

In a cross-linked polymer system both ends of the chromophores are linked to the polymer backbone leading to partial immobilization of the chromophores after poling. The efficiency of this technique relies on the percentage, nature and sites of cross-linking [4]. The system needs to be poled to destroy the symmetry of the system for a net effective dipole moment. Cross-linking is generally activated during or after completing the poling process. This is particularly challenging because if the cross linking occurs before sufficient poling, further movement of the chromophores is severely impeded during subsequent poling. Cross-linking process is done through various techniques such as thermal techniques and photochemical methods [2].

2.3.3 Glass transition temperature

The glass transition is the reversible transition in amorphous materials from a hard and relatively brittle state into a molten or rubber-like state. The temperature at which this transition takes place is known as glass transition temperature (T_g). This is an important quantity of a polymer especially because the poling process to induce EO effect in the polymer system is done at the T_g of the host polymer. Above T_g the molecules in the polymers are very flexible. When the material is cooled below T_g the polymer chain will no longer wiggle around making the system harder and sensitive to strain and pressure. T_g is intrinsic to the polymers and varies between polymers. The melting temperature of the polymer (T_m) is different from T_g . At T_m a polymer transforms to a liquid form. In most polymers both characteristic temperatures exist because of the presence of crystalline and amorphous domains in the system.

2.4 Organic nonlinear optical chromophores

Organic compounds with a high nonlinear optical response typically contain donor and acceptor groups that are separated by a conjugated polyene spacer (i.e., donor- π -acceptor) to create an asymmetric polarisability in the molecule. The high NLO response of the chromophores is due to the presence of the delocalised π -electrons. Molecules having extended overlapped π -bonds contain delocalised π -electrons that are shared by the entire system and these type of molecules are called conjugated molecules. Because of the characteristics of the electron donor and acceptor, and the ability of the conjugated bond to facilitate electron transfer within the system, a chromophore is also called a push-pull molecule [1, 2]. Nonlinearity of organic chromophores depends mainly on the change in polarisability of the electron in the π -orbitals as a result of an optimal combination of donor-acceptor strengths.

The macroscopic EO response of a polymeric material is strongly related to the properties of the organic chromophores, in particular, their hyperpolarisability and dipole moment. An ideal nonlinear optical chromophore can be expected to have an extended conjugated system, a low energy transition, and large dipole moment between the ground state and the first excited state of the electronic configuration [2]. An asymmetric charge distribution is introduced by including different functional groups to the molecule. Functional groups are classified as two groups based on

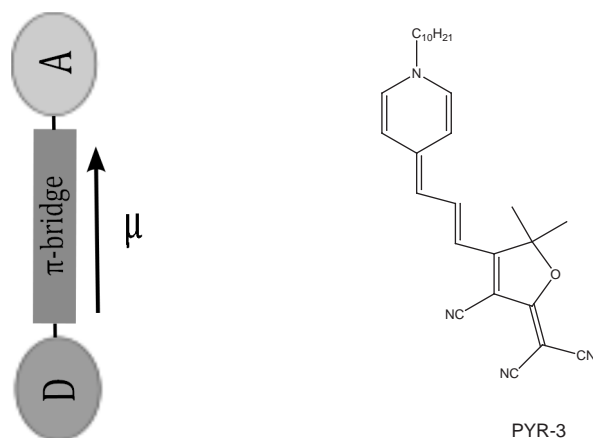


Figure 2.5 – (left) Schematic of a push-pull molecule (chromophore) with an electron donor (D) and an electron acceptor (A) connected by a conjugated π -bridge. (right) An example structure of an NLO chromophore.

their ability to donate or accept electron into the localised π electron system. A schematic of a nonlinear optical chromophore is shown in Fig. 2.5.

The key advantage of organic nonlinear optical materials is the possibility of altering the structure to optimize their nonlinear optical properties. The conjugation length, and the donor and acceptor group need to be tuned to achieve large molecular nonlinearity, while maintaining low scattering, low absorption at operating wavelengths and longer stability. The effects of altering chromophore structure to achieve large molecular and macroscopic nonlinearity is discussed in Chapter 5 and Chapter 7.

2.4.1 Microscopic NLO effect

The induced polarisation \vec{p} in a nonlinear optical chromophore in presence of an electric field is given by[2],

$$p_i(E) = \mu_i + \sum_j \alpha_{ij} E_j + \sum_{jk} \beta_{ijk} E_j E_k + \sum_{jkl} \gamma_{ijkl} E_j E_k E_l + \dots \quad (2.11)$$

where, μ_i is the ground state dipole moment, α_{ij} is the first order polarisability tensor and is related to the first derivative of the induced dipole moment, β_{ijk} is the second order polarisability tensor or the first hyperpolarisability, γ_{ijkl} is the third order polarisability tensor or the second hyperpolarisability tensor. The indices i ,

j , k , and l are associated with the orientation of the applied field E with respect to the molecular coordinate system.

The large nonlinearity of a A- π -D chromophore is due to strong charge transfer interaction between constituent donor and acceptor groups [13]. There is an optimal combination of the donor and acceptor strengths that will maximise β . The charge transfer contribution to the hyperpolarisability β can be optimized based on a quantum two-level model derived from the static perturbation theory[1]. The dominant contribution to the nonlinearity arises from the ground state dipole moment of the chromophore and the transition dipole moment from the ground state to the lowest excited state.[14, 15, 16]

$$\beta(-\omega_3; \omega_1, \omega_2) = \frac{e^3 \mu_0^2 \Delta\mu}{\hbar} \frac{\omega_0^2 (3\omega_0^2 + \omega_1\omega_2 - \omega_3^2)}{(\omega_0^2 - \omega_1^2)(\omega_0^2 - \omega_2^2)(\omega_0^2 - \omega_3^2)} \quad (2.12)$$

Where, ω_0 represent the resonance frequency for the transition from the ground state to the first excited state and ω_1 , ω_2 and ω_3 are the frequencies of three interacting waves [2]. The observed shift in the resonant frequency ω_0 of the system in dielectric medium is due to the local field effects [13]. μ_0 is the transition dipole moment between ground state and the first excited state and $\Delta\mu$ is the difference between electric dipole moments of ground state and the first excited state.

First hyperpolarisability for linear EO effect can be derived from Eq.2.12 by setting $\omega_1, \omega_3 = \omega$ and $\omega_2 = 0$. Then Eq.2.12 becomes,

$$\beta_{EO}(-\omega; \omega, 0) = \frac{e^3 \mu_0^2 \Delta\mu}{\hbar} \frac{(3\omega_0^2 - \omega^2)}{(\omega_0^2 - \omega^2)^2} \quad (2.13)$$

First hyperpolarisability for second harmonic generation comes from Eq.2.12 by setting $\omega_1, \omega_2 = \omega$ and $\omega_3 = -2\omega$. Then Eq.2.12 changes to,

$$\beta_{SHG}(-2\omega; \omega, \omega) = \frac{e^3 \mu_0^2 \Delta\mu}{\hbar} \frac{3\omega_0^2}{(\omega_0^2 - \omega^2)(\omega_0^2 - 4\omega^2)} \quad (2.14)$$

Eqs.2.12 and 2.14 show that there is a static hyperpolarisability term independent of the operating frequency, which is given as,

$$\beta_0 = \frac{3e^3 \mu_0^2 \Delta\mu}{\hbar \omega_0^2} \quad (2.15)$$

The key properties of chromophores leading to large macroscopic EO coefficients in macroscopic level are large first hyperpolarisability and dipole moment, which

together are known as the figure of merit of a chromophore (*Figure of Merit* = $\mu\beta$).

The first hyperpolarisability β is related to the EO coefficient in a poled polymer system through the relation [1],

$$r_{33}(-\omega; \omega, 0) = N \langle \cos^3 \theta \rangle f_0 f_\omega^2 \beta(-\omega; \omega, 0) \quad (2.16)$$

where N is the number density of chromophores, f are local field factors at the specified frequencies, and $\langle \cos^3 \theta \rangle$ is the thermal average for ordered chromophores for the angle between the poling field and the molecular dipole moment. A detailed discussion on translating the molecular first hyperpolarisability to the macroscopic EO effect is discussed in Chapter 5.

2.4.2 Bond length alternation

Optimising the first hyperpolarisability (β) of the organic NLO chromophores with a given conjugated π -bridge requires a specific donor acceptor strength that leads to a balance of electronic symmetry and polarisability that maximises β [17, 18]. This can be achieved with an optimal degree of mixing of two canonical resonance structures, one is neutral and other with a high degree of charge separation. Thus the structure and consequently the hyperpolarisability is determined by the relative energetics of these two forms [19]. The degree of mixing is strongly correlated to the structure of the molecule that is reflected in the difference between the average lengths of carbon-carbon single and double bonds. This difference $\langle \Delta r \rangle$ is called bond length alternation (BLA). BLA is a useful parameter to examine to establish a generalized structure-property relationship for the first hyperpolarisability of organic nonlinear optical chromophores.

The degree of BLA arises from the linear combination of the two charge transfer resonance forms of the molecule [22]. For unsubstituted conjugated π -bridges (polyenes), or chromophores with weak donor-acceptor pairs the neutral canonical form dominates in the ground state resulting, by convention, a large positive BLA. On increasing the donor-acceptor strength the charge separated form contributes more to the ground state reducing the BLA value. Upon achieving equal contribution from each the BLA reaches zero, resulting in the same average lengths for double and single bonds. Further, an increase in the donor acceptor strengths result in domination of the charge separated canonical form leading to, by convention, a negative BLA.

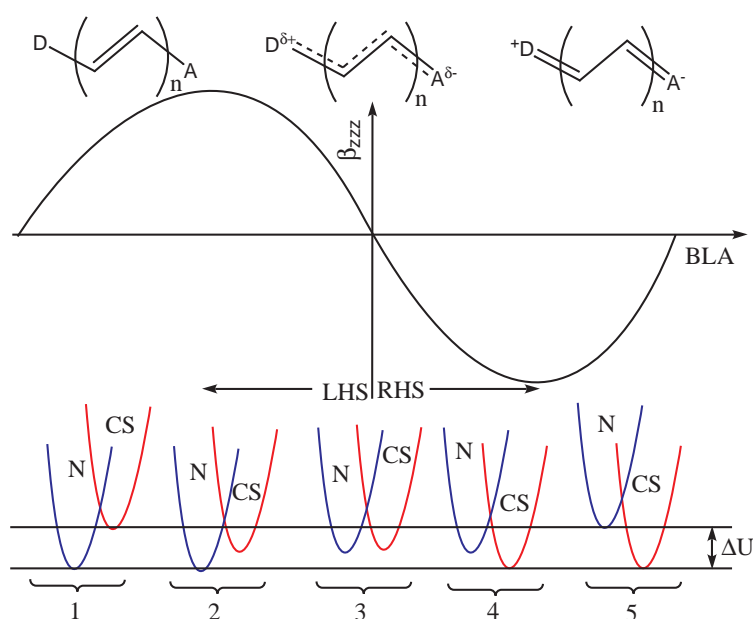


Figure 2.6 – Definition of regions of BLA correspond to the degree of mixing the neutral (N) and charge-separated (CS) resonance structures to the ground state. The nature of the conjugated π -bridge changes from neutral polyene-like (1) to polar cyanine-like (3) to very polar charge separated polyene-like (5) [20, 21].

The relationship between the hyperpolarisability and the BLA can be explained using the two-level model [15], where the first hyperpolarisability, β is given by [23, 21, 17],

$$\beta \propto (\mu_{ee} - \mu_{gg}) \frac{\mu_{ge}^2}{\omega_{ge}^2} \quad (2.17)$$

where ω_{ge} is the charge transfer excitation energy, μ_{ge} is the transition dipole moment for charge transfer excitation, and μ_{ee} and μ_{gg} are the excited and ground state dipole moments. The rationalization of first hyperpolarisability by two-level model thus involves three terms, they are (a) the difference between ground and excited state dipole moments $\Delta\mu = \mu_{ee} - \mu_{gg}$, (b) the transition dipole moment, and (c) the energy of the corresponding excitation. Out of these three components, the last two terms contribute to an inverse quadratic variation peaking at near zero value for BLA parameter. The first term $\Delta\mu$ is the strongest component and shows a sinusoidal variation with BLA parameter giving a sinusoidal relationship of the β and BLA. A schematic of β as a function of BLA and corresponding mixing of different energy states is shown in Fig. 2.6. By convention, the chromophores on the left hand side of the BLA diagram are classified as LHS (or neutral) chromophores

and the chromophores on the right hand side are classified as RHS (or, zwitterionic) chromophores. Studies on effects of BLA on the EO effect is discussed in Chapter 5 and the effects of the relationship of BLA with the optical stability of chromophores is discussed in Chapter 7.

2.5 Absorption

Absorption is the attenuation of electromagnetic radiation passing through a material due to the interaction of photons with medium. Two types of absorption processes that are relevant in the context of NLO materials are, the linear absorption and the nonlinear absorption (two-photon absorption).

2.5.1 Linear absorption

The resonant (or linear) absorption is a single photon process. Absorption in NLO chromophores is due to their charge transfer energy gap. An energy level diagram explaining the linear absorption by the chromophore molecules is shown in Fig. 2.7(b). The linear absorption process in NLO chromophores can be explained as follows. When the chromophores are exposed to radiation of energy above their charge transfer gap, the molecules in the ground state (S_0) are excited to a singlet (S_1) excited state. S_1 states generally have a very short life time of the order of nanoseconds [24]. Molecules in the S_1 state emit most of the energy via fluorescence and return to the S_0 state. A small fraction of the molecules in the S_1 state decays to the spin forbidden triplet excited state (T_1). The T_1 state has a relatively long life time compared to the S_1 state, and so T_1 returns to S_0 state via a non radiative transition. Resonant absorption is a linear optical process and is related to the energy (wavelength) of the radiation but does not depend on the intensity. The interaction of the excited energy states of the chromophore with triplet oxygen leading to the creation of highly reactive singlet oxygen that eventually lead to the photo induced degradation of chromophores [25, 24]. A schematic of the absorption process in chromophores is shown in Fig. 2.7.

2.5.2 Two-photon absorption

Two-photon absorption is the process of simultaneous absorption of two photons to excite a molecule from the ground state to an excited state. It differs from linear

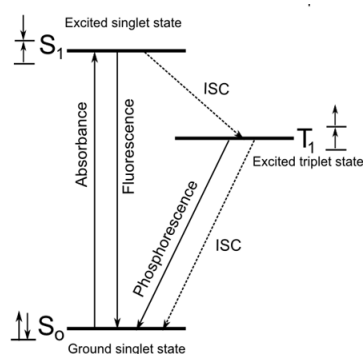


Figure 2.7 – Energy level diagram showing excitation of chromophores; ISC represents inter system crossing.

absorption in that the strength of absorption depends on the square of the light intensity, thus it is a nonlinear optical process. The energy difference between the lower and upper states of the molecule is equal to the sum of two photon energies. It is not necessary that both photons have same frequency [2].

Two-photon absorption is a third-order process. The imaginary part of the third-order nonlinear susceptibility, $\chi^{(3)}$ is related to the extent of two-photon absorption in a given molecule. The selection rules for two-photon absorption are therefore different than for linear absorption that is dependent on the first-order susceptibility.

2.5.3 Kramers-Kronig relation

Kramers–Kronig relations have constituted one of the principal tools in optical spectroscopy for the assessment of the optical properties of media from measured spectra. The basic idea is that the change in the refractive index caused by some excitation of a medium is related to the change in the absorption. As the change in the absorption is normally significant only in a limited range of optical frequencies, it is relatively easily measured. The real and imaginary parts of the complex refractive index are related through the Kramers–Kronig relations. For example, one can determine a material’s full complex refractive index as a function of wavelength from an absorption spectrum of the material.

Kramers–Kronig relations are often used to calculate the real part from the imaginary part (or vice versa) of response functions in physical systems based on the principle the causality implies the analyticity condition is satisfied, and conversely, analyticity implies causality of the corresponding physical system. If $\chi(\omega) = \chi_1(\omega) +$

$i\chi_2(\omega)$ is a complex function of complex variables ω and the functions $\chi_1(\omega)$ and $\chi_2(\omega)$ are real and analytic in the upper half plane of ω , and vanishes faster than $1/|\omega|$ as $|\omega| \rightarrow \infty$, then the Kramers-Kronig relations are given as,

$$\chi_1(\omega) = \frac{1}{\pi} P \int_{-\infty}^{\infty} \frac{\chi_2(\omega')}{\omega' - \omega} d\omega' \quad (2.18)$$

and

$$\chi_2(\omega) = -\frac{1}{\pi} P \int_{-\infty}^{\infty} \frac{\chi_1(\omega')}{\omega' - \omega} d\omega' \quad (2.19)$$

where P denotes the Cauchy principal value. A simplified Kramers-Kronig relation connecting the two components of complex refractive index of a dielectric material is given by,

$$\Delta n(\omega) = \frac{c}{\pi} \int \frac{\Delta\alpha(\omega') d\omega'}{\omega'^2 - \omega^2} \quad (2.20)$$

where $\Delta n(\omega)$ is the change in real part of refractive index as a function of frequency and $\Delta\alpha(\omega)$ is the corresponding absorption coefficient of the material.

2.6 Aggregation

The asymmetric distribution of electrons in a compound typically leads to intermolecular electrostatic interactions between neighbouring molecules in solution and films is known as aggregation or self-association [26]. Aggregation is present in non-linear optical chromophores because of the donor-acceptor groups and the ground state dipole moment of the chromophores especially at higher concentrations when the molecules are close enough to interact. Aggregation of chromophores induces deviations in the expected absorption spectra from the energy state of the system resulting in extra bands (or shoulders). The energy of these extra bands depend on the type of the aggregation present, either H (hypsochromic) or J (bathochromic) aggregations [27, 26]. Schematics of the two forms of aggregations are shown in Fig. 2.8. H-aggregation results in shoulders appearing on the high energy side of the main absorption band, whereas J-aggregation leads to shoulders on the low energy side. Organic chromophores with highly polar (i.e. zwitterionic) ground states often exhibit poor solubilities and tend to readily form aggregates. In solution, the degree of aggregation is related to the dielectric constant of the solvent and the

concentration.

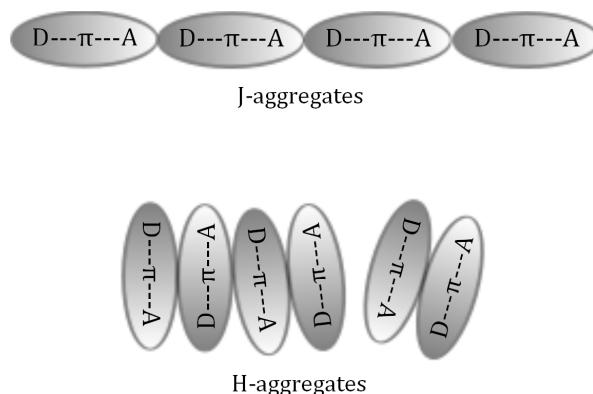


Figure 2.8 – Schematics of H- and J- aggregated chromophores.

Aggregation is a major challenge in developing EO polymers containing nonlinear optical chromophores. Aggregation limits the effective number density that can be achieved in an NLO polymer system. This leads to a reduced efficiency for translating the molecular NLO effect to macroscopic level. Higher loading reduces the average distance between chromophores leading to aggregation and thereby cancelling the effective dipole moments of the aggregated chromophores. Furthermore the presence of significant aggregation will also lower the overall poling efficiency of the final NLO material as well as increase the propensity for relaxation of the aligned dipoles post-poling. This will result in a gradual decline of the observed macroscopic response over time [1].

2.7 Solvatochromism

Effects of solvent polarity on the chromophores has a significant control on the behaviour of the chromophore in different solvents. Solvatochromism is the phenomenon of variations in the wavelength, intensity, and shape of the absorption spectra of chromophores in solution. The solvatochromism effect leads to a strong dependence of absorption and emission spectra with the solvent polarity. There exist two types of solvatochromism; Negative (hypsochromic) causing blue shift and positive (bathochromic) leading to red shift [28]. The extent of the solvatochromism depends on the difference in dipole moment between the ground and excited states of the chromophores. Solvatochromism is due to the differential solvation of the ground and first excited states of the chromophores [29]. If the solute dipole moment increases during

the electronic transition ($\mu_g < \mu_e$) a positive solvatochromism normally results. In the case of a decrease in the solute dipole moment upon excitation ($\mu_g > \mu_e$), a negative solvatochromism is usually observed. Difference in polarity of the ground and excited state of a chromophore lead to differential stabilization of the ground and excited states resulting in a change in the energy gap. Since the solvatochromism is related to the degree of mixing of two canonical forms of the ground state of the chromophores and thus can be used as a tool to measure the interactions between the solute and solvents that gives a hint to classify chromophores as neutral or zwitterionic [28]. Solvatochromism has a major role in determining the degree of aggregation of chromophores in different solvents [28]. In this study, in particular, solvatochromism has been used as a tool to classify the chromophores, in particular left hand side (neutral, LHS) and right hand side (zwitterionic, RHS). Solvatochromic tests gives supplementary and complementary data to the BLA parameter of the chromophores.

The $E_T(30)$ scale of solvent polarity

A paradoxical relationship observed in the shift of absorption peak of the dyes with solvent polarity have motivated researchers the introduction of a new parameter [29]. $E_T(30)$ value of solvents is based on a negatively solvatochromic ‘pyridinium N-phenolate betaine’ dye as probe molecule, and they are defined as the molar electronic transition energies (E_T) of the dissolved molecules measured in kcal mol⁻¹ at room temperature and normal pressure [29]. Solvents are classified based on their interaction with this dye. This is a useful solvent property to consider when discussing solvatochromism. The solvatochromic shifts of the solute have been found consistent with the $E_T(30)$ of the solvents [29]. It is beyond the scope of this thesis to go indepth into the chemistry of this property.

2.8 THz radiation

THz waves typically refer to the frequencies from 100 GHz (the high-frequency edge of the microwave band) to 10 THz (the low-frequency edge of far-infrared light). The THz radiation, which lies in the frequency gap between infrared and microwave region is at the interface between electronics and photonics. THz waves travelling through a material are affected by its complex dielectric constant. By analysing the amplitude and phase of the transmitted THz electric field gives detailed information

about the unique characteristics of a particular material, such as absorption and the refractive index of the material under study. This is the basic idea driving THz time domain spectroscopy. The key advantage of THz systems is that they allow non-destructive testing with safe, non-ionising radiation [30, 31]. Today THz technology is finding scope in a wide variety of applications such as communication, biological research, medical sciences, security screening and environmental monitoring [30, 32].

The THz Time Domain Spectroscopy (THz - TDS) is a Fourier transform infrared (FTIR) spectroscopic technique in which the properties of a material are probed with short pulses of THz radiation. The generation and detection scheme is capable of recording the effects caused by the sample on both the amplitude and the phase of the THz radiation. In this respect, the technique can provide more information than conventional FTIR spectroscopy, which is related to the amplitude only.

THz radiation has several distinct advantages over other forms of spectroscopy. Unlike X-rays THz radiation is safer for biological tissues because of its non-ionising nature. Many materials have unique spectral fingerprints in the THz frequency range, which means that THz radiation can be used to identify them [9]. In this thesis THz spectroscopy has been used to characterise organic NLO polymer films to estimate their transparency in THz region as well as to study the THz spectra of some organic compounds.

2.8.1 EO effect in THz technology

The EO method for detection of THz radiation is based on the basic Pockels effect where the change in the phase of a laser beam in the presence of the THz electric field, as shown in Fig. 2.3, is employed for the detection of THz radiation. Optical rectification and difference frequency generation are the two key physical properties of EO materials being employed in THz generation. THz generation from optical rectification of a femtosecond (fs) laser pulse is based on the difference frequency mixing of all frequencies within the bandwidth $\Delta\omega$ of a near infrared fs laser pulse. In general, optical rectification refers to the development of very low frequency polarisation when intense laser beams propagates through a material [33, 34]. The bandwidth of the THz pulse is determined by difference frequency generation by all frequencies within the bandwidth of the fs laser pulse. The amplitude of THz radiation is proportional to the EO coefficient of the material.

Efficient generation and detection of THz radiation by optical rectification (or

difference frequency generation) and Pockels effect require EO materials with large EO coefficients. In addition to a large EO coefficient, the material should be transparent to the THz and the optical radiation, and the refractive index for THz and optical frequencies need to be comparable providing sufficient coherence length. The intensity of THz radiation depends on the magnitude of EO effect while the bandwidth of THz radiation is determined by the coherence length. The material should have sufficiently large coherence length because THz emission strength as well as THz sensitivity of the material are proportional to the thickness of the material. Furthermore, the presence of infrared active phonons in the materials lead to strong absorption and dispersion of the refractive index at the THz frequencies resulting in phonon absorption bands. This limits the use of many materials for THz applications [9, 33].

2.9 Interaction of photons with phonons

This section describes infrared (IR) and Raman spectroscopy. Both IR and Raman spectroscopy measure the vibrational energies of molecules but they follow different selection rules. For a vibrational motion to be IR active, the dipole moment of the molecule must change. Therefore, for example, the symmetric stretch in CO_2 is Raman active but not IR active because there is no change in the dipole moment. The asymmetric stretch in CO_2 is IR active due to a change in dipole moment. For a transition to be Raman active there must be a change in polarisability of the molecule. An energy level diagram showing the transitions involved in IR absorption and Raman scattering is shown in Fig. 2.9.

2.9.1 Infrared absorption

Infrared absorption is due to the oscillations in the average dipole moment of a material caused by atomic vibrations. Absorption of infrared radiation is specific to the compounds with small energy differences in the possible vibrational and rotational states. A net change in the dipole moment is required to cause a change in inter or intra-molecular vibrational or rotational modes. The electrical field of the radiation interacts with variation in the dipole moment of the molecule. If the frequency of the radiation matches the vibrational frequency of the molecule then radiation will be absorbed, causing a change in the amplitude of molecular vibration. Infrared absorption occurs via oscillations in the volume average dipole

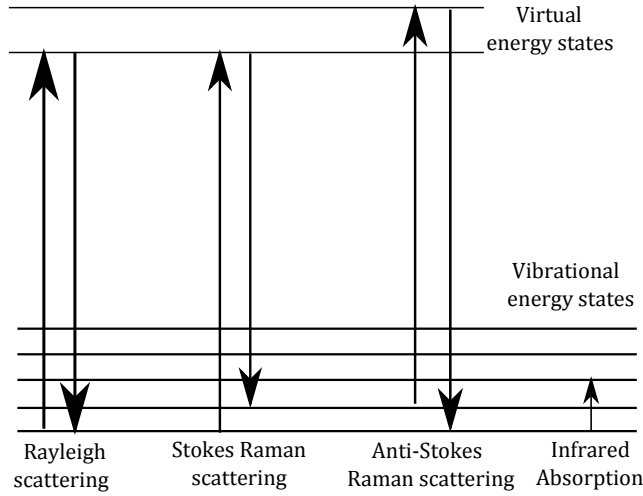


Figure 2.9 – Energy level diagram showing the transitions involved in IR absorption and Raman scattering.

moment caused by the atomic vibrations. In crystalline solids the crystal symmetry lead to the following conservation laws

$$\hbar\omega = \hbar\omega_R \quad (2.21)$$

$$\hbar k = \hbar k_R + \hbar\mathbb{G} \quad (2.22)$$

where ω is the incident photon energy, k is the photon wave vector, ω_R is the phonon frequency and k_R is the phonon wave vector and \mathbb{G} is the reciprocal lattice wave vector. The IR region of the electromagnetic spectrum, by convention, is usually divided into three regions, namely, the near-IR, mid-IR and far-IR, with respect to the visible spectrum. Infrared spectrum is generally denoted in reciprocal of wavelength, that is, per centimetre. Near-IR spans from wave-number 14000 cm^{-1} to 4000 cm^{-1} . The mid-IR is approximately 4000 cm^{-1} to 400 cm^{-1} and is usually used to study the fundamental vibrations and associated rotational-vibrational structure of gases, molecules and other materials. The far-IR region has the lowest energy in IR region which spans approximately the region between 400 cm^{-1} and 10 cm^{-1} bordering the microwave region. THz region ($0.1\text{ THz} - 10\text{ THz}$) covers the low regime of the far-IR region of the infrared spectrum. This region is generally used for rotational spectroscopy.

2.9.2 Raman scattering

When photons are scattered from an atom or molecule, most photons are elastically scattered (Rayleigh scattering), such that the scattered photons have the same kinetic energy (frequency) and wavelength as the incident photons. However, a small fraction are scattered with a frequency different from, and usually lower than, that of the incident photons. Scattered light that presents different frequencies to that of the incident radiation is known as Raman scattering. The new frequencies called Raman frequencies, are characteristic of the nature and physical state of the sample and independent of the incident radiation.

The frequency shifts are the measure of the amount of energy involved in the transition between initial and final states of the scattering molecule. The distribution of Raman lines is characteristic of the particular molecular species, with an intensity, which is proportional to the number of scattering molecules in the path of the light. Thus, Raman spectra are used in qualitative and quantitative analysis of molecules. Pure rotational shifts are small and difficult to observe, except for those of simple gaseous molecules. In liquids, rotational motions are hindered, and discrete rotational Raman lines are not found.

When light with frequency ω_l and amplitude E_0 interacts with a crystalline material through changes in the induced dipole moment, \vec{P} , with phonons with frequency ω_{ph} and this will depend on the polarisability matrix:

$$\vec{P} = \bar{\bar{\alpha}} \vec{E}_0 e^{i\omega_l t} \quad (2.23)$$

In case of single phonon scattering the polarisability can be expanded using a Taylor approximation in terms of the normal coordinate (Q) as:

$$\bar{\bar{\alpha}} = \bar{\bar{\alpha}}_0 + \left(\frac{\partial \bar{\bar{\alpha}}}{\partial Q} \right)_{Q=0} Q \quad (2.24)$$

where the normal coordinate is of the following form

$$Q = Q_0 e^{\pm i\omega_{ph} t} \quad (2.25)$$

Combining Eqs. 2.23, 2.24 and 2.25, the resulting dipole moment is of the following form:

$$\vec{P} = \bar{\alpha}_0 \vec{E}_0 e^{i\omega t} + \left(\frac{\partial \bar{\alpha}}{\partial Q} \right)_{Q=0} \vec{E}_0 Q_0 e^{i(\omega_l \pm \omega_{ph})t} \quad (2.26)$$

The second term in Eq. 2.26 represents the inelastic scattering. When a light beam with energy $h\omega_0$ much greater than the difference in energy between two vibrational or rotational levels of the molecule falls on a molecule, most of the photons pass by without interacting with the molecular system; but a small fraction, of the order of 10^{-7} are scattered. This scattering can be interpreted as due to the following process. The incident photon leads the molecule temporarily to a higher level of energy vibrational or rotational (virtual) state. This is not an allowed or stationary state, which quickly decays to an allowed energy level emitting a photon. The \pm sign in Eq. 2.26 explains the type of Stokes shift, plus sign gives anti-Stokes scattering and the minus sign Stokes scattering.

Chapter 3

Instruments and Techniques

This chapter gives an overview of the general instruments and techniques used to perform experiments to investigate properties of organic nonlinear optical (NLO) chromophores and characterise some useful organic compounds having potential in pharmaceutical and industrial applications. An introduction to the technique followed by a brief description of the instrument is given.

3.1 Spin coater

A vast majority of the work in this thesis is done based on thin polymer films. Thin films of thickness $1\ \mu\text{m}$ to $10\ \mu\text{m}$ are fabricated using spin processing technique. The spin coater used (WS-400E-6NPP-LITE by Laurell technologies corporation) is pictured in Fig. 3.1. This is a portable table top design allowing variable spin speed, acceleration and spin time according to the required film thickness and nature of the solvent. The substrates are held on the rotary stage by creating a vacuum externally. The instrument has a vacuum and lid interlock for safety. A detailed overview of the film fabrication method is given in Chapter 4. Further details of the instrument available at Ref. [35].

3.2 UV-Vis-NIR spectroscopy

Absorption spectroscopy is performed across a range of wavelengths where we need to investigate the linear absorption of the material. Absorption spectroscopy is a tool to identify and quantify the presence of a particular substance in a sample. The following instruments have been used for absorption spectroscopy during this



Figure 3.1 – A WS-400E-6NPP-LITE spin processor by Laurell Technologies Corporation. (a) Front view and (b) Rear-view of the instrument.

study. Generally the transmittance data is collected from the spectrometer and the absorption coefficient (α) of the films are estimated using the Beer's equation $\alpha = (-1/L)\ln(T)$, where L is the film thickness and T is the transmittance of the film. Absorption coefficients are generally quoted in cm^{-1} . The spectrometers can be set to give the absorbance (A) of the film, which is related to transmittance through the relation, $A = -\log(T)$.

3.2.1 Lambda 1050 UV/Vis/NIR spectrophotometer

The Lambda 1050 is a high end UV/Vis/NIR spectrophotometer designed to achieve a greater level of sensitivity, resolution and speed. It features two large sampling compartments and a variety of snap-in modules and accessories, including a general purpose optical bench, integrating spheres and a universal reflectance accessory. The Lambda 1050TM utilises three detectors for optimum energy detection across the entire wavelength range of the instrument, 175 - 3300 nm: A gridless photomultiplier tube (PMT) for detection in the UV/Vis, a high sensitivity Peltier cooled InGaAs detector for the 800 - 2600 nm region and a Peltier cooled PbS detector for the range from 2500 - 3300 nm. This offers a good combination of scanning speed and photodynamic range that can be achieved on a given sample type. Further instrumental details available at Ref. [36].

3.2.2 Varian Cary 50

The Cary 50 UV-Vis Spectrophotometer uses a Xenon flash lamp and can be used in the wavelength range between 190 - 1100 nm. The spectrophotometer can be used while the sample compartment is open without affecting the measured results. The Cary 50 is built by a dual beam, Czerny-Turner monochromator, with a 190 - 1100 nm wavelength range. It has approximately 1.5 nm fixed spectral bandwidth, full spectrum Xenon pulse lamp and dual Si diode detectors. The system scan speed is much faster than that of the Lambda 1050.

3.2.3 Fibre optic spectrometer

The Fibre optic spectrometer by Ocean Optics Inc. is useful to investigate broadband time dependent absorption spectra of chromophores. One key advantage of using this spectrometer is it sends a broad wavelength spectrum and records the absorption spectra at that range instead of scanning through different wavelengths as in other conventional spectrometers. This is particularly useful because of its flexibility to use in both transmission and reflection mode. An Ocean optics ST 2000 fiber optic spectrometer was used for transmittance and reflectance measurements. The spectrometer can be used between 250 - 1100 nm. The system is equipped with a powerful and stable Deuterium Tungsten Halogen light source. Further details about the instrument available at Ref. [37].

3.3 Measurement of thickness and refractive index

3.3.1 Prism coupler

Prism coupling is a technique to couple a substantial fraction of the radiation from laser source into a thin films with high accuracy. This technique can circumvent the need for polishing the edge of the film. One of the advantages of a prism coupler is the ability to couple a beam into a thin film with thickness much less than the beam waist. In the present context, prism coupling is used as a simple and efficient technique to measure the refractive indices and thickness of thin polymer films.

A monochromatic laser beam is directed through one side of the prism, the beam is then 'bend', and is normally reflected back out the opposite side into a photo detector. However, at certain values of the incident angle, the beam does not reflect back out, but is transmitted through the base into the film sample. These angles

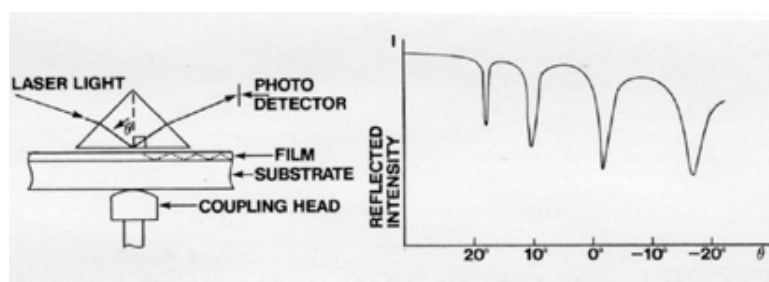


Figure 3.2 – Schematic of the measurement of film thickness using prism coupler. Left side is the schematic of geometry of the apparatus and shown right is the example for the coupling modes [38].

are called mode angles. An automated rotary table is used to change the incident angle of the laser. Refractive indices of a material are specific to the wavelength of the electromagnetic radiation being transmitted and this concept is employed for the estimation of refractive index. The first mode angle found determines the refractive index, and the angle difference from one mode to the next determines the sample thickness. The prism coupling technique offers greater index accuracy and resolution for thin film measurements because the measurements are sensitive only to the coupling angle and index of the prism.

Metricon 2010

Metricon 2010 (new model 2010M) is a computer controlled prism coupling instrument to estimate the refractive indices and thickness of films at different wavelengths, specifically, 633, 1314 and 1550 nm. The measurement of the refractive index at discrete laser wavelengths provide an accurate dispersion curve over a range of wavelengths. In most cases, index values calculated at intermediate wavelengths provide virtually the same accuracy as if that index had been measured at that wavelength.

Measurements are made using a computer-driven rotary table which varies the incident angle and locates each of the film propagation modes automatically. A minimum two mode angles are required to estimate film thickness and index. The entire measurement process is fully automated and the measurement takes less than a minute. A schematic of the measurement of thin film properties using the prism coupling technique is shown in Fig. 3.2.

The number of modes supported by a film generally increases with film thickness. If the film is thick enough to support two or more propagation modes, the

system calculates thickness and index for each pair of modes, and displays the average and standard deviation of these multiple estimates. The standard deviation calculation, unique to the prism coupling technique, is an indication of measurement self-consistency and a powerful means of confirming the validity of the measurement. Measurements of thickness and index can be made on most samples with thickness up to 10 - 15 μm . For thickness above 15 μm , the refractive index is still measurable using the bulk measurement technique although thickness and refractive index for many samples is often measurable at thicknesses up to 150 - 200 μm . Further details of Metricon 2010/M is available in Ref. [38].

3.3.2 DekTak profilometer

The Dektak is a stylus profilometer providing an accurate and a high resolution measurement of the surface shape and texture of thin films. The centrepiece of a Dektak is its measurement stylus, which runs over the surface as the sample is moved beneath it on the stage. A variety of stylus shapes and sizes are available to optimise measurement for particular applications. This is a contact measurement technique where a very low force stylus is dragged across a surface. The DekTak profilometer at IRL is capable of recording thickness variations in the range of 100 nm to 100 μm . The lateral resolution is limited by the tip shape. The system is connected to a PC for the analysis of the data. The DekTak is mostly used to determine film thickness of the polymer films, especially those whose thicknesses are either too thin or more than the upper limit of thickness that can be measured using the Metricon prism coupler accurately.

3.3.3 Interferometry technique

The interferometry technique is an indirect method to estimate thickness and refractive index of films. It relies on the interference effect of two or more light beams, e.g. from the air/film surface and the film/substrate interfaces, where the optical path difference is related to film thickness. This technique is developed based on assuming the system as a Fabry-Perot resonator with air on one side and glass on the other side. The thickness and refractive index are obtained by fitting the interference pattern of the simulated transmission spectrum with the measured transmission spectrum of the film. The transmission spectrum for a multi-layered structure shown in Fig. 3.3 as follows:

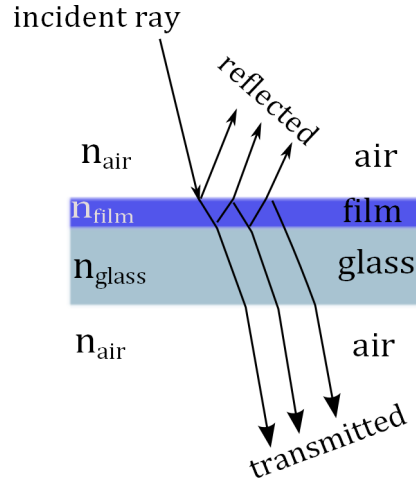


Figure 3.3 – Schematic of the transmission through a thin film on a glass substrate.

The phase difference φ between reflection for normal incidence is given by,

$$\varphi = \left(\frac{2\pi}{\lambda} \right) 2Ln_{\text{film}} \quad (3.1)$$

where L is the film thickness, λ is the wavelength and n is the refractive index. The transmittance through the film can then be estimated from the relation,

$$T = 1 - \frac{r_{12}^2 r_{23}^2 + 2r_{12} r_{23} \cos(\varphi)}{1 + r_{12}^2 r_{23}^2 + 2r_{12} r_{23} \cos(\varphi)} \quad (3.2)$$

with r_{12} and r_{23} respectively the amplitude reflection coefficients at the air-film and film-glass interface which can be calculated using the Fresnel equations and the refractive indices of air (n_{air}), glass (n_{glass}) and the film (n_{film}).

$$r_{12} = \frac{n_{\text{air}} - n_{\text{film}}}{n_{\text{air}} + n_{\text{film}}} \quad (3.3)$$

$$r_{23} = \frac{n_{\text{film}} - n_{\text{glass}}}{n_{\text{film}} + n_{\text{glass}}} \quad (3.4)$$

The thickness is obtained by assigning the values of n and L in Eqs. 3.2 and 3.1 to simulate a transmission spectrum that matches the measured spectrum.

3.4 Poling apparatus

The role of the poling apparatus is to heat the polymer to the glass transition temperature in the presence of a high electric field and then cool the sample down to room temperature with electric field on. This is a contact electrode, parallel plate poling system. The poling apparatus we have used to induce electro-optic effect on thin polymer films is pictured in Fig. 4.7. The heating stage of the system is controlled and monitored by an external temperature controller. A high poling field is also supplied and monitored via an external controller. The system comes with a purge system to avoid moisture and oxygen content in the poling chamber while the films are poled. Poling process and optimisation of poling conditions are discussed in Chapter 4.

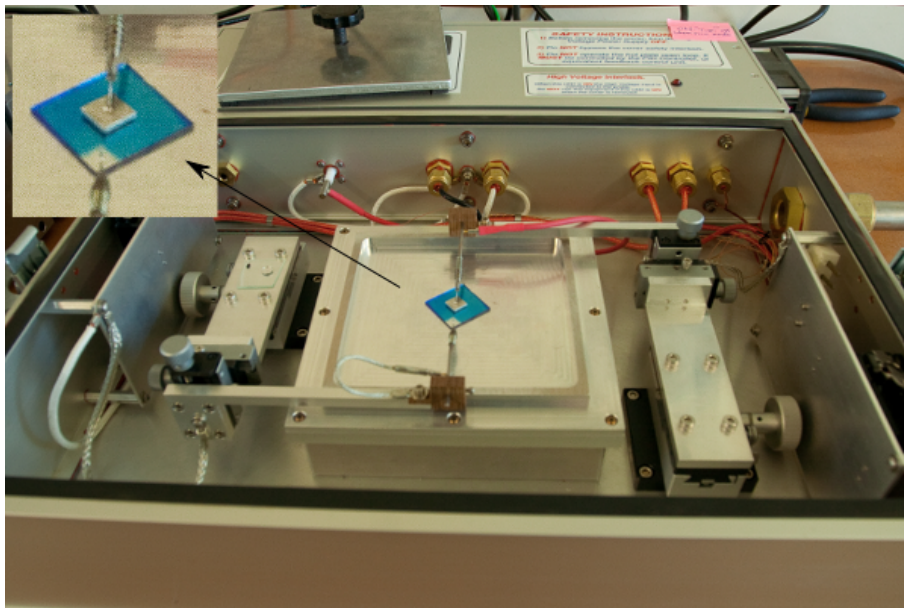


Figure 3.4 – Photograph of the poling apparatus being used in our laboratory; shown inset is the film with electric field applied across the block electrode and ITO layer over the glass.

3.5 Teng-Man apparatus

The Teng-Man apparatus is a simple modulation ellipsometry technique suggested by Teng and Man [39] and independently by Schildkraut [40] for measuring the electro-optic coefficient of nonlinear optical (NLO) materials. The simplicity of this technique compared to other techniques such as Mach-Zhender interferometer for the

measurement of electro-optic coefficient, made this technique popular among the researchers in the field of electro-optic materials [1].

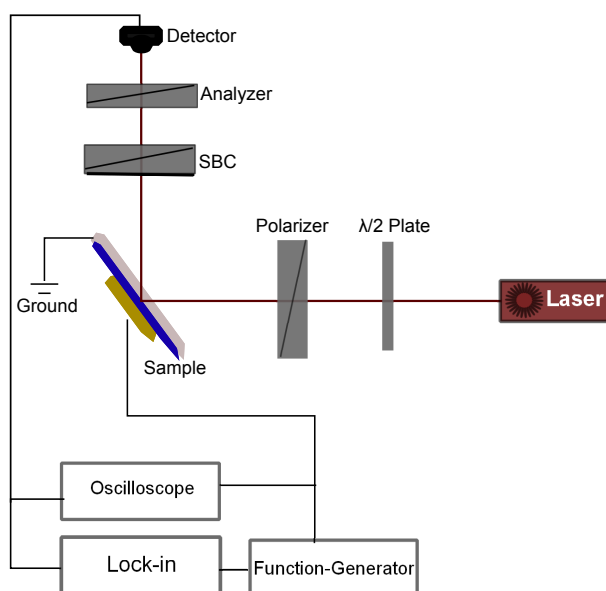


Figure 3.5 – Schematic of the Teng-Man modulation ellipsometry apparatus.

The apparatus can be explained as follows [41]: A laser beam is incident on the back side of the glass substrate at an angle θ . The laser beam passes through a polariser then through the glass plate, the ITO electrode, the polymer film and reflected back at the bottom of the gold electrode. The polarisation of the input beam is set 45° to the plane of incidence so the p and s components of the incident beam have equal amplitudes. The reflected beam then passes through a Soleil-Babinet Compensator (SBC), then through an analyser which is crossed with the polarisation of the input beam. A detector is employed to measure the intensity of the beam through the analyzer. The measurement is performed by applying a sinusoidal modulation voltage across the electrodes. The laser intensity for the SBC retardation and corresponding modulated intensities are detected using a Lock-in amplifier and an oscilloscope. The SBC allows an adequate choice of phase retardation. A schematic of the experimental setup is shown in Fig. 3.5 and the system we have used is pictured in Fig. 3.6. Optimization and analysis of this technique is discussed in Chapter 5, where this technique is employed to estimate the electro-optic coefficient of poled polymers.

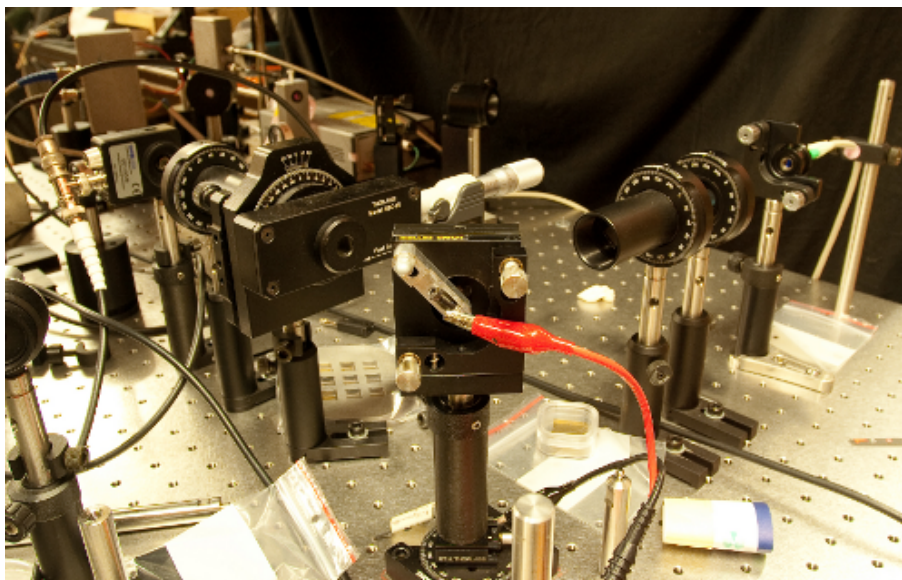


Figure 3.6 – Teng-Man experimental set-up used in our laboratory at IRL.

3.6 DSC-TGA

Differential Scanning Calorimetry (DSC) is a widely used technique to characterise the thermo-physical properties of polymers. In DSC the difference in the amount of heat required to increase the temperature of a sample and reference are measured as a function of temperature. Differential scanning calorimetry can be used to measure a number of characteristic properties of a sample. Using this technique it is possible to observe crystallisation events as well as glass transition temperatures (T_g). DSC analysis is important in the study of electro-optic polymers to understand the T_g of the polymer as is and the effective T_g after adding the chromophores. This helps choose correct poling temperature which is important to obtain maximum poling efficiency.

Glass transitions occur when the temperature of an amorphous solid is increased. These transitions appear as a step in the baseline of the recorded DSC signal. This is due to the sample undergoing a change in heat capacity, but no formal phase change occurs. As the temperature increases further, the amorphous solid will become less viscous. By increasing temperature further, the molecules may obtain enough freedom to spontaneously arrange themselves into a crystalline form. This is known as the crystallisation temperature (T_c). This transition from amorphous solid to crystalline solid is an exothermic process and results in a peak in the DSC signal. A

further increase in temperature makes the sample reaches its melting temperature (T_m). The melting process can be observed from an an endothermic peak appearing in the DSC curve.

Thermogravimetric Analysis (TGA) provides complimentary characterisation information to the most commonly used thermal technique, DSC. TGA measures the amount and rate of change in the mass of a sample as a function of temperature or time in a controlled atmosphere. The measurements are used primarily to determine the thermal and/or oxidative stabilities of materials as well as their compositional properties. The technique can analyse materials that exhibit mass loss due to decomposition, oxidation or loss of volatiles such as moisture. It is especially useful for the study of polymeric materials, including thermoplastics, thermosets, elastomers, composites, films, fibres, coatings and paints.

An SDT Q600 thermogravimetric analyzer by TA instruments was used to perform DSC and TGA measurements simultaneously in the temperature range from room temperature to 1500 °C. This instrument is used to obtain the glass transition temperature of polymers, and the decomposition and crystallisation temperature of chromophores.

3.7 Infrared spectroscopy

Infrared spectroscopy discussed in this section refers to far-infrared (far-IR) spectroscopy. The far-IR region covers the THz spectral spectral region. One of the major application of electro-optic polymers we develop is in THz applications. Therefore it is important to understand the properties of the materials in the THz region. Fourier Transform Infra-red (FTIR) spectroscopy is a general technique to obtain the infrared absorption spectrum of materials in Far-IR region. An FTIR spectrometer simultaneously collects spectral data in spatial domain and then transforms the data to the frequency domain using Fourier analysis. This technique offers a significant advantage over a dispersive spectrometer which measures intensity over a narrow range of wavelengths at a time. The following spectrometers have been used during the course of this thesis for material characterisation in the THz frequency range (0.1 - 10 THz).

3.7.1 Nicolet™ FTIR spectrometer

Nicolet™ FTIR spectrometers from Thermo Electron Corporation was used to study the far-IR spectrum of organic compounds. The system was built with a ‘Smart Purge’ system available for the Nicolet FTIR that automatically detects the opening of the spectrometer door. ‘Smart Purge’ then automatically increases the flow of purge gas in the spectrometer to blast the sample compartment area free from unpurged lab air. ‘Smart Purge’ automatically turns down when the spectrometer is ready to collect data, and provides a short purge recovery time in between successive samples, helping to ensure quick and efficient data collection. This is particularly useful while using in far-IR region which is heavily sensitive to water vapors. OMNIC software for Nicolet™ FTIR spectrometers provides a powerful interface for complete data collection and processing. Further details about the system available in Ref. [42]

3.8 THz time domain spectroscopy

Two types of terahertz (THz) systems have been used for material characterisation in this work. A photo-conductive antenna based THz system at the University of Auckland (UoA) and a commercial THz system at the University of Wollongong (UoW). The first one was used primarily to collect the THz spectra of polymer films to estimate their refractive index and absorption spectra in a frequency range between 0.1 and 1.1 THz. The second system has mostly been used to investigate the infrared vibrational modes in the THz frequency range for some organic crystals. This system has a frequency range of up to 2.5 THz. Schematic of a THz-TDS system is shown in Fig. 3.7.

In the THz systems using photo-conductive antenna, a DC-biased semiconductor has an electron-hole plasma created on a femtosecond timescale by an optical pulse. The rapid acceleration and separation of the electrons and holes create a transient current, then the macroscopic polarisation creates an opposing current that rectifies the DC field and the transient electric field determined by the time derivative of the current results in a radiated pulse. Finally, the semiconductor recovers to the original state in a time frame of the order of picoseconds, as explained in Refs. [43, 44]. The system at UoW is a commercial Z-3 THz time domain spectrometer supplied by Z-Omega corporation. This is pumped by a Toptica ultra-fast fiber optic laser

operating at its second harmonic frequency centered at 785 nm. More details about the Z-3 system is available in Ref. [45].

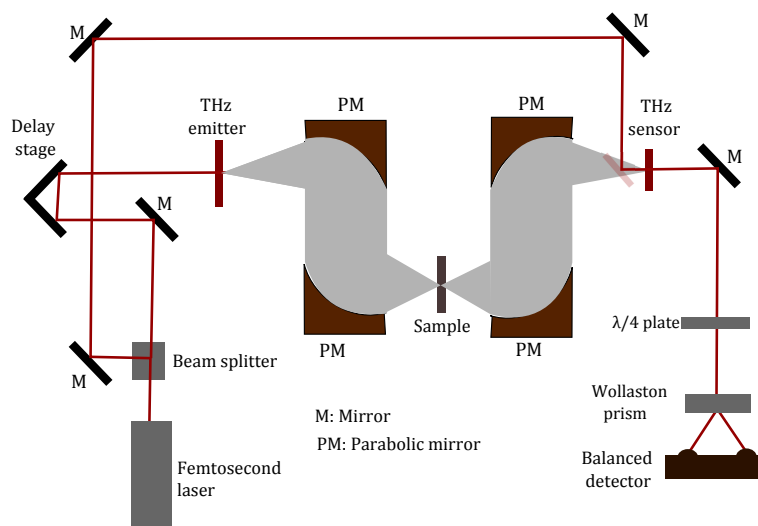


Figure 3.7 – Schematic of a THz-TDS system using optical rectification technique for THz generation and electro-optic sampling method for THz detection.

3.9 Raman spectroscopy

Jobin-Yvon Horiba T-64000 Raman spectrometer

A Jobin-Yvon Horiba T-64000 Raman Spectrometer with confocal Raman microscope at Victoria University of Wellington (VUW) was used for material characterisation in the THz frequency range. The system is a research grade, triple-grating T 64000 Raman spectrometer that is coupled with the confocal Raman microscope and equipped with a back-illuminated liquid nitrogen cooled CCD detector, 3 microscope objectives and a video camera. T-64000 has an integrated triple spectrometer design for unprecedented optical stability with three stage monochromator, with optics, aperture and coupling optimised for performance and stability, with multiple motorized switching mirrors for ease of operation. The key features of the T-64000 Raman spectrometer are its very high level of laser (stray light) rejection, good spectral resolution (0.1 cm^{-1}) and tunable laser filtering.

The Raman system at VUW can operate in 3 different configurations including direct single spectrometer, double subtractive stage (for very low frequency Raman

bands) as well as a triple-grating additive mode enabling low wavenumber measurements. In addition to standard Raman spectroscopy, the T-64000 system is also equipped with a confocal Raman Microscope (Olympus) that allows for confocal Raman mapping with high spatial resolution of structural variations and generation of distribution maps on samples. Further information about the system we have used at VUW available at Ref. [46].

3.10 Lasers

A variety of laser sources have been used in the course of this thesis. Here is a list of lasers used in different types of experiments. The selection is based on the wavelength, intensity and quality of the beam required to perform specific experiments. Diode lasers operating at 655, 760, 785, 904, 1314 and 1550 nm were used in this study depending on the wavelengths and power required for the application. The applications range from the measurement of electro-optic coefficient using Teng-Man apparatus discussed in Chapter 5, the diffraction method for the measurement of electro-optic coefficient discussed in Chapter 6 and photostability experiments discussed in Chapter 7. A He:Ne laser operating at 633 nm was used to excite the samples in Raman spectroscopy discussed in Chapter 8. The 488 and 514 nm lines of an Argon-ion laser were used to inscribe diffraction gratings in polymer films discussed in Chapter 6. A continuous wave Nd:YVO₄ laser operating at the second harmonic frequency, 532 nm was used for photodegradation experiments discussed in Chapter 7. Also, a Toptica ultrafast fibre laser was used to excite the THz emission to perform THz spectroscopy of organic samples discussed in Chapter 8.

Chapter 4

Fabrication and Processing of EO Polymers

This chapter discusses the preparatory work and general quantitative analysis involved in making samples to investigate the efficiency of electro-optic (EO) polymers. These include cleaning substrates for film deposition, preparation of solutions, spin processing and casting for film fabrication, drying to evaporate residual solvents, measurement of thickness and refractive indices of the films and estimation of chromophore concentration in the films. Details of electric field poling of thin films to induce EO effect and methods employed to optimise poling conditions are also discussed.

4.1 Preparation of ultra-clean substrates

The surface of the substrate needs to be dry and free from dust and oil to deposit optical quality thin films. In the present work two types of substrates have been used; glass slides coated with conducting transparent materials such as indium tin oxide (ITO) for poling, and plain glass substrates for the studies that do not require poled samples. Issues with the quality of spin-processed films on as-received glass slides such as film peeling, thickness inhomogeneities and pinholes motivated our team to adopt a rigorous cleaning procedure that is documented in detail in Ref. [47], which is adapted from Ref. [48]. Spin-processed films on glass slides cleaned with this procedure are found to be of higher quality and maintain homogeneity in experiments compared to the films on randomly cleaned slides. The size of the substrates used

for thin film deposition is 25 mm×25 mm with ~1 mm thickness. A summary of the glass-slide cleaning procedure discussed in Ref. [47] can be explained as follows.

1. *Washing* - Wash each slide individually with 5% Decon 90 (D90) solution, wiping each side with an unused section of the wipe. Place washed slides into a slide holder then transfer them into a beaker followed by filling the beaker with sufficient D90 solution to immerse the slide holder. Allow the slides to soak for 30 minutes, then place the beaker in the ultrasound bath for 10 minutes.
2. *Rinsing* - Perform the following procedure three times to rinse the D90 solution from the slides:
 - Remove floating contaminants by filling beaker with distilled water in the sink until it overflows and then drain beaker.
 - Partially cover slide holder with distilled water and swirl in beaker and then drain beaker.
 - Cover slide holder with distilled water and ultrasound for 10 minutes and drain the beaker.
3. *Rinsing* - Fill the beaker with sufficient isopropyl alcohol to immerse the slide holder. Allow the slides to soak for 30 minutes, then place the beaker in the ultrasound bath and ultrasound for 10 minutes.
4. *Drying* - In a clean room, drain beaker and rinse the slides two times with ultra pure distilled water to remove any fine dust contaminants. Then, air-dry the slides with filtered compressed air, and place slides, in holder, in the clean room oven set at 80 °C for at least a few hours to dry.

A slightly modified method is followed to clean ITO coated slides. Alkali and acid solutions may etch the thin ITO coating on the glass surface and thus D90 solution cannot be used for cleaning ITO coated slides. Isopropyl alcohol is used instead of D90 solution to clean the ITO coated slides keeping the rest of the procedures the same as followed for plain glass slides.

4.2 Polymer thin film fabrication

The EO polymer system used for the present study is a host-guest system. This is mainly because of the ease of fabrication and flexibility that allows to investigate properties of chromophores and the system. Spin coating and solution casting are two basic techniques used to deposit sol-gel coatings. Spin coating was used for relatively thin films, while solution casting was used for thicker films. Most of the experiments discussed in this thesis were performed on thin films with thickness between 1 and 10 μm . Spin coating is the preferred method to produce films in this range. Thick cast films of the range 30 μm to 1 mm were made to investigate spectroscopic studies such as terahertz time domain spectroscopy (THz-TDS), Fourier transform infrared (FTIR) spectroscopy and Raman spectroscopy. A systematic method to prepare thin and thick polymer films followed by our group that discussed in Ref. [49] is summarised in this section.

4.2.1 Host polymer

Chromophores and polymer must exhibit appropriate and comparable solubility in the spin casting solvents. Making optical quality thin films requires a balance between the solution viscosity and the solvent viscosity [1]. Host polymers need to have high thermal stability, low optical absorption, and a sufficiently high glass transition temperature (T_g). The polymer host needs to be selected in a way that its T_g be sufficiently higher than the device operating temperature and well below the decomposition temperature of the chromophore being doped into it. Having a T_g below the chromophores decomposition temperature is important to ensure the chromophores are not thermally degraded while poling at the T_g of the host polymer. Also, to be more suitable for commercial applications the host polymer must not have strong absorption or refractive index dispersion at the operating frequencies.

Presently our research is focused on the electro-optical and optical properties of newer chromophores synthesized in our research team, to develop more efficient EO polymers. We have tested three host polymers, they are, Poly(methyl methacrylate) (PMMA), Polysulfone, and Bayer APEC 9389 amorphous polycarbonate (APC). APC has mostly been used in this study because it has several advantages over other polymers mentioned, in particular, PMMA is not suitable for use in THz frequencies above 1.5 THz because of the phonon absorption and strong index dispersion, which is undesirable because the one major scope of this work is to use

the EO polymers for wideband THz applications. Polysulfone has similar T_g and decomposition temperatures as APC, however it does not adhere as well to the glass substrate, leading to the films peeling off from the substrate. Such peeling off occurs during processing of the films such as poling, measurement of EO coefficients and grating inscription, and is not favourable for accurate characterisation. Physical properties of the APC polymer are summarised in Table 4.1.

Table 4.1 – Physical properties of Bayer APEC 9389 Amorphous Polycarbonate (APC).

Property	Value	Source
ρ	1.120 g. cm ⁻³	Bayer APEC 9389 Data-sheet
ε_0	3.0	From Ref. [50]
T_g	218 °C	Bayer APEC 9389 Data-sheet
n_{633}	1.557	From Ref. [50]
n_{1300}	1.541	From Ref. [50]
n_{1550}	1.538	From Ref. [50]

4.2.2 Preparation of solution

The process of preparing solutions for film fabrication takes about 5 hours. This includes mixing of the chromophore with the polymer and solvent at the required proportions followed by stirring to dissolve and filtering out any insoluble impurities. Filtration should be followed by degassing in an ultrasound bath to remove air bubbles introduced while filtration. Structures of some of the chromophores used in this study is shown in Fig. 4.1. All the NLO chromophores used in this study are at least 98 % pure.

Solvent selection and mixing

Both chromophore and the host polymer should exhibit adequate and comparable solubility in the solvent, another important thing to be considered to improve film quality is the vapour pressure of the solvent. Preparation of optical quality films requires a balance between the viscosity and the solvent volatility [1]. The boiling point of the solvent has to be below the T_g of the polymer to avoid deformation during the drying process to evaporate the solvent.

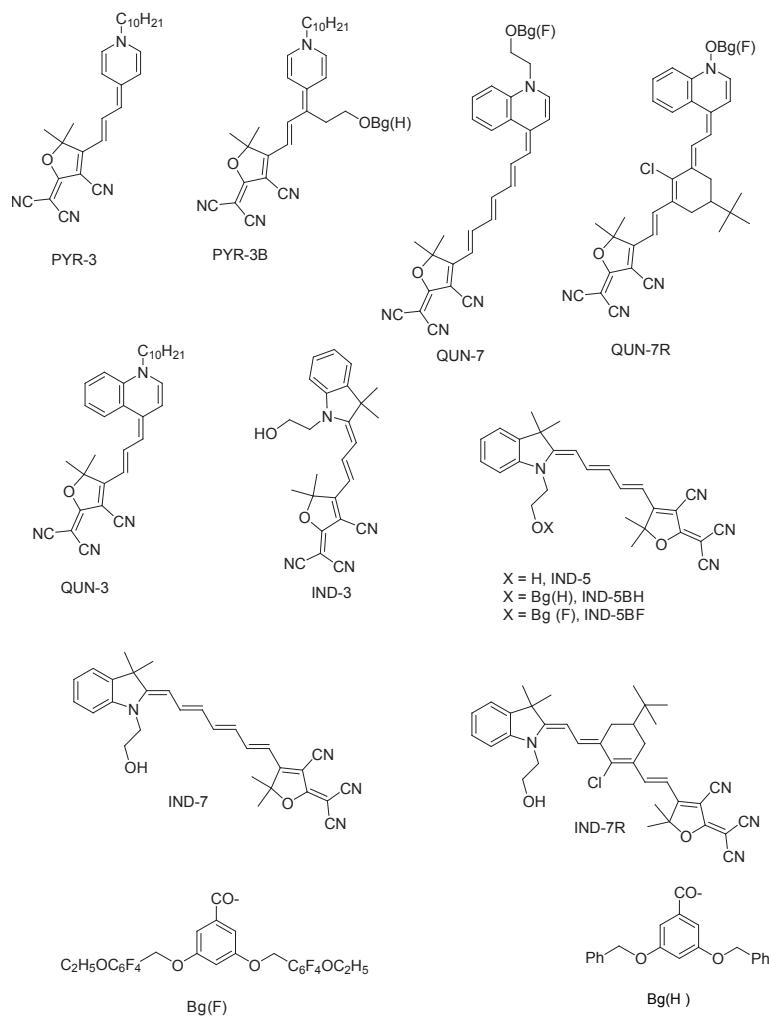


Figure 4.1 – Structures of the organic NLO chromophores used in the experiments in this thesis. The acronyms PYR, IND and QUN represent the donor group and the numbers indicate the conjugation length.

The standard solution is 1 g solids (host plus guest) in 10 g 1,1,2-Trichloroethane (1,1,2-TCE, 99.9% pure) to give a 9.1 wt.% solution. The volume of this solution should be just under 8 ml. The chromophore loading in the host-guest system is the weight percentage of chromophore in the polymer film. Example: for a 5 wt.% loading, 0.05 g of chromophore and 0.95 g of APC would be mixed. Solutions should be left to stir at 60 °C for at least 3 hours.

Filtering and degassing

Mixed solutions must be filtered and trapped gasses allowed to escape (degas) before films are processed. The standard procedure followed is to first filter at $0.45\ \mu\text{m}$ and then at $0.20\ \mu\text{m}$. It is possible to filter once at $0.20\ \mu\text{m}$ with dilute solutions, but at 9.1 wt.% the viscosity of the solution requires significant force to be applied to the syringe plunger to obtain solution flow through the filter. Solutions also may contain undissolved material which clogs the filter pores and requires force to be applied to the syringe plunger. This can splay the filter fibres, allowing larger particles than rated to pass [49].

The filtering process may introduce air into the solutions. So they must be degassed before processing into solid films. Failure to degas the solution leads to bubbles in the films. The solutions were degassed by placing them in an ultrasound bath on degas mode for approximately 10 minutes at $40\ ^\circ\text{C}$, then allowed to sit for 15 minutes for any remaining dissolved air to degas.

4.2.3 Solution casting for thick films

The procedure for fabrication of thick films requires substrates and solutions to be prepared as described in the preceding sections. “Thick” films for our purposes are films greater than $30\ \mu\text{m}$ thick, which cannot be produced on the spin-coater with adequate surface quality. The technique for thick film processing is “casting” – the surface of the substrate is covered with a volume of solution and left to dry for at least 24 hours at ambient temperature in a room free of vibration and air movement.

To obtain a host-guest polymer film of average thickness d on a substrate of area A , one can calculate the volume $V_{\text{film}} = dA$ of the film to be dispensed to result in a film of thickness d . Volume of solution dispensed for V_{film} can be estimated using the relation [49],

$$V_{\text{solution}} = \frac{V_{\text{film}}\rho_{\text{host}}}{c\rho_{\text{solvent}}} \quad (4.1)$$

where c is the concentration of the solution and ρ_{host} is the density of host and ρ_{solvent} is the density of the solvent. For a film made of host polymer APC and TCE as solvent $\rho_{\text{APC}} = 1.2\ \text{g}/\text{cm}^3$ and $\rho_{\text{TCE}} = 1.423\ \text{g}/\text{cm}^3$. As drying of thick films take several days and thus the atmosphere, positioning of the sample holder as well as vibration of the substrate can lead to inhomogeneity in film thickness.

Furthermore, conventional casting techniques often resulted in films with surface inhomogeneities or aggregated chromophore as the solvent evaporated.

4.2.4 Spin coating for thin films

Spin coating is the preferred method for application of thin, uniform films to flat substrates. An excess amount of polymer solution is dropped on top of a substrate mounted on the holder of spin coater and the substrate is then rotated at high speed in order to spread the fluid by centrifugal force. Rotation is continued for some time, with fluid being spun off the edges of the substrate, until the desired film thickness is achieved. The solvent is usually volatile, providing for its simultaneous evaporation. Details of the programmable spin coater we used is given in Chapter 3.

Spin speed, time, acceleration and solvent viscosity

Film thickness is largely a balance between the force applied to shear the fluid towards the edge of the substrate and the drying rate which affects the viscosity of the solution. Solvent viscosity, spin speed and spin time are the key parameters determining film thickness when spin coating. The spin speed of the substrate is related to the centrifugal force applied to the solution over the substrate as well as the relative velocity and characteristic turbulence of the air immediately above it. As the solution dries the viscosity increases until the radial force of the spin process can no longer appreciably move the solution over the surface of the substrate. At this point the thickness will not decrease significantly with spin time. Long spin times for quick drying solvents can create phase separation and inhomogeneity in the films.

The acceleration of the substrate towards the final spin speed can also influence the properties of the thin film. Since the solution begins to dry from the first part of the spin cycle, it is important to precisely control this acceleration. A major fraction of the solvent in the solution evaporates in the first few seconds of the process, thus accelerating to the required spin speed before the solvent dries completely is important. As the effects of spin time is related to the other parameters and solvent properties it has a strong control over the film quality [49].

Fig. 4.2 shows an example for the relationship between spin speed and film thickness, which was investigated previously by Quilty *et al.* [49] specifically for the

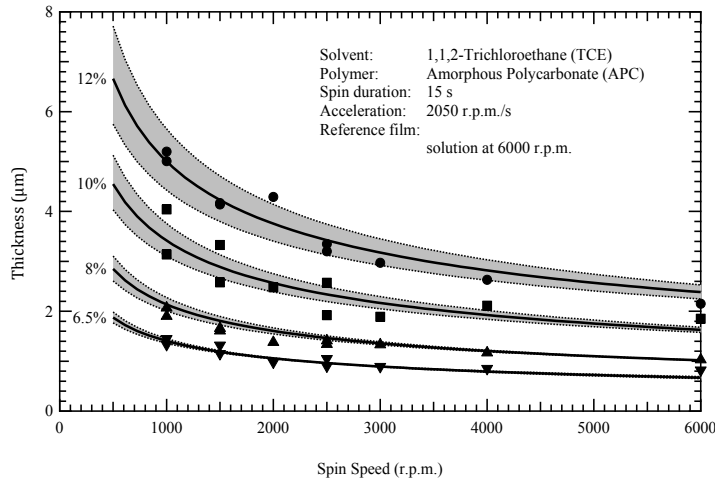


Figure 4.2 – Effects of spin speed and viscosity of the solution on determining the thickness of spin-processed films of APC in 1,1,2-TCE. Solid markers represent measured thicknesses, the solid curve is the least-squares fit to the entire data set. The grey band represents the spread of thicknesses [49].

polymer APC and the solvent TCE. Data shown in Fig. 4.2 is only valid for solutions of APC in TCE. Other host polymers and solvents may have different viscosity and, thus, different film thickness *vs.* spin speed curves.

An empirical equation relating the ratio of the thickness of two spin-processed films is given by the equation [51],

$$\frac{d_2}{d_1} = \left(\frac{\omega_2}{\omega_1} \right)^\alpha \left(\frac{c_2}{c_1} \right)^\beta \quad (4.2)$$

where d is the film thickness, ω the spin speed, c the solution viscosity, and α and β are parameters to be determined empirically. The empirically determined parameters from a fit curve for the data from the experiment shown in Fig. 4.2 are $\alpha = -0.41 \pm 0.04$ and $\beta = 2.07 \pm 0.15$ [49].

Drying procedures

The residual solvents in the film must be removed. However, rapid removal of the solvent lead to phase separation, leaving a non-equilibrium phase morphology that is likely to result from an interplay between bulk phase separation, surface and substrate interactions, the viscosity and volatility of the solvent.

The processed films must be dried at a temperature similar to that of the solvent boiling point to remove residual solvent from the film. Drying a film too rapidly

will cause micro-fracturing or even macroscopic cracking of the film. Therefore, both thick and thin films should be left at room temperature for some time before moving or attempting to dry at elevated temperature. Thin films were left overnight in the clean room before the drying procedure at elevated temperature and vacuum drying was followed; thick films are left over a prolonged time period before attempting to dry.

The following drying procedure was followed on plain APC thin films and was sufficient to dry the films without fracturing. The boiling point of TCE is 113 °C and will not evaporate in a timely manner at ambient temperature. After pre drying of the films at room temperature and ambient pressure the films were transferred to a room temperature oven and the temperature ramped to 80 °C at a rate of 1 °C/min and held for 12 hours. The temperature was then raised to 150 °C at a rate of 1 °C/min held for 2 hours under vacuum and then allowed to cool to room temperature. Thin films containing additives having low decomposition temperature such as anti-oxidants like β -carotene should be dried at lower temperature. These films need to be dried for longer times because it will take more time to dry as a result of drying at lower temperature. Furthermore, the films should not be exposed to light while drying to avoid any possible light induced degradation of the chromophores.

4.3 Measurement of thickness and refractive index

Film thickness and refractive index varies according to processing conditions, properties of polymers and the chromophores used in film fabrication. The thickness of films vary according to the requirement of the experiment, that ranges from 1 μm to several hundred microns. A Metricon Prism coupler explained in Chapter 3 is favoured for measuring in the range of 3 - 20 μm . Film thickness has also been measured from the interference pattern in the transmission spectra using an iterative method by matching the simulated pattern with the measured absorption spectrum. To measure the thickness of films with expected thickness less than 1 μm and more than 30 μm a DekTak profilometer is used. The refractive index of such films is measured using the bulk index measurement option from Metricon 2010.

The interferometry technique is particularly useful to estimate both refractive index and thickness of films from the absorption spectra using the technique of thin film interference. An example of this measurement done on a thin film made

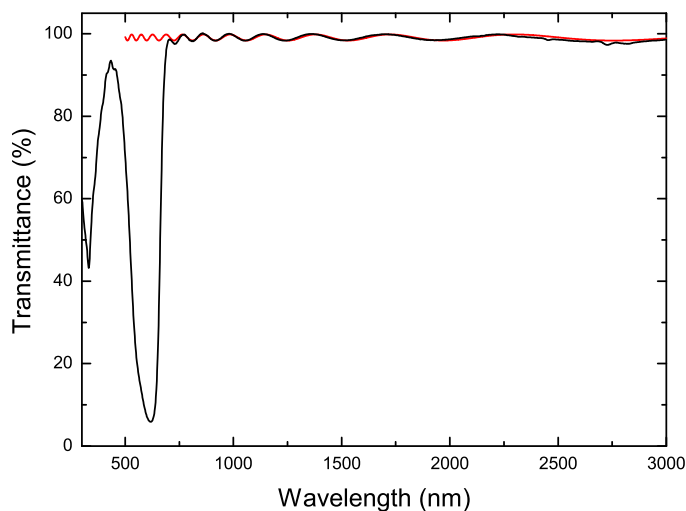


Figure 4.3 – Interferometry method for the measurement film thickness: Measured transmission spectrum of a 5 wt.% PYR-3/APC film (black solid lines) and the theoretical estimation of interference pattern in the transmission spectrum (red solid curve) using the film thickness and refractive indices of film, air and glass substrate [52].

of 5 wt% PYR-3 in APC is shown in Fig. 4.3. This technique is mostly used to measure the thickness of films less than $2\ \mu\text{m}$, as on such films the usability of prism coupling technique is limited when the measurements are done using 1300 nm or 1550 nm lasers. The refractive index values estimated using interferometry technique is approximate value only because refractive index is a function of wavelength but the value estimated here is an average value for the region of interest.

4.3.1 Refractive index dispersion

The refractive index of a material is a function of wavelength, thus the value of refractive index of a material at the measurement wavelength needs to be known for the estimation of other optical and EO properties of the material. The refractive index dispersion in a non-absorbing medium can be approximated using the Sellmeier approximation [53] if the Sellmeier coefficients of the material are known. The refractive index dispersion of the host polymer we used, APC, is estimated by first measuring the refractive indices at wavelengths 633, 1300 and 1550 nm using the Metricon prism coupler. These values are used to estimate the Sellmeier coefficients for the first approximation of the Sellmeier equation for the dispersion of refractive index as given by the Sellmeier equation for glass-like materials [53],

$$n^2(\lambda) = 1 + \frac{B_1 \lambda^2}{\lambda^2 - C_1} \quad (4.3)$$

Where $B_1 = 1.3654$ and $C_1 = 1.4 \times 10^{-14} \text{ m}^2$ are Sellmeier coefficients of APC derived from the measured values at three different wavelength using the Metricon. Refractive index of the films in the region of interest are determined by adding the change in refractive index due to the chromophores with the refractive index of the host polymer. Fig. 4.4 shows the change in refractive index Δn induced by the absorption of the chromophores estimated using Kramers-Kronig transformation. Total effective refractive index as a function of wavelength is estimated by adding Δn with the refractive index of the host polymer as shown in Fig. 4.4.

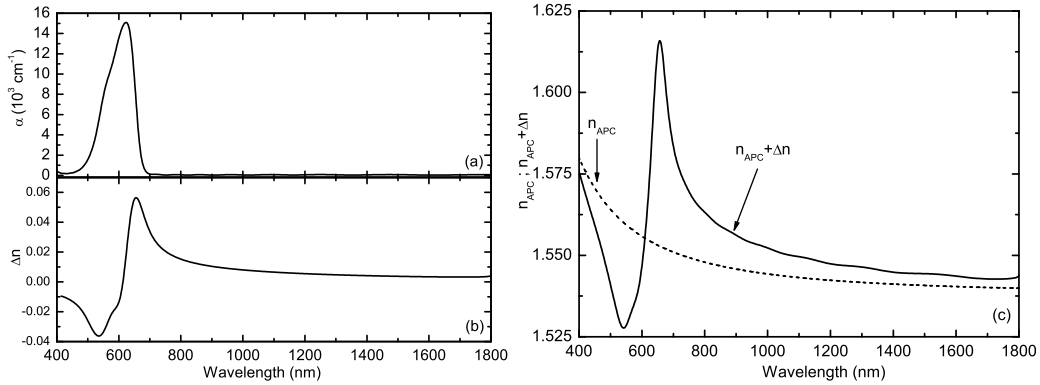


Figure 4.4 – (a) Absorption coefficient of a $2\mu\text{m}$ polymer film containing 5 wt% PYR-3 in APC. (b) Dispersion of change in refractive index Δn with wavelength calculated using the Kramers-Kronig transform from the absorption coefficient. (c) Refractive index dispersion of the host polymer APC estimated using first order Sellmeier equation on the measured values at 633, 1300 and 1550 nm, and the total effective refractive index of the polymer film.

4.4 Chromophore concentration in films

Concentration of chromophores in the films (N) is important for detailed quantitative and qualitative study of the guest-host polymer films. A good theoretical estimation of expected macroscopic electro-optic effect also requires understanding the number density of chromophores. Mixing proportion of chromophore and the polymer is not the sole factor determining chromophore concentration in the films. Thus it is important that it has to be determined after completing the film fabrication procedures. The procedure to estimate the concentration of chromophores in

polymer films discussed in Ref. [50] is reproduced below.

A reasonable approximation of N for polymer guest-host systems may be obtained by considering the weight percent loading of the chromophores in the host polymer

$$N = \frac{w\rho N_A}{M} \quad (4.4)$$

where $w = m_g/(m_g + m_h)$ is the fractional guest molecule loading and m_g and m_h are the masses of guest and host in the host-guest polymer, ρ is the density of the host-guest polymer in g/cm^3 , N_A is the Avogadro number $6.02214179 \times 10^{23} \text{ mol}^{-1}$ and M is the molar mass of the chromophore in g/mol . The density of the guest-host polymer ρ can be estimated from the following equation.

$$\rho = \frac{(m_{\text{guest}} + m_{\text{host}})}{(V_{\text{guest}} + V_{\text{host}})} \quad (4.5)$$

where V_{host} and V_{guest} are the volume contributions from the host and guest to the system. If the host and guest both contribute to the volume according to their densities then $V_{\text{host}} = m_{\text{host}}/\rho_{\text{host}}$ and $V_{\text{guest}} = m_{\text{guest}}/\rho_{\text{guest}}$. As typically the density of the host polymer is known but the density of the guest molecule is not, the approximation $\rho \approx \rho_{\text{host}}$ is often used. An alternate expression $\rho = \rho_{\text{host}}/(1-w)$ is sometimes employed, the latter expression is obtained from Eq. 4.5 if the volume contribution to the host-guest polymer of the guest V_{guest} is negligible. Eq. 4.4 then becomes

$$N = \left(\frac{w}{1-w} \right) \frac{\rho_{\text{host}} N_A}{M} \quad (4.6)$$

To estimate the fractional weight loading, Eq. 4.6 may be rearranged to obtain [24]

$$w = \frac{M N}{\rho_{\text{host}} N_A + M N} \quad (4.7)$$

The percentage weight loading follows, obviously, by multiplying the w obtained from Eq. 4.7 by 100.

4.5 Poling to induce electro-optic effect

In a nonlinear optical (NLO) guest host polymer system, the macroscopic EO effect is determined by the number density of the embedded NLO chromophores, their molecular hyperpolarisability (β_{zzz}) and the fraction of chromophores aligned in the

direction of applied field. The chromophores are originally randomly oriented in a chromophore-polymer system for the system to be in thermodynamic equilibrium, that means the resultant dipole moment of the system will be zero. A non-zero dipole moment, or a non-centrosymmetric alignment is required for finite second order susceptibility. In order to break the centrosymmetry of the film the chromophores need to be orientated in a desired direction. This is achieved by making the chromophores mobile in the system and simultaneously applying a high DC electric field along the direction the chromophores and then freezing the system. Chromophore mobility in the system is generally achieved by heating the polymer, ideally, above the glass transition temperature (T_g) of the host polymer. The chromophores need to be frozen in polar order by cooling the chromophore under the applied electric field [54]. The relationship between the second order NLO susceptibility, $\chi^{(2)}$ and β_{zzz} is given by the equation [55],

$$\chi_{333}^{(2)} = N\beta_{zzz}f_0f_\omega^2L_3\left(\frac{\mu_g f'_0 E_p}{k_B T_p}\right), \quad (4.8)$$

and χ^2 is related to the electro-optic coefficient r_{33} through the relation [56],

$$r_{33} = \frac{2}{n^4}\chi_{333}^{(2)}(-\omega; 0, \omega) \quad (4.9)$$

where ω is the frequency at which the electro-optic coefficient is measured, n is the refractive index of the material at the electro-optic coefficient measurement wavelength, N is the chromophore concentration in the polymer, f_0 , f_ω and f'_0 are local field factors which relate the externally applied electric field E_p to the internal field local to the molecule, μ_g is the molecule's ground-state dipole moment, E_p is the poling field, k_B is the Boltzmann constant and T_p is the temperature. The term L_3 is the 3rd-order Langevin function.

Eqs. 5.32 and 5.29 can be simplified to the form of a relation that links the macroscopic nonlinearity and molecular nonlinearity as a function of order parameter $\langle \cos \theta \rangle$ which plays a role in determining the maximum achievable macroscopic electro-optic activity from a given chromophore and a given concentration in the polymer as [1],

$$r_{33} = |2Nf\beta \langle \cos^3 \theta \rangle / n^4| \quad (4.10)$$

where $\langle \cos \theta \rangle = L_3(\mu E/k_B T)$, the term L_3 is the 3rd order Langevin function. Assuming a relatively low poling field, that is $\mu E/k_B T \leq 1$ one can write $\langle \cos^3 \theta \rangle = \mu E/5k_B T$ [2], which shows that the poling efficiency of given system is primarily directly proportional to the poling field. A schematic of the orientation of chromophores in a host-guest system before, during and after poling is shown in Fig. 4.5. Before poling, the chromophores are in isotropic random orientation, the chromophores align in the direction of poling field at the T_g during poling and after poling chromophores get frozen in partially ordered in one direction of poling field providing a non-zero net dipole moment.

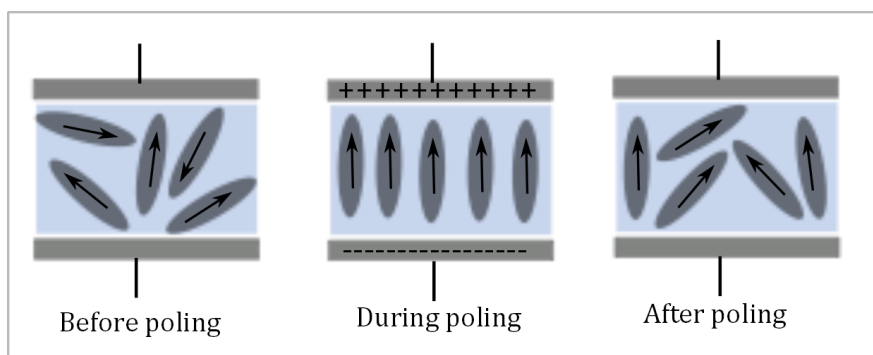


Figure 4.5 – Schematic of chromophore orientation in the polymer films before, during and after poling: The chromophores are in isotropic random orientation before poling, chromophores align in the direction of poling field at the T_g during poling and after poling chromophores are frozen partially ordered along direction of poling field.

4.5.1 Poling techniques

The poling process aligns the chromophores in a polymer system partially, or fully in ideal case, along the direction of the poling field resulting in a non-zero net dipole moment and losing the inversion symmetry of the system. Chromophores in the polymer can be aligned parallel or perpendicular to the plane of the polymer according to the direction of the electric field applied. An overview of some of the commonly used poling techniques are given below.

I. Electrode poling

In this technique, the polymer film is sandwiched between two parallel conducting plates [4, 13] and the electric field is applied across the electrodes at the glass transition temperature of the polymer in an inert atmosphere. The maximum electric field achieved is limited by the charge injection process at the regions of high electric

field at the edges of the electrode. This technique has been used to pole the EO chromophores throughout our experiments. A schematic of the experimental setup is shown in figure 4.6 and detailed description and optimisation of this technique is explained in Section 4.5.2.

II. Corona poling

Corona poling[57, 13] involves a localized partial breakdown of air at atmospheric pressure at very large inhomogeneous electric field. The corona poling apparatus consists of a sharp needle for the corona discharge over the sample, which is placed on a grounded conducting surface. Corona poling is done above the T_g of the host polymer and in an inert atmosphere. An ability to pole samples without the need for a top electrode as well as possible large area poling are the two main advantages of corona poling technique.

III. Electron beam poling.

In electron beam poling, the sample is charged with a constant current from a mono-energetic electron beam in the range of 2-40 keV. The electrons are decelerated and eventually trapped in the volume of the polymer film. Chromophores are oriented in the film by the electric field generated by the trapped charges in the polymer instead of the surface charge in the case of corona poling. The advantage of this technique is to create a periodic pattern of optical nonlinearity along the surface of the polymer. The possibility of chemical modification to the system is a major challenge that limit the applicability of this technique [58].

IV. Photothermal poling

In photothermal poling the polymer is heated using a focused laser beam to heat the polymer locally above its T_g of the host polymer. A simultaneously applied electric field orientate the chromophores along the direction of the electric field. This technique permit localised poling which make bidirectional poling, patterned and periodic poling possible [59].

V. Photo-induced poling

In photo-induced poling, mobility is induced by the *cis-trans* isomerisation cycles of the chromophores instead of heating to the T_g of the host polymer. This is possible in chromophores exhibit optical anisotropy such as *cis-trans* isomerisation.

The chromophores are brought through a large number of these isomerisation steps while applying a DC field perpendicular to the electric field of the pump beam enables the noncentrosymmetric alignment of chromophores [60].

4.5.2 Contact electrode poling

Out of many techniques that are being used to induce EO effect in polymers, we used electrode poling technique [61, 62, 63, 64] because of the simplicity of the technique. This is a simple and efficient method to induce polar order in NLO polymers. The polymer is sandwiched between two parallel electrodes and a high electric field is applied across the electrodes at a temperature close to the T_g of the film in an inert atmosphere. In this case the polar axis is perpendicular to the plane of the film. The role of the poling field is to electrodynamically orientate the chromophores in the direction of the electric field when the chromophores are mobile at the T_g of the system. A high electric field needs to be applied to obtain maximum polar order, however the electric field strength is limited by a number of factors, such as the charge induction process at the regions of high electric field, particularly the sharp edges of the electrode. Charge induction through any pinholes created while film fabrication or drying is another limiting factor. Also the dielectric breakdown of the polymer at high electric field is one of the major problems in contact electrode poling.

Care should be taken while making the film to get a uniform dust free surface [4]. Electrode poling is compatible for electro-optic activity and second harmonic activity. However the dielectric breakdown caused by film defects and inclusions as well as by increasing conductivity of polymer at T_g are the limiting factors of electrode poling [65]. The highest temperature of the whole poling process (T_p) should be at least as high as T_g for the material to be mobile enough to achieve a maximum degree of orientation within a reasonable time.

4.5.3 Optimising poling conditions

Efficient translation of high microscopic nonlinearity of NLO chromophores to a large macroscopic electro-optic effect is one of the main challenges in the fabrication of electro-optic polymers. In the weak field approximation, that is for relatively low poling field where $\mu E/k_B T \leq 1$, the EO coefficient (r_{33}) of a poled polymer film can be expressed as [33, 13, 56],

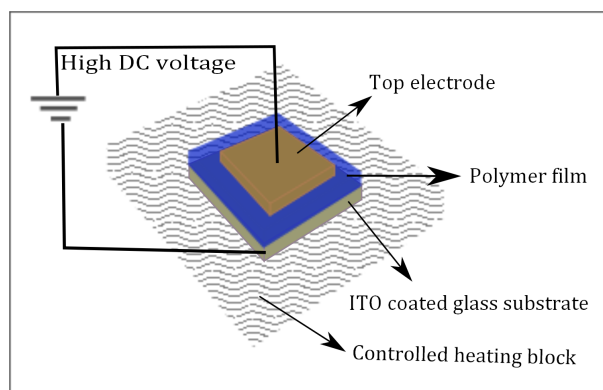


Figure 4.6 – Schematic of an *in situ* contact electrode poling system. Film is sandwiched between the ITO coating over the glass substrate and the gold-coated block electrode on the top. A high electric field is applied at the T_g of the host polymer and the temperature reduced to room temperature with the electric field on.

$$r_{33} = \frac{2}{n^4} f N \beta \left(\frac{\mu E_p}{5k_B T_p} \right) \quad (4.11)$$

Eq. 4.11 shows that the r_{33} of a poled polymer is determined by,

1. The dipole moment, μ and first hyperpolarisability, β of the embedded chromophores
2. Chromophore concentration in polymer, N
3. Poling temperature, T_p
4. Poling field, E_p

Chromophore properties μ and β are intrinsic to the chromophore and the local field factors f are intrinsic to the host-guest system. Chromophore dipole moment is crucial to align the chromophores in the direction of poling field, however, larger dipole moment may lead to undesired properties such as aggregation, and clustering. Poling field E_p and poling temperature T_p are the major physical quantities that can be tuned to achieve the maximum possible poling efficiency.

The EO coefficient of a poled system is related to the chromophore concentration (N) in the polymer system. N can be increased to achieve a high r_{33} , however it is limited by many factors such as aggregation, solubility and scattering loss. Lower solubility and resulting inhomogeneity and phase separation in the films are the major challenges during the fabrication of host-guest films with high chromophore

concentration. Electrostatic interaction between the chromophores is related to the inter-chromophore spacing. Higher concentrations lead to stronger aggregation. Methods to reduce aggregation by altering chromophore structure in guest host polymers is discussed in Chapter 5. In our experiments the chromophore concentration used are below the saturation limit.

Chromophore mobility at temperature much lower than T_g of the host polymer is generally very low and thus for better poling efficiency, the poling temperature needs to be close to the T_g of the host polymer but below the damage threshold of the system. At the poling temperature, the conductivity of the polymer rises and eventually one ends up destroying the system due to pinhole creation, dielectric breakdown etc. In the guest host systems we have investigated, with number density of chromophores, $N \approx 10^{19} / \text{cm}^{-3}$ the maximum poling field without dielectric breakdown was about $100 \text{ V}/\mu\text{m}$ at the poling temperature $180 \text{ }^\circ\text{C}$ which is close to but below the T_g of the APC when doped with the chromophores.

4.5.4 Dielectric breakdown

Dielectric breakdown is one of the main challenges while poling electro-optic polymers. Dielectric breakdown is mainly due to the defects in the films such as voids, impurities, etc. and also by the increased conductivity at high temperatures [65, 66]. In addition to the threat of catastrophic avalanche short circuit destroying the sample the pin-hole creation is also potentially undesired because it can lead to additional scattering losses when the films are used in integrated devices [65]. Poling induced scattering loss is related to the electro-optic coefficient and the wavelength of the laser, such as $(r_{33}/\lambda)^4$ [13].

In order to prevent destructive dielectric breakdown, the current through the film needs to be limited. Current flow through the polymer is recorded throughout the poling process to investigate the relation between the electric conductivity with temperature and also to monitor the poling process to ensure the samples are getting poled without a dielectric breakdown. At medium chromophore loading we find that the chromophore concentration is not related to dielectric breakdown. A plot of the temperature and current flow across the sample for a 5 wt.% PYR-3/APC film of thickness $\sim 3\mu\text{m}$ at a poling field of $60 \text{ V}/\mu\text{m}$ is shown in Fig. 4.7. Our results showed that the current flow is independent of temperature and applied field at lower temperature, followed by a temperature dependent current flow which starts

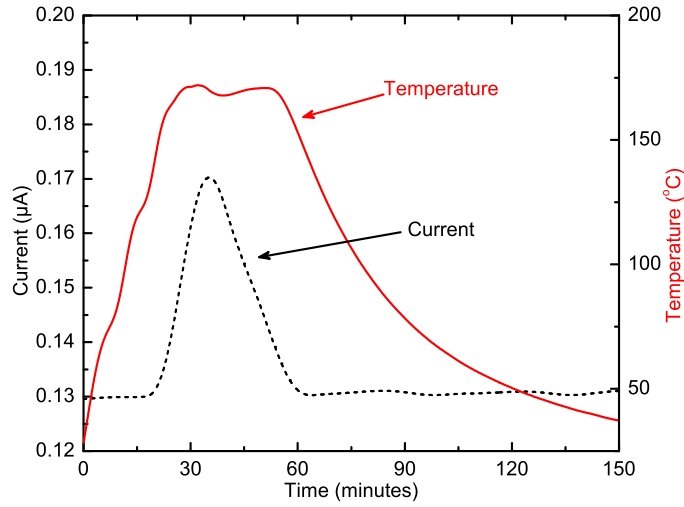


Figure 4.7 – Current flow across the film and temperature as a function of time during poling.

decaying once the temperature is lowered to room temperature. Samples for testing are poled at a temperature slightly below the T_g of the host polymer and also the poling field is chosen lower than the maximum possible.

The polymers used in film fabrication are generally insulators, however, their electrical properties in reality differ from ideal insulators. This can be attributed to the spatially localized energy states distributed within the classical energy gap that arise from the impurity centres or structural defects and act as a pseudo gap with a low state density [65]. A detailed theoretical background to the conduction mechanism while electrode poling of polymers is given in Ref. [65]. Thermally activated hopping or tunnel hopping between traps is one of the mechanisms leading to the volume conductivity of polymers. This is of particular interest because of its relevance to the conduction mechanism at poling temperature. Conductivity of the EO polymer is related to both temperature and electric field. At a given temperature, the current shows a linear relationship with the applied voltage at low poling voltage, while a near quadratic dependence is expected at high poling fields [66]. This property of the polymer can be attributed to a sharp dielectric breakdown when the poling voltage gradually rises at T_p .

Chapter 5

Measurement of r_{33} Using Modulation Ellipsometry

A large and stable electro-optic (EO) coefficient (r_{33}) over the course of the lifetime of devices is a key requirement to qualify an EO material to be used in devices. The development of new chromophores with high molecular NLO effects is important to improve the efficiency of polymer based EO materials. This chapter discusses the results from the measurement of the r_{33} of polymer thin films containing NLO chromophores synthesized by the Photonics team at Industrial Research Limited. Chromophores having a large first hyperpolarisability (β) are expected to give a large r_{33} at the macroscopic level. The effects of structural modifications of chromophores on the EO effect in the macroscopic level are discussed. The Teng-Man ellipsometry technique in reflecting geometry has been used for the measurement of r_{33} , and the measured values are analysed and compared with the theoretically calculated values using the chromophores intrinsic properties and poling conditions. The frequency dependence of r_{33} is investigated by varying the modulation frequency of the driving electric field. A mismatch observed between the experimental results and the theoretical estimation and the roll-off of the r_{33} with modulation frequency are discussed.

5.1 Teng-Man apparatus for the measurement of r_{33}

The modulation ellipsometry method suggested by Teng and Man [39] and independently by Schildkraut [40] is one of the most widely used techniques to estimate the

r_{33} of poled EO polymers. The basic experimental setup for the Teng-Man ellipsometry technique is explained in Chapter 3. The wavelength of the laser used in this study is 1314 nm and the angle of incidence is set at 45° unless otherwise mentioned. A wavelength 1314 nm was used as it is far from the absorption band of all the chromophores investigated, this is important to avoid any light induced degradation (see Chapter 7) of chromophores. The output power of laser was 9 mW with a beam size of 3 mm on the sample. The light intensity of this beam is well below the intensity required to damage polymers due to the heating effect [67, 24]. The output signal is detected by an InGaAs detector connected to an oscilloscope and Lock-in amplifier coupled with a function generator used to modulate the beam. The modulating frequency used throughout the measurement is 1 kHz unless otherwise mentioned. A phase retardation was induced using a Soleil-Babinet Compensator (SBC) to transmit half the maximum of the incident laser intensity where the maximum modulation intensity is expected [39, 41]. The r_{33} of poled polymer films are estimated using the formula suggested by Shuto [41].

Derivation of the Teng-Man formula

The equation to estimate the r_{33} using Teng-Man ellipsometry data is based on many assumptions. Therefore, it is useful to understand the evolution of this formula for a better understanding of the validity of this technique. The variation of the output laser intensity and the modulation amplitude as a function of total phase retardation are summarized in Fig. 5.1. Total phase retardation means the sum of the phase retardation induced by the Soleil-Babinet Compensator (SBC) and the phase retardation due to the EO effect.

The intensity of the laser beam (I_O) on the detector is given by,

$$I_O = I_{O, \max} \sin^2(\phi/2) \quad (5.1)$$

where $I_{O, \max}$ is the maximum intensity, and ϕ is the total phase retardation that is given by,

$$\phi = \psi_{sp} + \phi_B \quad (5.2)$$

where, ϕ_B is the phase retardation by the compensator and $\psi_{sp} = \phi_e - \phi_o$ denotes the phase difference between ordinary and extraordinary rays induced by

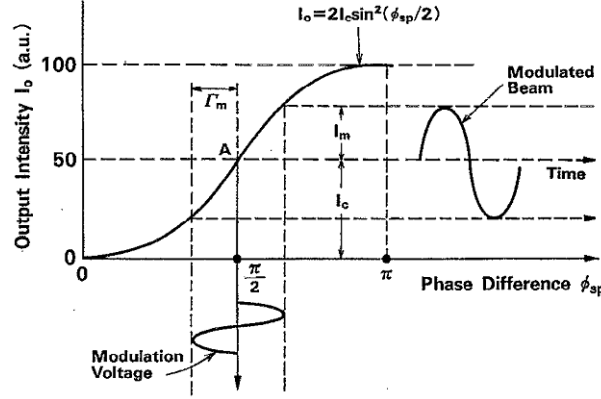


Figure 5.1 – Output laser intensity (I_o) and modulated intensity (I_m) as a function of SBC retardation [41].

birefringence due to the EO effect in the medium. A plot of the output laser intensity as a function of compensator readings is shown in Fig. 5.1. SBC is adjusted to find the points where the output intensity is half the maximum, by adjusting compensator induced phase retardation. Half maximum intensity is important because the modulation is maximum at this region as shown in Fig. 5.1.

The s and p waves of the beam are made equal using a $\lambda/2$ plate before it enters the polariser, both waves are in phase with each other. The s wave oscillates parallel to the plane of polymer along ordinary axis and thus the index of refraction for s wave is n_o .

$$n_s = n_o \quad (5.3)$$

The p wave has components that are both parallel and perpendicular to the film plane. So the parallel component has a refractive index n_o and the perpendicular component has n_e . Then it can be expressed as:

$$\frac{1}{n_p^2} = \frac{\cos^2 \alpha_p}{n_o^2} + \frac{\sin^2 \alpha_p}{n_e^2} \quad (5.4)$$

Using Snell's law,

$$\sin \theta = n_p \sin \alpha_p \text{ and } \sin \theta = n_s \sin \alpha_s \quad (5.5)$$

From Eqs. 5.4 and 5.5 we get,

$$\frac{1}{n_p^2} = \frac{1}{n_o^2} + \frac{1}{n_e^2} \times \left(\frac{1}{n_e^2} - \frac{1}{n_o^2} \right) \sin^2 \theta \quad (5.6)$$

thus,

$$n_p = n_o \left(1 + \left(\frac{1}{n_o^2} - \frac{1}{n_e^2} \right) \sin^2 \theta \right)^{1/2} \quad (5.7)$$

The change in refractive index by linear electro-optic effect (Pockels effect) is given by [1],

$$\delta n_o = n_o^3 r_{13} E/2 \text{ and } \delta n_e = n_e^3 r_{33} E/2 \quad (5.8)$$

A modulating voltage $V_m = V_0 \sin(\omega t)$ is applied across the film with thickness l , then the Eq. 5.8 becomes,

$$\delta n_o = n_o^3 r_{13} (V_m/2l) \text{ and } \delta n_e = n_e^3 r_{33} (V_m/2l) \quad (5.9)$$

From the ∞mm symmetry of the polymers we consider, $r_{13} \approx (1/3)r_{33}$, then Eq. 5.9 can be written as,

$$\delta n_o = n_o^3 r_{33} (V_m/6l) \text{ and } \delta n_e = n_e^3 r_{33} (V_m/2l) \quad (5.10)$$

Also assumed that, $\delta n_s = \delta n_o$. The phase mismatch between s and p waves due to change in index can be expressed as

$$\psi_{sp} = \frac{4\pi l}{\lambda} \left(n_o \cos \theta_0 - \frac{n_o}{n_e} (n_e^2 - \sin^2 \theta_1)^{1/2} \right) \quad (5.11)$$

$$\delta \psi_{sp} = \frac{\partial \psi_{sp}}{\partial n_o} \delta n_o + \frac{\partial \psi_{sp}}{\partial n_e} \delta n_e \quad (5.12)$$

where, θ_0 (θ_1) is the angle of ordinary (extraordinary) rays with respect to the normal to the plane of the film. Using Eq. 5.11 and by taking $n_o \approx n_e \approx n$ to estimate $\partial \psi_{sp}/\partial n_o$ and $\partial \psi_{sp}/\partial n_e$ the Eq. 5.12 becomes:

$$\delta \psi_{sp} = \frac{4\pi n^2 V \sin(\omega t)}{3\lambda} \frac{\sin^2 \theta}{(n^2 - \sin^2 \theta)^{1/2}} r_{33} \quad (5.13)$$

We know that, (see also Fig. 5.1),

$$I_O = I_{O, \max} \sin^2((\psi_{sp} + \phi_B)/2) \quad (5.14)$$

where, $I_{O, \max} \approx I_1$. The instantaneous variation in I_O by the variation in ψ_{sp} from the applied modulating field will be

$$\delta I_O = (I_{O, \max}/2) \sin(\psi_{sp} + \phi_B) \delta \psi_{sp} \quad (5.15)$$

The variation in output intensity δI_O will be the modulation intensity caused by the applied field can be denoted as I_m , and letting $I_{O, \max}/2 = I_c$, the half maximum of output intensity. Then we get:

$$\frac{I_m}{I_c} = \sin(\psi_{sp} + \phi_B) \delta \psi_{sp} \quad (5.16)$$

When $\psi_{sp} + \phi_B = \pi/2$ at A (or $3\pi/2$ at B in the other half of the full cycle) in Fig. 5.1,

$$I_m/I_c = \delta \psi_{sp} \quad (5.17)$$

Now, by using the value of $\delta \psi_{sp}$ from Eq. 5.13 and applying in Eq. 5.17 for the values of $\psi_{sp} + \phi_B = \pi/2$ or $3\pi/2$, ie, at A and B we get, the Teng-Man formula [39, 41] used to estimate r_{33} from modulation ellipsometry experimental data for poled polymers.

$$r_{33} = \frac{3\lambda}{4\pi} \frac{1}{V_m n^2} \frac{(n^2 - \sin^2 \theta)^{1/2}}{\sin^2 \theta} \frac{I_m}{I_c} \quad (5.18)$$

Where λ is the optical wavelength, θ is the angle of incidence, n is the refractive index of the material, I_m is the modulation intensity measured using lock in amplifier, V_m is the AC modulation voltage applied across the polymer and I_c is the half the maximum of the output laser intensity. The r_{33} is generally expressed in the reciprocal of the unit of electric field.

5.1.1 Teng-Man apparatus optimisation

Instrumentation for the Teng-Man apparatus we have used is similar to what is described in the literature [39, 41, 40]. The system has been calibrated using a z-cut LiNbO₃ crystal with an ITO coating on one side and a reflective gold coating on the other side. The EO coefficient measured for LiNbO₃ at 1314 nm was 29.5 ± 3 pm/V

which is close to the value reported in literature, 30.8 pm/V [6]. We have used a detachable block electrode instead of an evaporated gold electrode to permit non-destructive measurement. Using a block electrode can also avoid the chances of short circuiting when evaporating or sputter coating the reflective electrode over the sample in the presence of any minute pinholes created by the film fabrication, drying or poling processes. This section discusses the optimisation of the apparatus used to investigate the experimental data obtained matches with similar systems reported in literature.

Response to modulating voltage

It can be observed from Eq. 5.18 that once the experimental settings are fixed under a stable continuous wave (c.w.) laser pump beam, and the compensator is adjusted to get half maximum output intensity, all the variables in Eq. 5.18 are constants except V_m and I_m . By theory, the modulated intensity, I_m , should show a linear relationship with the applied modulating voltage, V_m . A plot of I_m vs. V_m for a film containing 5 wt.% PYR-3/APC is shown in Fig. 5.2. Experimental values show that, the slope I_m/V_m is a constant meaning the measured r_{33} is stable with voltage, as expected from the theory of Teng-Man ellipsometry technique [41, 39].

Response to compensator retardation

The Teng-Man measurement data for a 5 wt.% PYR-3B/APC [68] was collected for a set of measurements for different compensator retardations using a laser wavelength of 1314 nm, with an angle of incidence 45° , modulation frequency 1 kHz and modulating voltage of 3 V r.m.s across a $5 \mu\text{m}$ sample. In the derivation of Teng-Man formula, it has been assumed that the maximum modulation intensity is observed at the half maximum of the maximum laser output intensity. However, in the data shown in Fig. 5.3 the peak of modulation intensity is shifted from the half maximum points of the output intensity, indicated as A and B in Fig. 5.3. The shift from the ideal position is explained by the multiple reflection due to the multi-layered structure of the sample [69]. In general the average values of r_{33} for poled polymers are estimated by averaging the values obtained at points A and B as indicated in Fig. 5.3, by estimating I_m in Eq. 5.18 using the following Eq. [69, 70],

$$I_m = \frac{|I_m^A| + |I_m^B|}{2} \quad (5.19)$$

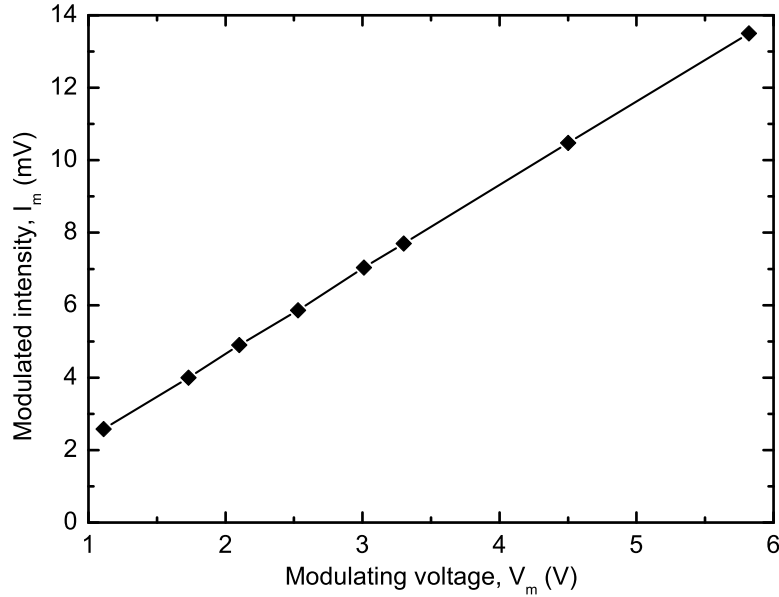


Figure 5.2 – Modulated intensity as a function of modulating voltage on a poled film containing 5 wt.% PYR-3B in APC. The half maximum intensity was 2 V and angle of incidence 45° . The EO coefficient was estimated to be 410 pm/V for this sample using Teng-Man ellipsometry technique.

In Fig. 5.4 a parametric plot was generated by the modulation amplitude recorded by the Lock-in as a function of the average output intensity of the laser beam through the analyser. As expected from theoretical predictions the plot follows an elliptical path and the length of the vertical axis is proportional to the magnitude of r_{33} . The slope of the vertical axis of the ellipse is an indication of the presence of error in the measurement, such as the multiple reflection from the multi-layered structure or the presence of any other effects [71, 72, 69]. It is possible that the ITO/Polymer/Metal interfaces can modulate the reflectivity via a Fabry-Perot resonance [72]. In our experiments we expect the air-gap between the film and the top electrode may lead to this deviation. The poling process can also be used to bake the sample by gently pressing the electrode over the sample. Baking the sample with an electrode is generally encouraged for measurements using detachable electrodes [71].

5.2 Temporal stability of induced EO effect

One of the major challenges of the polymer EO materials is the decay of the induced EO effect with time [73]. Chromophores in a poled host-guest polymer are in a thermodynamically metastable state and thus the system tends to relax to random

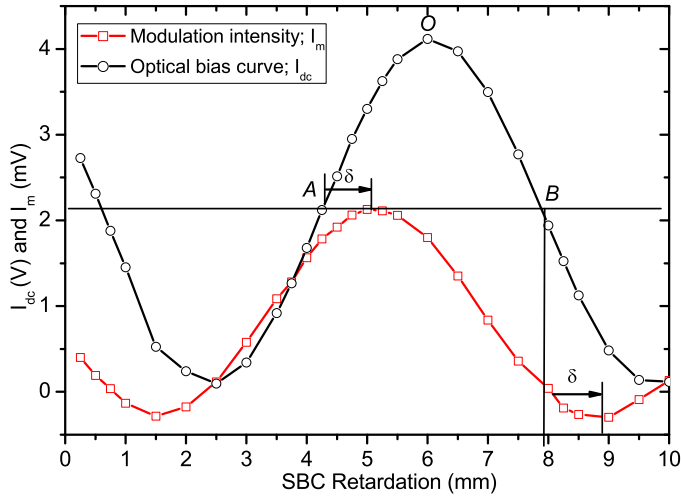


Figure 5.3 – Optical bias curve and modulated intensity obtained as a function of compensator position correspond to the phase retardation induced by the compensator. Maximum intensity of the optical bias curve is at point O, while A and B correspond to compensator settings for the total phase shift $\pi/2$ and $3\pi/2$. δ indicates the shift of the maximum of the optical bias curve for the modulated intensity from the ideal points A and B towards the direction indicated by the arrow.

orientations to achieve a stable low energy state [13, 73]. The decay of the EO effect arises from this relaxation of the polar orientation of the chromophores in the polymers originally induced by the poling process. The polar ordering eventually reverts to the randomised state by the orientational mobility of the aligned NLO chromophores as well as the relaxational motion of the polymers in its non-equilibrium state as discussed in Ref. [74].

5.2.1 Relaxation of the induced r_{33} of a PYR-3 system

NLO films containing 5 wt.% PYR-3 were prepared by mixing 5 wt.% PYR-3 in APC. The films were deposited onto indium tin oxide (ITO) coated glass substrates by spin coating and were dried in a vacuum oven at 150 °C. The thin films were poled at 100 V/ μm and 180 °C for 30 minutes. The poling temperature was below the APC glass transition temperature (218 °C) and far below the PYR-3 decomposition temperature (290 °C)[68]. The r_{33} was measured using the reflection mode Teng-Man modulation ellipsometry technique, a 1314 nm diode laser at a 45° angle of incidence was used. The measurement was continued for an extended period to monitor the temporal stability of the film (i.e. decay profile). The r_{33} was \sim 175 pm/V when measured immediately after poling [62], which is more than 5 times

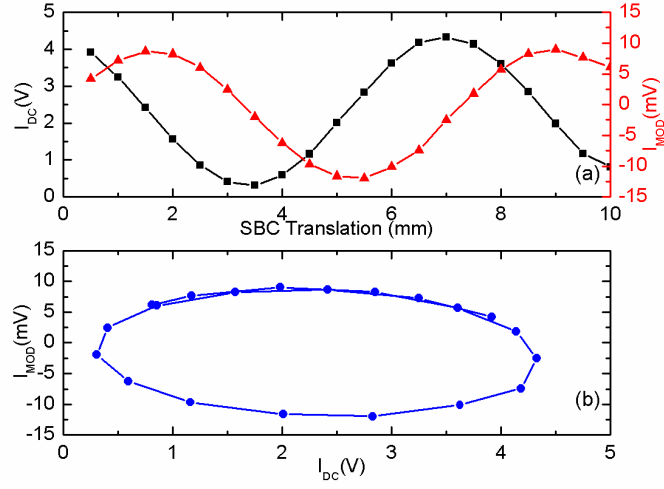


Figure 5.4 – Analysis of the Teng-Man ellipsometry data from a poled polymer: (a) Plot of modulated intensity, I_{MOD} (red symbols) and the output laser intensity, I_{DC} (black symbols) for a set of compensator positions. (b) Parametric plot of modulated intensity, I_{MOD} as a function of I_{DC} for the data shown in (a).

larger than that of a common inorganic crystal, LiNbO_3 [5, 7, 41].

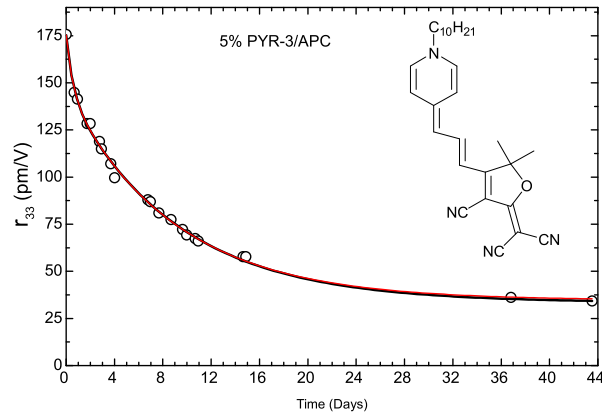


Figure 5.5 – Relaxation of r_{33} of a poled 5 wt.% PYR-3/APC film.

The decay profile of the r_{33} was measured after poling for a 5 wt.% PYR-3/APC film with chromophore concentrations of $8.62 \times 10^{19} \text{ cm}^{-3}$. It can be seen in Fig. 5.5 that the r_{33} continuously decays with time. The measured data can be fitted with a bi-exponential model developed as a simple extension to the Debye model, for the relaxation of EO activity in guest-host systems as explained later in this section. For Fig. 5.5 we show fits to the data following the relation,

$$r_{33}(t) = A_1 \exp(-t/\tau_1) + A_2 \exp(-t/\tau_2) \quad (5.20)$$

where t is the time, and τ_1 and τ_2 are the time constants. Applying this to the data we find that $A_1=107$ pm/V, $\tau_1= 312\pm 80$ hrs, $A_2= 66$ pm/V, and $\tau_2= 5200\pm 270$ hrs.

5.2.2 Analysis of the relaxation process

The relaxation of r_{33} of poled polymers depends on the nature of the system as well as the freedom the chromophore has to relax. Molecular dipoles are typically frozen in the ordered state below T_g , however, they are still prone to relaxation though the process is very slow. Chemical linking of the chromophore with the polymer like side chains or cross-linked polymers show a longer relaxation time (better stability) when compared to host-guest type polymers. There is the possibility of making the side-chain polymer. But the research on developing efficient NLO chromophores is more convenient when considering the host-guest polymers. Also, it is easier to optimise the chromophore loading and thereby achieve a direct comparison of the chromophores.

Modelling the relaxation of induced EO effect is useful for predicting the temporal stability of the electro-optic polymers. A great deal of research effort has been made on this topic since the development of NLO polymers [4]. The simplest model explaining the decay of r_{33} is the Debye model [74] where the relaxation is explained using a simple single exponential decay function as,

$$r(t) = r_0 \exp(-t/\tau) \quad (5.21)$$

where $r(t)$ is the electro-optic coefficient at time t and τ is the time constant. However, in practice, each chromophore experiences a different molecular environments that makes the relaxation of one, or one set, of chromophores different from the other [73, 74, 56]. This indicates, to model the relaxation of chromophores in a poled polymer there should be a number of time constants. The relaxation model can be given in a more practical case as a superposition of different Debye relaxation models as [74],

$$r(t) = \int_0^{\infty} \rho(\tau) \exp(-t/\tau) d\tau \quad (5.22)$$

where $\rho(\tau)$ is the Debye distribution function. Comparing the model with experimental conditions one can see that most of the chromophores differ little from

similar chromophores of the same group. So that one can simplify the continuous function as a bi- or tri- or higher exponential functions as [74],

$$r(t) = r_1 \exp(-t/\tau_1) + r_2 \exp(-t/\tau_2) + \dots \quad (5.23)$$

A double exponential decay function has been experimentally demonstrated by researchers in case of guest-host polymers made in PMMA [74, 75].

One of the most common exponential functions being used to model the relaxation of the EO effect in the EO polymers is the Kohlrausch-William-Watts (KWW) stretched exponential function [13] proposed initially by Kohlrausch and developed by Williams and Watts a century later [76],

$$\phi(t) = \exp[-(t/\tau(T))^p] \quad (5.24)$$

where p is the stretching parameter which ranges from 0 to 1, which describe the deviation from a single exponential. The time constant τ is a function of temperature, it is a reasonable assumption that the relaxation is related to the temperature, especially when it approaches the T_g of the polymer.

The KWW model can be related to the integral form of the Debye model [74] as,

$$\exp(-t/\tau(T))^p = \int_0^{\infty} \rho(\tau) \exp(-t/\tau) d\tau \quad (5.25)$$

Fitting parameters can be obtained by the measurement over a long period. It was observed from the experiment that the decay curve is a mix of multiple exponential decay curves with the decay constant increasing with time. The measurement needs to be continued until a satisfactorily large decay constant can be extracted from the data.

The decay time constant τ is strongly related to the glass transition temperature (T_g) of the host polymer. The simplest model for the relation between the relaxation time constant and temperature was proposed by Stahelin [77] as,

$$\tau(T) = \tau_0 \exp(B/(T_0 - T)) \quad (5.26)$$

where τ_0 and B are fitting parameters specific to the chromophore and the polymer and $T_0 \approx T_g + 50$ °C. Detailed investigation of the decay constant is beyond the scope of this thesis. The lowering of relaxation time with temperature is because of

the greater freedom for relaxation at higher temperature.

5.3 Structural alterations for improved molecular non-linearity

One of the significant challenges in the use of organic chromophores in NLO applications is to translate their high molecular NLO figure of merit to a high macroscopic EO coefficient. The magnitude of the EO coefficient is largely determined by inter-chromophore interactions at high concentrations, as well as the ability of the chromophore to orientate with an applied poling field and maintain some of this orientation over a period of time. Different strategies have been used including the use of bulky group derivatives of the conventional rod-like EO chromophores to enhance r_{33} and the temporal stability. Structural modifications include ring locking of the π -conjugated system along with the incorporation of bulky substitutes, e.g. diphenyl groups, onto this central ring system.

In an NLO chromophore, the π -electrons will almost always be polarised asymmetrically. Higher molecular nonlinearity can be obtained by tuning the bond length alternation (BLA) value of the chromophore [21, 18]. This can be achieved by a number of possible methods, including increasing the conjugation length through increasing the number of π -bonds [78, 79], and changing the strength of the donor and/or acceptor [79]. One of the main challenges in the development of efficient electro-optic materials at the application level is the poor efficiency in translating the large microscopic NLO property to the macroscopic level. Efficiency of poling can be improved by optimization of poling conditions, however, this is limited by many parameters as discussed in Chapter 4. At the chromophore level, the efficiency of the translation of the first hyperpolarisability to a macroscopic electro-optic effect is achieved by reducing aggregation. This is possible through increasing the planarity of the chromophores as well as by maintaining spacing between the chromophores via incorporating large bulky substitutes with the chromophores as shown in Fig. 5.7. Detailed analysis of the effects of the addition of bulky substitutes is discussed in following sections.

The synthesis of the new chromophores are based on the theoretical model of the first hyperpolarisability using the two-level model. The difference in the NLO response in these materials are expected to arise from the two level model developed

for the theoretical estimation of the molecular nonlinearity [80, 15].

$$\beta_{zzz} \propto (\mu_{ee} - \mu_{gg}) \frac{\mu_{ge}^2}{E_{ge}^2} \quad (5.27)$$

According to this model, the first hyperpolarisability is proportional to the difference in the highest occupied molecular orbital (HOMO) and lowest unoccupied molecular orbital (LUMO) states of the molecular orbitals ($\Delta\mu_{eg} = \mu_{ee} - \mu_{gg}$) and the square of the transition dipole moment (μ_{ge}). Also, β_{zzz} is inversely proportional to the square of the energy difference between the ground state and charge transfer (CT) excited state, E_{ge} .

Some of the methods being employed to improve the efficiency of organic NLO chromophores to achieve large microscopic nonlinearity include ring locking of the chromophore backbone, incorporation of donor/acceptor groups onto the conjugated interconnect, development of multi-chromophore macromolecular systems and inducing a very large twist angle between the donor and acceptor units in the chromophores. Some of the methods our group at Industrial Research Limited have employed to develop efficient chromophores whose macroscopic NLO properties have been investigated in this study are explained below. This section discusses the results from a systematic approach I have made to investigate the effects of structural alterations at the molecular level.

5.3.1 Effects of donor strength

Molecular nonlinearity of the chromophore is related to the donor-acceptor strength. By varying the strength of the donor and/or acceptor group the ground state polarization and the BLA value of a chromophore can be tuned. That is, the nature of the donor and acceptor is a key to determine the nonlinearity of a chromophore. Recent works carried out in our group [63, 81, 82, 79, 83, 84] and other research groups [1, 11, 12, 85], have reported a substantial change in hyperpolarisability by changing donor groups keeping the rest of the chromophore molecule the same. Structures of some of the chromophores synthesized in our team to investigate effects of donor strength are shown in Fig. 5.6. Effects of substituting different donor groups in a polyene chain containing same acceptor group on linear and nonlinear properties of chromophores are summarised in Table 5.1.

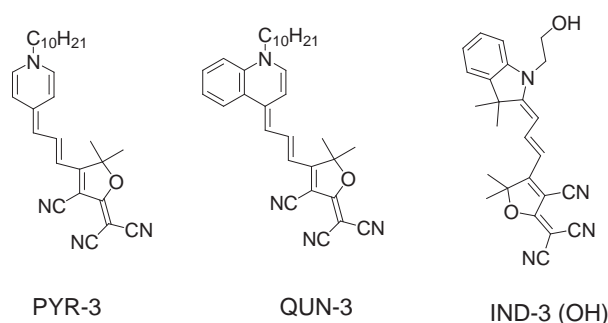


Figure 5.6 – Structures of the PYR-3, QUN-3 and IND-3 chromophores.

Table 5.1 – Effect of varying donor groups on the molecular NLO response of chromophores. β_{zzz} was measured at 1314 nm.

Structure	Chr.	Solvent	λ_{\max}	μ_{calc}	β_{zzz}	β_0
Ref.			nm	D	10^{-30} esu	10^{-30} esu
Fig. 5.6	PYR-3	CHCl_3	631	15.3	840 ± 70 [83]	470 ± 40
Fig. 5.6	QUN-3	CHCl_3	696	14.7	710 ± 30 [84]	400 ± 20
Fig. 5.6	IND-3	CHCl_3	602	8.7	820 ± 40 [79]	90 ± 5

5.3.2 Effects of conjugation length

For a chromophore with a given donor and acceptor, it has been reported that the hyperpolarisability is strongly related to the length of the conjugated π -bridge. Increasing conjugation length leads to an increase in both μ and β values of the chromophores and thereby enhances the figure of merit of the system. However, engineering the conjugation length require ensuring the modification does not adversely affect the properties of the chromophore such as optical and thermal stability as well as the solubility for device fabrication. An example for the change in the first hyperpolarisability by changing the donor group for a chromophore structure containing 3 conjugated π bridges and same acceptor group is shown in Table 5.1. Chromophore structures corresponding to the chromophore codes are given in Fig. 5.6. The length of conjugated π bridge is limited by reduced stability, reduced solubility and loosing planarity that eventually lead to a lower hyperpolarisability [1]. Also, the larger the separation between donor and acceptor the larger the dipole moment of the system which in turn leads to aggregation [86].

A set of chromophores having the same donor and acceptor but different conjugation lengths are shown in this section. A summary of the effects of changing

conjugation length is summarised in Table 5.2. This type of systematic study is useful to select the chromophores having a large microscopic NLO effect. In Table 5.2 the NLO effect increases when the conjugation length changes from 3 to 5. The enhancement of the NLO effect is not directly related to the conjugation length but it is decided by how the change in conjugation length alters BLA [79, 17].

Table 5.2 – Effect of conjugation length on the molecular NLO response of chromophores. β_{zzz} was measured at 1314 nm.

Structure Ref.	Chr.	Solvent	λ_{\max} nm	μ_{calc} D	β_{zzz} 10^{-30}esu	β_0 10^{-30}esu
Fig. 5.6	IND-3	CHCl_3	602	8.70	820 ± 40 [79]	90 ± 5
Fig. 5.10	IND-5	CHCl_3	698	11.13	1230 ± 120 [79]	130 ± 10
Fig. 5.11	IND-7	CHCl_3	794	11.26	960 ± 50 [79]	300 ± 20

5.3.3 Effects of ring-locking

Molecular nonlinearity of the chromophore is related to the BLA parameter and thus changing bond order is the ideal method to improve the molecular nonlinearity of a given pair of donor and acceptor. Ring-locking has been found to increase the rigidity and planarity of the chromophores [79]. Hyper-Rayleigh Scattering (HRS) measurements made on a series of chromophores showed an improvement of more than 50% in the first hyperpolarisability of in some cases [83]. It has been explained that the improvement is mostly by the bond length alternation via tuning the planarity of the chromophore molecule that leads to an efficient delocalisation of electrons [83, 79].

Table 5.3 – Effect of partial ring-locking at the conjugated π -bridge on the molecular NLO response IND-7 chromophore, β_{zzz} was measured at 1314 nm.

Structure Ref.	Chr.	Solvent	λ_{\max} (nm)	μ_{calc} (D)	β_{zzz} (10^{-30}esu)	β_0 (10^{-30}esu)
Fig. 5.11	IND-7	CHCl_3	794	11.26	950 ± 20 [79, 83]	290 ± 10
	IND-7R	CHCl_3	793	10.16	960 ± 50 [79, 83]	300 ± 20

In addition, for the chromophores explained in Table 5.3 a halogen atom (in this work Chlorine) was substituted in middle of the conjugated interconnect with a

variety of substitutes in order to assess the impact from both a steric and electronic point of view [79]. While extending the conjugation length between the donor and acceptor led to an increase in the first hyperpolarisability, configurational-locking of the polyene interconnect did not result in the expected enhancements to β . Though the enhancement in β was not as expected, the system is of interest to investigate if the modification leads to an enhancement in other properties of the system such as optical stability as discussed in Chapter 7.

5.3.4 Effects of bulky group substitution

Chromophores with highly polar (i.e. zwitterionic) ground states often exhibit poor solubilities as well as a tendency to readily form aggregates. This is clearly problematic when considering their use in NLO materials as this means they cannot be incorporated into host polymers at high chromophore loadings. Furthermore, the presence of significant aggregation will lower the overall poling efficiency of the final NLO material as well as increase the propensity for deleterious post-poling relaxation of the aligned dipoles. As a result, further structural modifications are often required to the active chromophores to minimize aggregation and the inclusion of bulky, “arene-rich” substitutes has been shown to be particularly effective in achieving this, thereby greatly increasing the observed macroscopic response in NLO materials [85].

Table 5.4 – Effect of bulky substitution on the molecular NLO response of PYR-3 chromophore, β_{zzz} was measured at 1314 nm.

Structure	Chr.	Solvent	λ_{\max}	μ_{calc}	β_{zzz}	β_0
Ref.			(nm)	(D)	(10^{-30} esu)	(10^{-30} esu)
Fig. 5.7	PYR-3	CHCl_3	631	15.3	840 ± 70 [83, 86]	470 ± 40
	PYR-3B	CHCl_3	634	15.3	1080 ± 40 [86]	570 ± 25

As the NLO compounds we have been developing will ultimately be used in polymer systems it is necessary to study their behaviour in environments similar to these. This is particularly important because the asymmetric distribution of electrons in a compound typically leads to intermolecular interactions between neighbouring molecules in both solution and/or the solid state. This phenomenon is very common in the cyanine and merocyanine dyes and is termed aggregation or

self-association. Aggregation of chromophores causes the shape of their UV spectra to deviate from normal and results in extra bands (or shoulders) appearing. The position of these shoulders will depend on the type of the aggregation present e.g. H (hypsochromic) or J (named after Jelly) aggregation [26]. This is a potential pitfall when considering their use in NLO materials as it means they may not be able to be incorporated into a host polymer at high loadings. Furthermore the presence of significant aggregation will also lower the overall poling efficiency of the final NLO material as well as increasing the propensity for relaxation of the aligned dipoles post-poling – this will result in a gradual decline over time of the observed macroscopic response.

The spacing caused by the bulky substituent can restrict inter-chromophore interactions as well as the relaxation of the chromophores after poling and thereby permits a larger chromophore loading leading to a large electro-optic coefficient and an enhanced thermal stability of polar order without compromising other key parameters. Addition of bulky groups does not necessarily change the magnitude of molecular NLO effect because the bulky group does not change the donor, acceptor or the length of conjugated π -bridge. However, addition of a bulky group plays two major roles in improving the electro-optic coefficient in macroscopic level. Microscopic linear and nonlinear optical properties of a zwitterionic chromophore PYR-3 and its derivative by substituting a hydrogenated bulky group (see Fig. 5.7) is shown in Table 5.4.

5.4 Effects of structural alternations at the macroscopic level

In this work we investigate how the structural alternations in the chromophore level have changed the properties of the system in macroscopic level. We are interested in investigating whether the structural alternations such as increasing the mixing of ground and charge transfer excited states via reducing the energy gap between these states, increasing the planarity of the system via annelation and ring locking, and addition of bulky substitutes for reduced aggregation have improved the overall efficiency of the chromophore in the device level. For the purpose of systematic analysis, the chromophore concentration in films, poling temperature and poling field were selected to be similar values.

5.4.1 Bulky substitution in PYR-3

Structures of the PYR-3 chromophore and the derivative PYR-3B synthesized by bulky group substitution are shown in Fig. 5.7. The absorption spectra of the films and solutions of PYR-3 and PYR-3B are shown in Fig. 5.8. PYR-3 has a shoulder for shorter wavelengths that can be attributed to H-aggregation [27, 26]. This is significantly reduced in the 8 wt.% PYR-3B/APC film, which is one of the beneficial effects of the bulky group. The thin films were poled using the contact plate electric field poling technique under an electric field of $100 \text{ V}/\mu\text{m}$ for 30 minutes. The measurements were done on thin films with different chromophore loading concentrations to find the highest r_{33} that can be achieved for a given chromophore. A reduction in r_{33} is expected to occur for high chromophore concentrations due to reduced spacing between the chromophores and inter-chromophore interactions. The maximum measured EO coefficient occurred for 10 wt.% PYR-3B loading and the value was $750 \text{ pm}/\text{V}$, which is ~ 25 times greater than that of LiNbO_3 .

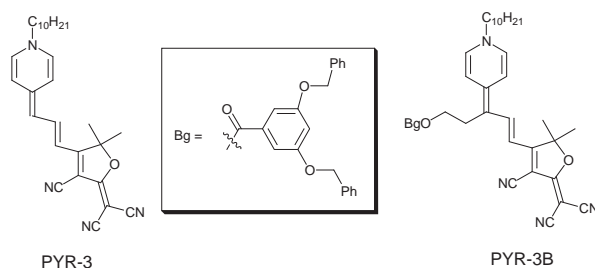


Figure 5.7 – Structure of PYR-3 chromophore and its bulky group derivative PYR-3B.

The temporal stability of r_{33} was measured after poling 8 wt.% PYR-3B/APC and 5 wt.% PYR-3/APC films with similar chromophore concentrations of $8.71 \times 10^{25} \text{ m}^{-3}$ and $8.62 \times 10^{25} \text{ m}^{-3}$, respectively. It can be seen in Fig. 5.9 that the r_{33} is lower and continues to decay in the 5 wt.% PYR-3/APC film even after 10 days while the 8 wt.% PYR-3B/APC film shows a significantly higher initial r_{33} and it reaches close to a stable value after 96 hours. The temporal decay in r_{33} can be characterised by a bi-exponential decay curve that was developed as a simple extension to the Debye model [74, 73] that has been found to provide reasonable fit to the data in guest host systems. In Fig. 5.9 we show fits to the data using,

$$r_{33}(t) = A_1 \exp(-t/\tau_1) + A_2 \exp(-t/\tau_2) \quad (5.28)$$

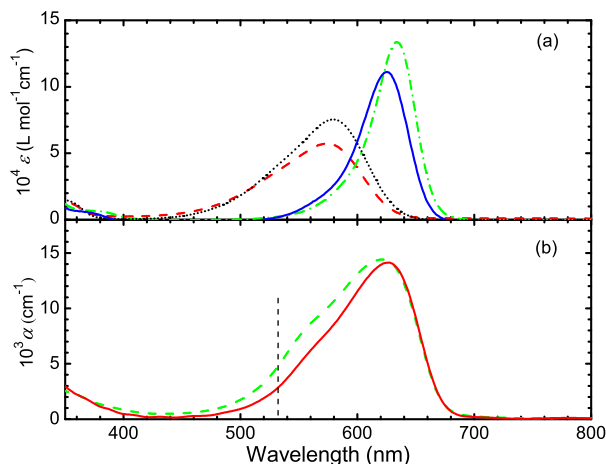


Figure 5.8 – (a) Plot of the molar extinction coefficient of PYR-3B in Methanol (red dashed curve), Chloroform (green dash-dotted curve), DMF (black dotted curve) and 1,1,2 Trichloroethane (blue solid curve). (b) Plot of the optical absorption coefficient of films made by mixing 8 wt.% PYR-3B (red solid curve) and 5 wt.% PYR-3 (green dashed curve) in APC.

where t is the time and we find that $A_1 = 107$ pm/V, $A_2 = 66$ pm/V, $\tau_1 = 90$ hrs, and $\tau_2 = 5000$ hrs for 5 wt.% PYR-3/APC and $A_1 = 220$ pm/V, $A_2 = 242$ pm/V, $\tau_1 = 30$ hrs and $\tau_2 = 15000$ hrs for the 5 wt.% PYR-3/APC film. Results show that the bulky substitution has led to a substantial enhancement in the stability of the induced EO effect. A promising result from bulky substitution has motivated further enhancement of the stability of the EO effect by adding mixed bulky groups. A systematic effect of bulky substitution in a different chromophore is given in Section 5.4.2.

5.4.2 Bulky substitution in IND-5

In this work the enhancement of temporal stability of the chromophores as a result of bulky group substitution is investigated. Structures of the IND-5 chromophore and its bulky group derivatives are shown in Fig. 5.10. IND-5 has five conjugated π -bridges connecting the donor and acceptor. The electron donor is the indolene group where in PYR-3 the donor was a pyridene group. In terms of the electronic charge transfer mechanism, IND-5 is a neutral chromophore falling in (left hand side) LHS of the BLA axis. The maximum electro-optic coefficient found on a poled polymer film containing 5 wt% IND-5 in APC was 206 pm/V at 1314 nm when measured immediately after poling under an electric field of 60 V/ μ m [63]. Comparison of the

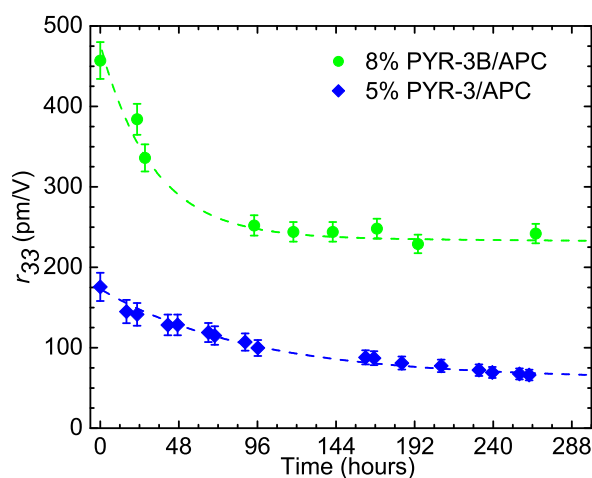


Figure 5.9 – Plot of the measured r_{33} of a $1.92 \mu\text{m}$ thick, 8 wt.% PYR-3B/APC film against time (green solid circles) and a bi-exponential fit to the data (green dashed line). Also shown is the r_{33} of a $2.1 \mu\text{m}$ thick, 5 wt.% PYR-3/APC film as a function of time (blue solid diamonds) and a bi-exponential fit to the data (blue dashed curve).

initial value and the values measured after 48 hrs, which is a reasonable time to observe the decay of EO coefficient in a host-guest system, are given in Table 5.5.

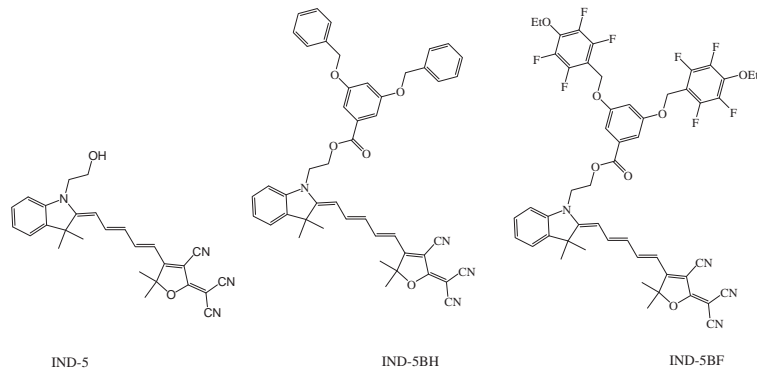


Figure 5.10 – Structures of the IND-5 chromophore and its bulky group derivatives.

5.4.2.1 Hydrogenated bulky group

In this work, the effects the addition of the bulky substitute with an LHS chromophore IND-5 is investigated. Results are similar to what is observed in the RHS chromophore, PYR-3 by the addition of bulky substituents. Decay profile have been investigated for 48 hours and the results are compared with that of IND-5. A large electro-optic coefficient compared to that without bulky substituent and improved temporal stability can be attributed to the initial fast decay in IND-5 system without

bulky substitutes. This is similar to the results observed in the PYR-3 system.

5.4.2.2 Fluorinated bulky group

The IND-5BF chromophore is analogous to the investigation made using hydrogenated bulky groups on polymers which have fluorine in place of hydrogen in the bulky substitute as shown in Fig. 5.10. Thin films of thickness about 3 microns have been prepared by mixing chromophores with a similar number density as that of IND-5BH. Films are poled under the same experimental conditions and measurements are done at equal intervals of time. The decay profile has been investigated for 48 hours and the results are compared with that of IND-5BH. The resulting decay profile is similar to that found in IND-5BH.

5.4.2.3 Mixed bulky groups

Identical results on systems with both types of bulky substituents are promising because the interaction between the fluorine and hydrogen atoms function to reduce the aggregation in poled system. The interactions between fluorine and hydrogen can support the parallel alignment of chromophore dipoles rather than undesired anti-parallel H-aggregate. Films have been prepared by mixing equal proportions of IND-5BH and IND-5BF and poled under similar condition followed for the system with individual bulky substitutions. The results are summarised in Table 5.5. The decay profile shows a substantial enhancement of the temporal stability of the r_{33} of the poled system.

Table 5.5 – Effect of bulky substitution on the macroscopic EO response of IND-5. Values of wt.%, poling field and poling temperature are approximate. IND-5 MIX is made of mixing equal fraction of IND-5BH and IND-5BF in APC.

Ch. code	wt% in APC	E_p (V/ μ m)	T_p °C	r_{33} (0 hrs) pm/V	r_{33} (48 hrs) pm/V	Percentage Loss (%)
IND-5	5	60	175	216	43	80%
IND-5BH	5	60	175	352	293	17%
IND-5BF	5	60	175	360	304	16%
IND-5 (MIX)	(2.5+2.5)	60	175	360	342	5%

5.4.3 Ring-locking of QUN-7 and IND-7

The films were prepared with similar chromophore loading using the chromophores with ring-opened and ring-locked chromophores shown in Fig. 5.11. It has already been reported [79] that there has not been any notable enhancement in the molecular NLO properties as a result of ring-locking in the chromophores investigated. The results from the measurement of the r_{33} of the system after poling the sample at similar conditions are summarized in Table 5.6. Results show that the structural alteration does not lead to the enhancement EO effect in the macroscopic level.

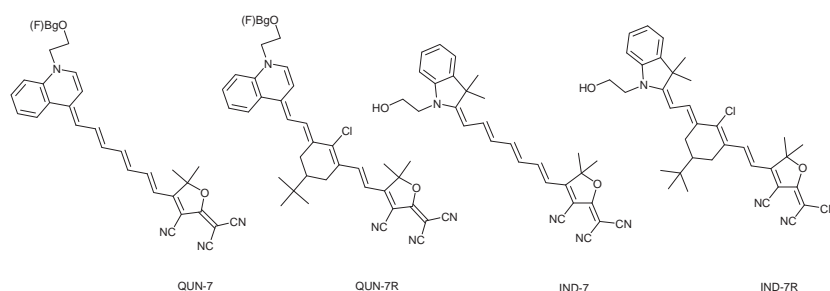


Figure 5.11 – Structures of the QUN-7 and IND-7 chromophores and their ring-locked structures QUN-7R and IND-7R.

Table 5.6 – Effects of ring-locking on the EO coefficient of IND-7 and QUN-7 chromophores.

Chromophore code	wt.% in APC	E_p (V/ μ m)	T_p ($^{\circ}$ C)	r_{33} (pm/V)
IND-7	5	\sim 60	\sim 170	\sim 640
IND-7R	5	\sim 60	\sim 175	\sim 217
QUN-7	5	\sim 63	\sim 175	\sim 315
QUN-7R	5	\sim 63	\sim 175	\sim 257

5.5 Theoretical calculation of r_{33}

A semi-empirical calculation was performed within our group to estimate the expected EO coefficient due to the contribution from the constituent chromophores. A summary of this calculation discussed in Ref. [50] is summarised in this section. The parameters used for the calculation are the first hyperpolarisability and dipole moment of the chromophore, chromophore concentration in the polymer, physical properties of the polymer and the poling conditions. It is useful to understand if the values measured are purely due to the molecular NLO effect of individual

chromophores.

EO coefficients of poled polymers from the hyperpolarisability, β , are calculated as follows: The relationship between the second order susceptibility $\chi^{(2)}$ and the EO coefficient r_{33} is given by the equation:

$$r_{33} = \frac{2}{n^4} \chi_{333}^{(2)}(-\omega; 0, \omega) \quad (5.29)$$

where $\chi_{333}^{(2)}$ is related to the microscopic molecular first hyperpolarisability β given as [55],

$$\chi_{333}^{(2)} = N \beta_{zzz} f_0 f_\omega^2 \langle \cos^3 \theta \rangle \quad (5.30)$$

where ω is the frequency at which the electro-optic coefficient is measured, n is the refractive index of the material at the electro-optic coefficient measurement wavelength, N is the number density of chromophores in APC. $\langle \cos^3 \theta \rangle$ corresponds to the weighted average of the angle between the direction of poling field and the chromophores dipole moment. $\langle \cos^3 \theta \rangle$ can be estimated using the 3rd order Langevin function $L_3(u)$, using:

$$L_3(u) = (1 + 6/u^2) \coth u - 3/u (1 + 2/u^2). \quad (5.31)$$

where $u = \mu_g f'_0 E_p / k_B T_p$. Then, Eq. 5.30 becomes [55, 56]:

$$\chi_{333}^{(2)} = N \beta_{zzz} f_0 f_\omega^2 L_3 \left(\frac{\mu_g f'_0 E_p}{k_B T_p} \right) \quad (5.32)$$

Combining Eqs. 5.32 and 5.29 will give:

$$r_{33} = \frac{2}{n^4} N \beta_{zzz} f_0 f_\omega^2 L_3 \left(\frac{\mu_g f'_0 E_p}{k_B T} \right) \quad (5.33)$$

The quantities f_0 , f_ω and f'_0 are local field factors which relate the externally applied electric field E_p to the internal field local to the molecule, μ_g is the molecule's ground-state dipole moment, E_p is the poling field, k_B is Boltzmann's constant and T_p is the poling temperature. For small values of u , that is $u \lesssim 1$, L_3 can be approximated as $L_3(u) \approx u/5$.

First hyperpolarisability dispersion

The value of β obtained from second-harmonic generation experiment is of second harmonic generation at optical frequency ω_{SHG} $\beta(-2\omega_{\text{SHG}}, \omega_{\text{SHG}}, \omega_{\text{SHG}})$, which need to be converted to the β_{EO} of the EO effect $\beta(-\omega_{\text{EO}}, 0, \omega_{\text{EO}})$ at the electro-optic coefficient measurement frequency ω to calculate r_{33} . One needs to estimate $\beta(-\omega_{\text{EO}}, 0, \omega_{\text{EO}})$ which is typically done by using dispersion equations derived from the two-level model [2, 50],

$$\beta_{\text{EO}} = \frac{(3 - \bar{\lambda}_{\text{EO}}^2)(1 - 4\bar{\lambda}_{\text{SHG}}^2)(1 - \bar{\lambda}_{\text{SHG}}^2)}{3(1 - \bar{\lambda}_{\text{SHG}}^2)^2} \beta_{\text{SHG}} \quad (5.34)$$

where $\bar{\lambda}_{\text{EO}} = (\lambda_{\text{max}}/\lambda_{\text{EO}})$ and $\bar{\lambda}_{\text{SHG}} = (\lambda_{\text{max}}/\lambda_{\text{SHG}})$, λ_{max} is the absorption maxima for resonant absorption, this can be estimated from the absorption spectra of the film, and λ_{EO} and λ_{SHG} are the wavelengths used for the electro-optical and second harmonic generation experiments respectively.

Local field factors

The approximate values of the local field factors for the films under consideration are [56, 55],

$$f_0 = \frac{\epsilon_r(n^2 + 2)}{n^2 + 2\epsilon_r} \quad (5.35)$$

and

$$f_\omega = (n^2 + 2)/3. \quad (5.36)$$

where ϵ_r is the relative static dielectric constant of the material and n is the refractive index at the measurement wavelength. f'_0 is same as f_0 but it corresponds to the ϵ_r at the poling temperature. In general f'_0 is taken as equal to f_0 but this make sense only for the polymers whose ϵ_r does not change substantially when going from room temperature to the poling temperature.

5.5.1 Translating microscopic quantities to r_{33}

The electro-optic coefficient r_{33} is generally quoted in S.I. units as pm/V while β in esu (cm^5/Fr , cm^5/esu , $\text{cm}^4/\text{statvolt}$ or simply esu), N in cm^{-3} , E_p in $\text{V}/\mu\text{m}$, μ_g in Debye (10^{-18} esu cm, statvolt cm^2 or esu) and T in $^\circ\text{C}$. To estimate r_{33} using Eq. 5.33 all the quantities need to be converted to a a single unit system. For convenience all

quantities are converted to the SI system in which r_{33} is generally quoted. Table 5.7 contains details of translating all quantities used in this calculation to SI system. The quantities n , ϵ_r , f_0 , f_ω , L_3 are dimensionless.

5.5.2 Calculation of r_{33} for a PYR-3/APC system

An example to calculate r_{33} from β for the chromophore, PYR-3, that has been investigated in great detail within our research group. The physical properties of PYR-3 are listed in Table 5.8.

Table 5.7 – Physical quantities used in the calculation of r_{33} in electrostatic and SI units (Reproduced from Ref. [50]).

Physical property	Quantity	Value in esu	Value in SI
β	1 cm ⁵ esu ⁻¹	1 cm ⁵ esu ⁻¹	4.19×10^{-10} m ⁴ V ⁻¹
μ_g	1 Debye	10^{-18} esu cm	3.336×10^{-30} C m
T_p	175 °C	-	473 K
E_p	75 V μ m ⁻¹	-	75×10^6 V m ⁻¹
k_B	-	-	1.3807×10^{-23} J K ⁻¹

Table 5.8 – Physical properties of the PYR-3 chromophore used in the calculation of r_{33} .

Property	Molar mass g mol ⁻¹	n_{1300}	λ_{\max} nm	μ esu cm	β_{SHG} (cm ⁵ esu ⁻¹)	T_d °C
Value	442.6	1.56	605	15.3×10^{-18}	840×10^{-30}	290

At 5 wt.% loading, the number density calculated as explained in chapter 4. which gives $N \approx 8 \times 10^{19}/\text{cm}^3$. Eqs. 5.35 and 5.36 will give $f_0 \approx 1.57$, $f_\omega \approx 1.48$, we have assumed $f_0 \approx f'_0$ in this calculation and thus $f_0 f_\omega^2 \approx 3.44$. For the EO effect measured at the wavelength of $\lambda_{\text{EO}} = 1310$ nm, $\bar{\lambda}_{\text{EO}} = 605 \text{ nm}/1310 \text{ nm}$ and $\bar{\lambda}_{\text{SHG}} = 605 \text{ nm}/800 \text{ nm}$ giving $\bar{\lambda}_{\text{EO}} \approx 0.4618$ and $\bar{\lambda}_{\text{SHG}} \approx 0.7562$. On substitution into Eq. 5.34 gives,

$$\beta_{\text{EO},1310} = 695 \pm 60 \times 10^{-30} \text{ cm}^5 \text{ esu}^{-1} \quad (5.37)$$

Substituting for N , $\beta_{\text{EO},1310}$ and $f_0 f_\omega^2$ in Eq. 5.33 and setting, $L_3 = 1$ to calculate the theoretical maximum r_{33} , we obtain the maximum r_{33} which may be expected

from the PYR-3 chromophore is [50],

$$r_{33,1310} = 27 \pm 2 \text{ pm/V} \quad (5.38)$$

The value shown in Eq. 5.38 is the maximum r_{33} that can be achieved in the ideal case. That is for 100% poling, which is not possible in a real case. A more realistic value of r_{33} can be calculated by considering the poling temperature and field used in our experiments. Then the argument to the Langevin function $L_3(u)$ is,

$$u = \frac{\mu_g f'_0 E_p}{k_B T_p}$$

where $\mu_g = (15.3 \text{ Debye}) = 51.0 \times 10^{-30} \text{ C m}$, in the absence of a measurement at the poling temperature we take $f'_0 \approx f_0 = 1.58$, and for poling fields $E_p \approx 75 \times 10^6 \text{ V/m}$ from Table 5.8, $(\mu_g f'_0 E_p) = 6.04 \times 10^{-21} \text{ J}$. For poling temperatures $T_p \sim 448 \text{ K}$, from Table 5.8 $k_B T_p = 6.19 \times 10^{-21} \text{ J}$, which gives $u = 0.98$, $L_3(0.98) = 0.187$ and thus a maximum expected r_{33} under the quoted experimental conditions is [50],

$$r_{33, 1310} = 5.1 \pm 0.4 \text{ pm/V}$$

This is about 3% of the experimentally measured value of 5 wt.% PYR-3/APC film shown in Fig. 5.5. This demands a detailed analysis to investigate the source of such a large discrepancy between the measured and theoretical estimate of r_{33} .

5.5.3 Mismatch between experiment and calculation

Observed electro-optic coefficients in poled polymers are up to two magnitudes larger compared to the theoretical estimation, using the values of first hyperpolarisability. This shows that the r_{33} of the chromophores measured using the Teng-Man modulation ellipsometry apparatus described in this chapter did not match the expected values calculated. For example, PYR-3/APC system described above has an r_{33} of $\sim 175 \text{ pm/V}$ when the maximum expected value of r_{33} for the same experimental conditions when calculated theoretically is $\sim 5 \text{ pm/V}$.

This discrepancy is much larger than the limit of the experimental error. Also, this type of over expectation in experiment is not unexpected because the r_{33} calculated from the hyperpolarisability is a pure electronic component due to the contribution from individual dipoles. However the measured r_{33} at low frequencies contains

contributions from many other factors in addition the electronic contribution [87, 2]. However in organic materials it is believed that non electronic contributions are relatively low compared to inorganic single crystals [87].

5.6 Analysis of the mismatch between experimental and calculated r_{33}

Presence of contributions from non electronic origin can be investigated from the response of the measured r_{33} with the modulating frequency. This is possible because only the contribution from the pure electronic origin retains the activity at high frequencies. A systematic analysis is performed that involves, analysing the dispersion of the r_{33} with the modulating frequency that is a direct test to understand if the large values are of purely of electronic origin (which is frequency independent). Other effects that are common in crystals such as the effect from acoustic and optical phonons as well as the inverse piezoelectric effect are also discussed in subsequent sections.

5.6.1 Frequency response of r_{33}

The r_{33} was measured using Teng-Man apparatus for a frequency range of 100 Hz to 100 kHz. Fig. 5.12 shows that the measured r_{33} decreases with increasing frequency. One can see that the estimated r_{33} using modulation ellipsometry undergoes a rapid reduction after 2.5 kHz. The value of r_{33} does not change significantly between 100 Hz and 2 kHz, this value is approximately 60 times larger than the value observed at 100 kHz. A similar roll-over of r_{33} with frequency was reported in Ref. [88]. The average low value of r_{33} (~ 2 pm/V) observed above 10 kHz is in agreement with the theoretically estimated value. Highest theoretical estimate of r_{33} for this system from individual chromophore contribution is about 5.1 pm/V [50].

An unexpected resonance in the measured data above a modulating frequency of 10 kHz was observed as shown in Fig. 5.12. As far as we are aware, a detailed explanation for the resonance behaviour of r_{33} measured using modulation ellipsometry are not available for polymers. This is particularly due to the fact that fewer studies have been performed to estimate r_{33} above 10 kHz. A large EO response at low modulating frequency can be attributed to the fact that r_{33} measured from modulation technique is due to the collective response of a number of polarisation mechanisms

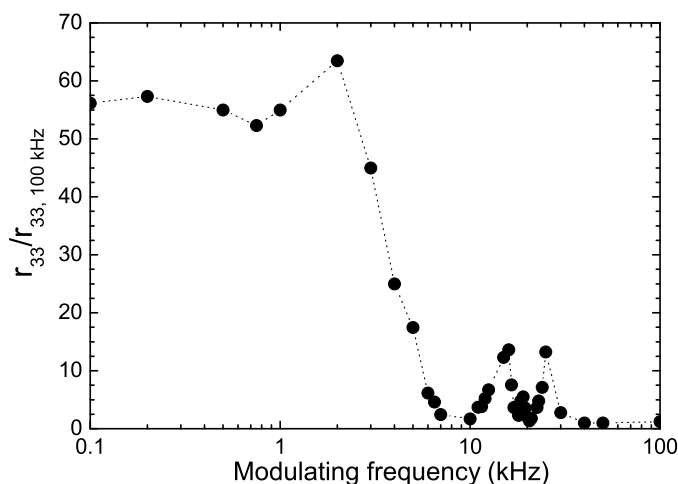


Figure 5.12 – Dependence of the EO coefficient on the modulation frequency measured at $\lambda = 1314 \text{ nm}$ for a $4 \mu\text{m}$ film made of 5 wt% PYR-3/APC.

contributing to the EO effect [87]. It is reported that this effect is reported very strong in EO crystals [89].

In the case of chromophores in a host-guest system, three major polarisation mechanisms have been reported that are contributing to the EO effect [87, 88], they are, (a) Orientational polarisation caused by the self alignment of chromophore dipoles under the influence of an external field, (b) Ionic and or atomic polarisation caused by electric field induced shift in the charged ions and (c) Electronic polarisation due to the distortion in the negatively charged electron cloud with respect to the nucleus. At low frequency, all the above polarisation mechanisms contribute to the EO effect. However, orientational and ionic polarisations are present only at lower frequencies and gradually disappear with increasing the modulation frequency. In EO crystals it has been explained that a number of processes contribute to the total EO effect. In particular, if the crystal is piezoelectric, the contributions are different when the frequency of the applied electric field is below or above the acoustic resonances of the system. Below these piezo-resonances, the crystal is free to deform, and the variation of the strain follows the applied electric field on the basis of the inverse piezoelectric effect. Subsequently, the corresponding birefringence change via the elasto-optic effect leads to an indirect contribution to the EO coefficient measured at constant stress [87]. If the frequency of the applied electric field is well above the frequencies of the acoustic resonances, the crystal is unable to deform itself and is thus virtually clamped, so that the EO coefficient, corresponding

to the direct EO effect, is measured at constant strain.

The resonance frequency observed in Fig. 5.12 is also present in the reports from the experimental investigations on chromophores as well as on nano-composites [88]. However, the resonance has not been analysed. In this work we investigate possible ways leading to a large r_{33} observed in our experimental studies based on different aspects of the possible ways of observing large EO coefficients at low frequencies. That includes the phenomena generally present in organic crystals [2, 87, 89], cluster formation in organic chromophores [88] and recent findings on possibility of enhanced EO effect due to the interaction between the chromophores leading to covalent or hydrogen bonding [90]. Other possible mechanical effects such as inverse piezoelectric effect as well as the transverse grating formation related to the acoustic velocity in the polymer are discussed.

5.6.2 Contribution from acoustic and optical phonons

Optical and acoustic phonons can contribute largely to the EO effect in crystals [2]. This contribution dominates the pure electronic contribution in some inorganic EO crystals such as LiNbO_3 [5, 7, 6]. The EO coefficient in crystals is a collective response of the contributions of electronic origin (r^e), optical contribution (r^o) and acoustic contribution (r^a) [89, 2]. That is,

$$r = r_e + r_o + r_a \quad (5.39)$$

In certain EO crystals the contributions from optical and acoustic phonons due to their crystalline nature contribute to the EO effect. At low frequencies these contributions are much larger than the pure electronic contribution.

The contribution from the acoustic and optical part can be explained by considering the field induced change in the optical dielectric constant ϵ_{ij} , that is [2, 91]:

$$d'_{ijk} = \frac{1}{4} \frac{d\epsilon_{ij}}{dE_k} \quad (5.40)$$

where $d_{ijk} = \chi_{ijk}^{(2)}$. Eq. 5.40 contributes to the optical and acoustic vibrational modes such as Raman and Brillouin scattering processes [89, 87]. The properties that determine the optical dielectric constant are the long wavelength optical mode displacement Q^n , elastic constant u_{lm} and the applied electric field E_k . In linear approximation [91] the Eq. 5.40 can be expanded as:

$$4d'_{ijk} = \left. \frac{d\epsilon_{ij}}{dE_k} \right|_{Q=u=0} + \sum_n \frac{d\epsilon_{ij}}{dQ^n} \frac{dQ^n}{dE_k} + \frac{d\epsilon_{ij}}{du_{lm}} \frac{du_{lm}}{dE_k} \quad (5.41)$$

This can be written in another form as:

$$4d'_{ijk} = 4d_{ijk}^{\text{EO}} + \sum_n \rho_{ij}^n \frac{\Delta_n \chi_{lk}}{e_l^n} + \rho_{ijlm}^* a_{lmk} \quad (5.42)$$

where ρ_{ij} is the Raman tensor that is non-zero only for Q^n is polar mode, e_l^n is the effective charge, $\Delta_n \chi_{lk}$ is the n^{th} mode contribution to the static susceptibility, ρ_{ijlm}^* corresponds to the photoelastic tensor and a_{lmk} is the piezoelectric tensor [2].

The first term of the Eq. 5.42 is purely electronic in origin, the second term corresponds to the optical mode that is non-vanishing only if the vibrational modes are both IR and Raman active and the third term is due to the photo-elastic effect. The photo-elastic effect can be caused by the elastic strain due to the inverse piezoelectric effect under an applied electric field. The acoustic contribution is due to this elasto-optic effect due to the strain caused by the electric field given by, $s_{jk} = a_{ijk} E_i$ [89]. The case of NLO chromophores is different from that of EO crystals because of their amorphous nature. However, the optical phonon contribution is possible in the push-pull molecules because they are simultaneously Raman and IR active [92]. NLO chromophores are push-pull molecules and simultaneous Raman and IR activity is reported as the nature of NLO chromophores [92]. This shows that the second term in Eq. 5.42 also is possible in the case of NLO chromophores. That is, the first two terms can potentially be due to the individual chromophore effect, with the contribution from electronic origin retaining its activity at higher frequencies while the second term is active only in the low frequency range. The third component of Eq. 5.42 is discussed in Section 5.6.3.

Crystallisation of a fraction of or all of the chromophores or the polymer itself at poling temperature can potentially show similar effects observed in EO crystals. Though the non-electronic contributions, in general, do not exceed the pure electronic contribution in the organic EO crystals such as DAST [2]. Crystallisation of the chromophore or polymer while drying or poling may possibly lead to such undesired effects. It is because the contribution from those effects disappears at high frequencies, in addition to the formation of crystals lead to crystalline phonon absorption, for example, in the THz frequencies. Crystallinity of the films was tested by performing small angle X-ray scattering on the films coated on plain glass and

ITO coated slides [93]. XRD analysis on film containing 5 wt.% PYR-3/APC on plain glass and ITO coated glass are shown in Fig. 5.13. The data show no signs of crystals.

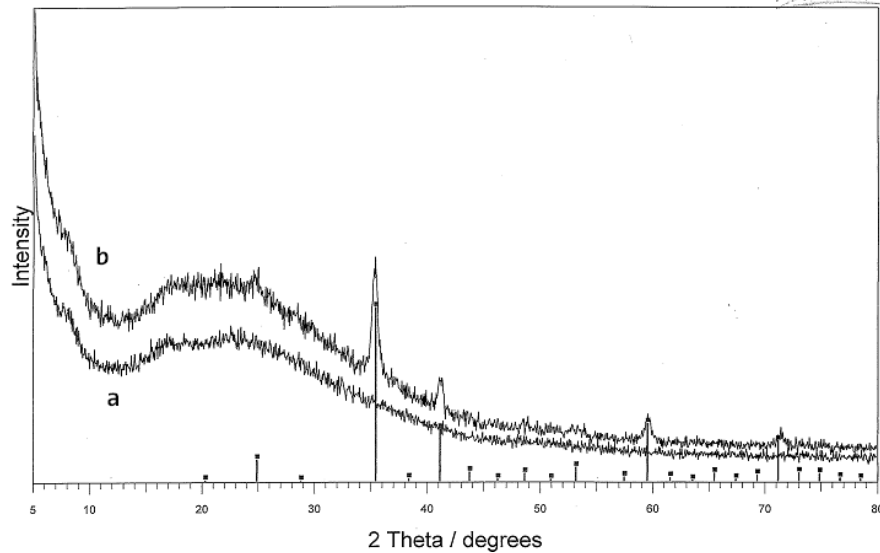


Figure 5.13 – Small angle XRD data of a 5 wt.% PYR-3/APC film on (a) glass and (b) ITO coated glass substrate (From Ref. [93]). XRD data does not show signs of crystals. The lines observed in (b) are from the ITO layer on the glass substrate.

5.6.3 Contribution from piezoelectric effect

This is the contribution from the third component of Eq. 5.42. If the material is piezoelectric, the contributions are different when the frequency of the applied electric field is below or above the acoustic resonances of the material. Below these piezo-resonances, the material is free to deform, and the variation of the strain follows the applied electric field on the basis of the inverse piezoelectric effect. Subsequently, the corresponding birefringence change via the elasto-optic effect leads to an indirect contribution to the EO coefficient measured at constant stress. Analysis of the measured data and a brief outline of the investigation of the other effects contributing the macroscopic electro-optic effect is discussed in the following Section.

The piezoelectric effect can mimic the EO effect via field induced phase variation through the inverse piezoelectric effect or via strain induced change in refractive index of the material [94, 87]. The linear EO effect is closely related to the inverse piezoelectric effect where application of an electric field to a non-centrosymmetric material leads to an actual change in materials shape. This additional contribution

to the change in index coefficients is given by [89, 2],

$$\Delta \left(\frac{1}{n} \right)_{kl}^2 = p_{ijkl} S_{ij} \quad (5.43)$$

$$S_{ij} = \Sigma a_{ijk} E_k \quad (5.44)$$

where S_{ij} is the strain tensor, p_{ijk} is the piezoelectric tensor and E is the applied electric field. This is analogous to the change in refractive index of the material due to the EO effect and cannot generally be differentiated from the purely electronic components of EO effect of the system due to the embedded chromophores.

An applied field can piezoelectrically change the thickness of the film as a function of the applied field. This can appear as the electro-optic effect while measuring the electro-optic coefficient via modulation ellipsometry technique. The relation between the change in the thickness of the film by an applied electric field due to the piezoelectric effect can be expressed using the equation [95, 96],

$$\Delta L_j = \Sigma a_{ij} E_j L_j \quad (5.45)$$

where L is the film thickness, a_{ij} is the piezoelectric tensor component and E is the applied field. The change in phase $\Delta\phi$ for the beam passes through the material due to this thickness change can be estimated by using the formula,

$$\Delta\phi = (2\pi/\lambda)\Delta(nL) \quad (5.46)$$

Either of these effects can contribute heavily to the induced phase by an applied modulating frequency. However these effects are present only at low modulating frequency and tend to saturate at high frequencies. This is because at high frequencies the inertia of the material prevents it straining macroscopically, so the contribution of this effect diminishes to zero [89, 95]. The observed effect from experiment shows the measured r_{33} reduce with modulation frequency as shown in Section 5.6.1. In this case, the change in phase as a function of applied field is additional to the actual change in the phase due to the EO effect [89, 95]. Although this phenomena can possibly explain the drop in EO effect with frequency, the resonance observed in the EO response of the film with frequency cannot be attributed to this effect. Section 5.6.4 discusses how the acoustic velocity in the polymer host can contribute to this phenomena.

5.6.4 Effects of acoustic velocity in the host polymer

The resonance behaviour of the measured EO coefficient measured using the Teng-Man ellipsometry is an issue that needs to be addressed. Tests have been made to investigate if the acoustic velocity of the modulating field in polymer can contribute to the resonance. This effect can create a transverse grating within the system depending on the modulating frequency. Eventually this grating can modulate the beam passing through the polymer and possibly mimic the EO effect. However, for this effect the thickness of the film need to be in the range of the acoustic wavelength in the polymer.

The reported values of the acoustic velocity in polymers ranges from 1000 - 4000 m/s [97]. This gives an acoustic wavelength in the range of 1 m to 4 m for 1 kHz. The acoustic wavelength drops down to the range of 10 mm to 40 mm for 100 kHz. That is, the acoustic wavelength is too large to create any transverse grating and/or resonance effect leading to the resonance behaviour or a large EO effect at low frequencies.

5.6.5 Contribution from the formation of chromophore clusters

Cluster formation is the process of two or more chromophore joining together. The formation of molecular clusters in a structure favouring the charge transfer is reported resulting in a strong enhancement of NLO response of the chromophores [90, 98, 99]. Intermolecular hydrogen bonding [90] or covalent bonding [98] can lead to the formation of molecular clusters. Contributions from clusters is different from the case that individual chromophores contribute to the macroscopic EO effect. That results in a significant enhancement in the first hyperpolarisability which is expected to follow a quadratic dependence with the number of monomers involved in the cluster formation [90, 88].

Balakina *et al.* [90] reported an enhancement of β up to 5 times in a linear cluster of 3 molecules formed by hydrogen bonding. This is reasonable from the theoretical expectation from the two level model of first hyperpolarisability that $\beta \propto \mu_{ge}^2$ [17, 2]. A detailed analysis of cluster formation via covalent bonding has been reported in Ref. [98]. A number of different types of cluster formation are discussed leading to a number of effects due to cluster formation.

The chromophores we have investigated have a large dipole moment [84] which in turn is possible to form clusters involving 2 or more chromophores. From the

research on similar system as discussed in Ref. [90] have found the hydrogen bonded dimers and higher order molecular structures have high first hyperpolarisability compared to the monomer units. Okuno *et al.* [98] reported the possibility of up to 2-5 times larger hyperpolarisability in covalently bonded dimers of dendrimers compared to monomer units. In effect there is a quadratic relationship between the enhancement of the hyperpolarisability and the number of chromophores involving in cluster formation. By considering Ref. [90] we can see that if three chromophores involved in forming a cluster, the effective NLO response is not 3β but 5β . That is the effective macroscopic NLO effect could be much larger than expected from the individual contribution by the constituent molecules. This is similar to the effect reported in Ref. [88] where the high EO coefficient observed at low frequencies drops at higher frequencies. The low frequency effect can be attributed to the permanent dipole moment of the clusters while the high frequency response originates from the individual chromophores. The large EO effect due to chromophore clusters cannot be used for high frequency applications because of the slow response of chromophore clusters to an applied field [88].

5.7 Conclusions

Experiments were performed on a range of chromophores to estimate their EO coefficients in polymers. Structural modifications have been demonstrated that lead to a large and stable EO effect in EO polymers. One of the key findings is the effect of the addition of a bulky group with chromophores, leading to a large enhancement of the macroscopic EO response relative to those that are not substituted with a bulky group. Both the value and temporal stability of the EO coefficient have been improved with a bulky substitution. This is achieved without comprising the NLO property of the chromophore molecule but by reducing the aggregation. Further to that, chromophores comprising of mixed bulky groups have performed even better because of the interaction between hydrogenated and fluorinated bulky groups that reduces the mobility as well as H-aggregation of the chromophores.

There is a mismatch between the measured value of EO coefficient at 1 kHz and the theoretically calculated values from the first hyperpolarisability. This effect was discussed based on the contribution from effects other than individual NLO response of chromophores. A similar divergence from theory has been observed in IND-5 by other groups [100] when the second harmonic generation coefficient, d_{33}

was estimated using the second harmonic generation method, and is in agreement with the values we have estimated for same chromophore but both diverge from the theoretically calculated value.

The high EO coefficient measured at low frequencies (below 10 kHz) is promising for applications such as modulators and switching circuits at this frequency range. However, the low values at high frequencies limit their use in high frequency applications for example THz generation and detection. The Teng-Man modulation ellipsometry method is particularly simple to evaluate poled polymers, however, it was not designed to measure the zero frequency value for the EO coefficient. There is a need for the development a method that can estimate the value of EO coefficient with a non oscillating field to get a complete profile of the frequency dependence of the EO coefficient. To contribute towards this, we have developed a new method to estimate the static component of EO coefficient of the poled polymers using a diffraction technique that is discussed in Chapter 6.

Chapter 6

Measurement of r_{33} Using Diffraction Method

The Teng-Man ellipsometry technique discussed in Chapter 5 has been demonstrated to over-estimate the electro-optic (EO) coefficient (r_{33}) of poled polymers. This is a major problem that needs to be addressed in order to estimate the EO coefficient purely due to the constituent chromophores embedded in the polymer matrix. The Teng-Man ellipsometry technique is driven by a modulating AC field and the EO coefficient estimated using this technique varies with the modulating frequency if the EO coefficient contains contributions from frequency dependent factors. This is undesired because, ideally, EO coefficient is expected to be independent of modulating frequency if it is purely of electronic in origin.

This chapter introduces a new technique to estimate the EO coefficient of organic NLO polymer films using the electric field dependent diffraction efficiency of diffraction gratings made on thin films. This technique does not require a modulating AC field and thus provides an estimate of the static EO coefficient. This is a particularly useful method to filter out the possible over-estimation of the EO coefficient due to non-electronic contributions such as the cavity resonance [101] and multiple reflection effects [102, 70]. The theory is derived and tested using AC and DC modulating fields and the limitations of this technique are discussed. The contribution of inverse piezoelectric effect and multiple interference effect to the diffraction efficiency are also discussed.

6.1 Diffraction gratings

Diffraction grating can be explained in general as an optical component with a periodic structure, which diffracts light into several beams travelling in different directions. Gratings are commonly used for deflection, coupling, modulation or filtering of optical beams to use in a range of applications such as monochromator[43], multiplexing[103], sensors[104] and holographic memory[105].

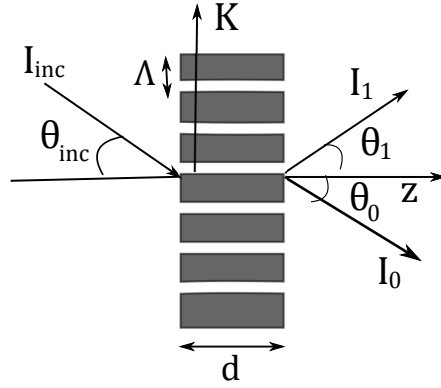


Figure 6.1 – The geometry of a thick periodic grating; I_{inc} is the incident wave, \mathbf{K} is the grating vector, Λ is the grating period, I_0 is the zeroth order beam, I_1 is the first order diffracted beam, d is the thickness of grating and θ is the angle corresponding to each beams.

A grating is characterised by the grating vector \mathbf{K} and period $\Lambda = 2\pi/\mathbf{K}$. The schematic and the geometry of a diffraction grating is shown in Fig. 6.1. The grating period, Λ of an ideal grating has to be wider than the wavelength, λ of interest to cause diffraction. Λ is related to the wavelength, λ of the beam subject to diffraction through $\Lambda = \lambda/(n \sin \vartheta)$, where n is the average refractive index of the grating and ϑ is the angle between the diffracted beam and the normal vector. When a plane wave of wavelength λ interacts with the grating, the diffracted light is composed of the sum of interfering wave components emanating from each slit in the grating. At any given point in space through which diffracted light may pass, the path length to each slit in the grating will vary. Since the path length varies, generally, so will the phases of the waves at that point from each of the slits, and thus will add or subtract from one another to create peaks and valleys, through the phenomenon of additive and destructive interference. The maxima occur at angles ϑ_m , which satisfies the grating equation:

$$\Lambda \sin \vartheta_m = |m|\lambda \quad (6.1)$$

where ϑ is the angle between the diffracted ray and the grating's normal vector and m is an integer representing the propagation mode of interest. When the light is incident at an arbitrary angle, the Eq. 6.1 changes to $\Lambda(\sin \vartheta_i + \sin \vartheta_m) = |m|\lambda$, where ϑ_i is the incident angle. Thick gratings are known as Bragg gratings where there is only one diffracted beam present.

Diffraction gratings can be created in which a number of properties of the incident light are modulated in a regular pattern. These include, transmission grating, reflection gratings, absorption grating, phase or index grating. In this chapter, in particular, the sinusoidal phase and mixed gratings are discussed for the estimation of the EO coefficient from the electric field induced variation in diffraction efficiency.

6.2 Diffraction efficiency

Diffraction efficiency is a measure of the extent to which energy of the incident light is transferred to the diffracted light. Diffraction efficiency, η can be expressed as a ratio of the power of the diffracted light beam P_{diff} to the incident power of the beam P_{inc} given by the relation:

$$\eta = \frac{P_{\text{diff}}}{P_{\text{inc}}} \quad (6.2)$$

The general grating equation is derived for a monochromatic plane wave ψ_0 with polarisation vector \mathbf{s}_0 and propagation vector $\boldsymbol{\sigma}_0$ incident on a grating at an angle ϑ using the following steps. The total electric field in a grating is given by [106]:

$$\mathbf{E} = \sum_{i=-\infty}^{\infty} \mathbf{s}_i \psi_i(z) \exp(-j \boldsymbol{\sigma}_i \cdot \mathbf{r}) \quad (6.3)$$

where, ψ_i is the amplitude and \mathbf{s}_i is the polarisation vector and $\boldsymbol{\sigma}_i = \boldsymbol{\sigma}_0 - i\mathbf{K}$ is the propagation vector of i^{th} diffracted wave, and $j = \sqrt{-1}$. Wave propagation through the grating can be expressed using the wave equation:

$$\nabla^2 \mathbf{E} - \nabla(\nabla \cdot \mathbf{E}) + k^2 \mathbf{E} = 0 \quad (6.4)$$

Consider Δn and $\Delta \alpha$ are the spatial modulation of the refractive index and absorption coefficient respectively. The propagation constant in Eq. 6.4 can be written in the form:

$$k^2 = n^2(2\pi/\lambda)^2 - j n(2\pi/\lambda)\alpha \quad (6.5)$$

Using the values of total refractive index $n = n_0 + \Delta n$ and absorption coefficient $\alpha = \alpha_0 + \Delta\alpha$ in Eq. 6.5 gives,

$$k^2 = \xi^2 - j2\alpha_0\xi + 2\xi[(2\pi/\lambda)\Delta n - j\Delta\alpha] \quad (6.6)$$

where, $\xi = 2\pi n_0/\lambda$ is the average propagation constant. The spatial modulations of the refractive index and the absorption coefficients can be expressed using a Fourier series expansion as,

$$\Delta n = \sum_{h=1}^{\infty} (n_{ch} \cos(h\mathbf{K}\cdot\mathbf{r}) + n_{sh} \sin(h\mathbf{K}\cdot\mathbf{r})) \quad (6.7)$$

$$\Delta\alpha = \sum_{h=1}^{\infty} (\alpha_{ch} \cos(h\mathbf{K}\cdot\mathbf{r}) + \alpha_{sh} \sin(h\mathbf{K}\cdot\mathbf{r})) \quad (6.8)$$

where the $n_{ch(sh)}$ and $\alpha_{ch(sh)}$ are the amplitudes of the h^{th} cosine (and sine) components of the refractive index and absorption coefficient respectively.

Applying Eqs. 6.7, 6.8 and 6.6 in Eq. 6.4 gives a set of coupled equation for the complex amplitude of the i^{th} diffracted wave as:

$$\frac{\partial\psi_i}{\partial z} + \left(\frac{\alpha_0 d}{\cos\vartheta} + j \frac{i(m-i)Q}{2\cos\vartheta} \right) \psi_i + j \frac{d}{2\cos\vartheta} \sum_{h=1}^{\infty} (\psi_{i-h} C_h + \psi_{i+h} D_h) = 0 \quad (6.9)$$

where, $Q = 2\pi\lambda d/n_0\Lambda^2$, which denotes the effective thickness of the grating determining whether the grating to be treated as “thin” or “thick” [107, 108], The Bragg integer, $m = 2n_0\Lambda \sin\vartheta/\lambda$, $C_h = (2\pi/\lambda)A_h - jB_h$, $D_h = (2\pi/\lambda)A_h^* - jB_h^*$, $A_h = n_{ch} - jn_{sh}$, and $B_h = \alpha_{ch} - \alpha_{sh}$.

Solutions to the Eq. 6.9 for “thin” and “thick” grating limits are given in Sections 6.2.1 and 6.2.2.

6.2.1 Small Q: “thin” grating

A grating is considered “thin” if $Q \lesssim 1$ [108, 106]. For a “thin” grating, by considering $Q = 0$ the Eqn. 6.9 will reduce to the form:

$$\frac{\partial \psi_i}{\partial z} + \frac{\alpha_0 d}{\cos \vartheta} \psi_i + j \frac{d}{2 \cos \vartheta} \sum_{h=1}^{\infty} (\psi_{i-h} C_h + \psi_{i+h} D_h) = 0 \quad (6.10)$$

The diffraction pattern is considered as a mix of phase and absorption grating. In the case of a sinusoidal grating, assuming the gratings are of same shape and in spatial phase, the transmittance of a thin mixed grating is given by:

$$T(x, z) = \exp \{ - [\alpha_0 + \Delta\alpha(x) + j 2\pi \Delta n(x)/\lambda] z / \cos \vartheta \} \quad (6.11)$$

Using the values of Δn and $\Delta\alpha$ from Eqs. 6.7 and 6.8 respectively and by dropping the phase factor for thin gratings, the transmittance can then be expressed as a complex Fourier series as [109]:

$$T(x, z) = \sum_{i=-\infty}^{\infty} \psi_i(z) \exp(j i \mathbf{K} x) \quad (6.12)$$

where, \mathbf{K} is the magnitude of the grating vector, \mathbf{K} and x is the coordinate in the direction of the grating vector. Differentiating Eq. 6.12 with respect to z using Eq. 6.11 gives Eq. 6.10. Then the amplitude of the diffracted wave can be expressed as:

$$\psi_i(z) = \frac{1}{2\pi} \exp(-\gamma_{\alpha_0} z) \times \int_0^{2\pi} \exp[-(\gamma_{\alpha_1} z g(\xi) + j 2\gamma_n z f(\xi))] \exp(-j i \xi) d\theta \quad (6.13)$$

where, $\gamma_n = \pi n_1 d / \lambda \cos \vartheta$, $\gamma_{\alpha_0} = \alpha_0 d / \cos \vartheta$, $\gamma_{\alpha_1} = \alpha_1 d / \cos \vartheta$, $\xi = \mathbf{K} x$. The functions $f(\xi)$ and $g(\xi)$ define the shape of grating modulation. The shape functions are defined by $\Delta n(\xi) = n_1 f(\xi)$ and $\Delta\alpha(\xi) = \alpha_1 g(\xi)$ where n_1 and α_1 define the amplitude of the refractive index and absorption modulation respectively. The advantage of Eq. 6.13 is that it will fit for any grating modulations of any arbitrary phase relationship [109].

In the case of an ideal sinusoidal grating, $f(\xi) = g(\xi) = \sin(\xi)$. In this case, Eq. 6.13 reduces to,

$$\psi_i(z) = (-1)^i \exp(-z\gamma_{\alpha_0}) J_i(2\gamma_n z - j\gamma_{\alpha_1} z) \quad (6.14)$$

where, J_i is an integer order Bessel function of the first kind.

Diffraction efficiency of each order can be estimated using the relation, $\eta_i = \psi_i \psi_i^*$.

For a pure phase grating, Eq. 6.14 reduces to the form:

$$\eta_i = \exp(-2\gamma_{\alpha_0}) J_i^2(2\gamma_n) \quad (6.15)$$

and in the case of a pure absorption grating Eq. 6.14 can be expressed in the form.

$$\eta_i = \exp(-2\gamma_{\alpha_0}) I_i^2(\gamma_{\alpha_1}) \quad (6.16)$$

where I_i denotes an integer order modified Bessel function.

A “thin” grating generally shows a large number of diffracted beams though the intensity drops substantially in the higher orders. This is one of the reasons for a “thin” mixed grating, the efficiency cannot be expressed as a superposition of the efficiencies of a phase and an absorption grating [106].

6.2.2 Large Q: “thick” grating

For a grating to be considered as “thick” the general condition is $Q \gg 1$. For a large value of Q , the coupled wave equation given in Eq. 6.9 will converge only if $i \neq 0$ or $i = m$. In our case there is only one diffracted beam and is a Bragg grating. The resulting two components can be written as [109]:

$$\frac{\partial \psi_0}{\partial z} + \frac{\alpha_0 d}{\cos \vartheta} \psi_i + j \frac{d}{2 \cos \vartheta} \psi_m D_m = 0 \quad (6.17)$$

$$\frac{\partial \psi_m}{\partial z} + \frac{\alpha_0 d}{\cos \vartheta} \psi_m + j \frac{d}{2 \cos \vartheta} \psi_m C_m = 0 \quad (6.18)$$

The solution to Eqs. 6.17 and 6.18 for the amplitude of the diffracted wave using the boundary conditions for a sinusoidal grating, $\psi_0(0) = 1$ and $\psi_m(0) = 0$ can be expressed as [109],

$$\psi_m(z) = -j \exp(-z\gamma_{\alpha_0}) (C_m/D_m)^{1/2} \times \sin[zd(C_m/D_m)^{1/2}/2 \cos \vartheta] \quad (6.19)$$

The diffraction efficiency, $\eta_m = \psi_m \psi_m^*$ can be estimated for a mixed grating assuming the amplitudes of the m^{th} sine components of the refractive index and absorption coefficients as zero. The expression for the efficiency of mixed gratings can be expressed as [108],

$$\eta = \exp(-2\gamma_{\alpha_0}) \{ \sin^2(\gamma_n) + \sinh^2(\gamma_{\alpha_1}/2) \} \quad (6.20)$$

The diffraction efficiency of a sinusoidal pure phase grating is given by the equation:

$$\eta = \sin^2(\gamma_n) \quad (6.21)$$

In the case of a pure absorption grating, there is no spatial modulation of refractive index and thus the coupling is due to the modulation of absorption coefficient. Diffraction efficiency for a pure sinusoidal absorption grating is given by,

$$\eta = \exp(-2\gamma_{\alpha_0}) \sinh^2(\gamma_{\alpha_1}/2) \quad (6.22)$$

6.2.3 Sinusoidal grating with small modulation

The diffraction efficiency of the polymer films under this study show small calculated efficiencies of less than 10%. For the thin films used in this study, $\gamma_n \lesssim 1$ which is sufficiently low to approximate $\sin \vartheta = \vartheta$ and $J_1(x) = x/2$ respectively. In effect, both “thin” and “thick” approximations are true in the gratings considered for this study. Diffraction efficiency for thin and thick limit of a phase grating reduces to a single equation for small phase modulation as:

$$\eta = (\pi n_1 d / \lambda \cos \vartheta)^2 \quad (6.23)$$

The expression for the grating efficiency for a purely absorption grating also ends up in the same form if the absorption is low for mixed grating. In the case of small modulation ($\gamma_{\alpha_0} < 1$) the diffraction efficiencies of the absorption grating for thin and thick limit can be matched by approximating $\sinh x = x$ and $I_1(x) = x/2$ for $x < 1$. Using this approximation, Eqs. 6.16 and 6.22 can be written as,

$$\eta = \exp(-2\gamma_{\alpha_0}) (\gamma_{\alpha_1}/2)^2 \quad (6.24)$$

A rigorous analysis of the mixed gratings of arbitrary Q has been discussed in Ref. [110], where the validity of coupled wave theory for films of thickness as small as $2 \mu\text{m}$ is demonstrated. The films used this study do not show diffracted beams except the first order for optimum grating without over-bleaching confirming that

our grating is a Bragg grating. Using a longer wavelength of 1310 nm, thicker film and smaller grating period gives a Q factor much greater than 10. For a grating period, $\Lambda = 2.85 \mu\text{m}$, and wavelength 760 nm and thickness $6 \mu\text{m}$ and average refractive index $n = 1.567$ the $Q \approx 2$. This shows that the gratings we used in this study are close to the “thin” limit. However, for sinusoidal grating with small modulation the thin and thick grating limit can be estimated using the same grating equation [106, 109].

6.3 Periodic gratings on poled polymers

Thin films with adequate chromophore concentrations and thicknesses were fabricated on indium tin oxide (ITO) coated glass substrates by mixing the 5 wt% of PYR-3 chromophore with amorphous polycarbonate (APC). Film fabrication and the drying process followed the method explained in Chapter 4. Thin films were poled using the contact plate electric field poling technique following the procedure described in chapter 4. EO coefficients of the poled films was measured using the Teng-Man modulation ellipsometry technique [39, 41] with a detachable reflecting block electrode, as described in chapter 5 to compare both measurement techniques.

6.3.1 Grating inscription using interferometry

Gratings were defined on the polymer films using a two beam interferometry technique. This technique to define periodic grating is based on the light induced degradation of chromophores. Continuous exposure to laser radiation of sufficient intensity in the absorption band of the chromophore bleaches the chromophores dispersed in the polymer matrix leading to a periodic modulation of the periodic refractive index of the material, $\tilde{n}(\mathbf{r})$. Periodic sinusoidal intensity variation is obtained from two interfering coherent beams. This is done by splitting a coherent laser beam with a non-polarising beam splitter and then allowing them to recombine. The intensity variation when two equally intense coherent beams of $I_1 = I_0 \exp(i\mathbf{k}_1 \cdot \mathbf{r}_1)$ interfere is,

$$I = 2I_0(1 + \cos(\mathbf{k}_1 \cdot \mathbf{r}_1 - \mathbf{k}_2 \cdot \mathbf{r}_2)) \quad (6.25)$$

Where, $\mathbf{k}_1 = \mathbf{k}_2 = \mathbf{k}$ is the wave vector and $\mathbf{r}_1 - \mathbf{r}_2$ is the path difference that lead to a sinusoidal intensity variation perpendicular to the plane of two interfering

beams. Eq. 6.25 can be rewritten in terms of the grating period, as,

$$I(y) = 2I_0(1 + \cos(Ky)) \quad (6.26)$$

where, y is along the direction of the grating vector, \mathbf{K} where $K = 2\pi/\Lambda$ and $\Lambda = \lambda/[2 \sin \vartheta]$ is the period of the sinusoidal intensity variation incident on the film. Periodic bleaching of the film leads to the creation of a grating with period Λ . The grating period is proportional to the wavelength of the writing beams and inversely proportional to the angle between interfering beams.

The schematic of the experimental setup is shown in the Fig. 6.2. A laser beam of wavelength 488 nm is split to two beams of nearly the same intensities and the beams are then directed to the film as shown in the figure. One of the diffracted beams, while writing the grating is used to monitor the diffraction efficiency. The spot size was approximately 2.2 mm and the incident angle, $\theta = 4.9^\circ$ For this settings, $\Lambda = 2.85 \mu\text{m}$. Fig. 6.3 shows diffraction efficiency estimated by measuring incident and first diffracted beam during the grating inscription. It is important to block the writing beam when the diffraction efficiency start saturating because over exposing the film will destroy the grating structure.

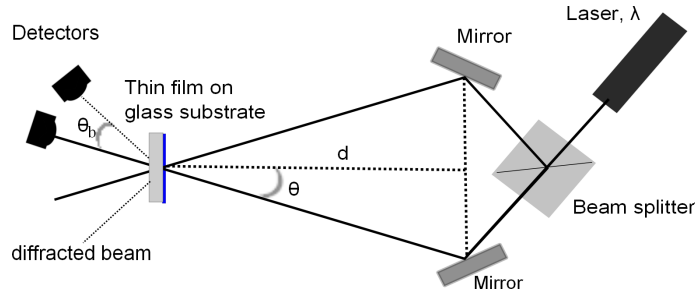


Figure 6.2 – Experimental set up used to inscribe Bragg grating on polymer thin films using two coherent interfering beams. One of the writing beams is used to probe the diffraction efficiency while burning the grating.

Three possible gratings created using two-beam interference method are as follows: Partial bleaching (Fig.6.3(b), region 1) result in very small modulation while over bleaching (Fig. 6.3(b), region 3) gives a clipped sinusoidal grating and the bleaching at 2) gives a near sinusoidal grating with maximum efficiency. A detailed analysis on the modulation of refractive index is given in Section 6.3.2.

From a set of measurements we have made to measure the diffraction efficiency of films after heating or poling in poling apparatus showed the poling process does

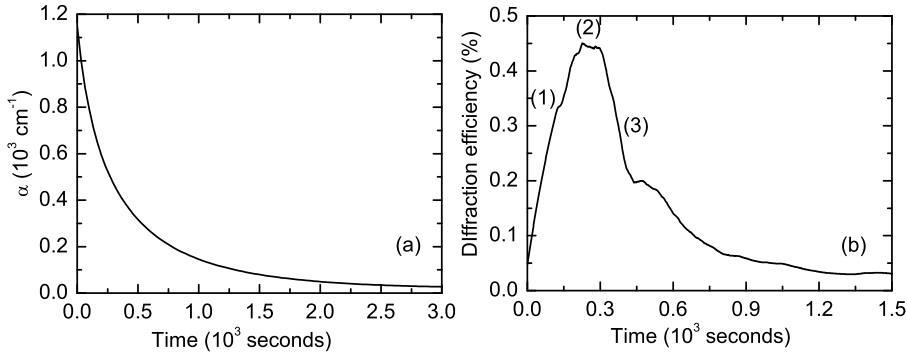


Figure 6.3 – (a) Absorption coefficient of a $\sim 6\mu\text{m}$ PYR-3/APC film at 488 nm during the grating inscription. (b) The first order diffraction efficiency measured during the the grating inscription. Regions (1), (2) and (3) are examples for three possible grating profile obtained: partial, optimum, and over bleached grating respectively.

not damage the grating. This is particularly useful because of the ease of handling and performing the measurement straight after poling.

6.3.2 Modulation of refractive index

A phase gratings on thin films is obtained by creating a periodic variation in the refractive index of the film. The complex refractive index variation along \mathbf{r} in an ideal sinusoidal grating will be of the form $\tilde{n}(\mathbf{r}) = \tilde{n}_0 + \tilde{n}_1 \cos(\mathbf{K} \cdot \mathbf{r})$ where \mathbf{K} is the grating vector and \tilde{n}_0 is the average value of the refractive index and \tilde{n}_1 is the amplitude of the modulation in the complex refractive index. The complex refractive index can be expressed as $\tilde{n}_1 = n_1 + i \frac{\alpha_1}{k}$, where $n_1 = \Delta n/2$, $\alpha_1 = \Delta \alpha/2$ and $k = 2\pi/\lambda$. $\Delta \alpha$ can be obtained from the measured transmittance data of the film as shown in Fig. 6.4(a) and Δn is estimated from $\Delta \alpha$ using the Kramers-Kronig approximation:

$$\Delta n(\omega) = \frac{c}{\pi} \int \frac{\Delta \alpha(\omega') d\omega'}{\omega'^2 - \omega^2} \quad (6.27)$$

The resultant $\Delta \alpha$ and Δn are shown in Fig. 6.4(a) and (b) respectively. The absorption spectrum of PYR-3/APC film shows that the grating can be treated as a pure phase grating at 760 nm and 1310 nm and as a mixed grating at 488 nm because of the absorption at 488 nm.

The refractive index variation from the intensity distribution expected from the ideal case is purely sinusoidal, however, it is based on the assumption that the bleaching process is linear. The time dependent decay of the absorption coefficient

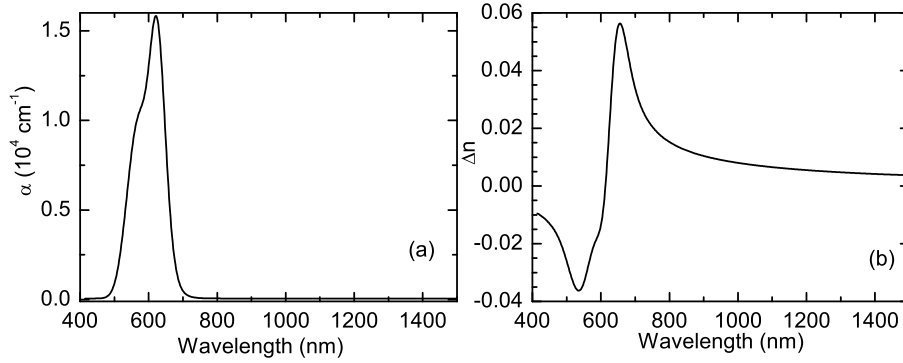


Figure 6.4 – (a) $\Delta\alpha$ as a function of wavelength and (b) the refractive index dispersion estimated for a 5 wt.% PYR-3/APC film using Kramers-Kronig approximation on $\Delta\alpha$.

α of PYR-3/APC given in Fig. 6.3 shows a nonlinear decay profile and hence a pure sinusoidal grating cannot be expected. Eq. 6.26 shows that the intensity profile of the writing beam on the sample has a sinusoidal pattern of period $\Lambda = 2\pi/K$, $I(y) = 2I_0(1 + \cos(Ky))$. The refractive index modulation depends on the change in absorption coefficient ($\Delta\alpha$) that is related to the light intensity. However, in the real case, for a moderate difference in intensity, $\Delta\alpha$ varies exponentially with intensity [24]. That is a sinusoidal intensity profile cannot create a sinusoidal $\Delta\alpha$ profile in organic chromophores.

In the ideal case, if the change in $\Delta\alpha$ with the energy per unit area on the film (E) is linear, that is $\Delta\alpha \propto E$, and $\Delta n \propto E$, the optical energy profile $E(y) = 2E_0(1 + \cos(Ky))$ creates a pure sinusoidal absorption and refractive index modulation of the form:

$$\Delta\alpha(y) = \alpha_0 - 2a E_0(1 + \cos(Ky)) \quad (6.28)$$

$$\Delta n(y) = \Delta n_0 - 2b E_0(1 + \cos(Ky)) \quad (6.29)$$

where a and b are constants. The ideal case of refractive index modulation using two-beam interference is a phase grating of purely sinusoidal modulation. However, even for moderate intensity variation, $\Delta\alpha$ follows an exponential relationship with optical energy incident on the film (see Fig. 6.5(a)). In Fig. 6.5 it can be shown that $\Delta\alpha/\Delta\alpha_0$ can be fitted to:

$$\Delta\alpha(E) = \Delta\alpha_0 \sum_{i=1}^3 c_i \exp(-E/\tau_i) \quad (6.30)$$

where E is the optical energy, $\sum c_i = 1$ are the coefficients and τ_i are the decay constants. It has been found that the variation in $\Delta\alpha$ for an optimum grating (shown as region (2) in Fig. 6.3) can be approximated as a single exponential. $\Delta\alpha(E) = \Delta\alpha_0 \exp(-a E)$ and also, $\Delta n = \Delta n_0 \exp(-b E)$. That is for an experimental $\Delta\alpha$, we get:

$$\Delta\alpha(y) = \alpha_0 \exp[-2aE_0(1 + \cos(\mathbf{K}y))] \quad (6.31)$$

$$\Delta n(y) = \Delta n_0 \exp[-2bE_0(1 + \cos(\mathbf{K}y))] \quad (6.32)$$

Eq. 6.32 shows that the grating profile when bleaching the film under moderate intensity consist of the the exponential profile over a sinusoidal modulation. Generally, the intensity E_0 correspond to linear relationship with $\Delta\alpha$ is very low. A real grating profile expected is shown in Fig. 6.5(b).

A special case of the general experimental condition is when the intensity is sufficiently low. Then the higher orders of the exponential series ($e^x = 1 + x + x^2/2! + \dots$) become negligible and Eqs. 6.31 and 6.32 can be approximated to Eqs. 6.28 and 6.29 respectively. Single exponential fit have been found used in other works of similar grating profiles [111].

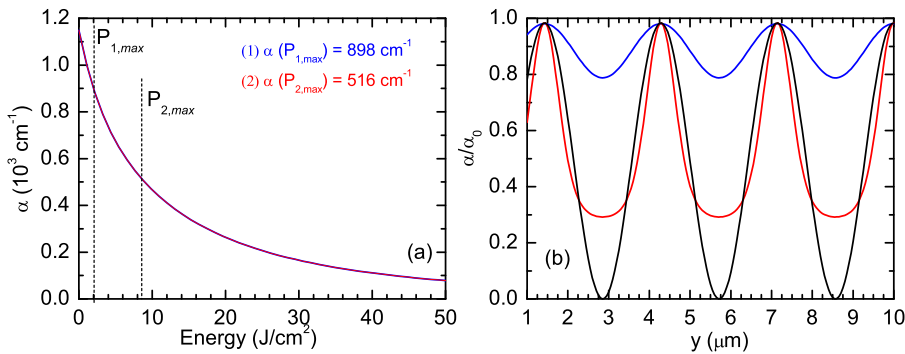


Figure 6.5 – (a) Change in $\Delta\alpha$ (488 nm) with incident energy when the grating inscribed on a $\sim 6 \mu\text{m}$, 5 wt.% PYR-3/APC film using two-beam interference; Vertical lines indicate $P_{1,\text{max}}$ and $P_{2,\text{max}}$ correspond to the regions (1) and (2) of Fig. 6.3(b) respectively. $\Delta\alpha$ at $P_{1,\text{max}}$ and $P_{2,\text{max}}$ are 898 cm^{-1} and 516 cm^{-1} respectively. (b) Modulation of $\Delta\alpha$ correspond to an ideal sinusoidal modulation (black solid curve), actual grating shape for maximum efficiency expected from Eq. 6.31 (red solid curve) and a pure sinusoidal modulation obtained for small intensity (blue solid curve).

Shown in Fig. 6.5(b) is the $\Delta\alpha(y)$ for an ideal case, for exposing the film to a small energy and the real case. It is found that the effective Δn is less than the value of Δn expected from the absorption spectrum of the film for ideal case (complete bleaching with sinusoidal profile). Also the grating modulation has deviated from sinusoidal modulation in the real case.

The modulation of the grating equation Eq. 6.13 can be expressed using,

$$f(\xi) = g(\xi) = \exp[-\tau(1 + \cos(\xi))] \quad (6.33)$$

where $\tau = -2aE_0$ and $\xi = \mathbf{K}y$. Then the equation for a realistic grating modulation obtained from two-beam interference can be expressed as:

$$\psi_i(z) = \frac{1}{2\pi} \exp(-\gamma_{\alpha_0} z) \times \int_0^{2\pi} \exp \quad (6.34)$$

$$[-(\gamma_{\alpha_1} z \exp[-\tau(1 + \cos(\xi))] + j 2\gamma_n z \exp[-\tau(1 + \cos(\xi))])] \exp(-j i \xi)$$

It is apparent that the Eq. 6.34 cannot be reduced to the form of Eq. 6.14. Developing an analytical solution for Eq. 6.34 is beyond the scope of this thesis.

6.3.3 Skin depth

Skin depth is defined as the depth at which the intensity of the radiation inside the material falls to $1/e$ of its original value at the surface. It is a measure of how deep light or any electromagnetic radiation can penetrate into a material. When electromagnetic radiation penetrates into a material the electromagnetic field interacts with the material and decays throughout the passage. In an absorbing material skin depth will generally be a function of the absorption coefficient of the material at the given wavelength. According to the Beer-Lambert law, the intensity of an electromagnetic wave inside a material falls off exponentially from the surface. The intensity of the radiation after travelling a distance z inside an absorbing material can be expressed using the relation $I(z) = I_0 \exp(-\alpha z)$. Now, the skin depth δ_p can be estimated by, $e^{-1} = \exp(-\alpha \delta_p)$ that can be reduced to the form, $\delta_p = 1/\alpha$.

Skin depth should be larger than the thickness of the film for good quality grating for a reasonably small intensity variation throughout the thickness of the film. Fig. 6.6 is a plot for the skin depth estimated from the absorption coefficient of a 5 wt.% PYR-3/APC film. Irradiating near the absorption maxima results in

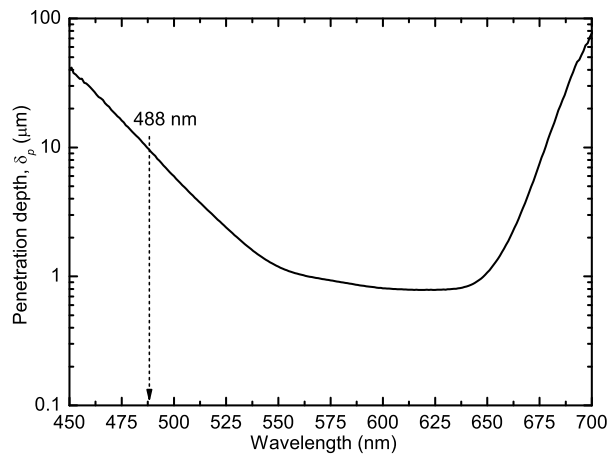


Figure 6.6 – Skin depth, δ_p , estimated for a 5 wt.% PYR-3/APC film in the visible spectrum. An arrow indicates the region of the wavelength of the laser used to inscribe the grating.

shorter penetration depth.

The selection of film thickness of about half that of the skin depth limits the intensity variation in the thickness of the film to within 20%. Another advantage of using a small thickness is the assumption of sinusoidal modulation closer to the ideal case. Thicker films lead to a large variation of intensity along the thickness of the film making the grating structure more complex.

6.3.4 Estimation of diffraction efficiency

Diffraction efficiencies have been calculated from the theoretical formula shown in Eq. 6.20 for laser wavelengths 488, 760 and 1314 nm (for a $6.1 \mu\text{m}$, 5 wt.% PYR-3/APC film). The expected and measured values of the first order diffraction efficiencies for this film are shown in Fig. 6.7. At 488 nm the grating is treated as a mixed grating due to the modulation of both absorption and refractive index at this wavelength. The diffraction efficiency is calculated for the grating using equation 6.20. At 760 nm and 1314 nm the material does not have any absorption component and thus it can be treated as a pure phase grating and the efficiency is estimated using equation 6.21.

The Q factor of a $6.1 \mu\text{m}$ 5 wt.% PYR-3/APC film with grating of period, $\Lambda = 2.85 \mu\text{m}$ is shown in Fig. 6.7(a). Diffraction efficiencies as a function of wavelength were estimated for a range of wavelengths using the approximation of “small modulation”. Theoretically estimated and measured values of the diffraction efficiency

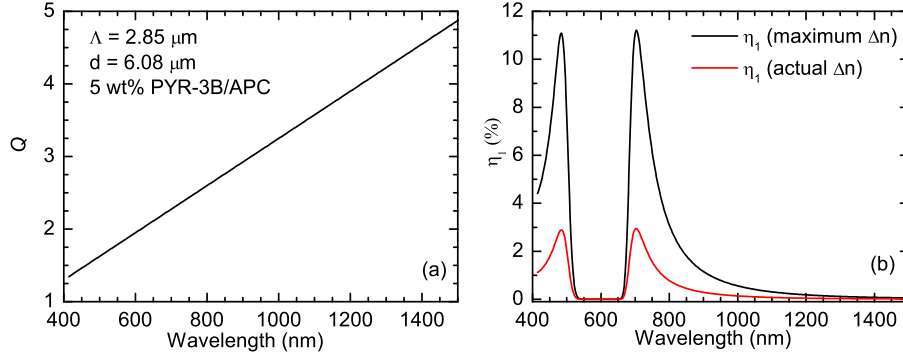


Figure 6.7 – (a) Q factor of a thin film made of 5 wt.% PYR-3/APC with thickness $6.08 \mu\text{m}$ and grating period $2.85 \mu\text{m}$. (b) Diffraction efficiency estimated for for small modulation.

Table 6.1 – Diffraction efficiency for the first order beam of a $6.1 \mu\text{m}$, 5 wt % PYR-3/APC film with grating period, $\Lambda = 2.85 \mu\text{m}$. n_{av} is the average refractive index of the film. Δn_{ideal} is the refractive index modulation estimated using Kramers-Kronig on $\Delta\alpha$ of the film for linear bleaching approximation, Δn_{real} is the refractive index modulation estimated using Kramers-Kronig on a realistic $\Delta\alpha$ considering nonlinear bleaching as shown in Fig. 6.5. $\eta_{\text{cal(ideal)}}$ and $\eta_{\text{cal(real)}}$ are the calculated diffraction efficiencies using Δn_{ideal} and Δn_{expt} respectively and η_{mea} is the measured diffraction efficiency.

$\lambda(\text{nm})$	n_{av}	Δn_{ideal}	Δn_{real}	$\eta_{\text{cal(ideal)}}$	$\eta_{\text{cal(real)}}$	η_{mea}
488	1.5303	0.0210	0.0128	5.20 %	1.3 %	0.45 %
760	1.609	0.0191	0.0116	10.9 %	2.8 %	0.32 %
1314	1.568	0.0047	0.0029	0.40 %	0.1 %	0.07 %

for the wavelengths of interest are summarized in Table 6.1. Results show that the measured diffraction efficiency is much lower compared to the theoretically estimated value. This is not unexpected due to a number of factors. One possible reason for the discrepancy is that the grating is not purely sinusoidal since the bleaching rate reduces once the inner depth of the film is considered and this will result in a grating modulation that changes with depth. A more detailed discussion on the photo induced bleaching of NLO chromophores is given in Chapter 7. To ensure maximum possible accuracy we have chosen the wavelength giving a penetration depth larger than the thickness of the film. The discrepancy between the theoretical and experimental values of diffraction efficiency is observed in other diffraction gratings, for example Refs. [111, 112, 64]. Furthermore, the grating equation is based on a number of assumptions that may not always be the case.

6.4 Estimation of r_{33} from diffraction efficiency

The estimation of EO coefficient from the electric-field induced change in diffraction efficiency uses the basic Pockels equation. That is, the modulation or change in refractive index under an applied electric field is proportional to the applied electric field. Theoretical formulation is based on the assumption that the material does not show absorption at the measurement wavelength. In Section 6.3.4 we show that equations for the “thick” and “thin” grating limits give the same equation for small value of modulations. In this case, the diffraction efficiency of a pure sinusoidal dielectric grating is:

$$\eta = \left[\frac{\pi n_1 d}{\lambda \cos \vartheta} \right]^2 \quad (6.35)$$

where, $n_1 = \Delta n/2$. Electric field induced change in refractive index of the material due to an external electric field is given by Pockels formula [1]:

$$\delta n(E) = -\frac{1}{2} n_0^3 r_{33} E \quad (6.36)$$

where n_0 is the ordinary refractive index of the material.

The diffraction efficiency when a constant electric field is applied can be obtained by using the change in refractive index $n_1(E) = n_1 - \delta n(E)$ in Eq. 6.35 gives:

$$\eta(E) = \frac{1}{4} \left[\frac{\pi d}{\lambda \cos \vartheta_b} \right]^2 (\Delta n - n_0^3 r_{33} E)^2 \quad (6.37)$$

Normalized change in diffraction efficiency due to an external field, $\xi(E)$ can be written as:

$$\Delta\eta/\eta_0 = \frac{\eta(E) - \eta_0}{\eta_0} = \frac{(n_0^3 r_{33} E - \Delta n) n_0^3 r_{33} E}{\Delta n^2} \quad (6.38)$$

For a moderate electric field, $\delta n(E) \ll \Delta n$ and thus Eq. 6.38 can be further simplified to,

$$\Delta\eta/\eta_0 = \frac{n_0^3 r_{33} E}{\Delta n} \quad (6.39)$$

The EO coefficient can be estimated from Eq. 6.39 as:

$$r_{33} = \frac{\Delta n}{n_0^3} \left(\frac{\Delta\eta}{\eta_0} / E \right) \quad (6.40)$$

where the average value of $\frac{\Delta\eta}{\eta_0}/E$ can be obtained from the slope of the linear fit to the plot of $\frac{\Delta\eta}{\eta_0}$ against modulating field E .

6.4.1 Condition of validity

The method of estimating the EO coefficient from the electric field induced diffraction efficiency is based on some assumptions. The change in intensity of the diffracted beam should be solely due to the modulation of the grating due to the modulation of the effective refractive index of the grating. Presence of any process additional to the modulation of the refractive index by the applied field can be tested using the principle of conservation of energy.

The energy transfer mechanism in a pure sinusoidal phase grating can be expressed as:

$$I_{\text{inc}} \approx I_0 + 2I_1 \quad (6.41)$$

Where, I_{inc} is the incident intensity, I_0 is the intensity of the zeroth order and I_1 is the intensities of the $\pm 1^{\text{st}}$ order. Any loss from the scattering as the transmission loss through the film and ITO layer, and the reflection loss at the surface of the reflecting electrode are neglected. For small modulation, in particular, as in the case of the system under study, I_1 is less than 5 % by theory and less than 0.5 % as observed from experiment. That is, the intensity of the first order beam is less than 1 % of the zeroth order because $I_0 \approx I_{\text{inc}}$ in this case.

Now, the change in I_1 due to the modulation of the refractive index by an applied field is based on the assumption that $\Delta n \ll \delta n$, where Δn is the modulation of the grating and δn is the change in Δn due to the applied field due to the EO effect. Then the maximum permitted change in the intensity of I_1 should be less than 100 %.

Considering these assumptions, the following properties are expected for the zeroth and first order diffracted beams for the validity of this technique: (1) The maximum change in the zeroth order beam should be less than 1 % for the full range of electric field used during measurement. (2) The maximum change in the first order diffracted beams, I_1 should be less than 100 %, that is $\Delta I_1 < I_1$, and (3) The change in intensity of I_0 should be approximately double that of the change in I_1 , that is $\Delta I_0 \approx 2\Delta I_1$. However, in effect, the change induced by the applied field on the zeroth order beam is negligible and potentially does not make any effect in the

zeroth order beam.

6.5 Experiment using DC modulating field

A schematic of the experimental settings for the measurement using DC electric field is shown in Fig. 6.8. A laser beam passes through an attenuator, a polariser and then through an optical chopper. A lock-in amplifier amplifier is used for accurately measuring minute changes in the first order diffracted beam due to the applied electric field. The polymer film, with grating, is placed between an ITO coated electrode and a detachable block electrode the same way it was placed in Teng-Man ellipsometry apparatus describer in Chapter 5. This is used to apply the electric field across the electrodes. The laser beam reflected off the back electrode get diffracted. Zeroth and first order diffracted beams are detected using photo-diodes which are connected to a multimeter or lock-in amplifier coupled with the optical chopper. The electric field is applied using a Thorlabs piezo driver that can be used to provide a DC or amplify an AC modulating voltage for up to 150 V. The angle of incidence used is $\sim 9^\circ$ from the normal to the film.

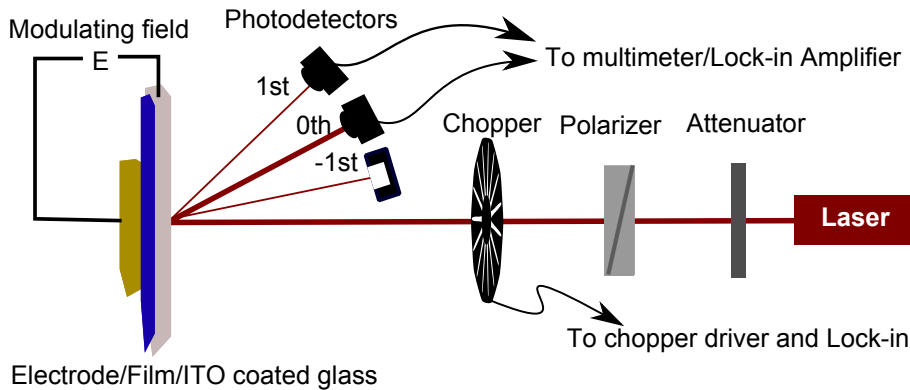


Figure 6.8 – Schematic of the experimental set up to estimate EO coefficient using diffraction technique with DC modulating field.

The diffraction efficiency of the film is measured for zero field and for a range of DC electric fields across the film. Fig. 6.9(a) shows the plot of diffraction efficiency against the applied field. Fig. 6.9(b) shows the change in diffraction efficiency over the zero field diffraction efficiency ($\Delta\eta(E)/\eta_0$) against applied electric field. EO coefficient of the material can be estimated from the slope of the linear fit to the data using Eq. 6.40.

6.5.1 Estimation of EO coefficient using DC field

Thin films of 5 wt.% PYR-3/APC with thickness approximately $6.1\mu\text{m}$ were fabricated following the procedure explained in Chapter 4. Films are poled using the contact plate electric field poling technique at $175\text{ }^\circ\text{C}$ under $E_p = 50\text{ V}/\mu\text{m}$ for 15 minutes. The measured electro-optic coefficient with Teng-Man apparatus using 760 nm approximately $170\text{ pm}/\text{V}$. A wavelength of 760 nm is preferred over the conventional 1310 nm because the diffraction efficiency is relatively low at 1310 nm because the diffraction efficiency reduces quadratically with wavelength (see Fig. 6.7). Furthermore, 760 nm is visible and thus it makes alignment of the experimental set up rather simple. The chopper frequency was set at 640 Hz .

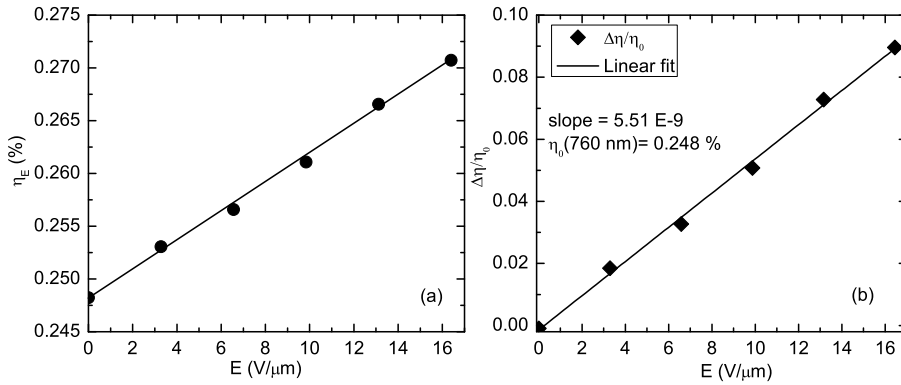


Figure 6.9 – (a) Diffraction efficiency for the first order diffracted beam, η as a function of applied DC field for a $6.06\mu\text{m}$ film of 5 wt% PYR-3/APC. (b) $\Delta\eta(E)/\eta_0$ vs. E for the same data; Slope of the linear fit is $5.51 \times 10^{-9}\text{ m}/\text{V}$, where η_0 is the first order diffraction efficiency with zero field.

The measured diffraction efficiency of a poled film with period, $\Lambda = 2.85\mu\text{m}$ without electric field at 760 nm was 0.248% . Diffraction efficiencies for a set of DC electric fields were measured using the experimental set up shown in Fig. 6.8. Measured diffraction efficiency as a function of applied DC field is shown in Fig. 6.9. The change in diffraction efficiency normalized with the efficiency at zero field, $\Delta\eta/\eta_0$ is plotted as a function of applied field. EO coefficients are estimated from the slope of the $\Delta\eta/\eta_0$ vs. E curve using Eq. 6.40.

The estimated EO coefficient is approximately $24\text{ pm}/\text{V}$. This is about an order of magnitude less than the value estimated from the Teng-Man ellipsometry technique at 1 kHz but still higher than the theoretically expected value from molecular first hyperpolarisability. A set of values of the change in diffraction efficiency and

corresponding change in refractive index for an applied field of $16 \text{ V}/\mu\text{m}$ is summarised in Table 6.2.

Table 6.2 – Measured and estimated values of diffraction efficiencies at $16 \text{ V}/\mu\text{m}$ for a 5 wt.% PYR-3/APC film for the values of EO coefficient estimated from theoretical calculation, this experiment and Teng-Man ellipsometry method; Diffraction efficiency at $E = 0$ was 0.248 %.

	Theoretical	Diffraction	Teng-Man
$\eta(E)$	0.252 %	0.264 %	0.373 %
$\Delta\eta$	0.0036 %	0.016	0.125
δn	3.04×10^{-4}	0.0015	0.0106
r_{33}	5 pm/V	24 pm/V	175 pm/V

The measurement with DC field satisfies the condition for the validity of this technique. Measured values of the zeroth order intensity did not show any notable change with the modulating voltage. This is because the change in intensity of first diffracted beam (I_1) due the modulation of the grating is less than 10 % ($\Delta I_{1,\text{max}} \approx 0.1 I_1$), where I_1 is about 0.05 % I_0 , and thus the effective change in I_0 due to the modulation is within 0.005 %. This is in a good agreement with the condition of the validity of using the diffraction technique for the estimation of EO coefficient.

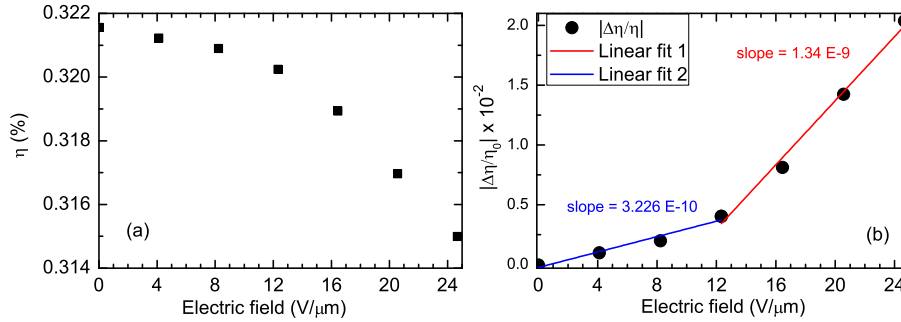


Figure 6.10 – (a) Diffraction efficiency as a function of applied DC field for a $6.1 \mu\text{m}$ film of 5 wt.% PYR-3/APC with $170 \text{ pm}/\text{V}$ when measured using Teng-Man modulation ellipsometry. (b) $\Delta\eta(E)/\eta_0$ vs. electric field for the same data; Linear fit for two segments of the plot are $3.226 \times 10^{-10} \text{ m}/\text{V}$ and $1.34 \times 10^{-9} \text{ m}/\text{V}$ respectively. The corresponding EO coefficients are $5.91 \text{ pm}/\text{V}$ and $1.44 \text{ pm}/\text{V}$ respectively.

A set of measurements made using a DC electric field on different films show that the effect of external electric field on diffraction efficiency varies from sample to sample. The relative change in diffraction efficiency with electric field observed in Fig. 6.9 is opposite to the that of observed in a different film shown in Fig. 6.10. The diffraction efficiency is reduced with applied field and in some cases the data cannot

be fitted linearly. This is an indication that the electric field induced modulation measured using the diffraction method is not of purely electronic origin ascribed to the EO coefficient. This cannot be detected using the Teng-Man ellipsometry method. A detailed analysis using AC field can possibly explain the source of the overestimation by Teng-Man ellipsometry method discussed in Chapter 5. Detailed analysis of this phenomena is discussed in Section 6.7 by using the data from AC measurement.

6.6 Experiment using AC modulating field

The validity of using an AC modulating field for the measurement of EO coefficient is tested in this section. When using AC fields, the experimental set up will become rather simple because the set up does not require an optical chopper since the lock-in can be coupled with the modulating field. The experimental set up for the estimation of the EO coefficient using AC modulating field is shown in Fig. 6.11.

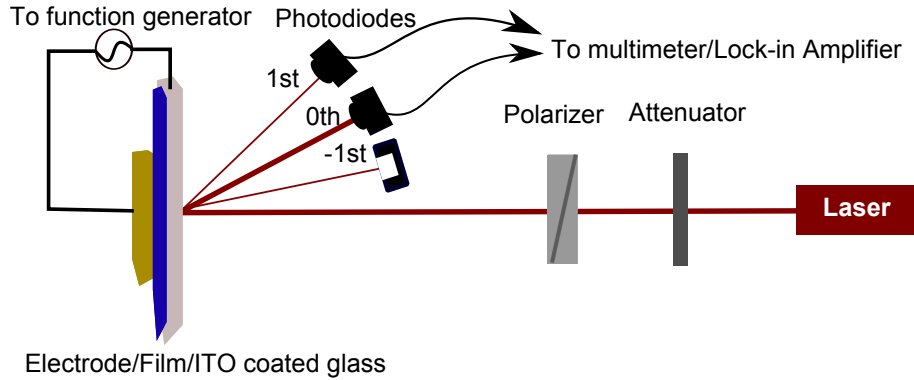


Figure 6.11 – Schematic of the experimental set up to estimate r_{33} using diffraction technique with an AC modulating field with a modulating frequency of 1 kHz.

In the presence of an AC modulating field, $E(\omega) = E_0 \cos(\omega t)$, Eq. 6.38 simplifies to,

$$\Delta\eta/\eta_0 = \frac{2\delta n_{E_0} \cos(\omega t)}{\Delta n} \quad (6.42)$$

where, the $2\delta n_{E_0} = n_0^3 r_{33} E_0$. Also, by considering $\delta n \ll \Delta n$, the second harmonic term will be filtered out by the lock-in amplifier. Then Eq. 6.42 reduces to the same form as Eq. 6.39 used in the case of static electric field. The EO coefficient can be estimated from the slope of the $\Delta\eta/\eta_0$ vs. E plot using Eq. 6.40.

6.6.1 Estimation of EO coefficient using AC field

Experiments with an AC modulating field have been made in a similar way to those done using a DC field. The only difference is that the optical chopper is not required in this set up because the driving function generator can be used to couple with the lock-in amplifier. The film used for this measurement is from the same batch used for DC measurements in Section 6.5.1. The thickness of the 5 wt.% PYR-3/APC film used is $6.08 \mu\text{m}$. The poling conditions are similar to the procedure followed for the experiment with DC field. The measured EO coefficient using Teng-Man apparatus at 760 nm wavelength and 1 kHz was approximately 182 pm/V.

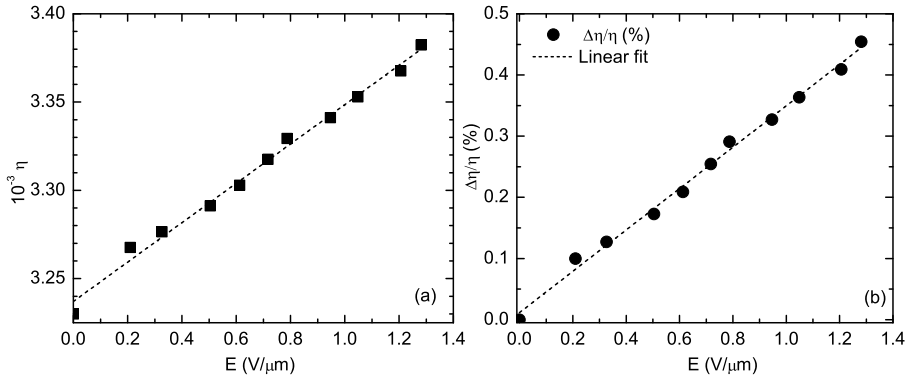


Figure 6.12 – (a) Diffraction efficiency for the first diffracted beam as a function of applied field for a poled $\sim 6 \mu\text{m}$ thick 5 wt.% PYR-3/APC film. The AC modulation frequency was 1 kHz. (b) $\Delta\eta/\eta$ as a function of applied AC modulating field. Slope of the linear fit to the $\Delta\eta/\eta$ vs. E curve is $3.38 \times 10^{-9} \text{ m/V}$.

The measured diffraction efficiency of a poled film with period, $\Lambda = 2.85 \mu\text{m}$ without electric field at 760 nm was 0.32%. Shown in Fig. 6.12(a) a plot of the diffraction efficiency using data shown in Fig. 6.13(b). The change in diffraction efficiency normalized with the zero field efficiency, $\Delta\eta/\eta_0$ was plot as a function of applied field. The slope of $\Delta\eta/\eta_0$ vs. E curve was estimated from the data shown in Fig. 6.12(b). EO coefficient is estimated from the slope using Eq. 6.40. The estimated EO coefficient is, $r_{33} \approx 17.8 \text{ pm/V}$. This is less than the value measured on the same sample using Teng-Man ellipsometry technique but comparable to the values estimated from diffraction method using DC field. However, it is still an order of magnitude higher than the value of EO coefficient expected from theory. General issues observed with an AC modulating field is discussed in Section 6.7.1.

To test the validity, the change in zeroth order beam was measured with zero field and with AC modulation as shown in Fig. 6.13. The change in zeroth order

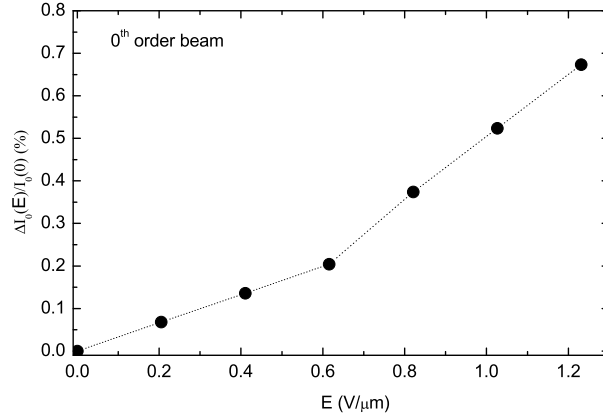


Figure 6.13 – Plot of the effect of AC modulation on the zeroth order beam. This kind of strong modulation on zeroth order was not observed during the measurements using DC field.

beam is too large compared to the expected change because of the energy transferred to the first order beam due to the modulation. This is significantly different from the case of DC measurements where the change in the intensity of zeroth order was negligible. Also, this breaks the condition for the validity of this technique because there are other processes happening in this case other than the modulation of the grating with the applied field. The unexpected modulation in zeroth order is likely to be due to the inverse piezoelectric effect.

6.7 Analysis of diffraction technique

6.7.1 Effects of modulating frequency

Using an AC modulating field is a rather simple method compared to using DC and it permits measurement at different modulating frequencies. One of the major advantages of using an AC modulation technique is it can uncover many problems associated with the measurement of EO coefficient of a poled polymer using Teng-Man ellipsometry. In the Teng-Man method such effects cannot be observed as independent issues instead it is observed as part of the EO effect.

The direction of change in diffraction efficiency varies from case to case. When the measured data is in phase with modulating field the intensity of the zeroth order beam decreases with the applied voltage while it increases when the diffracted beam intensity is 180° out of phase with the modulating frequency. This is primarily attributed to the presence of other factors contributing to modulate the intensity

of the diffracted beam such as modulation of the incident beam due to the inverse piezoelectric effects. That shows the phase between the modulating frequency and the zeroth order beam can be in phase or out of phase.

The effect of modulating frequency on the diffraction efficiency was investigated for a set of frequencies range from 100 Hz to 30 kHz. The measured diffraction efficiency have been found to vary with modulating frequency as shown in Fig. 6.14. This is similar to the effect observed in the Teng-Man modulation ellipsometry experiment. This can be attributed to the presence of low frequency components of the EO effect as discussed in Chapter 5. Contributions from the modulation of the film thickness also can contribute significantly in diffraction technique, that is explained in following sections.

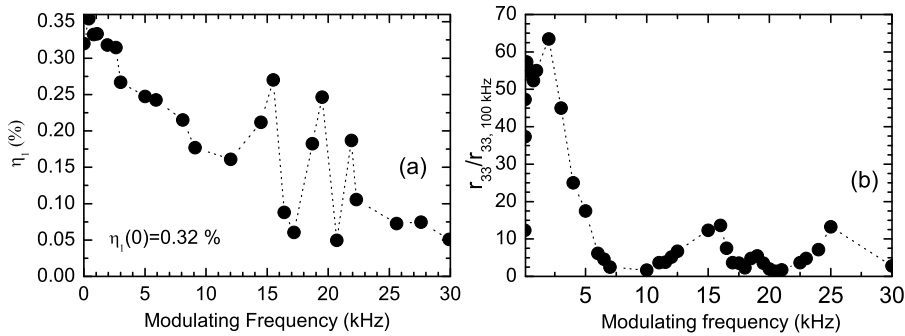


Figure 6.14 – (a) Diffraction efficiency as a function of modulating frequency for a $6.1 \mu\text{m}$ PYR-3/APC film for a 760 nm beam. The modulating field was $0.82 \text{ V}/\mu\text{m}$. (b) A similar effect observed in the r_{33} measurement using Teng-Man modulation ellipsometry.

6.7.2 Change in diffraction efficiency with lock-in phase settings

The changes in diffraction efficiency with applied field have been found to vary from one film to other. That is in some cases the applied field makes additive change in the diffraction efficiency while it reduces the diffraction efficiency in others. However, it has been observed that this effect is specific to the film. This is observed in the experiments using both AC and DC modulating fields. The phase of the lock-in signal when doing AC measurements was analysed in detail for further analysis of this phenomena. The diffraction efficiency has been found to decrease if the phase of the output voltage of the detector is in phase with the modulating frequency. When the detector output is out of phase with the modulating frequency the diffraction efficiency reduces with applied voltage. That is, the intensity of the first order

diffracted beam observe systematic change with modulating voltage depending on the phase.

This effect can potentially be due to the change in transmittance because of the thin film interference effects due to the multi-layered structure of sample. If the material is EO active, its refractive index varies with the applied field and this can make a small change in the transmitted intensity. However the contribution of small change in refractive index because of the EO effect is negligible compared to the effect due to small variation in thickness. Thickness variation can be due to the piezoelectric property of the film. If the material has a piezoelectric property, the applied electric field can make a small change in the thickness of the film and that can also change the transmitted intensity. In addition, the piezoelectric effect can vary the diffraction efficiency when an electric field is applied across the grating due to the change in thickness.

6.7.2.1 Inverse piezoelectric effect

A strain induced by the applied electric-field can induce a small variation in piezoelectric properties. Similar to the EO effects the piezoelectric effect is also linearly related to the applied field [2]. More discussion on piezoelectric effect is presented in Chapter 5 in the analysis of EO measurement. The change in thickness, Δd as given Ref. [95, 96] is $\Delta d_k = \sum_j a_{kj} E_j d_k$, where E is the electric field, a is the piezoelectric tensor component. This shows that the piezoelectric effect can directly modulate the grating due to the change in thickness.

The diffraction efficiency for low modulation is $\eta = [\pi n_1 d / (\lambda \cos \vartheta)]^2$. Where the diffraction efficiency is proportional to the film thickness and any variation in thickness can make field induced change in the diffraction efficiency. However, this is negligibly small because even a 1% change in thickness can effectively change only 0.01% of the diffraction efficiency. The piezoelectric coefficient should be sufficiently large to make such a large change in diffraction efficiency as expected from experiments. However, as far as we are aware the polymer host we used, APC, has not been reported having a such a large piezoelectric activity. In addition to that, if the thickness change is the cause of the modulation, the change in the diffraction efficiency should always have to be in one direction. However, in our case, the diffraction efficiency as well as the phase varies from one film to other. Another possible way that the thickness change can effectively modulate the diffracted beam

is through the interference effect as described in following section.

6.7.2.2 Interference effect

The multilayer structure of the film lead to an interference pattern on the beam transmitted through the system. The equation for transmittance through an air/glass/film/air configuration can be defined using the relation:

$$T = 1 - \frac{r_{12}^2 r_{23}^2 + 2r_{12} r_{23} \cos(\varphi)}{1 + r_{12}^2 r_{23}^2 + 2r_{12} r_{23} \cos(\varphi)} \quad (6.43)$$

where, $\varphi = (2\pi/\lambda)2dn_{\text{film}}$, d is the film thickness, r_{12} and r_{23} are the amplitudes of reflection coefficients at the air-film and film-glass interface. Reflection coefficients are estimated using the Fresnel equations on the refractive indices of air (n_{air}), glass (n_{glass}) and the film (n_{film}).

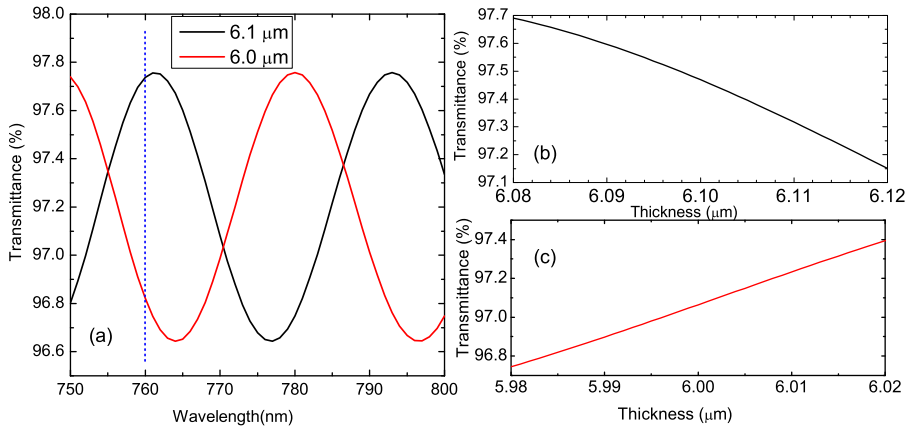


Figure 6.15 – (a) Change in the effective transmittance simulated for a 6.0 μm and a 6.1 μm PYR-3/APC film due to the thin film interference effect; vertical dashed line shows the wavelength of interest, 760 nm. (b) Change in effective transmittance at 760 nm for a PYR-3/APC film for a small variation in thickness from 6.1 μm. (c) The same as in (b) for 6.0 μm.

Thin film interference phenomena can amplify the possible chance of change in the film thickness due to inverse piezoelectric effect. This effect is additional to the electro-optic effect. Fig.6.15(a) shows the simulated transmittance data as a function of wavelength for films deposited on glass substrate with thickness 6.0 μm and 6.1 μm. The transmittance is simulated using the refractive index of air, glass and the estimated refractive index of the polymer film. In Figs.6.15(b) and (c) the transmittance is plotted for 760 nm for small changes in thickness. It can be seen

that a small change in thickness lead to a large change in the transmittance for a given wavelength.

If the applied field can change the film thickness via an inverse piezoelectric effect, it leads to a modulation of transmitted intensity as a function of applied field. The direction of the change in transmitted intensity is related to the position of the wavelength over the sinusoidal interference pattern. The direction of change in transmittance varies with wavelength, thickness, and refractive index of the film. A small reduction in thickness from 6.1 μm film in Fig. 6.15(b) increases the transmitted intensity while a similar thickness change in a 6.0 μm film shown in Fig. 6.15(c) will result in a reduction of transmitted intensity.

Now, combining the piezoelectric effect with the interference effect on transmission, one can see that the response of the transmitted intensity, and hence the diffraction efficiency, changes with applied field. This effect can be additive or subtractive depending on whether the change in thickness increases or decreases the transmittance. This determines the phase between the transmitted signal and modulating voltage and can explain the $\Delta\eta/\eta$ going up or down with applied field for different thicknesses. This effect can also be present in the Teng-Man ellipsometry method, resulting in a large overestimation of the EO coefficient of the samples measured. For thinner films, this effect is small, and large for thick films. Also the effect is reduced when going towards higher wavelength as expected from Eq. 6.43.

The relative change in the transmitted intensity of zeroth order and first order diffracted beam as a result of applied electric field can be used to investigate whether the effect is from the modulation of diffraction efficiency by EO effect or due to other effects. In the case of modulation of grating by an applied field due to EO effect, we show that $\Delta I_0 \approx 2\Delta I_1$. That is,

$$\Delta I_0 \approx -2\Delta\eta I_0 \quad (6.44)$$

Eq. 6.44 shows that the resulting the change in I_0 is very small due to a modulation of the diffraction efficiency. However, in the case of other effects, such as interference effect, the modulation effect is similar on both diffracted and zeroth order beams. If η is the modulation due to, for example, interference effect, the change in intensity of each beam is relative to their intensity. That gives $\Delta I_1 \approx \eta\Delta I_0$ then the change in the zeroth order beam will be,

$$\Delta I_0 \approx \Delta \eta I_0 / \eta \quad (6.45)$$

Eqs. 6.44 and 6.45 show that the change in the zeroth order beam, ΔI_0 is $1/2\eta$ times larger in presence of any effects other than the modulation of the grating due to the EO effects. A large modulation of the zeroth order beam in the AC measurement (see Fig. 6.13) and switching of phase and a related direction of modulation of the diffraction efficiency can be attributed to this effect. A large change observed in the intensity of zeroth order is a sign of presence contribution from the non-electronic component. Although similar effect can be observed in using the Teng-Man method the experimental settings of that technique does not provide options of this type. Instead it give an estimate of the sum of all the effects as EO coefficient though different groups suggested methods to reduce some of the effects contribution to the over estimation of the measured EO coefficients. These include corrections for multiple reflection effects explained in Chapter 5.

6.8 Conclusions

A new technique for the measurement and analysis of the EO coefficient using a diffraction method is proposed. The main advantage of this method is that it doesn't require a modulating AC field, rather it measures the static EO coefficient of the material using a DC electric field. Measurement of EO coefficient using this technique can eliminate the multiple reflection effect [70] and cavity resonance [101] that are considered as two major issues associated with the measurement of the EO coefficient using Teng-Man ellipsometry. The validity of this method is tested for both AC and DC modulating fields. Measurement using AC field does not satisfy the condition for the validity of this technique, though it can be refined out by further improvement of this technique. The results in Figs. 6.12 and 6.13 suggest that interference effect dominates.

Measured EO coefficients using this technique have also been found larger than the theoretically expected value but an order of magnitude less than the value estimated by Teng-Man technique. Also, in the experiments using AC fields, the effect of modulating frequency on the measured EO coefficient is similar to what is observed from Teng-Man ellipsometry. The resonance frequency was found in the same frequency range in both techniques on films of different thickness. This is a useful

information because this may affect the performance of this polymer system in that frequency range.

The main motivation of this technique was analysis of the over-estimation of EO coefficient measured using the Teng-Man ellipsometry. In the Teng-Man ellipsometry technique the modulation of the reflected (or transmitted, in transmission mode) beam is considered solely due to the EO coefficient because the measurement is done using the reflected beam. Results of this study show that the high “diffraction” efficiencies are actually due to an electric field induced modulation of the film thickness or interference effect. Thus the EO coefficient is likely to be no more than a couple of pm/V.

Chapter 7

Photostability of NLO Chromophores

The development of next generation ultra-fast photonic devices relies on efficient electro-optic (EO) materials. EO polymers have been demonstrated to show a very large EO coefficient when compared to inorganic EO crystals [1]. Despite the promise of high electro-optic coefficients compared to their inorganic counterparts one of the significant challenges that has hindered the commercial uptake of organic electro-optic materials is the photo induced degradation of the NLO chromophores [1, 25, 24]. In general, electro-optic chromophores developed for photonic applications do not absorb in the telecommunication wavelength, for instance 1300 or 1550 nm. However, their strong absorption in the visible region may consequently lead to the degradation of the system when exposed to the visible region of electromagnetic spectrum. To operate the device for a prolonged period of time under a high photon flux it is important that the components have sufficient photostability. Investigations towards a better understanding of the photodegradation mechanism of organic NLO chromophores dispersed in polymer matrices and methods to enhance optical stability are discussed in this chapter.

A photodegradation model based on a distribution in the photodegradation quantum efficiencies is presented. Effects of environmental parameters such as light intensity, oxygen concentration etc on the photostability of the chromophores are investigated. A systematic approach is followed to investigate how the chromophore structure, chromophore concentration in the films, aggregation, and the quantum chemical mixing of the ground state and the charge separated state as defined by

bond length alternation are related to photostability. Three types of NLO chromophores, PYR-3 [84], IND-7 [81] and QUN-7 [84], and their derivatives [113, 81] were used for this study. Structures of all the chromophores used in this study are shown in Chapter 4. These chromophores are synthesized within the IRL photonics group for the development of polymers having a large EO effect.

7.1 Light induced degradation of NLO chromophores

Continuous exposure of NLO chromophores to light in the absorption band or in the higher energy region transform them to compounds having no NLO property. Fig. 7.1 shows the absorption spectrum during progressive bleaching of a solution containing the chromophore IND-7 in CHCl_3 with UV radiation of 365 nm. Fig. 7.2 shows the absorbance of IND-7 chromophores in CHCl_3 while diluting the solution. In both cases one can see the absorption of the solution getting reduced. A similar effect is observed in both cases and can be explained by the exposure to the radiation leads to a diminishing number of the chromophore molecules in the solution. The normalised absorption data of the solution while diluting is different from that when optically degrading the solution. This is because of transformation of the chromophores to the degraded products. Degraded products do not generally show a NLO effect or absorption in the main absorption band of the chromophores. The other effects that can be observed when bleaching the chromophores compared to diluting is the tendency of blue shifting of the main absorption peak and strengthening of the secondary absorption maximum. The optical bleaching process leads to an appearance of a new peak in the high energy region outside the main absorption band, due to the absorption of the bleached products.

In this chapter, in particular, different aspects of the process photo-induced degradation of organic NLO chromophores in polymer matrices are investigated. The drop in the absorption of the films containing chromophores due to bleaching is similar to what is observed in the solution. An example for the bleaching of 3 wt.% IND-7/APC film when exposed to an expanded 655 nm is shown in Fig. 7.3. In which the absorption spectra gradually reduces with time. Normalised absorption spectra while bleaching reveal other changes with bleaching; they are: (1) the secondary absorption maxima (the shoulder at the high energy side of the absorption spectra) reduces faster than the main absorption maxima. (2) New absorption bands developing above 900 nm and below 550 nm - this is primarily attributed to the absorption

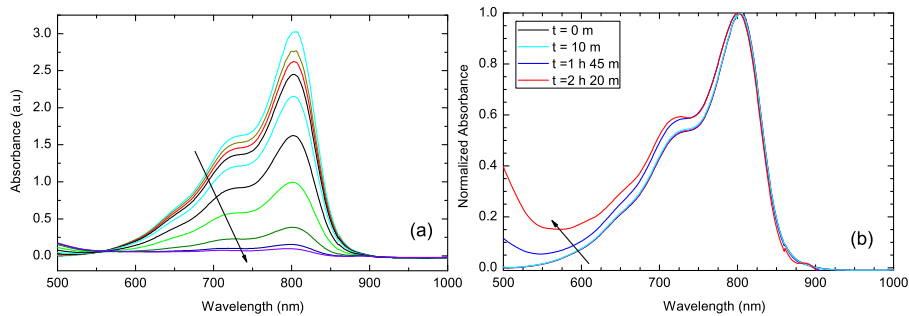


Figure 7.1 – (a) Absorption spectra during progressive bleaching of of IND-7 solution in CHCl_3 by exposure to UV radiation at 365 nm; The arrow indicates increasing exposure time from 10 mts to 9 hrs. (b) Normalised absorbance.

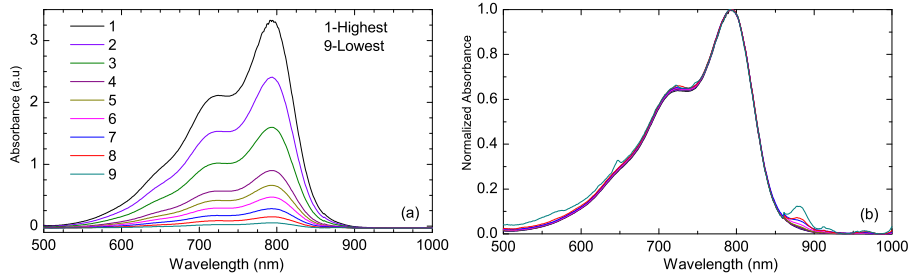


Figure 7.2 – (a) Absorption spectrum of IND-7 solution in CHCl_3 at different concentrations. (b) Normalised absorbance.

of the bleached products. (3) The red-shift of λ_{max} with bleaching time. The absorption band appearing above 900 nm is not observed in the solution. This could be due to the degraded product showing absorption above 900 nm is not stable in the CHCl_3 solution. Also, the relative change in intensity of the secondary absorption peak of the film is different from that in the solution.

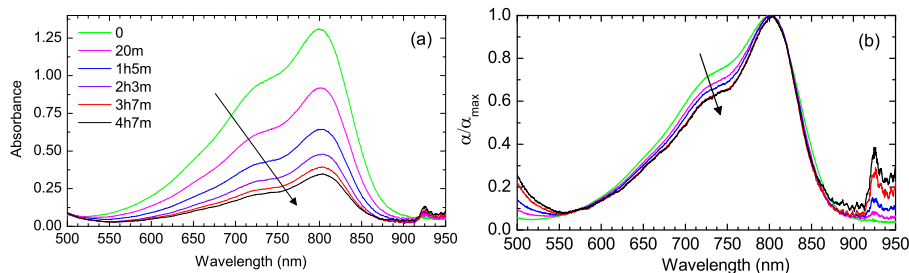


Figure 7.3 – (a) Absorbance of a 3% IND-7/APC film while progressive bleaching using a 655 nm beam, arrow indicates increasing bleaching time (b) Normalised absorbance.

The process of photodegradation due to the resonant absorption of light can be explained as follows. The chromophore molecules shift from ground state to

the excited state by absorbing light. At this point there is a certain probability that the molecule undergoes an irreversible photochemical transformation to new molecules that effectively have no NLO response. The average number of photons required to photodegrade a chromophore is characteristic to the physical state of the system containing chromophores and is denoted as B (or often $B_{1/e}$ or $\beta_{1/e}$). Another common expression representing the optical stability of chromophores is the photodegradation quantum efficiency, which is denoted as $B^{-1} = 1/B$ which is the reciprocal of average number of photons required to bleach a chromophore molecule. The physics and chemistry of basic photodegradation mechanism is explained in Sections 7.1.1 and 7.1.2.

7.1.1 Photodegradation mechanism

Several processes can lead to the photodegradation of organic NLO chromophores. The most effective is the oxygen mediated process involving singlet oxygen [24, 25, 114]. Singlet oxygen ($^1\text{O}_2$) is generated by transferring energy of a sensitizer molecule to a triplet oxygen ($^3\text{O}_2$). NLO chromophores in their excited state act as efficient sensitizers for the production of singlet oxygen. Any excited state with a sufficient long lifetime to allow intermolecular interactions will be quenched by oxygen, because the energy transfer of both the excited singlet and triplet state is spin-allowed. The energy of the oxygen excited states is lower than the triplet states of most organic triplets and the small size of O_2 molecules allows for a rapid diffusion in most media. As a result, no other intermolecular quenching mechanism can compete with the oxygen mechanism [115]. The most important processes involving the degradation of chromophores can be illustrated using the following reactions [115, 25]:



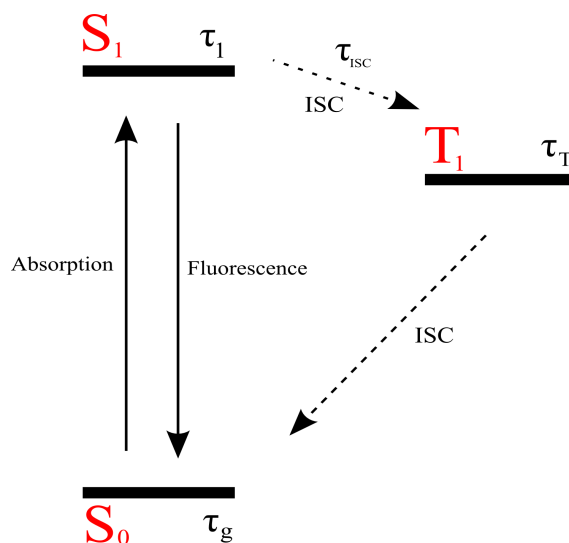
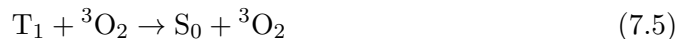


Figure 7.4 – Energy level diagram for a chromophore molecule, where S_0 is the ground state (with lifetime τ_g), S_1 the singlet excited state (with lifetime τ_1), T_1 the triplet excited state (with lifetime τ_T) of the chromophore molecule, ISC is the inter system crossing.



Where S_0 is the ground state, S_1 the singlet excited state and T_1 is the triplet excited state of the chromophore molecule. The main pathway of singlet oxygen generation is through quenching of the first excited triplet state by oxygen by the spin-allowed process as shown in process 7.4. T_1 generally has a long lifetime because the $T_1 \rightarrow S_0$ transition is spin-forbidden [115]. The chromophore molecule, M , in the ground state, S_0 , reacts with the singlet oxygen to give the peroxide of the material which is generally expected to be the main bleached product [25, 24].



By assuming Eq. 7.6 is the main process bleaching the chromophore which involves the ground state molecule and singlet oxygen, two of the methods to increase the photostability of the material could be quenching of the singlet oxygen, depletion of the ground state molecule or stopping reactions leading to the creation of the singlet oxygen. Singlet oxygen can be deactivated through a number of different processes, in order of increasing rate constants these are, radiative processes, electronic to vibrational deactivation, charge-transfer quenching, chemical reactions

and electronic energy transfer. Electronic energy transfer is only important when molecules with triplet state energies slightly lower than the singlet oxygen energy level are present. Usually in polymers the lifetime of singlet oxygen is limited by the electronic to vibrational deactivation of the singlet oxygen state by neighbouring polymer units and this occurs in a time frame of several tens of μs [115]. On the other hand in our case the singlet oxygen can also react with the double bond of the chromophore and undergo an irreversible chemical reaction. This pathway can have a higher rate constant than the vibrational deactivation and will probably limit the singlet oxygen lifetime [52].

7.1.2 Photochemistry of photo-oxidation

Recent investigations carried out within our group on the degradation a PYR-3 chromophore have explained one of the dominant photodegradation pathway, as shown Fig. 7.5. Mass spectroscopy and NMR spectroscopy performed on freshly made and optically degraded chromophores have been performed to investigate the bleaching process. The proportion of the new molecules in the bleached products data have demonstrated the degradation mechanism shown in Fig. 7.5 is the main photodegradation pathway [52].

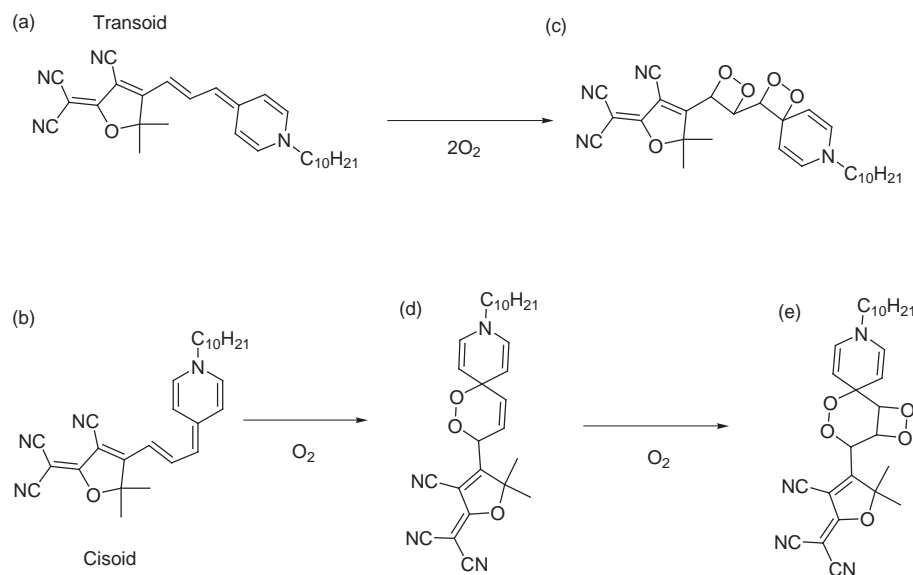


Figure 7.5 – (a) The trans and (b) the cis form of a PYR-3 chromophore (c), (d) and (e) the expected products formed after photo-oxidation process. .

7.1.3 Basic photodegradation model

The time dependent photodegradation model was based on the following assumptions, the process is a one photon process, each molecule has a certain probability of being transformed into a bleached molecule after having absorbed a certain number of photons, uniform distribution of isotropic molecules and a uniform photon flux and the photodegraded product does not absorb light at the irradiation wavelength. The first photodegradation model proposed by Dubois [114] was developed using the following rate equations.

$$\frac{\partial N(t, z)}{\partial t} = -\sigma N(t, z) B^{-1} n(t, z) \quad (7.7)$$

$$\frac{\partial n(t, z)}{\partial z} = -\sigma N(t, z) n(t, z) \quad (7.8)$$

where $N(t, z)$ is the chromophore density, $n(t, z)$ is the photon flux at time t and distance z into the film from the surface of the film, σ is the absorption cross section of the chromophore at the given wavelength and $B^{-1} = 1/B$ is the intrinsic photodegradation quantum efficiency. A solution to the above differential equations assuming the photodegraded product does not absorb light at the irradiation wavelength can be expressed in terms of the instantaneous transmittance through the film [114] by,

$$T(t) = \frac{T(\infty)}{1 + [T(\infty) \exp(\sigma N(0)L) - 1] \exp(-\sigma n_0 t / B)} \quad (7.9)$$

with L defined as the film thickness, $N(0)$ the initial chromophore concentration, $T(\infty)$ the transmittance after bleaching. This equation can be further simplified by rewriting in the form [114],

$$F(t) = \frac{T(\infty)/T(t) - 1}{T(\infty)/T(0) - 1} = \exp(-\sigma n_0 t / B) \quad (7.10)$$

Using $\beta = \sigma n_0 t$ this reduces to

$$F(\beta) = \exp(-B^{-1}\beta) \quad (7.11)$$

If all the assumptions are correct a single exponential decay can be expected for $F(\beta)$ and the photodegradation quantum efficiency can be found as the value

of β when $F(\beta) = 1/e$ [114]. Based on this model, the photodegradation quantum efficiency, B^{-1} is independent of light intensity, oxygen concentration in the film, and $F(\beta)$ follow an exponential relationship with β . However, all these three expectations are not satisfied in reality.

7.2 Experimental setup

Photodegradation experiments were made in air at atmospheric pressures and ambient temperature (15 °C to 21 °C) under a range of optical wavelengths and intensities. A schematic representation of the experimental setup is shown in Fig. 7.6 and the photograph of an experimental set up is shown in Fig. 7.7. To obtain a good quality Gaussian beam profile a spatial filter was used in the laser path and the beam was expanded and a small pinhole was kept on the the surface of the sample to get uniform irradiation over the film.

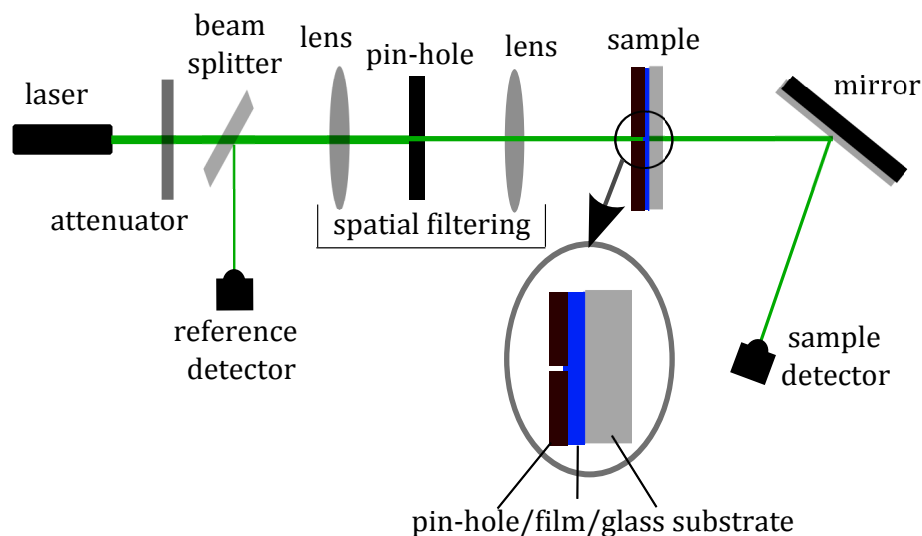


Figure 7.6 – Photodegradation experimental set up.

Before starting the experiment the film thickness, chromophore concentration in the film and the absorption spectra of the film were collected. The transmittance of the film was recorded as a function of time during photodegradation. A beam splitter placed before the sample was used to reflect part of the laser beam to a reference photo-diode and the transmitted beam was detected using another photo-diode. The use of two photo-diodes nullifies any small laser power fluctuations. The laser intensity on the film was varied by using neutral density filters or by adjusting

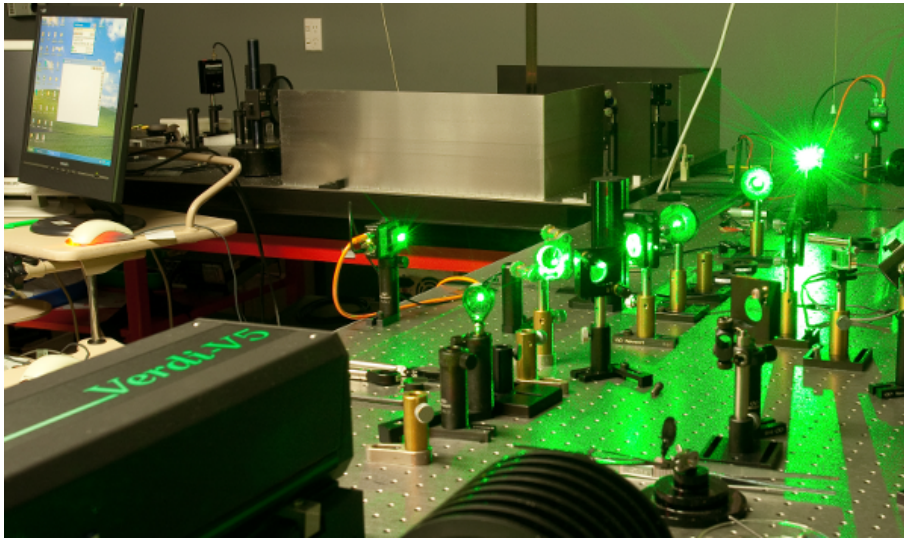


Figure 7.7 – Picture of a photodegradation experimental set using a 532 nm Nd:YVO₄ laser beam.

the laser power. The number density (concentration) of chromophores in polymer matrix was estimated using the method described in chapter 4. Number densities of a range of chromophores used in this study correspond to the loading in APC are given in Table 7.1.

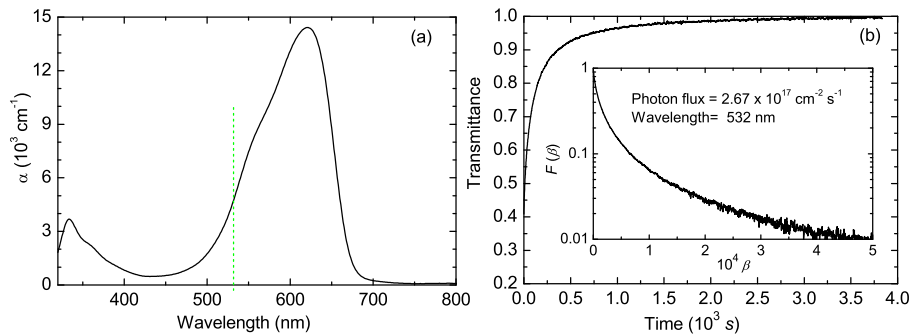


Figure 7.8 – (a) Absorption coefficient of a 2.4 μm , 5 wt% PYR-3/APC film, vertical dashed line indicates the wavelength used for photodegrading this film. (b) Transmittance as a function of time while photodegrading this film with a 1 mW/mm² 532 nm laser beam; Inset is the data in (b) plot for $F(\beta)$ vs. β .

Fig. 7.8(a) shows the absorption spectra of a 2.4 μm , 5% PYR-3 film in APC. Shown in Fig. 7.8(b) is the data when photodegrading the with at 1 mW/mm². A plot of transmittance against the time of exposure to radiation and corresponding $F(\beta)$ vs. β plot is given. The photodegradation quantum efficiency estimated from the experiment, B^{-1} is 1/1200 ($B = 1200$), which is the value of β when $F(\beta) = 1/e$.

Table 7.1 – Chromophore number densities correspond to the chromophore loading in APC.

Chromophore code	Loading percentage in APC	Number density (cm^{-3})
PYR-3	5	8.370×10^{19}
PYR-3	10	1.538×10^{20}
PYR-3	15	2.510×10^{20}
PYR-3B	8	9.281×10^{19}
IND-7	3	2.360×10^{19}
IND-7	5	3.767×10^{19}
IND-7	8	6.098×10^{19}
IND-7R	5	3.825×10^{19}
QUN-7	5	3.626×10^{19}
QUN-7R	5	3.437×10^{19}

Experimental results show that the the plot of $F(\beta)$ vs. β shows a deviation from the single exponential. This is different from what is expected in the Dubois [114] model based on the assumption that $F(\beta)$ vs. β can be fitted to a single exponential and the model does not consider oxygen concentration in the film. This model was improved based on the results from experiments using different oxygen partial pressures and optical intensities [24, 67].

7.3 Effects of light intensity and oxygen partial pressure

Photodegradation quantum efficiency is specific to a chromophore determined by the chemical nature of the molecule. Further to that, photodegradation quantum efficiency of a system is related to many external factors including light intensity, oxygen partial pressure, chromophore concentration in the films and film thickness. This section deal with the effects of light intensity and oxygen partial pressure on the photodegradation of NLO chromophores.

To investigate the effects of photon flux (light intensity) on photodegradation, a series of photostability experiments were made in air over a range of optical intensities on different chromophores. In Fig.7.9 the evolution $F(\beta)$ against β at

different optical intensities are plotted for films of 5 wt.% IND-7/APC. The average amount of photons needed to degrade a chromophore decreased by more than an order of magnitude, that is from 61000 to 1258 with the decrease in intensity from 35 mW/mm² down to 0.17 mW/mm². In Fig. 7.10 $\beta_{1/e}$ is plotted for a set of photodegradation experiments made on 5 wt.% IND-7/APC films using a 655 nm laser. An exponential dependence of $\beta_{1/e}$ was observed with light intensity. Fig. 7.10(b) shows intensity dependent data for a broader intensity range made on 5 and 15 wt.%PYR-3/APC. PYR-3 is used for convenience because it can be degraded using high power Nd:YVO₄ laser that can help with experiments at higher light intensities. The trend of the intensity dependence of photodegradation is similar for two of the chromophores investigated as shown in Fig. 7.10.

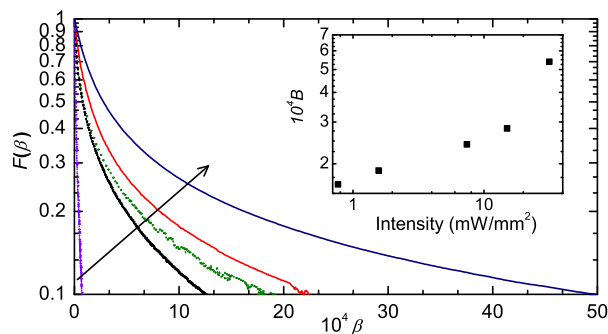


Figure 7.9 – $F(\beta)$ against β plot for the photodegradation data obtained by optically degrading a 5 wt.% IND-7/APC film at different light intensities, arrow indicates increasing intensity; 0.17, 1.5, 7.5, 15.7, 35 mW/mm²; Inset is a plot of $B = \beta_{1/e}$ against laser intensity.

The effects of incident light intensity on the bleaching rate has been the subject of recent studies [25, 116, 24]. With increasing light intensities there seems to be an increase in the average amount of photons needed to degrade a chromophore. It was suggested in [25] that this increase in photostability is due to the depletion of the chromophore ground state population. Only the chromophores in the ground state can undergo degradation and thus depletion of ground state leads to an enhancement of photostability [25]. Chromophores in the triplet state do not contribute to the absorption of light and hence the diminished population of the ground state can lead to a reduction in the absorption [25]. However, in other reports as given in Ref. [116] and the research performed in our group [117] have found that the depletion of oxygen which is being used in the degradation reaction is the reason for the increase in stability with optical intensity [24].

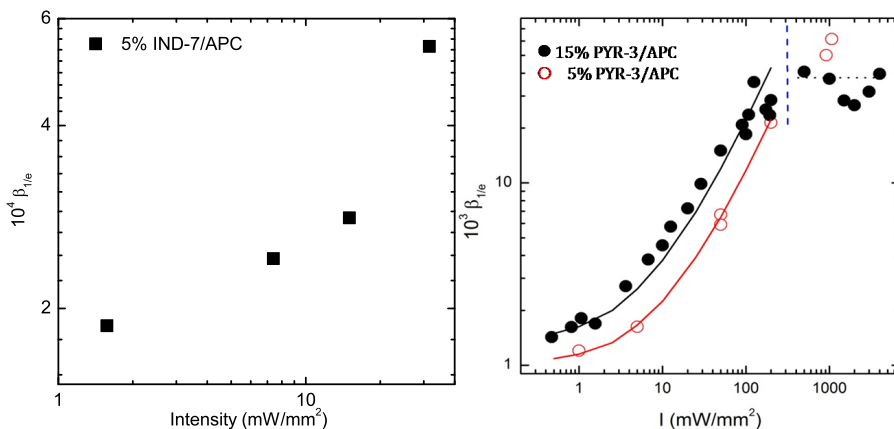


Figure 7.10 – Plot of photodegradation quantum efficiency as a function of light intensity: (left) for $2\ \mu\text{m}$ 5% IND-7/APC film and (right) for a 5% and 15% PYR-3 film in APC [24].

From the intensity dependent photodegradation experiments made on PYR-3 experiments there are three different regimes. At low light intensities the concentration of oxygen in the film can be regarded as constant because of the fast diffusion of oxygen into the film which compensates the oxygen used during the degradation process. The diffusion Eq. 7.16 can be set to zero and the bleaching rate is in this case linearly dependent on the light intensity. This case has been widely studied and used to model the formation of waveguides using photodegradation. When the light intensity is increased, the oxygen concentration N_{ox} cannot be considered constant in time and space and the oxygen diffusion equation has to be included and the photodegradation rate is limited by the diffusion rate of oxygen into the film. There will be oxygen depletion due to photo-oxidation of the chromophores and the oxidation rate will become linearly dependent on the local oxygen concentration. The local oxygen concentration will be inversely proportional to the intensity and thus a systematic decrease of the photodegradation quantum efficiency with intensity is observed. When the light intensity is increased above a certain value, thermal effects start to play a major role in the degradation of the chromophore-polymer guest-host system [24].

It was suggested that the photostability increase at high intensities is due to depletion of the chromophore ground state S_0 [25]. However, studies by our group have demonstrated it is the depletion of oxygen and not the depletion of ground state is leading to a high photostability at higher intensities [24, 118]. The influence of this can be demonstrated using a simple three level model for the chromophore as shown

in Fig. 7.4. The lifetime of the singlet excited state S_1 of PYR-3 was measured and varies between 0.5 ns and 3.3 ns depending on the PYR-3 concentration [67], while the lifetime of the triplet excited state of PYR-3 is unknown, but is typically in the range of ms to s for chromophores [119, 120]. The rate equations for such a system are [117]:

$$\frac{\partial N_g}{\partial t} = -\frac{N_g}{\tau_g} + \frac{N_1}{\tau_1} + \frac{N_T}{\tau_T} \quad (7.12)$$

$$\frac{\partial N_1}{\partial t} = \frac{N_g}{\tau_g} - \frac{N_1}{\tau_1} - \frac{N_1}{\tau_{isc}} \quad (7.13)$$

$$\frac{\partial N_T}{\partial t} = \frac{N_1}{\tau_{isc}} - \frac{N_T}{\tau_T} \quad (7.14)$$

with N_g the average occupancy of the S_0 ground state, N_1 the average occupancy of the S_1 excited state, N_T the average occupancy of the T_1 triplet state, τ_1 the singlet excited state lifetime, τ_{isc} the inter-system crossing lifetime from S_1 to T_1 , τ_T triplet excited state lifetime. τ_g the lifetime of the ground singlet state and can be estimated as $\tau_g = \sigma n$ with σ the absorption cross section at the wavelength used and n the photon flux.

The intensity dependent photodegradation is a result of oxygen mediated photodegradation. The result can be summarised as follows: At low intensities the oxygen concentration can be regarded as constant (Dubois model [114]) and at higher intensities the oxygen content will decrease rapidly after illumination starts and it will be almost completely depleted. In this case the photodegradation rate will be limited by the oxygen diffusion rate into the film. Recent investigations by our group [24, 118] on 10 wt.% PYR-3/APC with approximately $2 \mu\text{m}$ thickness have demonstrated the photostability has a reciprocal relationship with oxygen partial pressure [24].

7.4 Modified model of photodegradation

Observations discussed in Section 7.3 show that the photostability of chromophores has a strong relationship with light intensity. Our group [118, 24, 121] has investigated that the photodegradation quantum efficiency is related to the oxygen concentration in the film. The Dubois model [114] does not, however, consider the oxygen

concentration in the film which has been motivated the development a photodegradation model considering the oxygen concentration [24].

By considering the effects of oxygen concentration in the film, the photodegradation differential equations in Eq. 7.7 have been modified to the following rate equations [24],

$$\frac{\partial N(t, z)}{\partial t} = -\sigma N(t, z)n(t, z)N_{ox}(t, z)/a_{ox} - \sigma N(t, z)B_0^{-1}n(t, z) \quad (7.15)$$

$$\frac{\partial N_{ox}(t, z)}{\partial t} = D \frac{\partial^2 N_{ox}(t, z)}{\partial z^2} + \frac{\partial N(t, z)}{\partial t} \quad (7.16)$$

where $N(t, z)$ is the chromophore number density, $n(t, z)$ is the photon flux, N_{ox} is the oxygen concentration, a_{ox} is a constant specific to the chromophore, σ is the absorption cross section of the chromophore at the wavelength used in the experiment, B_0 is the inverse of intrinsic photodegradation quantum efficiency and D is the oxygen diffusivity specific to the polymer.

The intensity dependent photodegradation shown in Fig. 7.10 leading to a systematic increase in $\beta_{1/e}$ with increasing irradiation intensity can be explained by a time dependent oxygen content within the films as expected from Eqs. 7.15 and 7.16. For high intensities, the oxygen concentration in the film is quickly depleted by chromophore photodegradation and the photodegradation probability will be limited by the oxygen diffusion rate into the films. For low intensities, the photodegradation rate is low enough that there will be nearly a constant oxygen concentration though the films and hence $\beta_{1/e}$ is expected to be lower. For very low intensities, the oxygen concentration in the film will not change significantly with time and hence it is expected that $F(\beta)$ should be described by Eq. 7.11, which is consistent with the data of 5 and 15 wt.% PYR-3/APC in Fig. 7.10(b) for the lowest intensity.

Eq. 7.16 describes the time evolution of the oxygen concentration in the film, which will be a balance between oxygen diffusing into the film and oxygen used during the degradation process. The first term in Eq. 7.15 describes the oxygen mediated degradation pathway and the second term the residual degradation by other mechanisms. When oxygen is present in the film $1/B_0$ is expected to be a couple of orders smaller compared to N_{ox}/a_{ox} and in this case the second term can be neglected [24]. In the absence of oxygen the first term will become zero and in this case the transmittance in time, $T(t)$, can be approximated by the photodegradation

model by Dubois [114].

The modelled $F(\beta)$ vs. β for different intensities is shown in Fig. 7.11 (a) together with the experimental data. The increase in the photodegradation quantum efficiency with intensity can be described well with this model for the first part of the degradation as can be seen in this figure. At longer times there is a deviation of the calculated transmittance with the experimental data, which could be explained by a number of factors such as the existence of different photodegradation quantum efficiencies and/or different absorption cross sections arising from a polarisation dependent transition probability [67]. This show that the photodegradation model needs further improvement by considering multiple photodegradation quantum efficiencies.

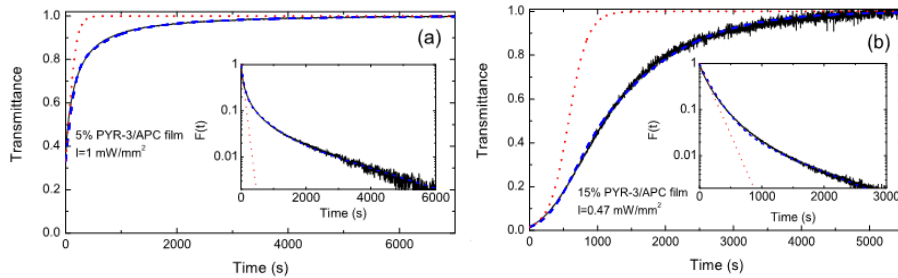


Figure 7.11 – Plot of the transmittance $T(t)$ against time during illumination at 532 nm for (a) a $2.4\ \mu\text{m}$ 5% PYR-3/APC film with an incident intensity $1\ \text{mW}/\text{mm}^2$, and (b) a $2.05\ \mu\text{m}$ 15% PYR-3/APC film with an incident intensity $0.47\ \text{mW}/\text{mm}^2$. The insets show the corresponding $F(t)$. The dotted curves are the modelled data for short times assuming only one photodegradation quantum efficiency where $B = 1100$ and 1400 for 5% and 15% PYR-3 by weight, respectively. The dashed curves are the modelled curves assuming three B' values.

7.4.1 Model based on multiple photodegradation pathways

It is apparent from Figs. 7.8, 7.9 and 7.11 that the evolution of $F(\beta)$ with time cannot be fitted to a single exponential. The deviation from the expected single exponential needs to be investigated to develop a more realistic model. Better understanding of the photodegradation mechanism is important to develop new methods for enhanced optical stability of the chromophores. The departure of $F(\beta)$ plot from single exponential was reported previously from measurements on 10 wt.% PYR-3/APC thin films [24, 118] where the measurements are done without a pinhole and hence it was expected that the departure from a single exponential could be due to a varying laser intensity across the film [24, 118, 121]. However, this is not

the case in the new set of experiments we made because we used an expanded laser beam and a $100\ \mu\text{m}$ pinhole to ensure that the intensity was constant across the film. Experiments were repeated using a further expanded beam and a 1 mm pinhole to avoid the diffraction effect caused by the small pinhole in the range of film thickness. This was confirmed by optical microscopy after photodegradation where the resultant bleached area was circular and with the same diameter as the pinhole. Most of the previous reports of chromophore photo-bleaching also find that Eq. 7.9 does not provide a good fit for all times and hence Equation. 7.9 is used to model the data for short times only [114, 122]. This has also been done for our data and we show in Fig. 7.11 $T(t)$ and $F(t)$ for 5 wt.% PYR-3/APC and 15 wt% PYR-3/APC where $B = 1100$ and 1400 , respectively.

The failure of Eqs. 7.9 and 7.10 to provide a good fit to the data over a large time range suggests that there is a polarisation-dependent photodegradation or there is a distribution in the photodegradation quantum efficiencies. The first possibility could occur if the S_0 to S_1 transition probabilities strongly depend on the polarisation of the incident beam. Simulation results provided by Quilty [123] showed light polarised perpendicular to the bridge contributes less than 10% of the absorption and shows peaks at higher energies which are attributable to transitions within the donor and acceptor rings [67]. Thus, the absorption cross section depends on the angle between the electric field of the incident light and the principal chromophore axis, which results in a orientational distribution of the absorption cross section if PYR-3 is randomly orientated in the PYR-3/APC films. The second possibility could occur if, for example, there existed an intermediate product that then photodegraded [124, 125]. However, we expect this is unlikely in our case because there is no evidence for another absorption peak above 450 nm during bleaching and there is no significant absorption above 450 nm after complete bleaching. Note that *trans*- and *cis*- isomers of PYR-3 might be expected to occur in the film because NMR of the starting powder shows that both isomers exist. However, the S_0 to S_1 transition probabilities are not expected to be significantly different for both isomers. To be able to characterise our photostability data, we consider a model where there are 3 photodegradation quantum efficiencies and/or 3 different absorption cross sections arising from a polarisation dependent transition probability and/or a distribution in the photodegradation quantum efficiency. We also include oxygen diffusion into the films and oxygen-mediated photodegradation. The resultant differential equations can be written as [67],

$$\frac{\partial m(\beta, z)}{\partial z} = -\bar{\sigma}N(\beta, z)m(\beta, z) \quad (7.17)$$

$$\frac{\partial N(\beta, z)}{\partial \beta} = -\bar{\sigma}m(\beta, z)\frac{N_{ox}(\beta, z)}{N_{ox}(0)}\sum_{i=1}^3 N_i(\beta, z)\frac{\sigma_i}{\bar{\sigma}B_i} \quad (7.18)$$

$$\frac{\partial N_{ox}(\beta, z)}{\partial \beta} = D'\frac{\partial^2 N_{ox}(\beta, z)}{\partial z^2} + \frac{\partial N(\beta, z)}{\partial \beta} \quad (7.19)$$

where $\beta(t) = n_0 \times t$, $m(\beta, z) = n(t, z)/n_0$, $n(t, z)$ is the photon flux at time t and at distance z into the film, $N(\beta, z)$ is the total chromophore concentration, $N_{ox}(\beta, z)$ is the oxygen concentration in the films, $D' = D/n_0$, and D is the oxygen diffusivity in the films. The three chromophore concentrations are $N_1(\beta, z)$, $N_2(\beta, z)$, and $N_3(\beta, z)$ where the corresponding absorption cross sections are σ_1 , σ_2 , and σ_3 , and the average number of photons required to degrade a chromophore at room temperature and pressure are B_1 , B_2 , and B_3 , respectively. We previously showed that the average number of photons required to degrade a chromophore is inversely proportional to the oxygen partial pressure. The average absorption cross section is $\bar{\sigma} = [\sigma_1 N_1(0) + \sigma_2 N_2(0) + \sigma_3 N_3(0)]/N(0)$.

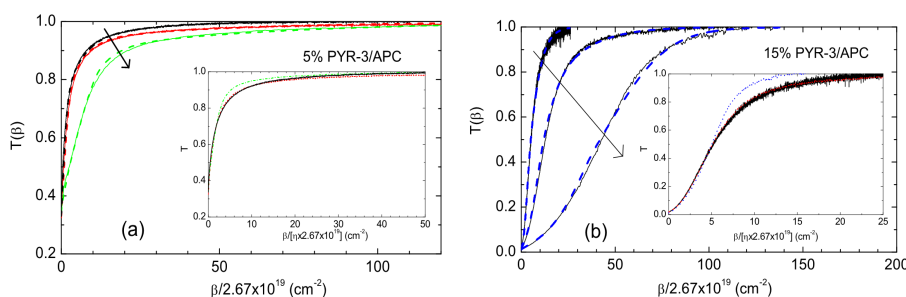


Figure 7.12 – Plot of the transmittance against $\beta/2.67 \times 10^{19}$ (solid curves) for (a) a $2.4 \mu\text{m}$ thick 5% PYR-3/APC films and (b) a $2.05 \mu\text{m}$ thick 15% PYR-3/APC film. The arrows show increasing intensity of $1 \text{ mW}/\text{mm}^2$, $5 \text{ mW}/\text{mm}^2$, and $50 \text{ mW}/\text{mm}^2$ for the 5% films and $0.47 \text{ mW}/\text{mm}^2$, $6.8 \text{ mW}/\text{mm}^2$, and $29 \text{ mW}/\text{mm}^2$ for the 15% films. The excitation wavelength was 532 nm . Also shown are the modelled data assuming three B' values (dashed curves) and a time-dependent reduction in the oxygen concentration by chromophore photodegradation. Insets: Corresponding plots of the transmittance against $\beta/(\eta 2.67 \times 10^{19})$ where η is the photostability enhancement factor for (a) $1 \text{ mW}/\text{mm}^2$ (solid curve) $5 \text{ mW}/\text{mm}^2$ (dashed curve) and $50 \text{ mW}/\text{mm}^2$ (dot dash curve) and (b) for $0.47 \text{ mW}/\text{mm}^2$ (solid curve), $6.8 \text{ mW}/\text{mm}^2$ (dashed curve) and $29 \text{ mW}/\text{mm}^2$ (dotted curve).

One of the key merits of this model is that it removes the dependence on the initial photon flux and enables data to be compared when the incident photon flux

is varying. Analytical solution similar to that derived for the Dubois model [114, 24] is, unfortunately, not possible for this differential equations. A fit to the experimental transmittance data was found via numerical solution using the finite difference method in pascal. The data in Fig. 7.12 were modelled using this model where the optical intensities are low enough so that the oxygen concentration in the films can be considered constant. It can be seen that the use of 3 photodegradation quantum efficiencies and/or absorption cross sections provide a good fit to the data. The measured average absorption cross section, at 532 nm was $5.5 \times 10^{-17} \text{ cm}^{-2}$ for the 5 wt.% PYR-3/APC film and $7.8 \times 10^{-17} \text{ cm}^{-2}$ for the 15 wt.% PYR-3/APC film.

Table 7.2 – Table of parameters used to model the transmittance data in Fig. 7.11 and Fig. 7.12 for 2.4 μm thick 5% PYR-3/APC films at 532 nm. The initial chromophore number density, $N(0)$, was $8.37 \times 10^{19} \text{ cm}^{-3}$.

Light intensity, I (mW/mm ²)	1	5	50
$N_1(0)/N(0)$	0.7	0.71	0.71
$N_2(0)/N(0)$	0.23	0.2	0.2
$N_3(0)/N(0)$	0.07	0.09	0.09
B'_1	980	980	980
B'_2	6900	6900	6900
B'_3	29400	78400	78400
$N_{ox}(0)$ (cm ⁻³)	3.36×10^{18}	3.36×10^{18}	3.36×10^{18}
D (cm ² s ⁻¹)	–	3.2×10^{-8}	3.2×10^{-8}

The resultant fit parameters are listed in Tables 7.2 and 7.3 where $B'_i = \frac{\bar{\sigma}}{\sigma_i} B_i$. The 5% PYR-3/APC film can be fitted with a main component where $B'_1 = 980$. The corresponding main component for the 15 wt.% PYR-3/APC was $B'_1 = 1073$. These values are similar and indicate that the main photodegradation quantum efficiency does not strongly depend on the PYR-3 concentration. The results from photodegradation measurements at a range of intensities for 5 wt.% PYR-3/APC and 15 wt.% PYR-3/APC films are plotted in Fig. 7.12, where the film thicknesses were 2.4 μm and 2.05 μm , respectively. The transmittance data are plotted against $\beta/2.67 \times 10^{19}$ where $2.67 \times 10^{19} \text{ cm}^{-2}$ is the photon flux for an incident intensity of 100 mW/mm². Note that the maximum optical intensities are below the thermal damage threshold, which is 300 mW/mm² for 15 wt.% PYR-3/APC films.

Table 7.3 – Table of parameters used to model the transmittance data in Fig. 7.11 and Fig. 7.12 for 2.05 μm thick 15% PYR-3/APC films at 532 nm. The chromophore number density, $N(0)$, was $2.51 \times 10^{20} \text{ cm}^{-3}$.

Light intensity, I (mW/mm ²)	0.47	6.8	29
$N_1(0)/N(0)$	0.66	0.62	0.64
$N_2(0)/N(0)$	0.12	0.28	0.26
$N_3(0)/N(0)$	0.22	0.1	0.1
B'_1	1073	1073	1073
B'_2	5360	7660	25300
B'_3	8940	35800	31600
$N_{ox}(0)$ (cm ⁻³)	3.36×10^{18}	3.36×10^{18}	3.36×10^{18}
D (cm ² s ⁻¹)	–	1.35×10^{-8}	1.35×10^{-8}

The transmittance data were modelled using Eqs. 7.17-7.19. The best-fit curves for some of the data are plotted in Fig. 7.12 and the resultant best-fit parameters are listed in Tables 7.2 and 7.3. Note that $N_{ox}(0)$ is in the range of values obtained from solubility measurements on some other polymers where saturated oxygen concentrations range from approximately 1.9×10^{18} to $1.9 \times 10^{19} \text{ cm}^{-3}$ [126]. The oxygen diffusivities are reasonable given that measurements on some other polymers provide diffusivities as low as $2.4 \times 10^{-8} \text{ cm}^2 \text{ s}^{-1}$ [127]. We first consider the results from fitting the 5 wt.% PYR-3/APC thin film data. It is clear in Table 7.2 that the data can essentially be fitted with the same parameters and the only change is an increase in B' for the small fraction (N_3) that has the highest B' value. This shows that the photostability enhancement for high incident optical intensities can be reasonably described by oxygen-mediated photodegradation for low PYR-3 concentration.

It can be seen that $T(\beta)$ increases slowly for samples bleached at higher optical intensities. This enhancement can also be seen in the insets to Fig. 7.12 where $T(\beta)$ is plotted against β/η where η is the photostability enhancement factor obtained by scaling to the data with the lowest optical intensity. The data fall on a common curve for low intensities. For high intensities there is a small deviation for large β values. The resultant photostability enhancement factor is plotted in Fig. 7.13 for the different PYR-3 concentrations and a range of optical intensities, where it can show that the enhancement factor is higher for the higher PYR-3 concentrations.

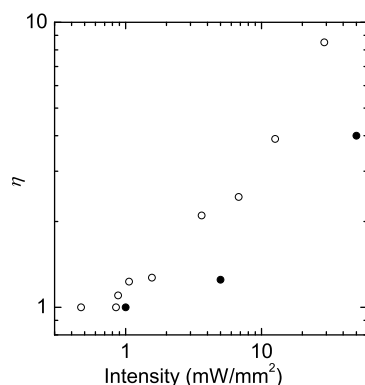


Figure 7.13 – Plot of the photostability enhancement factor, η , against light intensity at 532 nm for (a) a 2.4 μm thick 5% PYR-3/APC (filled circles) and (b) a 2.05 μm thick 15% PYR-3/APC (open circles).

7.5 Effects of film thickness

Physical conditions of the films can make a strong influence on the photostability of the chromophores dispersed in them. Experimental results of the photodegradation experiments made on 5 wt.% PYR-3/APC films of three different thickness are summarised in Fig. 7.14. Results show that, at a given intensity, the effective photostability of chromophores at a given intensity and oxygen partial pressure is directly proportional to the film thickness. Data shown in Fig. 7.14 shows the average photostability of the PYR-3 chromophore in APC has a linear relationship with film thickness, for a small thickness range of 2.4 μm to 7.5 μm .

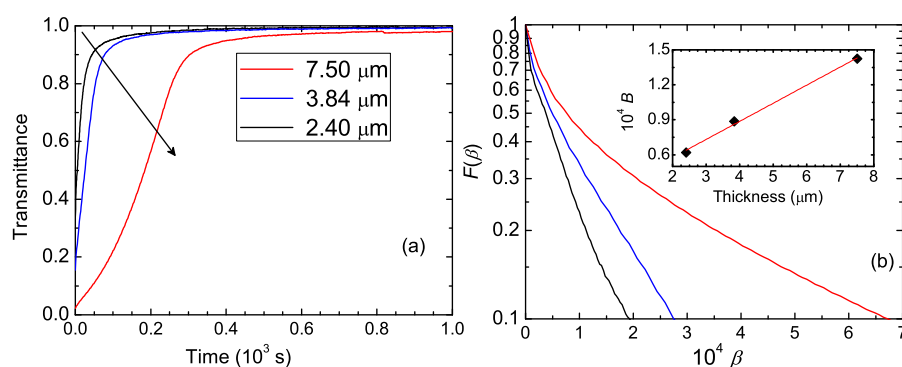


Figure 7.14 – (a) Transmittance data when photodegrading 5 wt.% PYR-3/APC films of 2.4 μm , 3.84 μm and 7.5 μm using 532 nm and intensity 50 mW/mm². (b) $F(\beta)$ vs. β plot for the same data. Inset shows the value of $B = \beta_{1/e}$ vs. film thickness.

It has already been demonstrated that the degraded product of PYR-3 does not absorb radiation at the irradiation wavelength [24, 67]. This result showed the

high photostability in this case is not due to the activity of bleached products. Transmittance of thick films are not expected to show any scattering losses that may lead to a reduction in the effective light intensity. The reduced photon flux with thickness due to the absorption by the chromophore molecules as observed from Eq. 7.17. The light intensity drops to $1/e$ value for thickness of about $2.5\mu\text{m}$. The film thicknesses need to be within the skin depth for the irradiating wavelength to get a good estimate of the photodegradation quantum efficiency. The intrinsic photodegradation quantum efficiency of the chromophore does not actually vary with thickness. The high estimate with thickness observed is due to the reduction in photon flux.

7.6 Effects of chromophore concentration

We have observed an enhancement in photostability when the chromophore concentrations are increased. Effects of chromophore concentration in films for a set of concentrations for IND-7 chromophores are shown in Fig. 7.15. This is similar to what is observed in the case of PYR-3 for 5 wt.% and 15 wt.% as shown in Fig. 7.11. However the change is large in the case of IND-7 compared to PYR-3. In PYR-3 $\beta_{1/e}$ for 5 wt.% and 15 wt.% are 1100 and 1400 respectively for the films of approximately $2\mu\text{m}$ thicknesses and light intensity $1\text{mW}/\text{mm}^2$. In the case of IND-7 for similar film thickness, the photostability, $\beta_{1/e}$, at a light intensity $15.7\text{mW}/\text{mm}^2$ nearly doubles when going from 3 wt.% to 8 wt.%. The increasing chromophore concentration effectively lead to a higher photostability in both chromophores we have investigated. The large change in IND-7 compared to PYR-3 is not unexpected because the effect of concentration is large at higher intensities. This can be observed in the intensity dependent photodegradation data of PYR-3 for 5 wt% and 15 wt% loading shown in Fig. 7.13.

One of the possible explanations for the enhancement of photostability by the chromophore concentration is due to the quenching of the singlet excited state via a non-radiative decay process [67]. This is possible by an exchange of the excited state energy between chromophores leading to a non-radiative recombination site. Chromophore aggregates can be considered as non-radiative recombination sites. Thus it is possible that higher concentration leads to increased aggregation and thereby an enhancement in the non-radiative decay process. This phenomena can be explained using the result that the quenching of average photoluminescence (PL) lifetime at

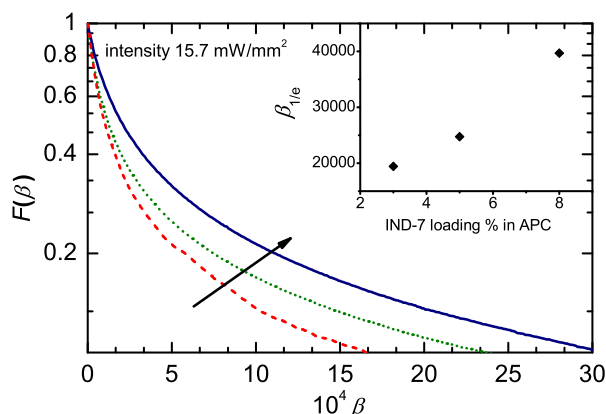


Figure 7.15 – Plot of $F(\beta)$ against β plot for three concentrations of IND-7 chromophores in APC with $2.1\mu\text{m}$ thickness when photodegradating with 655 nm laser and intensity 15.7 mW/mm^2 . Inset is the plot of $\beta_{1/e}$ against chromophore loading by wt% in APC.

higher concentrations that eventually leads to a reduction in the creation of singlet oxygen which in turn leads to an enhanced photostability. PL lifetime data showing the quenching of the singlet excited state lifetime with increasing chromophore concentration is explained in Ref. [67]. A substantial reduction in the average PL lifetime was observed when the chromophore concentrations increase from 0.1% to 10% [67].

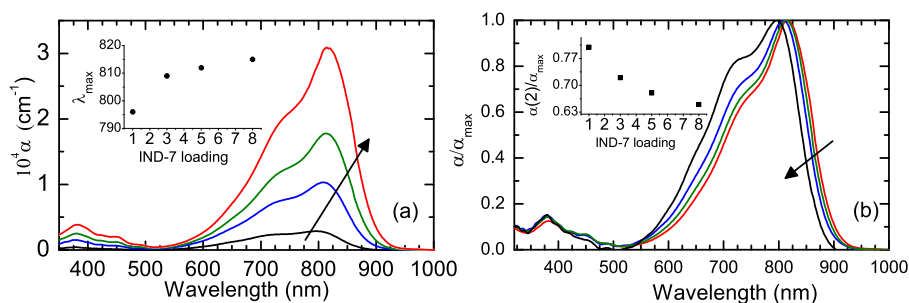


Figure 7.16 – (a) Absorption spectra of 1% (black solid curve), 3% (blue solid curve), 5% (green solid curve) and 8% (red solid curve) IND-7 film in APC; Inset is the plot of shift in the absorption maxima, λ_{max} with chromophore loading in APC. (b) Normalised absorption coefficient of the absorption spectrum, arrow indicates increasing concentration; Inset is the relative change in secondary maxima with λ_{max} .

Unfortunately, lifetime measurements were unable to be performed for IND-7 chromophores because the emission band of the chromophore is above 800 nm , which is beyond the limit of the experimental facility we have. The absorption spectra of 1% , 3% , 5% and 8% loading of IND-7 in APC is shown in Fig. 7.16. There

is a red-shift of absorption maxima with increasing concentration that is a sign of increased inter chromophore interactions at higher chromophore concentrations. The red-shift could also be due to an increased dielectric constant at higher loadings. One or more shoulders are observed in the absorption band of chromophores with long conjugation length [26, 84, 81]. Chromophores having a longer conjugation length are expected to be more susceptible for aggregation than those with a small conjugation length [26]. This could possibly be a reason for the large enhancement of photostability in IND-7 compared to PYR-3.

7.7 Strategies to achieve high photostability

Photodegradation experiments as well as results from the literature show that photodegradation can be reduced by reducing the oxygen concentration in the film. Other methods to enhance the photostability of chromophores are by quenching of the triplet state of the chromophore which is reacting with oxygen to produce singlet oxygen leading to the degradation of chromophores. Quenching of singlet oxygen is another possible way to reduce the rate of photodegradation. Also, it has been reported that the photostability of chromophore is an intrinsic property of the molecule. This section explain experimental results from systematic experiments to test the photostability of new chromophores synthesized by our group at IRL. Also, the effect of structural modifications made for high NLO effects is investigated. The effect of singlet oxygen quencher β -carotene to enhance photostability and the mechanism of enhancement is discussed.

Photostability of an NLO chromophore is highly structure dependent [128, 129, 124]. Investigating new chromophores with large and stable EO response together with adequate optical stability have been a subject of interest [113, 130, 63, 81]. We have made photostability experiments on chromophores of different classes. Some of them found to be more photostable than others. In all our photodegradation experiments the acceptor group is kept constant and the changes made are in the conjugation length as well as the donor group. Following sections investigate how some structural modifications made on chromophore molecules affect the photostability.

7.7.1 Bulky substitution on PYR-3

The inclusion of substituents that give the chromophore a more oblate, or disc shaped structure, are known to be the most effective in the work discussed in Chapter 5 towards developing chromophores showing a high and temporally stable electro-optic response, we have investigated a high and stable electro-optic response by the addition of a bulky substitute with PYR-3. The structure of the new chromophore with bulky substitution is shown in Fig. 7.17. The stability as well as a higher electro-optic response was achieved through reducing aggregation by reducing the interaction between neighbouring chromophores due to the bulky substituent. We have investigated how the substitution of bulky group have influenced optical stability of the system. It is important to ensure that improving one of the properties of the chromophore does not adversely affect other qualities of the system.

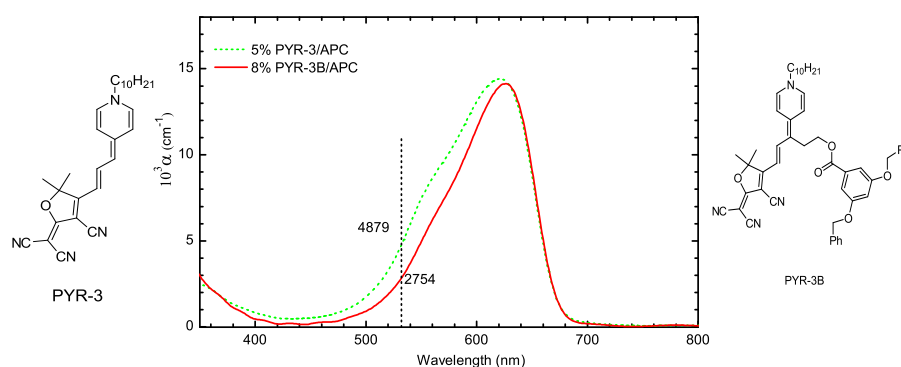


Figure 7.17 – Structures and absorption spectra of PYR-3 and PYR-3B in the films made of similar chromophore concentration and thicknesses in APC. Dashed line indicates the wavelength used to degrade the chromophores.

Fig. 7.18(a) shows the transmittance of both PYR-3 and PYR-3B having similar chromophore concentration in the film as a function of the number of photons times the irradiation time (total number of photons). The plot of $F(\beta)$ vs. β is shown in Fig. 7.18(b). Photodegradation experiments made at two different intensities show that the optical stability of the chromophore was not affected by the bulky substitute. Instead, an enhancement of photostability, though very little, was observed. Photodegradation experiments done at two different intensities and the results show that the trend is similar in both chromophores. The result show that the enhancement of NLO effect obtained by a bulky substitution in PYR-3 is achieved without compromising photostability of the system.

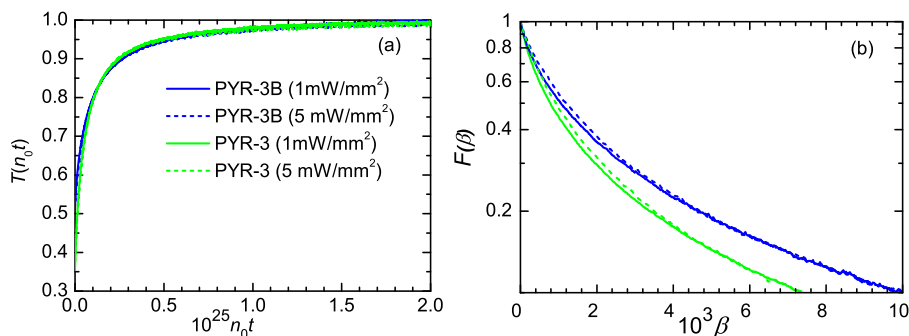


Figure 7.18 – (a) Plot of the transmittance at 532 nm against incident photon flux for a 8 wt.% PYR-3B/APC film (2.40 μm thick) with incident laser intensities of 1 mW/mm² (blue solid curve) and 5 mW/mm² (blue dashed curve), and a 5 wt.% PYR-3/APC film (2.37 μm thick) with incident laser intensities 1 mW/mm² (green solid curve) and 5 mW/mm² (green dashed curve) at room temperature. (b) Plot of $F(\beta)$ against β for incident laser intensities of 1 mW/mm² (solid curves) and 5 mW/mm² (dashed curves). The curves with high $F(\beta)$ values are from the 8 wt.% PYR-3B/APC film.

7.7.2 Partial ring-locking on IND-7 and QUN-7

The motivation to include partial ring-locking was based on the concept that the planarity of the chromophore can be increased as a result of ring-locking and that may possibly give a large molecular NLO activity. This will eventually lead to a large EO coefficient at the macroscopic level[83]. Ring-locking is also expected to increase the thermal stability of the chromophores [83]. Two chromophore used for the investigation of the effect of ring locking are QUN-7 and IND-7. The structures of IND-7 and QUN-7 and their ring-locked derivatives as well as the normalised absorption coefficients in films are shown in Figs. 7.21 and 7.19. The change in absorption spectra of the chromophores after ring locking have been analysed. The ring-locking lead to a red shift in the absorption maxima for QUN-7 (see Fig. 7.21) while in the case of IND-7 ring-locking broadened the spectrum with nearly the same intensity for both primary and secondary absorption maxima (see Fig. 7.19).

Fig. 7.20 shows the photodegradation experimental data for IND-7 and IND-7R chromophores in APC at similar chromophore loading with similar film thickness. The films are irradiated with a 655 nm laser at similar intensity. The average B value of IND-7 at 15.7 mW/mm² is 27258, while that for IND-7R is 20171. The result show that IND-7 is more photostable than IND-7R. That is the ring-locking lead to a reduction in the photostability of IND-7 chromophore.

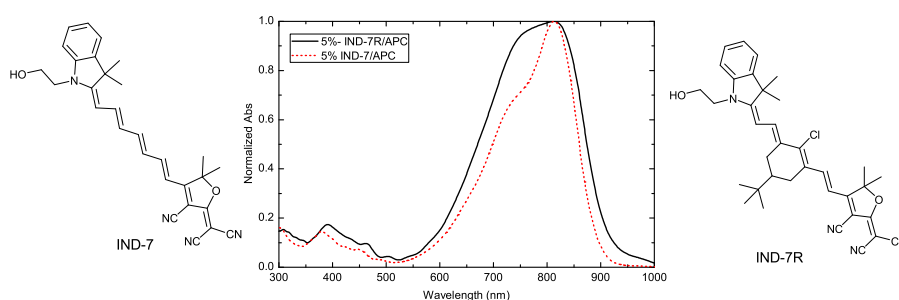


Figure 7.19 – Structures and absorption spectra of IND-7 and IND-7R in the films made of mixing similar chromophore concentrations, 5 %, and thicknesses, $2.2 \mu\text{m}$, in APC.

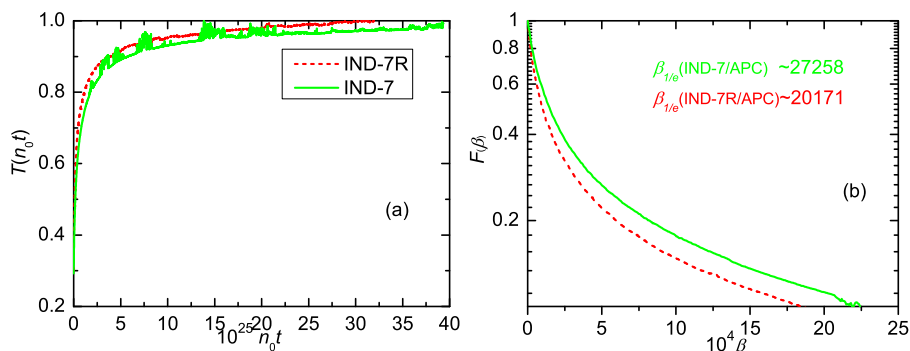


Figure 7.20 – (a) Plot of the transmittance at 655 nm against time for a $2.2 \mu\text{m}$ thick 5 wt.% IND-7/APC film (green solid curve) and a $2.1 \mu\text{m}$ thick 5 wt.% IND-7R/APC film (red dashed curve) for incident laser intensity of $35 \text{ mW}/\text{mm}^2$ (b) Plot of $F(\beta)$ against β .

Photodegradation experiments were performed in QUN-7 and QUN-7R chromophores. The films of QUN-7 and QUN-7R are prepared using similar chromophore concentrations and similar film thicknesses ($\sim 5 \mu\text{m}$) and are degraded using the same wavelength at similar optical intensity. This is important because it has been shown in previous sections that the physical conditions such as light intensity, chromophore concentration and film thickness can largely influence the estimated photostability of films. The results show a very large enhancement in the photostability after ring-locking. Photodegradation experimental results for QUN-7 and QUN-7R are shown in Fig. 7.22. The average B value of QUN-7 at the experimental conditions is 53290 and 216300 respectively at a light intensity of $10 \text{ mW}/\text{mm}^2$.

Results from the photodegradation experiments made on each set of films under similar experimental conditions that in IND-7 chromophores a reduced photostability as a result of ring-locking and a substantial enhancement in photostability in the

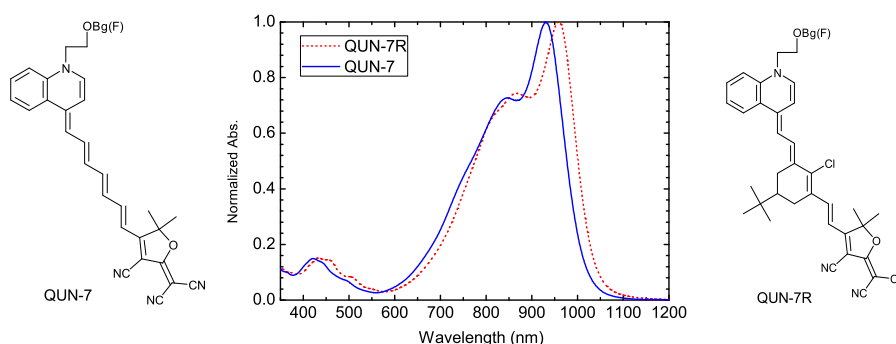


Figure 7.21 – Structures and absorption spectra of QUN-7 and QUN-7R in the films made of mixing similar chromophore concentrations in APC.

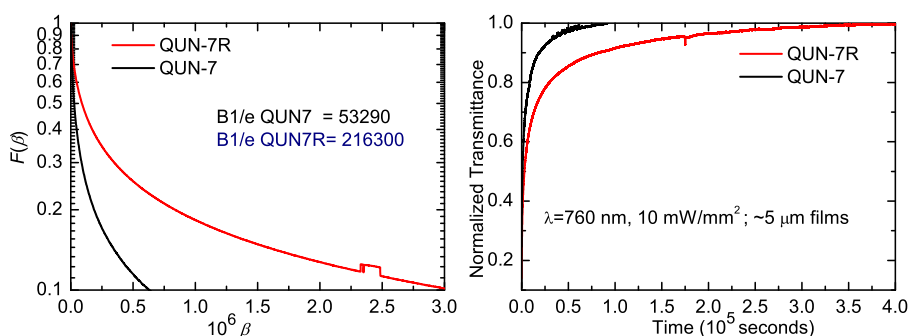


Figure 7.22 – (a) Plot of the Plot of $F(\beta)$ against β at 760 nm for a $5.1 \mu\text{m}$ thick 5 wt.% QUN-7/APC film (black solid curve) and a $5.06 \mu\text{m}$ thick 5 wt.% QUN-7R/APC film (red solid curve) for incident laser intensity of $10 \text{ mW}/\text{mm}^2$ (b) Plot of transmittance against time.

case of QUN-7 after ring-locking. The paradoxical behaviour that the ring-locking functions in opposite ways for IND-7 and QUN-7 needs further explanation. This effect is explained using the concept of bond length alternation (BLA) in Section 7.8.

7.7.3 Addition of singlet oxygen quencher

It has been explained from the intensity dependent photodegradation that the enhancement in photostability is due to the oxygen depletion. Previous studies have showed the exclusion of oxygen can lead to an enhancement in photostability [118, 24]. By adding additives to the polymer film it is possible to increase the photostability. These additives can improve the stability through different means of interaction, such as chemically reacting with singlet oxygen [131], quenching of singlet oxygen or quenching the chromophore singlet or triplet state [132, 125]. Structure of the oxygen quencher β -carotene we have used in our studies is shown in Fig. 7.23.

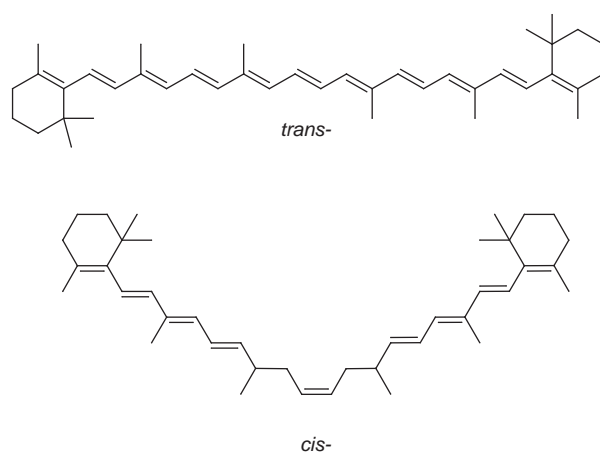


Figure 7.23 – Structure of *trans*- and *cis*- isomers of β -carotene.

Shown in Fig. 7.25(a) is the absorption coefficient from films with 5 wt.% PYR-3/APC and different β -carotene weight percentages. It was not possible to make films with more than 10% β -carotene by weight due to the limited solubility of β -carotene [67]. The broad band at ~ 465 nm arises from β -carotene [133]. This band has been attributed to a S_0 to S_2 transition that is electric dipole allowed and the resultant oscillator strength is high and, as expected, the lifetime of the excited state is very short (~ 100 fs) [133]. Unlike PYR-3, inter-system crossing is not expected. However energy transfer can occur as mentioned above for example via 1^1O_2 to 3^1O_2 and S_0 to T_2 . The band at ~ 330 nm arises from PYR-3 and β -carotene.

The results from photostability measurements at 532 nm and with intensities of 50 mW/mm² are plotted against $n_0t/(2.67 \times 10^{19})$ in Fig. 7.25(b) for a 5 wt% PYR-3/APC film and a similar film with 5 wt% β -carotene. It is apparent that there is an additional enhancement due to β -carotene. This photostability enhancement factor, ξ , can be obtained by scaling the data in Fig. 7.25(b) onto a common curve where the x-axis is $n_0t/(\xi \times 2.67 \times 10^{19})$. This has been done and the results can be seen in the inset to Fig. 7.25(b) where we find an enhancement factor of 6.7. Thus, there is clearly enhanced photostability by adding β -carotene, but it appears that β -carotene is also being degraded. This is unlikely to be due to direct excitation of β -carotene at 532 nm. This can be seen in Fig. 7.25(a) where the absorption coefficient from a 5 wt.% PYR-3/APC/10 wt.% β -carotene film is plotted before and after partial bleaching with a weak beam at 655 nm. It is clear that PYR-3 and β -carotene are being degraded even though the β -carotene absorption coefficient is negligible at this wavelength. Thus, it is likely that singlet oxygen is being generated

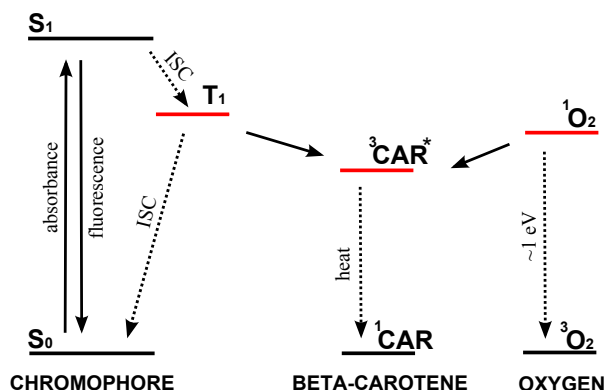


Figure 7.24 – Energy level diagram showing excitation of the PYR-3 chromophore (left) to the S_1 state, inter-system crossing (ISC) to the T_1 state, energy transfer to β -carotene (middle) that leaves PYR-3 in the ground S_0 state and β -carotene in the triplet excited state, and finally multi-phonon decay from the β -carotene excited triplet state to the singlet ground state. Also shown is another possible mechanism where ISC generates singlet oxygen. This can be followed by energy transfer from singlet oxygen (right) to β -carotene (middle) that leaves oxygen in the lower energy triplet state, and multi-phonon relaxation from the β -carotene triplet state to the singlet ground state.

by PYR-3 that then photodegrades β -carotene. The energy level diagram showing the quenching of triplet excited state as well as singlet oxygen are shown in Fig. 7.24.

7.8 Influence of bond length alternation on photostability

Effects of structural modification have been a subject of interest because similar type of ring-locking on two types of chromophores works paradoxically. Initially, the ring-locking was introduced to achieve larger hyperpolarisability via bond length alternation (BLA), together with a large optical stability. We find that in one of the chromophores, QUN-7, the ring-locking increases the optical stability while in other, IND-7 ring-locking reduced the stability. In this work we investigate how the electronic structure as well as the bonding of polyene chain are influenced by ring-locking. There are numerous research articles on the effects of BLA on molecular NLO effects of chromophores [23, 22, 19, 21]. However, as far as we are aware, the influence of BLA, which has a strong relationship with the strength of conjugated π -bridge has not been investigated so far. This section explain the relation between the photostability and NLO effect of a chromophore with a given donor-acceptor pair based on the concept of BLA.

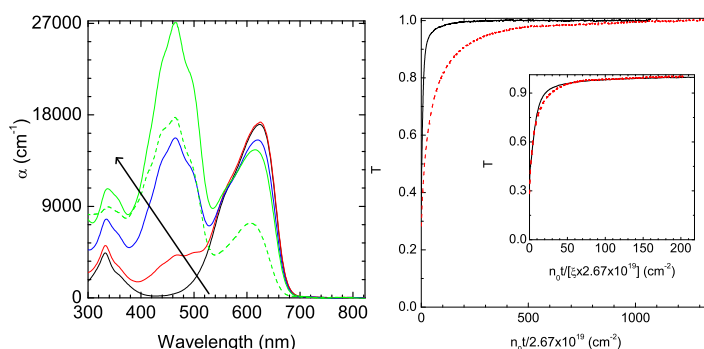


Figure 7.25 – (left) Absorption coefficient for films containing 5% PYR-3/APC and 0%, 1%, 5% and 10% β -carotene (solid curves). The arrow shows increasing β -carotene concentration. The 5% PYR-3/APC/10% β -carotene film was also illuminated at 655 nm with a wide beam and the resultant curve after partial photodegradation is also shown (dashed curve). Plot of the transmittance against $n_0 t / (2.67 \times 10^{19})$ during 50 mW/mm^2 illumination at 532 nm for (a) a $2.4 \mu\text{m}$ thick film with 5% PYR-3/APC (solid curve) (b) a $2.12 \mu\text{m}$ thick 5% PYR-3/APC with 5% β -carotene (dashed curve). Inset: Plot of the same data but now against $n_0 t / (\xi \times 2.67 \times 10^{19})$ where ξ is the β -carotene photostability enhancement factor.

In Section 7.7.2 we showed the effects of ring-locking on the photostability of a set of chromophores. Now, we explain how ring-locking related to BLA and thereby the molecular NLO effect. By combining these two effect it is possible to explain both NLO effect and photostability in terms of BLA.

7.8.1 Effects of ring-locking on the BLA of IND-7

The BLA values estimated from crystallography studies and are further verified using the solvatochromism analysis. The IND-7 molecule was found to show a slightly RHS nature with BLA value -0.0144 \AA . After ring-locking at the centre of the conjugated π -bridge, the resulting IND-7R chromophore have shifted towards LHS positioning in the neutral polyene limit having larger BLA value. Absorption spectra of IND-7 and IND-7R are shown in Fig. 7.26 and the structural and electronic properties are summarized in Table 7.4.

Bond lengths of the chromophores are estimated from the crystallography data. Average length of double bond of the conjugated bridge of IND-7, $D_{av} = 1.40178 \text{ \AA}$ and average single bond length is, $S_{av} = 1.3873 \text{ \AA}$, so the BLA is $S_{av} - D_{av} = -0.0144 \text{ \AA}$ [82]. In the case of IND-7R, $D_{av} = 1.3751 \text{ \AA}$ and $S_{av} = 1.410 \text{ \AA}$ giving $\text{BLA} = +0.035 \text{ \AA}$ [79]. That is according to BLA values, IND-7 is slightly RHS chromophore but the magnitude of BLA is very low, and IND-7R is LHS and the

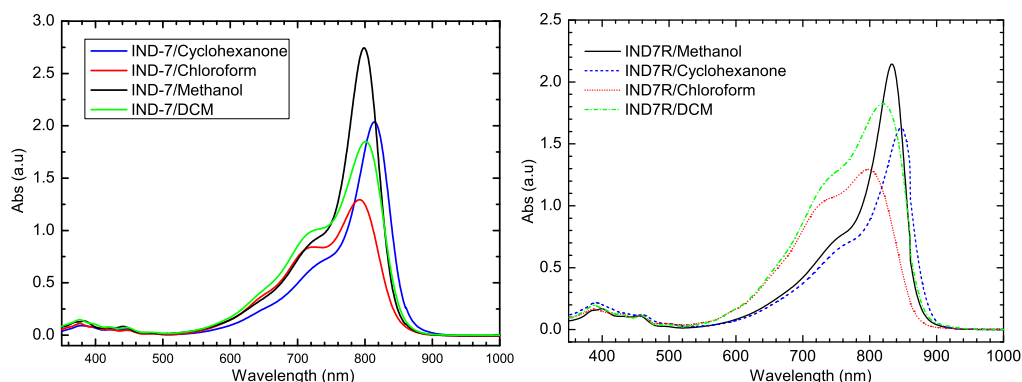


Figure 7.26 – Absorption spectra of (a) IND-7 and (b) IND-7R in solutions of different $E_T(30)$ values. A very small blue-shift observed in λ_{max} for IND-7 with $E_T(30)$ is sign of small RHS nature, a large red-shift of λ_{max} with $E_T(30)$ in IND-7R represent its LHS nature.

magnitude of BLA is relatively large. Chromophores solvatochromism [28] behaviour was also investigated to confirm whether the molecule is LHS (neutral) or RHS (zwitterionic) from their interaction with solutions of different $E_T(30)$ values.

Both tests hint to the same result that the magnitude of BLA for IND-7R is larger than that for IND-7. That is in terms of BLA, the result from Section 7.7.2 can be explained that increasing magnitude BLA value of IND-7 chromophore caused a reduction in photostability.

Table 7.4 – Structural and electronic properties of IND-7 and IND-7R. Absorption maxima, λ_{max} , in films and in selected solvents having different $E_T(30)$ values are summarized.

Chromophore / Solvent property	$\lambda_{max}(\text{nm})$					BLA (A)
	Films	CHCl_3	DCM	Methanol	Cyclohex.	
IND-7	813	791	801	799	815	-0.0144
IND-7R	813	800	820	850	870	+0.0350
ϵ_r (Solvent)	–	4.8	9.08	33.0	18.2	–
$E_T(30)$ (Solvent)	–	39.1	40.7	55.4	39.8	–

7.8.2 Effects of ring-locking on the BLA of QUN-7

Absorption spectra of QUN-7 and QUN-7R are shown in Fig. 7.27 and the structural and electronic properties are summarized in Table 7.5. The solvatochromism test

shows that both QUN-7 and QUN-7R are RHS chromophores with strong zwitterionic character. QUN-7 and QUN-7R did not give high quality crystals to perform the direct bond length measurement from the crystallography data. The BLA values of these chromophores were estimated using “Molecular Orbital PACKage” (MOPAC) calculation using the ChemDraw[®] Ultra software. Calculated BLA of QUN-7 is -0.091 Å and that of QUN-7R is -0.062 Å. The calculated BLA values are reconfirmed using the solvatochromism test. The interaction of the chromophore with solvents of $E_T(30)$ values are similar to what is expected from the calculated BLA.

Results show that ring-locking cause a reduction in the magnitude of BLA of QUN-7. The findings can now be explained in Section 7.7.2 in terms of BLA that the photostability increased when the magnitude of BLA approaches zero. Effect of BLA on photostability is similar to what is observed in the case of IND-7.

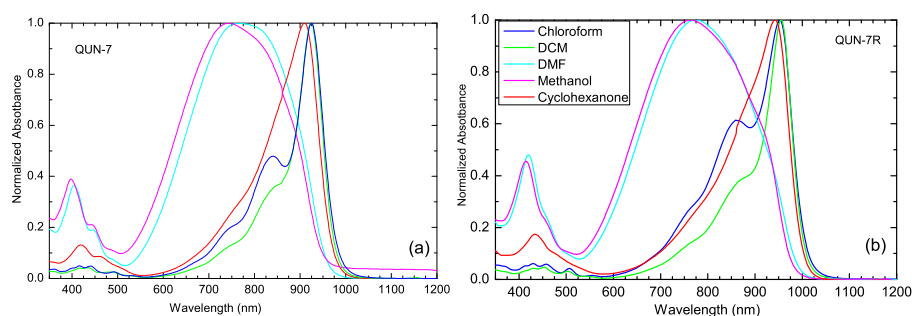


Figure 7.27 – Normalised absorption spectra of (a) QUN-7 and (b) QUN-7R in solutions of different $E_T(30)$ values. Both chromophores show large red-shift of λ_{max} with $E_T(30)$ representing their RHS nature.

Table 7.5 – Structural and electronic properties of QUN-7 and QUN7R. Absorption maxima, λ_{max} , in films and in selected solvents having different $E_T(30)$ values. The symbol, * indicates the BLA values are semi empirical values calculated using MOPAC.

Chromophore / Solvent property	λ_{max} (nm)					BLA (Å)
	Film	CHCl ₃	DCM	Methanol	Cyclohex.	
QUN-7	928	925	924	742	910	-0.091*
QUN-7R	957	952	955	766	942	-0.062*
ϵ_r (Solvent)	–	4.8	9.08	33.0	18.2	–
$E_T(30)$ (Solvent)	–	39.1	40.7	55.4	39.8	–

7.8.3 Trade-off between hyperpolarisability and photostability

The relationship between BLA and the molecular NLO effect has been identified previously where BLA can be used as a universal parameter determining the molecular nonlinearity of a push-pull chromophore [18, 23, 19, 21, 134]. However, the effects of BLA on the photostability of chromophores has not been investigated so far.

Table 7.6 – Relationship between the magnitude of BLA values and corresponding photostability (B) of IND-7 & IND-7R ($\sim 2 \mu\text{m}$ thick, light intensity $35 \text{ mW}/\text{mm}^2$), and QUN-7 & QUN-7R ($\sim 5 \mu\text{m}$ thick, light intensity $10 \text{ mW}/\text{mm}^2$) for similar chromophore loading.

	BLA	B		BLA	B
IND-7	0.0144	27258	QUN-7	0.091	53290
IND-7R	0.0350	20171	QUN-7R	0.062	216300

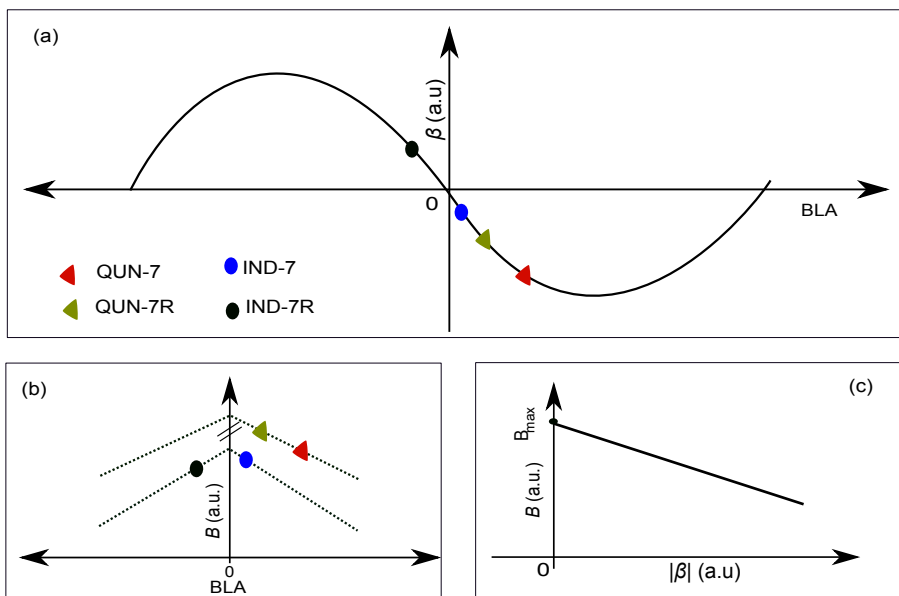


Figure 7.28 – (a) Schematic representation of shifting the BLA values of IND-7 and QUN-7 when ring-locking. BLA approaching zero reduce the molecular hyperpolarisability responsible for the NLO property of chromophore. (b) Schematic representation of change in photostability for IND-7 and QUN-7 with BLA from the data given in Table 7.6. (c) Schematic of the relation between first hyperpolarisability β_0 and photostability B . Change in BLA may or may not be linear, it can be other forms depending on the change in bond strength when the nature of the conjugated π -bridge approaches neutral polyene limit.

Our results show that, for a push-pull system with a given donor and acceptor, there is a trade-off between the optical stability and NLO property of the chromophores. That is a larger BLA correspond to a large first hyperpolarisability [19]. However, at the same time our results show that larger the magnitude of BLA value lead to a reduced photostability. Also, we found the reduction in photostability with BLA is related only to the magnitude of the BLA value and not the sign. In the case of first hyperpolarisability also, the hyperpolarisability is related to the magnitude and not the sign of the bond order alternation. The findings are summarized in Table 7.6 and a schematic representation is shown in Fig. 7.28.

Combining the result from our photostability experiments, and the well established concept of the relation between BLA and first hyperpolarisability show a trade-off between both. That is for a given donor-acceptor pair, any structural alterations leading to increase the molecular NLO effect result in a reduced photostability. There is a trade-off between the NLO effect and optical stability of NLO chromophores. The experiments have been made only on four different chromophore with two set of donor and acceptor. A more detailed study is required to generalize this effect as a universal relationship as observed in the case of BLA and first hyperpolarisability.

7.9 Conclusions

Photodegradation quantum efficiency of the chromophores at different chromophore concentration as well as light intensities were performed and the mechanism of enhanced photodegradation quantum efficiency at high optical intensity is explained using a model based on oxygen mediated photodegradation. Photodegradation model based on multiple photodegradation quantum efficiencies has been used to explain a more realistic photodegradation mechanism. The effect of chromophore concentration on photostability is explained using the inter-chromophore energy transfer mechanism. Methods to enhance optical stability via quenching of singlet oxygen and by quenching of triplet excited state of the chromophore were investigated using a singlet oxygen quencher β -carotene. Effects of structural alterations on photostability of chromophores are investigated. Addition of bulky group for enhanced EO response showed no reduction in optical stability demonstrating an over-all enhancement in efficiency due to the bulky substitution. A paradoxical result from ring-locking in two different chromophores were explained using BLA

parameter. A trade-off between the NLO property and photostability is observed in the chromophore of a given donor-acceptor pair.

Further studies need to be done on the relationship between BLA and photostability. Currently, investigations were done only on a set of four chromophores. Also, two of the chromophores did not give good crystals that made the crystallography study difficult. To extend this study experiments need to be done on a number of chromophores made of same donor and acceptor but different BLA values. This will help to develop a general relationship between BLA and photostability that leads to develop a correlation between the optical stability and molecular first hyperpolarisability.

Chapter 8

Material Characterisation at THz Frequencies

This chapter is divided mainly into two sections. The first part deals with the evaluation of the efficiency of polymer electro-optic (EO) materials to use as active components of terahertz (THz) devices. The second part of this chapter discusses the characterisation of some organic materials in the THz frequency range using Raman and THz spectroscopy.

One of the key benefits of using organic EO polymer materials as active components of THz generation and detection system is their applicability in the wider THz region. This is possible because of the lack of a strong absorption or refractive index dispersion in amorphous polymer materials in the THz frequency range [33]. The properties of polymers can vary from one material to another. For example, PMMA polymers show absorption of THz radiation above 1.6 THz [10]. This demands the polymer host used in film fabrication as well as the polymer containing the chromophore to be tested in THz frequency range. This will help ensure sufficient coherence length for THz generation from optical radiation using the property of the EO polymers. The power of THz radiation generated using EO process is proportional to the square of the thickness of EO material as long as the phase matching conditions are satisfied. The efficiency of THz detection is also proportional to the thickness of the polymer film. However, it is important that the maximum thickness of the material should not exceed the coherence length. Another key requirement to qualify an EO material for THz applications is the absence of crystalline phonons that are active in the THz region. The efficiency of THz generation and detection using a polymer

EO material made of PYR-3 chromophore and amorphous polycarbonate (APC) is discussed in this chapter. The following paragraph gives an introduction to the experiments performed to investigate the properties of some organic materials in the THz region using infrared (IR) and Raman spectroscopy.

Hydrogen bonded carboxylic acid dimers are being extensively studied to obtain a better understanding of systems with intermolecular hydrogen bonds, which are strong enough to determine the structure of the compound. Researchers have proposed novel techniques to acquire more information about the Fermi resonance in hydrogen bonded compounds by analysing both low and high frequency vibrational modes of the molecules [135]. A detailed understanding of the spectra at low wavenumbers is necessary to achieve further improvements in this field. In a molecule with a centre of symmetry it is expected that vibrations that are Raman active are IR inactive and vice-versa because of the different selection rules. Both IR and Raman active spectra are required to obtain a more detailed information about the vibrational modes of materials under study. Conventional Fourier transform IR (FTIR) spectrometers can cover most of the THz region. However, exploring the IR active vibrational modes in the lower THz frequency region is primarily hindered by poor access to the THz frequencies. Most of the vibrational modes related to intermolecular hydrogen bonding have clearly identifiable signatures in this region. Low wave-number Raman and the corresponding IR spectra in the THz region for benzoic acid and some of its derivatives as well as other materials such as Aspirin, 4-nitrotoluene (4-NT) and 2,4-dinitro toluene (2,4-DNT) are discussed. Effects of temperature on the low energy vibrational modes of the 2,4-DNT and salicylic acid are investigated using low energy Raman spectroscopy. The experimental data were interpreted using the literature values as well as results from density-functional theory (DFT) calculations using the GAUSSIAN 09 [136] package.

8.1 THz generation and detection using EO polymers

Difference frequency generation (DFG) or optical rectification (OR) using the electro-optic (EO) effect of materials is an efficient method to generate THz radiation [33]. Inorganic EO materials are usually not suitable for wideband THz generation and detection because of the presence of crystalline phonons leading to the absorption of THz radiation. Strong absorption and dispersion of refractive index are characteristic to the EO crystals in the wider THz region. This section discusses the results

from the calculations using the THz dielectric properties of polymer EO materials containing organic NLO polymers to investigate their efficiency for THz generation and detection. In particular, investigating their refractive index and absorption in the THz frequency range as well as estimating the coherence length for THz generation and detection. This is important because THz power as well as the detector sensitivity are proportional to the thickness of the EO material if the thickness of the material is less than its coherence length [9, 137].

8.1.1 Phase matching

A phase-sensitive NLO processes requires minimum phase mismatch for the maximum result, this means ensuring a proper phase matching between the interacting waves along the propagation direction. Amplitude contributions from different locations to the output wave that are all in phase at the end of the nonlinear crystal is maintained only when the phase matching condition is satisfied. For example, in a second harmonic generation (SHG) process if two waves with the same wave vector k_1 interact to give the second harmonic k_2 , the phase mismatch between the two waves can be expressed using the refractive indices of the material for the fundamental and the second harmonic signal, $\Delta k = 2\pi(2\frac{n_1}{\lambda_1} - \frac{n_2}{\lambda_2})$. The distance that a signal can go through a medium without changing a relative phase difference between two waves in the medium is referred as coherence length, that can be expressed as, $L_c = \frac{\pi}{\Delta k}$. Maximum coherence length is achieved when Δk is zero. Because of the dispersion of the refractive index of a medium, phase matching occurs only for a narrow range of frequencies. In the context of THz generation using optical rectification, the appropriate velocities that need to be considered are the optical group velocity associated with the short pump pulse and the THz phase velocity associated with the generated wave. The coherence length is small if the difference in optical group index and THz refractive index is large [33].

8.1.2 Phase matching for THz generation

Optical rectification is one of the most common techniques being used for THz generation using electro-optic EO materials. THz generation using optical rectification involves difference frequency wave mixing between Fourier components of the same optical pulse. The output THz power, $P(\omega_{\text{THz}}, L)$, in this case can be expressed using the equation [137],

$$|E(\omega_{\text{THz}}, L)|^2 = \frac{\omega_{\text{THz}} d_{\text{eff}}^2 E_0^4 \tau^2}{8\pi c^2 n_1^2} L^2 \exp(-\tau^2 \omega_{\text{THz}}^2 / 4) \text{sinc}^2(\Delta k L / 2) \quad (8.1)$$

where ω_{THz} is the angular frequency of THz radiation, d_{eff} is the effective second order NLO coefficient ($d_{\text{eff}} = \chi^{(2)}/2$), L is the film thickness and τ is the pulsewidth.

Eq. 8.1 shows that the power of THz radiation generated using OR is proportional to the squares of the thickness and the EO coefficient of the emitter. However, in the presence of a phase mismatch (i.e. $\Delta k \neq 0$), for maximum output power the thickness of the emitter is limited to the coherence length (L_c). The coherence length for THz generation using near infrared laser pulse is given by [34],

$$L_c = \frac{\pi}{\Delta k} = \frac{\pi c}{\omega_{\text{THz}} |n_g - n_{\text{THz}}|} \quad (8.2)$$

where,

$$n_g = \frac{c}{v_g} = n_{\text{opt}} - \lambda_{\text{opt}} \left(\frac{\partial n_{\text{opt}}}{\partial \lambda} \right) \Big|_{\lambda_{\text{opt}}} \quad (8.3)$$

In Eqs. 8.2 and 8.3, c is the light velocity, ω_0 is the frequency of pump beam, n_{opt} is the refractive index at optical pump beam wavelength λ_{opt} , and v_g and n_g are the optical group velocity and refractive index respectively.

If the refractive indices of the pump beams and the THz waves are identical, then the bandwidth of THz radiation depends only on the pulse width of the incident pump beams. The importance of considering the coherence length is related to the fact that the THz amplitude generated through wave mixing increases with the thickness of the nonlinear medium. The linear electro-optic effect experienced by the pump signal is proportional to the film thickness. However, if there is a phase mismatch, the resulting THz amplitude will drop considerably and this leads to the importance of finding the material which provides a large coherence length and hence efficient THz generation and detection [33, 34]. It can be shown that the power will vary periodically and reach a maximum when the thickness of the film is the same as coherence length.

It is noteworthy that in an electro-optic material, the THz emission strength increases with increasing thickness of the material but due to the increase in phase mismatch the bandwidth decreases with increasing thickness. Which means that the bandwidth of THz signal has a reciprocal relationship with the THz power unless

$$\Delta k = 0 [9].$$

8.1.3 Phase matching for THz detection

Electro-optic sampling is being used as an efficient technique for THz detection, where an EO material is used as the active material. The change in phase of the probe beam due to the THz electric field is used to detect THz radiation in this technique. The prominent feature of this method is it can simultaneously measure the amplitude and phase of the THz pulse. The electric field of the THz radiation induces a change in the refractive index of the EO material through the EO effect as $\delta n = -n^3 r_{33} E_{\text{THz}}$, where n is the refractive index for the probe beam in the material, r_{33} is the EO coefficient of the material. Then the phase retardation can be expressed as, $\phi \propto \delta n \frac{l}{\lambda}$, where λ is the wavelength of the probe beam and l is the thickness of the sensor. The sensitivity of the detector is thus directly proportional to the EO coefficient of the detector as well as the thickness of the detector. That is phase matching has to be satisfied in THz detection using EO sampling [34].

8.2 Properties of polymers in THz region

Amorphous polymeric EO materials are not prone to strong absorption or dispersion of the refractive index associated with the lattice phonon resonance observed in crystals. This property qualifies the polymer materials to be used in wide band and gap-free THz generation and detection where many of the inorganic crystals show poor performance [138]. Furthermore, the phase mismatch between the pump and THz waves have been found very little in polymer materials leading to an increased coherence length and thereby achieving powerful THz radiation. In this work the APC polymer as well as the film made of APC and PYR-3 are analysed in THz frequency regime. Experiments made to investigate the presence of any strong absorption or index dispersion in chromophores are discussed. Polymer samples for THz-TDS were prepared by solution casting technique as explained in Chapter 4. Samples of higher thickness are preferred over thinner films mainly because the Etalon effect due to the multiple reflection at the air/sample/air interface [9]. THz-TDS data of polymer films is provided by the THz research group at the University of Auckland. The time domain data was then converted into frequency domain using the Fourier transform analysis using the procedure explained in the following section.

8.2.1 THz time domain spectroscopy

The concept of THz-TDS is collecting information about the materials dielectric properties as the THz pulse passes through the material. The change caused to the amplitude and phase of the sample data compared to the reference data is used to extract the refractive index and the absorption spectrum of the material. For the analysis of the polymer films Details of experimental set up of THz-TDS system have been discussed in Ref. [9]. The basic principle of transforming the THz -TDS data of a sample to the material properties such as refractive index as well as the absorption coefficient is explained below.

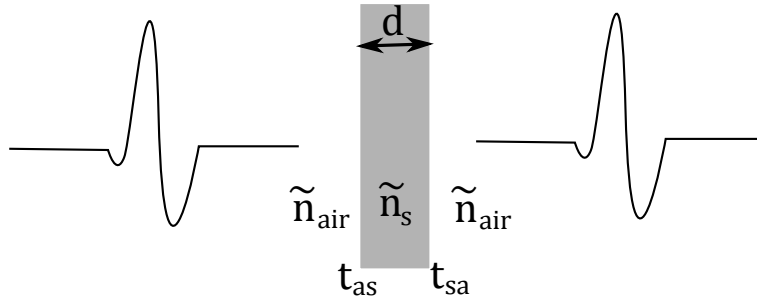


Figure 8.1 – Scheme of THz-TDS in transmission mode.

Fig. 8.1 shows the schematic of a sample with thickness d and a complex refractive index \tilde{n}_s placed on the path of a THz beam. Electric field of THz signal in time domain $E(t)$ can be transformed to frequency domain using the basic Fourier transform method as:

$$E(\omega) = \frac{1}{2\pi} \int_{-\infty}^{\infty} \exp(-i\omega t) E(t) dt \quad (8.4)$$

Assuming the thickness of the sample is d , the electric field transmitted through the sample and the reference can be written as,

$$E_S(\omega) = E(\omega) \phi_S(\omega, d) t_{as} t_{sa} \quad (8.5)$$

$$E_R(\omega) = E(\omega) \phi(\omega, d) \quad (8.6)$$

where ϕ_S is the phase retardation due to the sample, t_{as} and t_{sa} are the transmission coefficients at air/sample and sample/air respectively that can be related to the complex refractive index of the sample $\tilde{n}_s (= n_r + jn_i)$ using the relation,

$$t_{as} = \frac{2}{1 + \tilde{n}_s} \quad (8.7)$$

$$t_{sa} = \frac{2\tilde{n}_s}{1 + \tilde{n}_s} \quad (8.8)$$

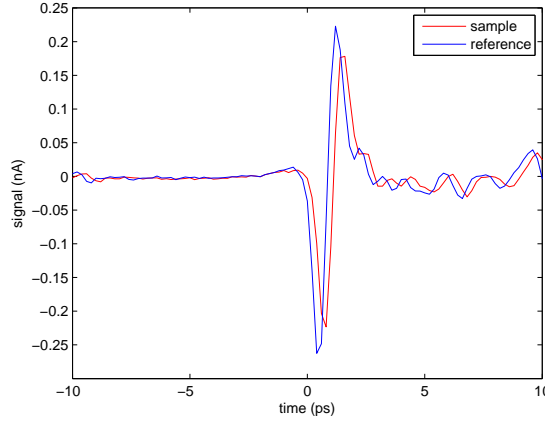


Figure 8.2 – Time domain THz data collected for a $320 \mu\text{m}$ 5 wt.% PYR-3/APC film with air as reference. Time delays are relative to each another.

The phase delay of the THz pulse passing through the sample of thickness d in frequency domain can be written as,

$$\phi_s(\omega, d) = \exp\left(-i \frac{\tilde{n}_s \omega d}{c}\right) \quad (8.9)$$

Fourier transform of the data was done using a Matlab program and phase delay due to the sample is obtained unwrapping the phase of the Fourier transform output in frequency domain. The refractive index and absorption coefficient of the sample can be estimated using the equations,

$$n_r(\omega) = 1 + \frac{c}{\omega d} \phi_s \quad (8.10)$$

and,

$$\alpha(\omega) = -\frac{2}{d} \ln \left(\frac{(n_r(\omega) + 1)^2}{4n_r(\omega)} \frac{E_s(\omega)}{E(\omega)} e^{-i\phi_s(\omega)} \right) \quad (8.11)$$

Fig. 8.2 shows the THz time domain data of a sample and the reference data under investigation. The time delay and the change in amplitude between the sample

and reference is due to the phase retardation due to the complex refractive index of the material.

8.2.2 Absorption in the THz region

Absorption of NLO polymers in the frequency region is investigated to test the interaction of the EO polymer with electromagnetic radiation in the THz frequency range. THz-TDS have been made on films containing 5 wt.% PYR-3/APC with $320\ \mu\text{m}$ thickness. Results show no strong absorption in the THz region. Fig. 8.3 show the absorption of EO polymers in THz frequency region measured using THz-TDS and for wider frequency range collected using a FTIR spectrometer. The results matches with the recent results reported in Ref. [10] based on the study of a number of organic NLO materials in a range of polymer materials.

The offset in the FTIR absorption spectra is attributed to the frequency independent absorption of APC. There is no strong absorption observed between 0.2 and 10 THz for this material. Strong absorption peaks observed above 10 THz is not a problem because it is outside our frequency of interest.

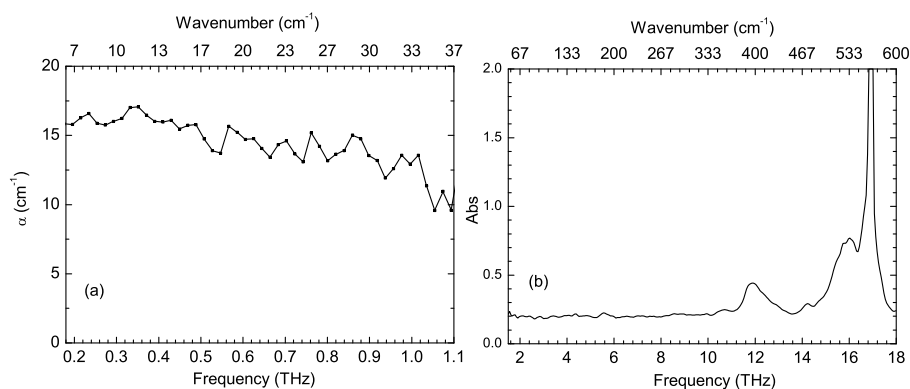


Figure 8.3 – (a) Absorption spectrum of a 5 wt% PYR-3/APC film between 0.2 and 1.1 THz estimated from THz-TDS data (b) Absorption spectrum of a similar film between 2 and 18 THz obtained using a FTIR spectrometer.

8.2.3 THz refractive index

The refractive index of film made of APC mixed with 5 wt.% PYR-3 in the THz frequency is shown in Fig. 8.4(a). The short frequency range (0.2 to 1.1 THz) is due to the small bandwidth of the THz system we have access to. Apart from the expected noise fluctuations the data show no dispersion of refractive index in

THz region. In general, the chromophores do not cause substantial change in the refractive index of the host film, that is if the host polymer APC does not show any strong refractive index dispersion, the same can be expected for the film containing the chromophores for small loading percentages [10]. The refractive index estimated for the THz frequency range is used to calculate the coherence length for THz generation.

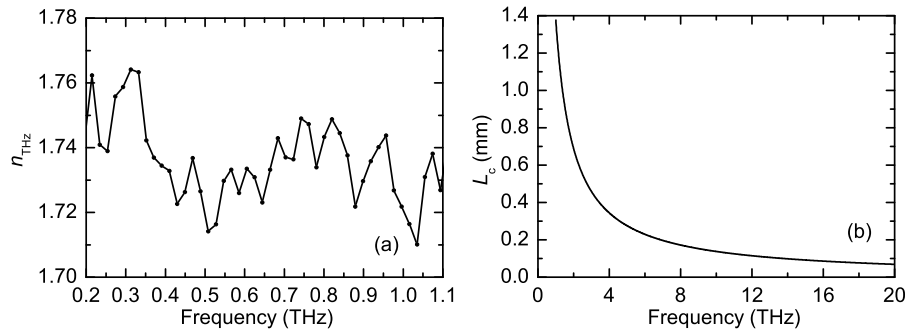


Figure 8.4 – (a) Refractive index of a 5 wt% PYR-3/APC for the range 0.2 to 1.1 THz. (b) Calculated coherence length for THz generation via optical rectification using a femtosecond pulse centred at 1550 nm in a PYR-3/APC film using the THz refractive index and optical group index at 1550 nm.

8.2.4 Coherence length for THz generation using PYR-3/APC

The refractive indices are measured for a set of wavelengths using the Metricon (see Chapter 3) and the refractive index dispersion with wavelength is approximated by the Sellmeier equation to estimate the optical group index using the data in Fig. 4.4 (in Chapter 4) where $n_{opt} = 1.528$. The coherence length for THz generation was then estimated using the THz refractive index and the optical group index. The simulation of coherence length is based on the assumption that the material shows no refractive index dispersion in the THz region outside the range we have measured.

The coherence length is calculated for THz generation using a femtosecond beam with centre frequency 1550 nm and using optical rectification technique is shown in Fig. 8.4(b). The result show that L_c for THz generation of bandwidth up to 10 THz using a 5 wt.% PYR-3/APC film is more than 150 μm . Such a large coherence length together with a large EO coefficient show that EO polymers have potential to be used for wideband generation and gap-free detection of THz radiation. Research groups, for example as shown in Ref. [138] demonstrated high power, wide band

generation and gap-free detection of THz radiation for the range of up to 10 THz.

There is a trade-off between THz power and bandwidth, that is a wider bandwidth lead to a shorter coherence length and thus one may ends up with choosing thinner EO material. This lead to a lower THz power. Very large EO coefficient of the EO polymers can also be a solution. It is because of two useful properties of polymers. First is, the small dispersion of refractive index observed in polymer EO materials and second one is the very large EO coefficient of the polymer EO materials. It makes possible to get better power output by using thinner films and thus better bandwidth [33].

8.2.5 Raman and IR on APC film

In most cases Raman scattering is sensitive to the degree of crystallinity in a sample. Typically, a crystalline material yields a spectrum with very sharp, intense Raman peaks, while an amorphous material show broader less intense Raman lines. Pure amorphous, or pure crystalline can be considered as spectral extremes, and a Raman spectrum from an intermediate state will have characteristics which are intermediate in terms of peak intensity and width. Differences between intermediate states can be subtle, and it is often useful to have high spectral resolution capability so that minor spectral changes can be confidently characterised. Raman spectrum of APC film is shown in Fig. 8.5. The data shows a broad Raman response with no sign of any strong lines in the THz region. This is useful to reconfirm the result observed from the FTIR spectrum of APC.

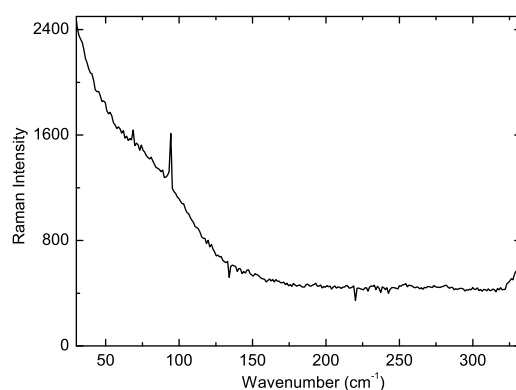


Figure 8.5 – Low wavenumber Raman spectra of APC.

8.3 Low energy vibrational spectra of organic crystals

Benzoic acid crystals are being used extensively for investigating the properties of intermolecular hydrogen bonds. This is because the molecules are planar with a C_s symmetry group that crystallises into a monoclinic unit cell with a $P2_1/c$ space group that has 4 molecules in the unit cell [139]. The crystalline form consists of two monomers linked by hydrogen bonds leaving a centrosymmetric structure. Benzoic acid and its derivatives generally exist in dimer form in crystals as shown in Fig. 8.6. We report low wave-number Raman and the corresponding IR spectra in the THz region for benzoic acid and two of its derivatives, 2-hydroxy and 3-hydroxy benzoic acids. The experimental data were interpreted using the calculated literature values as well as results from density-functional theory (DFT) calculations at the level of B3LYP/6-31G* using the GAUSSIAN 09 [136] package.

8.3.1 Experimental details

Samples for the THz and FTIR spectroscopy measurements were prepared by mixing 5 - 20 wt% of the crystalline powders with a commercial polymer powder branded as Polyblend 100XF (PB100XF) supplied by Micropowder Inc., USA. Polyblend 100XF (PB100XF) is a mixture of high density poly ethylene (HDPE) and poly tetra fluoro ethylene (PTFE). The selection of PB100XF for preparing samples for THz-TDS and FTIR spectroscopy was motivated by the recent report by Scherger *et al.* [140] that pressed pellets of a mixture of PB100XF can be used to make low-loss THz lenses [140]. Use of PB100XF for sample preparation instead of conventional additives, such as polyethylene provided sturdy pellets compared to pressed pellets of polyethylene. Also, there is no strong absorption or refractive index dispersion for this material in the wider THz frequency range except for a relatively narrow absorption band near 6 THz as shown in Fig. 8.8.

Pellets with a thickness of 1.0 to 1.5 mm and a diameter of 9 mm were pressed in a die at 4500 psi for 30 seconds. THz spectra in the 0.5 to 2.5 THz frequency range were collected using a Z-Omega (Z-3) THz system at University of Wollongong. The system was purged with nitrogen gas. This THz system gave spectral features up to 2.5 THz ($\sim 80\text{ cm}^{-1}$). Far-IR absorption for energies above 80 cm^{-1} were collected using a Nicolet FTIR Spectrometer at Massey University. The system has got a smart purge system to reduce water vapour in the measurement chamber. This is particularly important for low wavenumber region because of the strong absorption

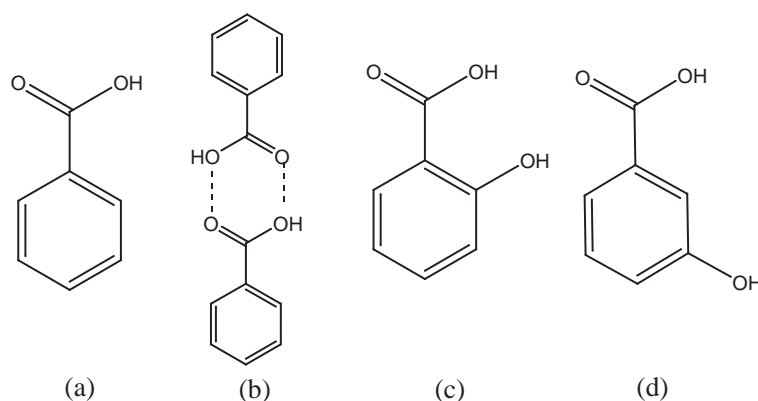


Figure 8.6 – Structures of the compounds considered for this study; Benzoic acid (a) monomer and (b) dimer, (c) 2-hydroxy benzoic acid, and (d) 3-hydroxy benzoic acid.

band of water molecules in this frequency range.

Samples for Raman spectroscopy were prepared using standard procedures to grow crystals from the compounds in powder form purchased from Sigma Aldrich. The low wave-number Raman spectra of the crystals under study were investigated using a Jobin-Yvon Horiba T6400 triple grating Raman Spectrometer integrated with a confocal microscope with an objective set to 50x. The system was pumped by a He-Ne laser at 633 nm. Low temperature Raman spectra were recorded using the same spectrometer employing a computer controlled cooling system marketed by Linkam scientific instruments that uses cooled nitrogen gas.

8.3.2 Spectrum of benzoic acid derivatives

Structures of the benzoic acid and its derivatives such as 2-hydroxy benzoic acid (salicylic acid) and 3-hydroxy benzoic acid are shown in Fig. 8.6. Results from the Raman experiment on benzoic acid derivatives is shown in Fig. 8.7. Data from THz and FTIR spectroscopy for these compounds are shown in Fig. 8.8. The calculated and literature values for the vibrational modes and the mode assignments are summarised in Table 8.1 along with the results from our calculations using time dependent density functional theory (DFT) at the level of B3LYP/6-31G* using the package GAUSSIAN 09 [136]. The experimental values show a reasonably good agreement with the calculated values from literature and our DFT calculations.

Results from the Raman and IR spectroscopy in THz energy region are compared. The most exciting feature of this comparative study of benzoic acid derivatives using both Raman and THz spectroscopy is that the spectra is more dense in the

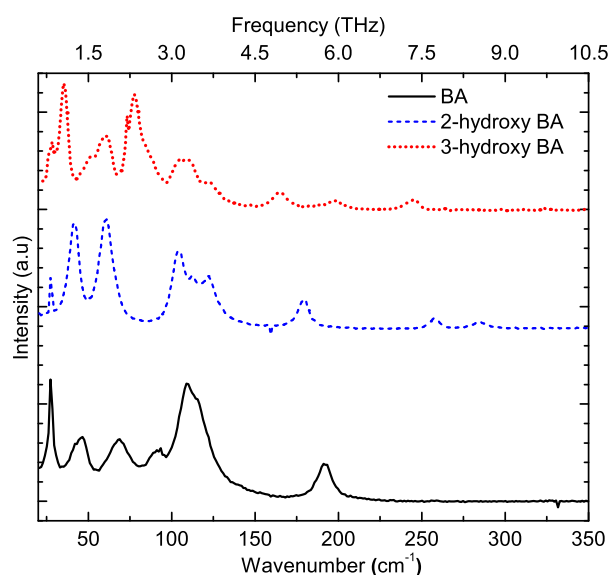


Figure 8.7 – Raman spectra of benzoic acid, 2-hydroxy benzoic acid, and 3-hydroxy benzoic acid for energies corresponding to the THz region.

THz frequency regime for both Raman and IR spectroscopy. In addition, despite similar structure, these materials have well differentiable spectral features making fingerprint of the material mostly between 1 and 3 THz. This is an example for the use of THz spectroscopy for identification of materials. Mode assignment shows that the vibrational modes of benzoic acid derivatives follow the general selection rule of spectroscopy, that is, in a centrosymmetric material both Raman and IR modes are not allowed simultaneously. However, because of the density of the spectrum the modes are observed close to each other.

8.3.3 Spectrum of aspirin

Acetylsalicylic acid (Aspirin) is a salicylate drug, often used to reduce fever, and as an anti-inflammatory medication. Salicylic acid has been found as one of the major impurities in Aspirin, this is because Aspirin is rapidly hydrolysed to salicylic acid which is also an active component [144, 145]. Though Salicylic acid is responsible for some of the beneficial properties of aspirin such as its anti-inflammatory action, presence of salicylic acid in aspirin often cause adverse effects such as gastric irritation during oral aspirin administration. It has long been an interesting subject of interest to detect the salicylic acid impurity in aspirin. That involves, high performance

Table 8.1 – Summary of the experimental and calculated (in brackets) vibrational modes of benzoic acid (BA), 2-hydroxy benzoic acid (3-OH BA) and 3-hydroxy benzoic acid (3-OH BA). The calculated values were obtained from our DFT calculations and literature values [135, 139, 141, 142, 143]. The modes are assigned based on the simulation as well as the available literature values; τ : torsion, mr: monomer rocking, v : stretching, δ : shearing, τ : torsion, β : in-plane bending and γ : out-of-plane bending.

BA (cm^{-1})	2-OH BA (cm^{-1})	3-OH BA (cm^{-1})	Approximate description	Active in
17 (21)	20 (21)	18 (21)	butterfly	IR
27 (21)	27 (21)	27 (21)	butterfly	Raman
34 (32)	34 (32)	34 (32)	torsion ‘twist’	IR
41 (40)	40 (40)	41 (40)	mr ‘oop’	IR
47 (45)	42	35	mr ‘oop’	Raman
49 (51)	52	49	v (OH \cdots O)	IR
58 (59)	66 (68)	58 (59)	cogwheel	IR
68 (68)	50 (68)	61 (60)	cogwheel	Raman
71 (68)	76	71	cogwheel	IR
82 (85)	–	82 (85)	τ (-COOH)	IR
91 (87)	–	–	v (OH \cdots O) ‘in-plane’	Raman
108 (103)	–	109 (103)	δ (OH \cdots O)	Raman
109 (105)	106 (103)	105 (105)	δ (OH \cdots O)	IR
114 (111)	112 (111)	–	δ (OH \cdots O)	Raman
121 (122)	126 (126)	122 (122)	v (OH \cdots O)	Raman
–	163 (168)	162 (168)	γ (Ph \cdots COOH)	IR
–	174 (175)	–	γ (Ph \cdots COOH)	IR
–	179 (175)	–	γ (Ph \cdots COOH)	Raman
–	–	165 (170)	v (CH)	Raman
191 (196)	–	198 (196)	τ (CC)	Raman
–	257(336)	245(336)	τ (CC)	Raman
–	284 (283)	–	v (CO \cdots O)+ β (CC)	Raman
288(283)	–	295 (283)	v (CO \cdots O)+ β (CC)	IR

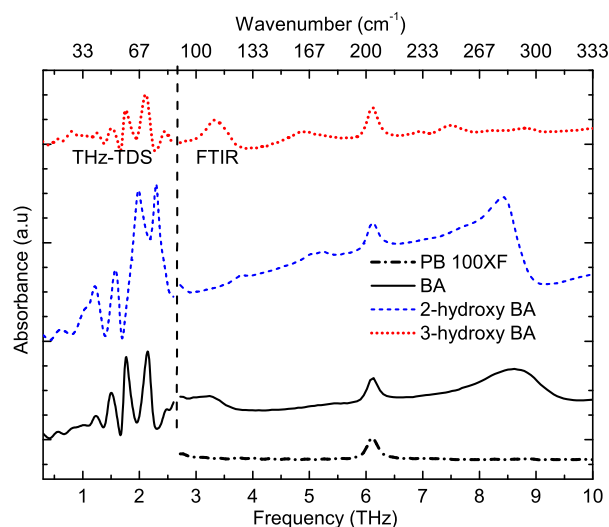


Figure 8.8 – Infrared absorption spectra of benzoic acid, 2-hydroxy benzoic acid, and 3-hydroxy benzoic acid for the THz region. Also shown is the spectra of PB100XF (dash-dotted curve). The FTIR spectroscopy data were translated vertically to match the THz-TDS.

liquid chromatography (HPLC) [146]. THz spectra of these two materials have already been discussed elsewhere and more advanced THz spectroscopic techniques on the investigation of the fingerprints of these compounds are discussed in Ref. [147]. In this section Raman spectra of aspirin and salicylic acid in the THz energy region is compared to investigate the fingerprint of these two materials in THz frequency range. Fig. 8.9 shows the Raman spectrum of Aspirin in the low wavenumber region. A clearly identifiable Raman signature observed in the THz region is an example for the use of THz frequency range for material characterisation.

8.3.4 Spectrum of nitro derivatives of toluene

Aromatic compounds containing nitro (NO_2) groups are sensitive to the THz frequency range because the vibrations associated with the benzene ring such as the information shown in Table 8.1 are present with substantial shifting of the vibrations due to the nitro group. In additions to that the torsion of the nitro group as well as the intermolecular modes leaves fingerprint of nitro- containing aromatic group in the THz frequency region. In this section two of the nitro derivatives of toluene, namely 4-Nitrotoluene (4-NT) and 2,4-Dinitrotoluene (2,4-DNT), are studied to show their Raman fingerprints in THz region. THz spectroscopy of these materials have been discussed in articles such as, for example, Ref. [148]. Low wavenumber Raman

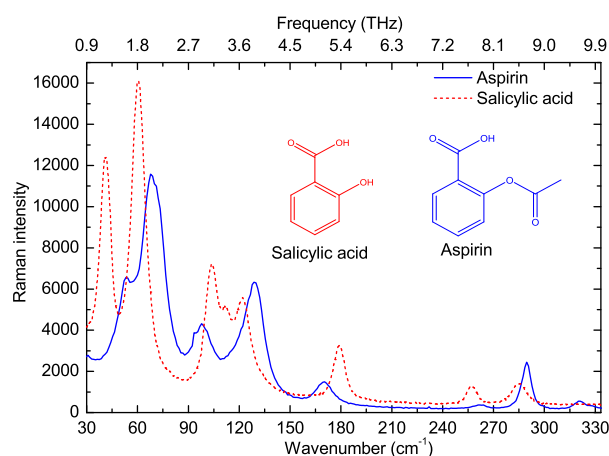


Figure 8.9 – Low wavenumber Raman spectrum of Aspirin and Salicylic acid. Structure the monomer units of both compounds are shown inset.

spectroscopy of 4-NT and 2,4-DNT shown in Fig. 8.10 are compared to show the signatures of these compounds in the Raman spectrum in the THz frequency range.

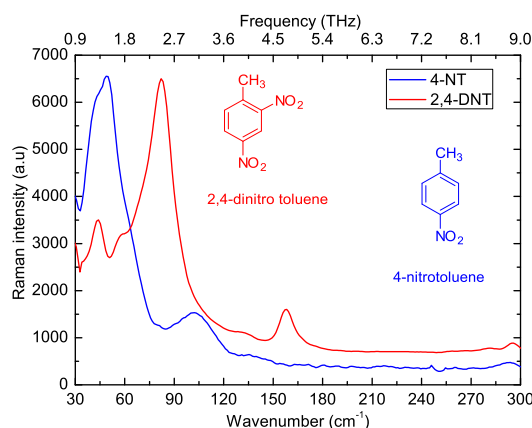


Figure 8.10 – Low wavenumber Raman on 4-nitro toluene (4-NT) and 2,4-dinitro toluene (2,4-DNT) in the THz frequency range.

8.4 Temperature dependence of low energy vibrational modes

Temperature dependent vibrational spectra at low wavenumber are considered to be particularly useful in understanding the complex inter- and intra- molecular vibrations and the role of hydrogen bond interactions. For example, temperature dependent low energy far-IR studies of the vibrational modes in carboxylic acids

and benzoic acid by Takahashi *et al.* [149] showed that there were additional absorption peaks that cannot be observed or resolved at room temperature. While THz measurements have been made on 2-hydroxy benzoic acid at 13 K, 80 K, and room temperature [150], there are no reports of temperature dependent Raman spectra in the low energy region. Also we have investigated the effect of temperature of the low energy Raman spectrum of 2,4-DNT. Experimental results from the temperature dependent low energy Raman spectroscopy are discussed in following section.

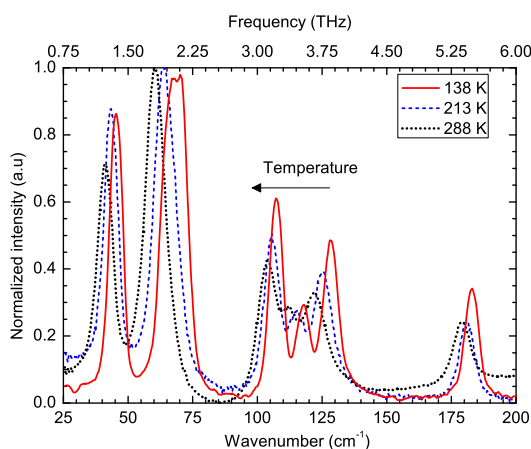


Figure 8.11 – Raman spectra of 2-hydroxy benzoic acid (Salicylic Acid) for energies in the THz region and at 138 K (solid curve), 213 K (dashed curve), and 288 K (dotted curve). The spectra have been scaled to the same peak height at 68 cm^{-1} .

8.4.1 Temperature dependence in salicylic acid

The Raman spectra at 138 K, 213 K and 288 K are shown in Fig. 8.11. It can be seen that there is a shift in the Raman peaks to lower wave-numbers (red shift) as the temperature is increased. This was also observed in a recent THz study at 13 K, 80 K and 295 K [150]. There is also a broadening of the vibrational modes at higher temperatures that suppresses some of the modes. For example, the 288 K peak at 112 cm^{-1} corresponds to hydrogen bond shearing and it is difficult to see because of the more intense 106 cm^{-1} (hydrogen bond shearing) and 126 cm^{-1} (hydrogen bond stretching) peaks. The temperature dependent broadening of vibrational modes can be attributed to a change in the length and strength of hydrogen bonding with temperature due to the symmetry induced breakdown of the Born-Oppenheimer approximation as discussed in detail in [151] and references therein. Broader peaks were also observed at room temperature from THz measurements on polycrystalline

salicylic acid samples [150] where more peaks are observed at 13 K. However, the temperature dependent broadening is not as dramatic in our Raman data when compared with the THz data. This may be due to the use of single crystals in our study when compared with powders in the THz study.

8.4.2 Temperature dependent Raman in 2,4-DNT

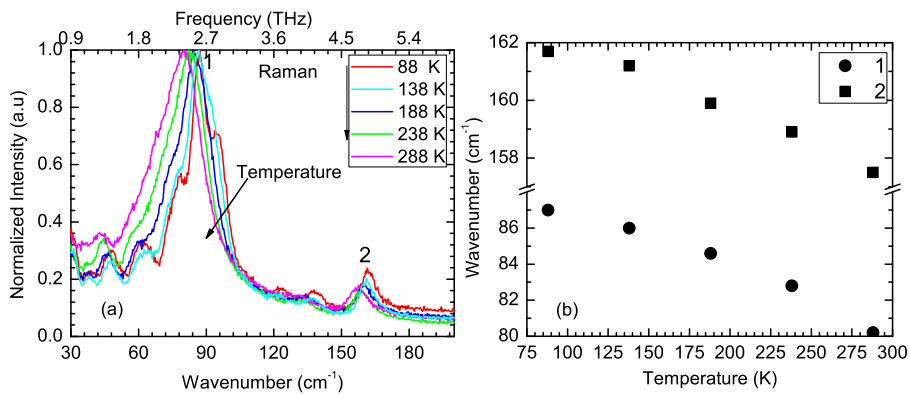


Figure 8.12 – (a) Temperature dependent low wavenumber Raman spectrum of 2,4-DNT; Temperature ranges from 88 K to 288 K. (b) Temperature dependence of the energy of Raman lines indicated as 1 and 2 in (a).

Temperature dependence of Raman spectra have been studied in 2,4-DNT for the temperature ranges from 88 K to 288 K. The results are shown in Fig. 8.12(a). We have used a wider temperature range compared to the experiments performed on salicylic acid as shown in previous section.

The effects of temperature we observed on the low energy Raman spectrum of 2,4-DNT can be summarised as follows: (1) A line broadening with increasing temperature. (2) Red-shift with increasing temperature as summarised in Fig. 8.12(b). The line broadening with temperature can be attributed to the distribution in the distance between monomers. The red shift appears due to the thermal expansion of the hydrogen bonding that leads to a reduced bond strength resulting in a red-shift of the corresponding Raman peak.

8.5 Conclusions

A systematic scheme for the evaluation of EO polymers in THz frequency region is discussed. The EO polymer made of APC and an organic NLO chromophore, PYR-3, has a large coherence length for THz generation through optical rectification of

a near IR pulse. Also, the polymer shows no strong absorption in the wider THz region. A THz system using the EO polymers discussed in this study is being developed in our group in IRL.

Raman and IR infrared spectra in the THz frequency range were measured for some organic compounds. The experimental data show good agreement with the theoretical calculations and reported literature values. The low energy Raman spectra of 2,4-DNT was measured down to 88 K, we find that there is a broadening of the vibrational modes when approaching room temperature. Using recrystallised compounds for Raman spectroscopy helped us experimentally find some of the theoretically expected modes of 2,4-DNT that were not reportedly found experimentally. Temperature dependent Raman on salicylic acid is consistent with a previous temperature dependent THz study. However, the Raman spectra are not as broadened by temperature when compared with the THz spectra, which is likely to be due to the use of single crystals in our study. We find that that PB100XF (by Micropowder Inc., USA) is an efficient, cost effective and stable additive for sample preparation for THz spectroscopy.

Chapter 9

Summary

The motivation of this study was to research and develop new materials for THz generation and detection. Properties of electro-optic (EO) polymers containing organic nonlinear optical (NLO) chromophores have mainly been investigated in this thesis. This includes fabrication of polymer EO films, general quantitative analysis, measurement of their electro-optical and photo-chemical properties, and investigating their properties in the terahertz (THz) frequency range.

The results from measurements of the EO coefficient, r_{33} , on polymers based on chromophores synthesized from our group are discussed in Chapter 5. Experiments have been made on a range of chromophores to estimate their r_{33} in poled polymers. Structural modifications made on the chromophores have been demonstrated to lead to a large and stable EO effect. One of the key findings is the effect of bulky substitution. This leads to a significant enhancement of the efficiency of the NLO chromophores with a large EO activity together with a long term stability of the EO activity. Further experiments to investigate the effect of photostability of this structural modification have demonstrated that the large EO activity was achieved without compromising any other qualities. There is a large difference between the measured value of r_{33} at 1 kHz and the theoretically calculated value from the first hyperpolarisability. This effect is discussed based on the contribution from effects other than the individual NLO response of chromophores. A low r_{33} at high frequency makes the EO polymers studied in the thesis not particularly useful in THz applications. However, a large EO activity at low frequency may allow them to be used in low frequency applications such as EO modulators and wavelength shifters.

Modulation of diffraction efficiency in a grating using the NLO chromophores using a static electric field was demonstrated in Chapter 6. This method is based on the modulation of the refractive index by the applied field. The motivation for this technique is to estimate the EO coefficient at zero applied field and to compare the resultant r_{33} with that estimated from the Teng man method. It was found that the measured EO coefficient is not purely due to the contribution from individual chromophores. The measured EO effect is over-estimated due to the modulation of film thickness by the inverse piezoelectric effect and thin film interference.

Photostability experiment was made on a range of NLO chromophores in different physical conditions and the results reported in Chapter 7. A photodegradation model based on multiple photodegradation quantum efficiencies has been developed. This shows good agreement with the experimental data. The photodegradation quantum efficiency of the chromophores at different chromophore concentrations as well as light intensities were measured and the mechanism of enhanced photodegradation quantum efficiency at high optical intensity is explained using a oxygen mediated photodegradation model. The effect of chromophore concentration on photostability is explained using the inter-chromophore energy transfer mechanism. Methods to enhance optical stability via quenching of singlet oxygen and also by quenching of triplet excited state of the chromophore are investigated using beta-carotene. Effects of structural alterations on the photostability of chromophores was also investigated. The addition of a bulky group for enhanced EO response showed no reduction in optical stability demonstrating an over-all efficiency by the bulky substitution. A paradoxical result from ring-locking in two different chromophores is explained using the bond length alternation (BLA) parameter. A trade-off between the NLO property and photostability is observed in the chromophores of a given donor-acceptor pair when tuning the BLA parameter for high molecular nonlinearity.

A systematic scheme for the evaluation of EO polymers in THz frequency region is discussed in chapter 8. Simulations demonstrated the polymer films made using our NLO chromophores in APC showed excellent phase matching for THz generation. A large coherence length is important for the generation of high power and wide-band THz radiation. The importance of low energy vibrational spectroscopy for material characterization and identification is discussed. The Raman and IR spectrum in the THz region are compared for a set of carboxylic acid dimers. A new host matrix was used to perform THz spectroscopy. It is found that PB100XF

is an efficient, cost effective and stable additive for sample preparation in THz spectroscopy. Temperature dependent low wave number Raman studies were made to investigate the effect of temperature on low energy vibrational modes. Inhomogeneous line broadening and red shifts are the two major effects observed when the temperature increases from low temperature to room temperature in low wave number Raman spectroscopy.

Future prospects

The EO materials have turned out to be showing less EO activity at high frequencies. However, the high r_{33} show that it can be used in low frequency applications. The resonance observed in Teng-Man ellipsometry is not favored when the polymers are used for switching in that frequency range. So the thickness effect on this resonance needs to be performed before using these materials for applications such as low frequency optical switching devices. The effects of interference on the measurement of EO coefficient can be significantly reduced by using thin films. The modulation of the film thickness by the electric field and a resulting modulation of the interference can be used in diffraction grating to make low frequency modulators.

Further studies need to be done on the relationship between BLA and photostability. Currently the studies have been done only on two types of two different chromophores. Also, two of the chromophores did not give good crystals that made the crystallography study difficult. To extend this study, experiments need to be done on more chromophores derived from the same donor-acceptor pair but having different BLA values obtained by ring-locking or changing conjugation length. This can help to develop a general relationship between BLA and photostability similar to the relationship between the BLA and the molecular NLO property of the chromophores.

The temperature dependent vibrational spectra needs to be done by THz and Raman measurements to get a complete temperature dependence of the low energy vibrational modes of the compounds that have been studied in this thesis. The vibrational modes are relatively close in the low energy region and this can be used as a tool to investigate Fermi resonances and inhomogeneous broadening that are observed in the compounds investigated.

Bibliography

- [1] L. R. Dalton. Nonlinear optical polymeric materials: From chromophore design to commercial applications. In Kwang-Sup Lee, editor, *Polymers for Photonics Applications I*, volume 158 of *Advances in Polymer Science*, pages 1–86. Springer Berlin / Heidelberg, 2002.
- [2] Ch. Bosshard, K. Sutter, Ph. Pretre, J. Hulliger, M. Florsheimer, P. Kaatz, and P. Gunter. *Organic Nonlinear Optical Materials.- Advances in Nonlinear Optics Series, Vol 1*. Gordon and Breach Science Publishers SA, Switzerland, 2001.
- [3] M. J. Weber. *Handbook of Optical Materials*. CRC Press, 2002.
- [4] D. M. Burland, R. D. Miller, and C. A. Walsh. Second-order nonlinearity in poled-polymer systems. *Chem. Rev.*, 94:31–75, 1994.
- [5] J. D. Zook, D. Chen, and G. N. Otto. Temperature dependence and model of the electro-optic effect in LiNbO₃. *Appl. Phys. Lett.*, 11:159–161, 1967.
- [6] E. H. Turner. High frequency electro-optic coefficient of lithium niobate. *Appl. Phys. Lett.*, 8:303–304, 1966.
- [7] K. F. Hulme, P. H. Davies, and V. M. Cound. The signs of the electro-optic coefficient for lithium niobate. *J. Phys. C: Solid State Physics*, 2:855–57, 1969.
- [8] R. E. Nahory and H. Y. Fan. Optical properties of zinc telluride. *Phys. Rev.*, 156:825–833, Apr 1967.
- [9] I. Wilke and S. Sengupta. *Nonlinear Optical Techniques for Terahertz Pulse Generation and Detection – Optical Rectification and Electrooptic Sampling*, volume Terahertz Spectroscopy of *Optical Science and Engineering*. CRC Press, 2007.

- [10] P. D. Cunningham, N. N. Valdes, F. A. Vallejo, L. M. Hayden, B. Polishak, X.-H. Zhou, J. Luo, A. K.-Y. Jen, J. C. Williams, and R. J. Twieg. Broadband terahertz characterization of the refractive index and absorption of some important polymeric and organic electro-optic materials. *J. Appl. Phys.*, 109(4):043505, 2011.
- [11] H. Ma, A. K.-Y. Jen, and L. R. Dalton. Polymer based optical waveguides: materials, processing and devices. *Adv. Mater.*, 2002.
- [12] L. R. Dalton. Rational design of organic electro-optic materials. *J. Phys.: Condens. Matter*, 15:R897–R934, 2003.
- [13] S. Bauer. Poled polymers for sensors and photonic applications. *J. Appl. Phys.*, 80(10):5531–58, 1996.
- [14] D. R. Kanis, M. A. Ratner, and T. J. Marks. Design and construction of molecular assemblies with large second-order optical nonlinearities. Quantum chemical aspects. *Chem. Rev.*, 94(1):195–242, 1994.
- [15] J. L. Oudar. Optical nonlinearities of conjugated molecules. stilbene derivatives and highly polar aromatic compounds. *J. Chem. Phys.*, 67(2):446, 1977.
- [16] S. J. Lalama and A. F. Garito. Origin of the nonlinear second-order optical susceptibilities of organic systems. *Phys. Rev. A*, 20:1179, 1979.
- [17] G. Bourhill, J.-L. Bredas, L.-T. Cheng, S. R. Marder, F. Meyers, J. W. Perry, and B. G. Tiemann. Experimental demonstration of the dependence of the first hyperpolarizability of donor-acceptor-substituted polyenes on the ground-state polarization and bond length alternation. *J. Am. Chem. Soc.*, 116(6):2619, 1994.
- [18] S. R. Marder, D. N. Beratan, and L.-T. Cheng. Approaches for optimizing the first electronic hyperpolarizability of conjugated organic molecules. *Science*, 252(5002):103, 1991.
- [19] S. R. Marder, L.-T. Cheng, B. G. Tiemann, A. C. Friedli, M. Blanchard-Desce, J. W. Perry, and J. Skindhøj. Large first hyperpolarizabilities in push-pull polyenes by tuning of the bond length alternation and aromaticity. *Science*, 263(5146):511–514, 1994.

- [20] C. B. Gorman and S. R. Marder. An investigation of the interrelationships between linear and nonlinear polarizabilities and bond-length alternation in conjugated organic molecules. *Proc. Natl. Acad. Sci. USA*, 90(23):11297–11301, 1993.
- [21] S. R. Marder, C. B. Gorman, F. Meyers, J. W. Perry, G. Bourhill, J.-L. Brédas, and B. M. Pierce. A unified description of linear and nonlinear polarization in organic polymethine dyes. *Science*, 265(5172):632, 1994.
- [22] S. R. Marder, J. W. Perry, B. G. Tiemann, C. B. Gorman, S. Gilmour, S. L. Biddle, and G. Bourhill. Direct observation of reduced bond-length alternation in donor/acceptor polyenes. *J. Am. Chem. Soc.*, 115(6):2524, 1993.
- [23] G. Bourhill, J.-L. Bredas, L.-T. Cheng, S. R. Marder, F. Meyers, J. W. Perry, and B. G. Tiemann. Experimental demonstration of the dependence of the first hyperpolarizability of donor-acceptor-substituted polyenes on the ground-state polarization and bond length alternation. *J. Am. Chem. Soc.*, 116(6):2619, 1994.
- [24] S. G. Raymond, G. V. M. Williams, B. Lochocki, M. D. H. Bhuiyan, A. J. Kay, and J. W. Quilty. The effects of oxygen concentration and light intensity on the photostability of zwitterionic chromophores. *J. Appl. Phys.*, 105(11):113123, 2009.
- [25] G. Gupta, W. H. Steier, Y. Liao, J. Luo, L. R. Dalton, and A. K.-Y. Jen. Modeling Photobleaching of Optical Chromophores: Light Intensity Effects in Precise Trimming of Integrated Polymer Devices. *J. Phys. Chem. C*, 112:8051–8060, 2008.
- [26] G. J. Smith, C. L. Dunford, A. J. Kay, and A. D. Woolhouse. The effects of molecular aggregation and isomerization on the fluorescence of push-pull hyperpolarizable chromophores. *J. Photoch. Photobio. A*, 179:237, 2006.
- [27] P. C. Ray and J. Leszczynski. Nonlinear optical properties of highly conjugated push-pull porphyrin aggregates: Role of intermolecular interaction. *Chem. Phys. Lett.*, 419:548, 2006.
- [28] A. Marini, A. Muñoz-Losa, A. Biancardi, and B. Mennucci. What is solvatochromism? *J. Phys. Chem. B*, 114(51):17128–17135, 2010.

- [29] C. Reichardt. Solvatochromic dyes as solvent polarity indicators. *Chem. Rev.*, 94(8):2319–2358, 1994.
- [30] M. Tonouchi. Cutting-edge terahertz technology. *Nature Photonics*, 1:97–105, 2007.
- [31] Y. Levy, M. Dumont, E. Chastaing, P. Robin, P. A. Chollet, G. Gadret, and F. Kajzar. *Nonlinear Optics*, 4:1–19, 1993.
- [32] D. M. Mittleman, M. Gupta, R. Neelamani, R. G. Baraniuk, J. V. Rudd, and M. Koch. *Appl. Phys. B*, 68:1085–1094, 1999.
- [33] A. M. Sinyukov and M. L. Hayden. Efficient electrooptic polymers for thz applications. *J. Phy. Chem. B*, 108(25):8515–8522, 2004.
- [34] A. Nahata, A. S. Weling, and T. F. Heinz. A wideband coherent terahertz spectroscopy system using optical rectification and electro-optic sampling. *Appl. Phys. Lett.*, 69(16):2321–2323, 1996.
- [35] Laurell Technologies Corporation, www.laurell.com.
- [36] Perkin Elmer Inc. Lambda 1050 spectrophotometer, www.perkinelmer.com.
- [37] Ocean Optics. Inc. S2000 miniature fiber optic spectrometer, www.oceanoptics.com.
- [38] Metricon Corporation. The Metricon model 2010/M prism coupler, www.metricon.com.
- [39] C. C. Teng and H. T. Man. Simple reflection technique for measuring the electro-optic coefficient of poled polymers. *Appl. Phys. Lett.*, 56(18):1734–1736, 1990.
- [40] J. S. Schildkraut. Determination of the electrooptic coefficient of a poled polymer film. *Appl. Opt.*, 29(19):2839–2841, 1990.
- [41] Y. Shuto and M. Amano. Reflection measurement technique of electro-optic coefficients in lithium niobate crystals and poled polymer films. *J. Appl. Phys.*, 77(9):4632–4638, 1995.
- [42] Thermo Scientific. Nicolet FTIR Spectrometer, www.thermoscientific.com.

- [43] D. Psaltis. Coherent optical information systems. *Science*, 298:1359, 2002.
- [44] P. U. Jepsen, R. H. Jacobsen, and S. R. Keiding. Generation and detection of terahertz pulses from biased semiconductor antennas. *J. Opt. Soc. Am. B*, 13(11):2424–2436, 1996.
- [45] Z-Omega Terahertz Corporation. Z-3 Terahertz Time Domain Spectrometer, www.zomega-terahertz.com.
- [46] Victoria University of Wellington. Raman laboratory, www.victoria.ac.nz/raman/.
- [47] J. W. Quilty. Glass slide cleaning procedure for the preparation of ultra-clean surfaces for spin processing. Technical report, Industrial Research Limited, Wellington, New Zealand, 2008.
- [48] G. V. M. Williams. *The properties of a-Ge/a-SiO superlattices*. PhD thesis, Victoria University of Wellington, New Zealand, 1990.
- [49] J. W. Quilty. Host-guest polymer films: Spin-processing and casting for photonics research. Technical report, Industrial Research Limited, Wellington, New Zealand, 2010.
- [50] J. W. Quilty. Calculation of macroscopic optical nonlinearity from microscopic optical nonlinearity. Technical report, Industrial Research Limited, Wellington, New Zealand, 2011.
- [51] F. Fitrilawati, M. O. Tjia, S. Pfeiffer, H.-H. Horhold, A. Deutesfeld, H. Eichenner, and C. Bubeck. Planar waveguides of ppv derivatives: attenuation loss, third-harmonic generation and photostability. *Opt. Mater.*, 21:511 – 519, 2003.
- [52] S. Janssens. *New materials for ultrafast switching and optical regeneration*. PhD thesis, Victoria University of Wellington, 2012.
- [53] W. Sellmeier. Zur Erklärung der abnormen Farbenfolge im Spectrum einiger Substanzen. *Annalen der Physik und Chemie*, 219:272–282, 1871.
- [54] K. D. Singer, J. E. Sohn, and S. J. Lalama. Second harmonic generation in poled polymer films. *Appl. Phys. Lett.*, 49(5):248–250, 1986.

- [55] D. R. Robello, P. T. Dao, J. Phelan, J. Revelli, J. S. Schildkraut, M. Scozzafava, A. Ulman, and C. S. Willand. Linear polymers for nonlinear optics. 2. synthesis and electrooptical properties of polymers bearing pendant chromophores with methylsulfonyl electron-acceptor groups. *Chem. Mat.*, 4(2):425–435, 1992.
- [56] K. D. Singer, M. G. Kuzyk, and J. E. Sohn. Second-order nonlinear-optical processes in orientationally ordered materials: relationship between molecular and macroscopic properties. *J. Opt. Soc. Am. B*, 4(6):968–976, 1987.
- [57] K. D. Singer, M. G. Kuzyk, W. R. Holland, J. E. Sohn, S. J. Lalama, R. B. Comizzoli, H. E. Katz, and M. L. Schilling. Electro-optic phase modulation and optical second-harmonic generation in corona-poled polymer films. *Appl. Phys. Lett.*, 53(19):1800–1802, 1988.
- [58] G.-M. Yang, S. Bauer-Gogonea, G. M. Sessler, S. Bauer, W. Ren, W. Wirges, and R. Gerhard-Multhaupt. Selective poling of nonlinear optical polymer films by means of a monoenergetic electron beam. *Appl. Phys. Lett.*, 64(1):22–24, 1994.
- [59] Ş. Yilmaz, S. Bauer, and R. Gerhard-Multhaupt. Photothermal poling of nonlinear optical polymer films. *Appl. Phys. Lett.*, 64(21):2770–2772, 1994.
- [60] Z. Sekkat and M. Dumont. Photoassisted poling of azo dye doped polymeric films at room temperature. *Appl. Phys. B: Lasers and Optics*, 54:486–489, 1992.
- [61] J. W. Quilty, G. V. M. Williams, D. Bhuiyan, M. Ashraf, S. Raymond, and A. J. Kay. The electro-optic response of a zwitterionic non-linear optical (NLO) material. *AIP Conference Proceedings*, 1151(1):79–81, 2009.
- [62] Y. Kutuvantavida, G. V. M. Williams, J. W. Quilty, M. D. H. Bhuiyan, and A. J. Kay. High electro-optic coefficient in organic nlo polymers: Poling and study of the relaxation process. *Materials Science Forum*, 700:154, 2011.
- [63] M. D. H. Bhuiyan, G. J. Gainsford, Y. Kutuvantavida, J. W. Quilty, A. J. Kay, G. V. M. Williams, and M. R. Waterland.

- Synthesis, structural and nonlinear optical properties of 2-(3-cyano-4-5-[1-(2-Hydroxyethyl)-3,3-Dimethyl-1,3-Dihydro-Indol-2-ylidene]-Penta-1,3-dienyl-5,5-dimethyl-5h-furan-2-ylidene)-malononitrile. *Mol. Cryst. Liq. Cryst.*, 548(1):272–283, 2011.
- [64] J. W. Quilty and G. V. M. Williams. Tunable bragg gratings in polymer thin films. *Materials Science Forum*, 700:158, 2011.
- [65] M. Sprave, R. Blum, and M. Eich. High electric field conduction mechanisms in electrode poling of electro-optic polymers. *Appl. Phys. Lett.*, 69(20):2962–2964, 1996.
- [66] G. M. Sessler, B. Hahn, and D. Y. Yoon. Electrical conduction in polyimide films. *J. Appl. Phys.*, 60(1):318, 1986.
- [67] G. V. M. Williams, Y. Kutuvantavida, S. Janssens, S. G. Raymond, My T. T. Do, M. D. H. Bhuiyan, J. W. Quilty, N. Denton, and A. J. Kay. The effects of excited state lifetime, optical intensity, and excited state quenchers on the photostability of zwitterionic chromophores. *J. Appl. Phys.*, 110(8):083524, 2011.
- [68] D. J. Clarke, A. P. Middleton, A. Teshome, M. D. H. Bhuiyan, M. Ashraf, G. J. Gainsford, I. Asselberghs, K. Clays, G. J. Smith, and A. J. Kay. Synthesis and properties of zwitterionic chromophores containing substituents for shape control. In *AIP Conf. Proc.*, volume 1151, pages 90–93, 2009.
- [69] D. H. Park, C. H. Lee, and W. N. Herman. Analysis of multiple reflection effects in reflective measurements of electro-optic coefficients of poled polymers in multilayer structures. *Opt. Express*, 14(19):8866 – 8884, 2006.
- [70] D. H. Park, C. H. Lee, and W. N. Herman. Analysis of multiple reflection effects in reflective measurements of electro-optic coefficients of poled polymers in multilayer structures. *Opt. Express*, 14(19):8866–8884, 2006.
- [71] F. Michelotti, G. Nicolao, F. Tesi, and M. Bertolotti. On the measurement of the electro-optic properties of poled side-chain copolymer films with a modified teng-man technique. *Chem. Phys.*, 245:311 – 326, 1999.

- [72] E. M. McKenna, A. S. Lin, A. R. Mickelson, R. Dinu, and D. Jin. Comparison of r_{33} values for AJ404 films prepared with parallel plate and corona poling. *J. Opt. Soc. Am. B*, 24(11):2888–2892, 2007.
- [73] K. D. Singer and L. A. King. Relaxation phenomena in polymer nonlinear optical materials. *J. Appl. Phys.*, 70(6):3251–3255, 1991.
- [74] R. D. Dureiko, D. E. Schuele, and K. D. Singer. Modeling relaxation processes in poled electro-optic polymer films. *J. Opt. Soc. Am. B*, 15(1):338–350, 1998.
- [75] T. Goodson and C. H. Wang. Dipolar orientational relaxation in guest/host amorphous polymer probed by second harmonic generation. *Macromolecules*, 26(8):1837–1840, 1993.
- [76] G. Williams and D. C. Watts. Non-symmetrical dielectric relaxation behaviour arising from a simple empirical decay function. *Trans. Faraday Soc.*, 66:80–85, 1970.
- [77] M. Stähelin, D. M. Burland, M. Ebert, R. D. Miller, B. A. Smith, R. J. Twieg, W. Volksen, and C. A. Walsh. Re-evaluation of the thermal stability of optically nonlinear polymeric guest-host systems. *Appl. Phys. Lett.*, 61(14):1626–1628, 1992.
- [78] A. Teshome, M. D. H. Bhuiyan, M. Ashraf, G. J. Gainsford, A. J. Kay, S. V. Cleuvenbergen, I. Asselberghs, and K. Clays. Optimizing the second-order nonlinear optical response in some indoline based chromophores at the molecular and macroscopic levels. *Proc. SPIE*, 8113:81130G1–81130G14, 2011.
- [79] M. D. H. Bhuiyan, M. Ashraf, A. Teshome, G. J. Gainsford, A. J. Kay, I. Asselberghs, and K. Clays. Synthesis, linear and non linear optical (nlo) properties of some indoline based chromophores. *Dyes and Pigments*, 89(2):177–187, 2011.
- [80] J. L. Oudar and D. S. Chemla. Hyperpolarizabilities of the nitroanilines and their relations to the excited state dipole moment. *J. Chem. Phys.*, 66(6):2664–2668, 1977.
- [81] M. D. H. Bhuiyan, M. Ashraf, A. Teshome, G. J. Gainsford, I. Asselberghs K. Clays, and A. J. Kay. *Dyes and Pigments*, submitted to, 2010.

- [82] G. J. Gainsford, M. D. H. Bhuiyan, and A. J. Kay. 2-(3-Cyano-4-7-[1-(2-hydroxyethyl)-3,3-dimethylindolin-2-ylidene]hepta-1,3,5-trienyl-5,5-dimethyl-2,5-dihydrofuran-2-ylidene)malononitrile. *Acta Cryst. E*, 67(11):o3026, 2011.
- [83] A. Teshome, A. J. Kay, A. D. Woolhouse, K. Clays, I. Asselberghs, and G. J. Smith. Strategies for optimising the second-order nonlinear optical response in zwitterionic merocyanine dyes. *Opt. Mater.*, 31(4):575 – 582, 2009.
- [84] A. J. Kay, A. D. Woolhouse, Y. Zhao, and K. Clays. Synthesis and linear/nonlinear optical properties of a new class of 'RHS' NLO chromophore. *J. Mater. Chem.*, 14(8):1321–1330, 2004.
- [85] T.-D. Kim, J.-W. Kang, J. Luo, S.-H. Jang, J.-W. Ka, N. Tucker, J. B. Benedict, L. R. Dalton, T. Gray, R. M. Overney, D. H. Park, W. N. Herman, and A. K.-Y. Jen. Ultralarge and thermally stable electro-optic activities from supramolecular self-assembled molecular glasses. *J. Am. Chem. Soc.*, 129(3):488–489, 2007.
- [86] G. J. Smith, A. P. Middleton, D. J. Clarke, A. Teshome, A. J. Kay, M. D. H. Bhuiyan, I. Asselberghs, and K. Clays. The effect of solvent on the excited vibronic states and first hyperpolarizability of push pull merocyanines. *Opt. Mater.*, 32:1237, 2010.
- [87] R. Spreiter, Ch. Bosshard, F. Pan, and P. Günter. High-frequency response and acoustic phonon contribution of the linear electro-optic effect in dast. *Opt. Lett.*, 22(8):564–566, 1997.
- [88] F. Zhang. *Electro-optic Properties of Semiconductor Nano-crystals And Electro-optic Polymers And Their Applications*. PhD thesis, VirginiaTech University, The United States, 2002.
- [89] Ch. Bosshard, K. Sutter, R. Schlessler, and P. Günter. Electro-optic effects in molecular crystals. *J. Opt. Soc. Am. B*, 10(5):867–885, 1993.
- [90] M. Y. Balakina and O. D. Fominykh. The quantum-chemical study of small clusters of organic chromophores: Topological analysis and nonlinear optical properties. *Int. J. Quantum Chem.*, 108(14):2678–2692, 2008.

- [91] P. Guenter. Electro-optical and nonlinear-optical materials. *Ferroelectrics*, 24(1):35–42, 1980.
- [92] M. D. Zoppo, M. Tommasini, C. Castiglioni, and G. Zerbi. A relationship between raman and infrared spectra: the case of push-pull molecules. *Chem. Phys. Lett.*, 287(1-2):100 – 108, 1998.
- [93] J. W. Quilty. X-ray diffraction data. *Private Communication, Industrial Research Limited*, 2011.
- [94] M. Abarkan, J. P. Salvestrini, M. Aillerie, and M. D. Fontana. Frequency dispersion of electro-optical properties over a wide range by means of time-response analysis. *Appl. Opt.*, 42(13):2346–2353, May 2003.
- [95] S. Ducharme, J. Feinberg, and R. R. Neurgaonkar. Electrooptic and piezoelectric measurements in photorefractive barium titanate and strontium barium niobate. *Quantum Electronics, IEEE Journal of*, 23(12):2116–2121, 1987.
- [96] M. Brucherseifer, M. Nagel, B. P. Haring, H. Kurz, A. Bosserhoff, and R. Burtner. Label-free probing of the binding state of dna by time-domain terahertz sensing. *Appl. Phys. Lett.*, 77(24), 2000.
- [97] M. Sinha and D. J. Buckley. *Acoustic Properties of Polymers*. Springer, 2007.
- [98] Y. Okuno, S. Yokoyama, and S. Mashiko. Interaction between monomeric units of donor-acceptor-functionalized azobenzene dendrimers: Effects on macroscopic configuration and first hyperpolarizability. *J. Phys. Chem. B*, 105(11):2163–2169, 2001.
- [99] S. D. Bella, M. A. Ratner, and T. J. Marks. Design of chromophoric molecular assemblies with large second-order optical nonlinearities. a theoretical analysis of the role of intermolecular interactions. *J. Am. Chem. Soc.*, 114(14):5842–5849, 1992.
- [100] A. Teshome, M. D. H. Bhuiyan, M. Ashraf, G. J. Gainsford, A. J. Kay, S. V. Cleuvenbergen, I. Asselberghs, and K. Clays. Optimizing the second-order nonlinear optical response in some indoline based chromophores at the molecular and macroscopic levels. In *Proceedings of SPIE*, volume 8113, 2011.

- [101] A. Inoue, S.-I. Inoue, and S. Yokoyama. Enhanced electro-optic response of a poled polymer in a reflective microcavity. *Opt. Comm.*, 283(14):2935 – 2938, 2010.
- [102] L. Jin, K. Yonekura, and K. Takizawa. Effect of multiple reflections on accuracy of electro-optic coefficient measurements. *Jpn. J. Appl. Phys.*, 46(12):7904–7911, 2007.
- [103] I. Nee, O. Beyer, M. Müller, and K. Buse. Multichannel wavelength-division multiplexing with thermally fixed bragg gratings in photorefractive lithium niobate crystals. *J. Opt. Soc. Am. B*, 20(8):1593, 2003.
- [104] G. Brambilla and V. Pruneri. Enhanced photosensitivity in silicate optical fibers by thermal treatment. *Appl. Phys. Lett.*, 90(11):111905, 2007.
- [105] M. Haw. Holographic data storage: The light fantastic. *Nature*, 422:556, 2003.
- [106] R. Magnusson and T. K. Gaylord. Analysis of multiwave diffraction of thick gratings. *J. Opt. Soc. Am.*, 67(9):1165–1170, 1977.
- [107] R. Alferness. Analysis of propagation at the second-order bragg angle of a thick holographic grating. *J. Opt. Soc. Am.*, 66(4):353–362, 1976.
- [108] H. Kogelnik. Coupled wave theory for thick hologram gratings. *Bell Syst. Tech. J.*, 48(9):2909, 1969.
- [109] R. Magnusson and T. K. Gaylord. Diffraction regimes of transmission gratings. *J. Opt. Soc. Am.*, 68(6):809, 1978.
- [110] F. G. Kaspar. Diffraction by thick, periodically stratified gratings with complex dielectric constant. *J. Opt. Soc. Am.*, 63(1):37–45, 1973.
- [111] G. V. M. Williams, C. Dotzler, A. Edgar, and S. G. Raymond. Ultraviolet induced absorption and bragg grating inscription in $\text{RbCdF}_3:\text{Mn}^{2+}$. *J. Appl. Phys.*, 102(11):113106, 2007.
- [112] S. G. Raymond, P. Wagner, M. Panczyk, G. V. M. Williams, K. J. Stevens, I. Monfils, D. Hirst, J. Whaanga, Y. Kutuvantavida, M. D. H. Bhuiyan, and A. J. Kay. Development of fibre bragg grating based strain/temperature sensing system. Proc. SPIE 8258, Organic Photonic Materials and Devices XIV, 82581L:82581L–82581L–8, 2012.

- [113] A. Teshome, A. J. Kay, A. D. Woolhouse, K. Clays, I. Asselberghs, and G. J. Smith. Strategies for optimising the second-order nonlinear optical response in zwitterionic merocyanine dyes. *Opt. Mater.*, 31:575, 2009.
- [114] A. Dubois, M. Canva, A. Brun, F. Chaput, and Jean-Pierre Boilot. Photostability of dye molecules trapped in solid matrices. *Appl. optics*, 35:3193, 1996.
- [115] C. Schweitzer and R. Schmidt. Physical Mechanisms of Generation and Deactivation of Singlet Oxygen. *Chem. Rev.*, 103:1685–1757, 2003.
- [116] Y.-H. Kuo. *Optical trimming of electro-optical polymer devices using photo-bleaching*. PhD thesis, University of Southern California, 2006.
- [117] S. G. Raymond, G. V. M. Williams, B. Lochocki, M. D. H. Bhuiyan, A. J. Kay, and J. W. Quilty. The effects of oxygen concentration and light intensity on the photostability of zwitterionic chromophores. *J. Appl. Phys.*, 105:113123, 2009.
- [118] S. G. Raymond, G. V. M. Williams, M. T. T. Do, S. Janssens, B. Lochocki, M. D. H. Bhuiyan, and A. J. Kay. Photoluminescence and optical studies of photodegradation in nonlinear optical organic chromophores. *Proceedings of SPIE Europe, Optics and Optoelectronics*, 7354, 2009.
- [119] S. Ito, H. Katayama, and M. Yamamoto. Excited Triplet State of Carbazole Chromophore and the Triplet Energy Migration in Poly[(carbazolyethyl methacrylate)-co-(methyl methacrylate)] Film. *Macromolecules*, 21:2456, 1988.
- [120] R. A. Keller and L. J. Dolby. Intramolecular Energy Transfer between Triplet States of Weakly Interacting Chromophores.3 Compounds in Which the Chromophores Are Separated by a Rigid Steroid Bridge. *J. Am. Chem. Soc.*, 91:1293, 1969.
- [121] M. T. T. Do, S. Janssens, S. G. Raymond, G. V. M. Williams, D. H. Bhuiyan, and A. J. Kay. Photodegradation of Nonlinear Optical Organic Films with Varying Optical Intensity. *Proceedings of the Australasian Conference on Optics, Lasers and Spectroscopy (ACOLS)*, 2009.

- [122] Y. Ren, M. Szablewski, and G. H. Cross. Waveguide photodegradation of nonlinear optical organic chromophores in polymeric films. *Appl. optics*, 39:2499, 2000.
- [123] J. W. Quilty. *Private Communication, Industrial Research Limited*, 2011.
- [124] A. G. Gonzalez, G. I. Stegeman, A. K-Y. Jen, X. Wu, M. Canva, A. C. Kowalczyk, X. Q. Zhang, H. S. Lackritz, S. Marder, S. Thayumanavan, and G. Levina. Photostability of electro-optic polymers possessing chromophores with efficient amino donors and cyano-containing acceptors. *J. Opt. Soc. Am.*, 18(12):1846 – 1853, 2001.
- [125] D. Rezzonico, M. Jazbinsek, P. Gunre, C. Bosshard, D. H. Bale, Y. Liao, L. R. Dalton, and P. J. Reid. Photostability studies of pi-conjugated chromophores with resonant and nonresonant light excitation for long-life polymeric telecommunication devices. *J. Opt. Soc. Am. B*, 24:2199, 2007.
- [126] A. Penzkofer and Y. Lu. Fluorescence quenching of rhodamine 6g in methanol at high concentration. *Chem. Phys.*, 103:399, 1986.
- [127] A. Polyakova, R. Y. F. Liu, D.A. Schiraldi, A. Hiltner, and E. Baer. Oxygen-Barrier Properties of Copolymers Based on Ethylene Terephthalate. *J. Polym. Sci. Pol. Phys.*, 39:1889–1899, 2001.
- [128] A. G. Gonzalez, M. Canva, and G. I. Stegeman. Systematic behavior of electro-optic chromophore photostability. *Opt. lett.*, 25:323, 2000.
- [129] A. G. Gonzalez, M. Canva, G. I. Stegeman, R. Twieg, K. P. Chan, T. C. Kowalczyk, X. Q. Zhang, H. S. Lackritz, S. Marder, and S. Thayumanavan. Systematic behavior of electro-optic chromophore photostability. *Opt. Lett.*, 25(5):332–334, 2000.
- [130] L. M. Hayden, G. F. Sauter, F. R. Ore, P. L. Pasillas, J. M. Hoover, G. A. Lindsay, and R. A. Henry. Second-order nonlinear optical measurements in guest-host and side-chain polymers. *J. Appl. Phys.*, 68(2):456–465, 1990.
- [131] G. V. Zakharova and A. K. Chibisov. Photostability of Pseudoisocyanine J Aggregates in Polymer Films and Ways of Its Improvement. *Photochemistry*, 43:294, 2008.

- [132] I. V. Golovnin, A. A. Bakulin, S. A. Zapunidy, E. M. Nechvolodova, and D. Y. Paraschuk. Dramatic enhancement of photo-oxidation stability of a conjugated polymer in blends with organic acceptor. *Appl. Phys. Lett.*, 92:243311, 2008.
- [133] T. Polivka and V. Sundstrøm. Dark excited states of carotenoids: Consensus and controversy. *Chem. Phys. Lett.*, 477:1 – 11, 2009.
- [134] M. Blanchard-Desce, V. Alain, P. V. Bedworth, S. R. Marder, A. Fort, C. Runser, M. Barzoukas, S. Lebus, and R. Wortmann. Large quadratic hyperpolarizabilities with donor-acceptor polyenes exhibiting optimum bond length alternation: Correlation between structure and hyperpolarizability. *Chem. Eur. J.*, 3(7):1091–1104, 1997.
- [135] M. Boczar, Ł. Boda, and M. J. Wójcik. Theoretical modeling of the O–H stretching IR bands of hydrogen-bonded dimers of benzoic acid in S_0 and S_1 electronic states. *J. Chem. Phys.*, 127(8):084307, 2007.
- [136] M. J. Frisch, G. W. Trucks, H. B. Schlegel, G. E. Scuseria, M. A. Robb, J. R. Cheeseman, G. Scalmani, V. Barone, B. Mennucci, G. A. Petersson, H. Nakatsuji, M. Caricato, X. Li, H. P. Hratchian, A. F. Izmaylov, J. Bloino, G. Zheng, J. L. Sonnenberg, M. Hada, M. Ehara, K. Toyota, R. Fukuda, J. Hasegawa, M. Ishida, T. Nakajima, Y. Honda, O. Kitao, H. Nakai, T. Vreven, J. A. Montgomery, Jr., J. E. Peralta, F. Ogliaro, M. Bearpark, J. J. Heyd, E. Brothers, K. N. Kudin, V. N. Staroverov, R. Kobayashi, J. Normand, K. Raghavachari, A. Rendell, J. C. Burant, S. S. Iyengar, J. Tomasi, M. Cossi, N. Rega, J. M. Millam, M. Klene, J. E. Knox, J. B. Cross, V. Bakken, C. Adamo, J. Jaramillo, R. Gomperts, R. E. Stratmann, O. Yazyev, A. J. Austin, R. Cammi, C. Pomelli, J. W. Ochterski, R. L. Martin, K. Morokuma, V. G. Zakrzewski, G. A. Voth, P. Salvador, J. J. Dannenberg, S. Dapprich, A. D. Daniels, Ö. Farkas, J. B. Foresman, J. V. Ortiz, J. Cioslowski, and D. J. Fox. Gaussian 09 Revision A.1. Gaussian Inc. Wallingford CT 2009.
- [137] K. L. Vodopyanov. Optical generation of narrow-band terahertz packets in periodically inverted electro-optic crystals: conversion efficiency and optimal laser pulse format. *Opt. Express*, 14(6):2263–2276, 2006.
- [138] C. V. McLaughlin, L. M. Hayden, B. Polishak, S. Huang, J. Luo, T. D. Kim, and A. K.-Y. Jen. Wideband 15 THz response using organic electro-optic

- polymer emitter-sensor pairs at telecommunication wavelengths. *Appl. Phys. Lett.*, 92(15):151107, 2008.
- [139] L. Colombo and K. Furić. Low-frequency raman spectrum of benzoic single crystals. *Spectrochimica Acta Part A: Molecular Spectroscopy*, 27(9):1773 – 1784, 1971.
- [140] B. Scherger, M. Scheller, C. Jansen, M. Koch, and K. Wiesauer. Tera-hertz lenses made by compression molding of micropowders. *Appl. Opt.*, 50(15):2256–2262, 2011.
- [141] M. Boczar, K. Szczeponek, M. J. Wójcik, and C. Paluszkiwicz. Theoretical modeling of infrared spectra of benzoic acid and its deuterated derivative. *J. Mol. Struct.*, 700(1-3):39 – 48, 2004.
- [142] G. Klausberger, K. Furić, and L. Colombo. Vibrational spectra and normal mode calculations of benzoic acid single crystals. *J. Raman Spectroscopy*, 6(6):277–281, 1977.
- [143] U. Strom and P. C. Taylor. Temperature and frequency dependences of the far-infrared and microwave optical absorption in amorphous materials. *Phys. Rev. B*, 16:5512–5522, 1977.
- [144] C. G. Kontoyannis and M. Orkoula. Quantitative non-destructive determination of salicylic acid acetate in aspirin tablets by raman spectroscopy. *Talanta*, 41(11):1981 – 1984, 1994.
- [145] F. E. Blondino and P. R. Byron. The quantitative determination of aspirin and its degradation products in a model solution aerosol. *J. Pharmaceutical and Biomedical Analysis*, 13(2):111 – 119, 1995.
- [146] S. L. Ali. Application of gas-liquid chromatography and high-performance liquid chromatography to the analysis of trace amounts of salicylic acid, acetylsalicylic anhydride and acetylsalicylsalicylic acid in aspirin samples and aspirin formulations. *J. Chromatogr.*, 3(126):651–663, 1976.
- [147] N. Laman, S. S. Harsha, and D. Grischkowsky. Narrow-line waveguide terahertz time-domain spectroscopy of aspirin and aspirin precursors. *Applied Spectroscopy*, 62(3), 2008.

-
- [148] Y. Chen, H. Liu, and X.-C. Zhang. THz spectra of 4-NT and 2, 6-DNT. *Proc. SPIE*, 6212(62120P):7, 2006.
- [149] M. Takahashi, Y. Kawazoe, Y. Ishikawa, and H. Ito. Interpretation of temperature-dependent low frequency vibrational spectrum of solid-state benzoic acid dimer. *Chem. Phys. Lett.*, 479(4-6):211 – 217, 2009.
- [150] S. S. Harsha, J. S. Melinger, S. B. Qadri, and D. Grischkowsky. substrate independence of thz vibrational modes of polycrystalline thin films of molecular solids in waveguide thz-tds. *J. Appl. Phys.*, 111(2):023105, 2012.
- [151] R. C. Dougherty. Temperature and pressure dependence of hydrogen bond strength: A perturbation molecular orbital approach. *J. Chem. Phys.*, 109(17):7372–7378, 1998.

List of Publications

1. G. V. M. Williams, Y. Kutuvantavida, S. Janssens, S. G. Raymond, My T. T. Do, M. D. H. Bhuiyan, J. W. Quilty, N. Denton and A. J. Kay, "The effects of excited state lifetime, optical intensity and oxygen quenchers on the photostability of zwitterionic chromophores", *J. Appl. Phys.*, 110, 083524 (2011).
2. M. D. H. Bhuiyan, G. J. Gainsford, Y. Kutuvantavida, A. J. Kay, J. W. Quilty, and G. V. M. Williams, and M. R. Waterland, "Synthesis, Structural and Nonlinear Optical Properties of 2-(3-Cyano-4-5-[1-(2-Hydroxyethyl)-3,3-Dimethyl-1,3-Dihydro-Indol-2-ylidene]-Penta-1,3-dienyl-5,5-Dimethyl-5H -Furan -2-ylidene)-Malononitrile", *Mol. Cryst. Liq. Cryst.*, 48, 272-283 (2011).
3. Y. Kutuvantavida, G. V. M. Williams, S. Janssens, S. G. Raymond, M. D. H. Bhuiyan, and A. J. Kay, "Photostability Study of Structurally Modified Electro-Optic Chromophores and the Effect of Singlet Oxygen Quenchers", *Proceedings of the IQEC/CLEO Pacific Rim 2011*, Optical Society of America, C1092, (2011).
4. Y. Kutuvantavida, G. V. M. Williams, J. W. Quilty, M. D. H. Bhuiyan and A. J. Kay, "High Electro-Optic Coefficient in Organic NLO Polymers: Poling and Study of the Relaxation Process", *Materials Science Forum*, 700, 154-157 (2012).
5. S. G. Raymond, P. Wagner, M. Panczyk, G. V. M. Williams, K. J. Stevens, I. Monfils, D. Hirst, J. Whaanga, Y. Kutuvantavida, M. D. H. Bhuiyan and A. J. Kay, "Development of fibre Bragg grating based strain/temperature sensing system", *Proc. SPIE* 8258, 82581L (2012).
6. Y. Kutuvantavida, G. V. M. Williams, E. M. Pogson, M. D. H. Bhuiyan,

K. Radhanpura, and R. A. Lewis, "Material Characterization at Low Frequencies Using THz and Raman Spectroscopy", *IEEE Conference Proceedings: 37th International Conference on Infrared, Millimeter, and Terahertz Waves (IRMMW-THz 2012)*, 6380457, 1-3 (2012)